Università degli Studi di Trieste

XXXI Ciclo di Dottorato in Fisica

GRAPHENE GROWTH ON CRYSTALLINE AND POLYCRYSTALLINE NICKEL SURFACES: INSIGHT FROM NUMERICAL SIMULATIONS

PhD STUDENT:
Virginia Carnevali

PhD SUPERVISOR:
Prof. Maria Peressi

PhD COORDINATOR:
Prof. Livio Lanceri

Academic year 2017 - 2018

Università degli Studi di Trieste

XXXI Ciclo di Dottorato in Fisica

GRAPHENE GROWTH ON CRYSTALLINE AND POLYCRYSTALLINE NICKEL SURFACES: INSIGHT FROM NUMERICAL SIMULATIONS

PhD STUDENT:
Virginia Carnevali

PhD SUPERVISOR:
Prof. Maria Peressi

PhD COORDINATOR:
Prof. Livio Lanceri

Academic year 2017 - 2018

"Per tutto quello che é stato: grazie.

A tutto quello che verrá: sí."

Takashi Paolo Nagai

Abstract

Research in epitaxial graphene on transition metals has witnessed an unprecedented prosperity for the last decade, owing to the rich electronic and chemical properties induced at the interfaces. Moreover, the use of graphene-based materials in the field of catalysis has attracted increasing interest in the last few years. Indeed, due to its large exposed surface area, graphene is expected to be an excellent support material for catalysts. The ability to tune its structure, controlling for instance the abundance and the nature of defects or the zoo of the moiré domains formed according to the local registry with the substrate, has added significant versatility to graphene-based metal-free catalytic systems. The close-packed (111)/(0001) faces of fcc/hcp transition metals are generally used as catalytic substrates for graphene epitaxial growth on single crystal surfaces, due to their high thermodynamic stability and compatible symmetry with graphene.

In this thesis, we start analysing epitaxial graphene on single crystal (111) and (100) Nickel surfaces as fundamental starting points to model the case of cheaper polycrystalline Nickel substrates. Through *ab-initio* computational techniques based on Density Functional Theory (DFT) we characterize the ground state structure and the electronic properties of the system, while its dynamical evolution is studied through a home-made Kinetic Monte Carlo (KMC) code. Both simulation methods are thoroughly explained in the first part of the thesis. The results are continuously compared with the experimental findings, giving both a critical feedback of the quality of our studies and helping the understanding and the interpretation of the experimental observations.

Graphene can be easily grown by Chemical Vapor Deposition (CVD) on polycrystalline nickel substrate, adapting itself to crystal surface modulations without any lattice break or discontinuity. The configuration of graphene depends on the mismatch and the misorientation angle between the hexagonal graphene lattice and the one of the underlying Nickel surface (Ni(111), Ni(100), Ni(010) etc.). A part from the case of graphene on Ni(111) surface, in general the epitaxial graphene is not flat and the modulation of its structure can originate local peculiar environments for nanoconfined catalysis.

First, we characterized by Scanning Tunneling Microscopy (STM) simulations and experimental measurements the intrinsic vacancy defective structures of epitaxial graphene on (111) Nickel surface (Gr/Ni(111)). Trapping of Nickel adatoms is generally favored on these structures, whereas empty vacancies are not and the stability and the bonding configuration of the observed Ni-doping defects are discussed in light of the calculated charge distribution.

Concerning the stable structures of graphene on (100) Nickel surface (Gr/Ni(100)), a systematic study has been done in function of the misorientation angle between the two lattices. DFT simulations shed light on spatial corrugation and interfacial interactions: depending on the misorientation angle, graphene is either alternately physi- and chemisorbed or uniformly

chemisorbed, the interaction being modulated by (sub) nanometer-sized moiré superstructures. The electronic properties were investigated combining Scanning Tunneling Microscopy (STM) and Scanning Tunneling Spectroscopy (STS) simulations, highlighting the peculiarities of the different moiré regions, in excellent agreement with the experimental findings. Ni(100) micrograins appear to be a promising substrate to finely tailor the electronic properties of graphene at the nanoscale, with relevant perspective applications in electronics and catalysis. Furthermore, we addresses the problem of the moiré superlattices stability. KMC and DFT simulations have been used to study the evolution of the moiré patterns induced by carbide segregation at the Gr/Ni(100) interface observed by cooling down the sample.

The last part of this thesis has been devoted to simulate the interaction of graphene with a simple model of polycrystalline Nickel, combining together (100)-(111)-(010) surfaces. Evidence of surface steps bunch opening in Gr/Ni(100) system has been experimentally observed by STM, and always the graphene foil follows the surface modification without breaking. A systematic study for different stepped surfaces, with single- or multilayer steps with (111) or (110) facets, has been addressed in order to understand how one single layer of graphene can adapt to a stepped surface.

Contents

List of Acronyms

BZ Brillouin Zone

Co Cobalt

Cu Copper

CVD Chemical Vapour Deposition

DB Dangling Bond

DV Displacement Vector

DFT Density Functional Theory

DoS Density of States

fcc Face Centered Cubic

FFT Fast Fourier Transform

GGA Generalized Gradient Approximation

Gr Graphene

h hollow

HK Höhenberg-Kohn

HTST Harmonic Transition State Theory

ILDoS Integrated Local Density of States

KS Kohn-Sham

LDA Local Density Approximation

LDoS Local Density of States

LMTO Linearized Muffin-Tin Orbital

KMC Kinetic Monte Carlo

NCPP Norm-Conserving Pseudopotentials

MD Molecular Dynamics

MEP Minimum Energy Path

ML Monolayer

n-moiré	network moiré
NEB	Nudged Elastic Bands
PBC	Periodic Boundary Conditions
PDoS	Projected Density of States
PP	Pseudopotentials
PW	Plane Waves
QE	Quantum ESPRESSO
s-moiré	stripe moiré
st	subtop
STM	Scanning Tunneling Microscopy
STS	Scanning Tunneling Spectroscopy
TM	Transition Metals
TMD	Transition Metal Dichalcogenide
TS	Transition State
TST	Transition State Theory
UHV	Ultra High Vacuum
USPP	UltraSoft Pseudopotentials
V	Vacancy

Introduction

In the present PhD thesis the interaction of graphene with crystalline and polycrystalline nickel surfaces, both from structural and electronic point of view, will be analyzed. In particular the graphene growth over Ni(111) and Ni(100) single crystal surfaces will be addressed, using quantum mechanical electronic structure simulations. The same will be done on stepped surfaces, which combine both (111) and (100) facets.

The aim of this work is to investigate in depth the structural and electronic properties of such systems for potential catalytic or electronic applications. The stability of these systems is fundamental and it will be studied through quantum mechanics and semi-empirical (based on quantum mechanics) methods. In the first part of the thesis, the computational methods used in this work will be described in detail, while in the second part all the main results will be presented. Computational details of the simulations are shown in a separate section at the end of each chapter of the results. Additional technical issues and secondary results will be explained in the Appendixes.

Ni(111) already captured the attention thanks to its catalytic activity in the synthesis of high quality graphene at temperature as low as 450 °C [1]. Due to this peculiarity, graphene on Ni(111) has been widely inspected both from experimental and theoretical point of view [2–5]. Recent studies revealed the actual possibility to introduce doping defects in graphene to tune its properties [6–8]. It has been shown that by adding proper gaseous precursor during the Chemical Vapor Deposition (CVD) process [9] or by means of low-energy ion implantation [10, 11], substitutional nitrogen atoms can be trapped inside carbon vacancies, strongly modifying the graphene electronic structure [9, 12]. These evidences introduce in the scientific scenario a new appealing way in functionalizing graphene by transition metal dopants. In particular, it is possible to induce a magnetic moment [13] and to add chemical activity [14, 15], enhancing the catalytic behavior of the layer with respect to small gaseous molecules of environmental importance [16]. From the theoretical side the literature lacks most. Studies on graphene doped vacancy defects over the (111) copper surface have been done, shedding light on how the substrate drastically changes the abundance and formation of these structures together with their diffusion energy barriers [17]. Although it appears really interesting for catalysis, less attention has been devoted to graphene with vacancy defects on Ni(111) and their electronic properties [18].

In this PhD thesis we have characterized graphene vacancy defects on Ni(111). Starting from experimental STM images with unprecedented resolution, we have done a wide analysis about the structural and electronic properties of vacancy defects, considering also the cases when Ni adatoms adsorb at the edge of the vacancy. Through ab-initio density-functional theory calculations we have identified the ground state atomic configuration of different defects. We have also simulated constant current scanning tunneling microscopy maps and compared with high-resolution scanning tunneling microscopy measurements as further confirmation of the correct identification of the vacancy defect structure. Finally, we have discussed the stability and the bonding configuration of the observed Ni-doping defects in light of the calculated charge distribution and we have demonstrated that the nickel atoms trapped inside the defects are more strongly bound to the edge of the defect than to the substrate.

Ni(100) is less studied as potential substrate for the graphene growth [19, 20] with respect to Ni(111), while it is well known for its surface reconstruction ("clock reconstruction") originated by the carbide formation (Ni_2C) [21, 22]. This occurs, to less extent, also on the Ni(111) surface [23]. However, the geometry mismatch between the hexagonal and square lattices of graphene and Ni(100), respectively, opens an interesting window for nano-confined catalysis. It has been already demonstrated that large lattice mismatch between graphene and its grow substrate, e.g. graphene on ruthenium (0001), rhodium (111), rhenium (0001), etc., cannot be accommodated by the elongation of the C-C bonds. As a consequence, moiré superstructures generally composed of a single rotational domain are found, giving origin to a strongly interacting systems; the accumulated strain is released by a significant buckling of the graphene lattice, which leads to alternate strongly- and weakly-interacting regions across the moiré supercells [17, 24–28]. Meanwhile, graphene adsorbed on few transition metals, such as copper and iridium, has a weak interaction with the overstrate and this turns into a large graphene-substrate interfacial spacing out of the range of chemisorption, smaller spatial corrugation of moirés with respect to strongly-coupled systems, and limited rotational alignment between graphene and the substrate [29–33]. Concerning the graphene ground state structure on (100) substrates (Cu(100), Ir(100) and Fe(100)), it is already known that the lattice mismatch induces a wide scenario of moiré superstructures (from striped- to network morphology), characterized by varying interaction strength with the substrate [34–37]. However, the issue of symmetry-mismatched graphene-metal interfaces is still only partially explored and sometimes controversial [20, 38] and, moreover, the literature on graphene adsorbed on Ni(100) substrate is quite limited.

In this PhD thesis the graphene moiré configurations over the Ni(100) substrate have been studied through ab-initio quantum mechanical simulations. It has been theoretically demonstrated that, as in the case of Cu(100), Ir(100) and Fe(100), the structural mismatch between graphene and Ni(100) is the origin of a huge zoo of moiré configurations depending on the misorientation angle between the graphene and nickel lattices. Two different moiré patterns have been simulated, stripe and network moiré, highlighting their structural and electronic properties and comparing them with the experimental findings, with an excellent agreemet. In particular, a coexistence of well-defined phys- and chemisorbed regions in the stripe-moiré has been found, thus suggesting a possible environment for selected catalysis due to the confined nano-environments at the graphene-nickel interface or above graphene.

As regards the graphene growing methods on metallic substrates, chemical vapor deposition (CVD) is the most used to achieve large area of graphene [39]. This technique can induce several different kinds of defects in the graphene sheet that are strictly related to the growth conditions (i.e. temperature and hydrocarbon flux) such as graphene rotational domain boundaries [40]. However, there have been only a few studies of the defects that may form during growth by CVD processes at metal surfaces [41] with respect to the kind of defects that this technique could potentially induce and their electronic properties.

In this PhD thesis we have studied some particular defects of the graphene stripe moiré on Ni(100) when graphene is grown by CVD. We have demonstrated through ab-initio quantum mechanical simulations that the big bright regions in the graphene moiré due to the local detachment of the chemisorbed regions of the moiré are due to the presence of some exceeding carbon atoms at the graphene-nickel interface. We have also wrote from scratch a Kinetic Monte Carlo code in order to study the evolution of these detachments and their stability in time, showing a strong correlation between the carbon concentration, the carbide formation and the detachments stability.

Finally, if we want to rationalize the behavior on realistic substrates used for graphene growth and applications, polycrystalline transition metal substrates are the one typically utilized. This is because polycrystalline metals used for graphene growth are generally composed of grains exposing a variety of surface orientations, e.g. (111), (100), and (110) orientations in fcc transition metals [1, 42, 43]. Furthermore, polycrystalline metallic surfaces can contain highly stepped regions, step bunches, grain boundaries and even amorphous areas. This constitutes the "material gap" that affects not only the conventional surface science experiments typically performed using single-crystal samples, but also simulations, that become much more complicated when more realistic systems are considered.

In this PhD thesis we have studied through ab-initio quantum mechanical simulations combined with a pure geometrical model the stability of Ni(100) bare stepped surfaces. We have found a decrease of step formation energy with the increase of the length of the terraces. The graphene ground state structure on Ni(100) stepped surfaces has been also addressed. Ab-initio quantum mechanical simulations indicate that the optimization of interface bonding and graphene lattice stress release are the driving force of the wide narrow nickel staircases at constant width. Excellent agreement has been found between STM simulations and measurements of sequences of constant terraces with the same width of graphene in the stripe-moiré configuration over the Ni(100) stepped surfaces.

These topics were treated in collaborations with other research groups. All the experimental measurements presented in this work have been acquired by the Surface and Reactivity Group led by Prof. G. Comelli from the University of Trieste and Dr. C. Africh from the "Istituto Officina dei Materiali" (IOM) of the Italian National Research Council (CNR), with the valuable contributions of Dr. L. L. Patera, G. Prandini and M. Jugovac for the project of graphene on Ni(111) and Dr. Z. Zou, Dr. A. Sala, Dr. M. Panighel and Dr. C. Cepek for the project of graphene on Ni(100).

As regards dynamical simulations, a collaboration with the Computer Simulations of Nanomaterials Group in Cordóba (Argentina) led by Prof. M. M. Mariscal has been carried on during all the three years of the PhD, spending more than two months in the first and second year at the Chemistry Faculty of the University of Cordóba. This collaboration was very useful and fruitful for learning the basic concepts of Kinetic Monte Carlo (KMC) simulations and, thanks to the essential contribution of Dr. G. J. Soldano, for developing from scratch a KMC code to study the carbon segregation process at graphene-Ni(100) interface.

Computational resources have been obtained from CINECA through the ISCRA initiative and the agreement with the University of Trieste.

In the following, a summary of the contents of each chapter is presented:

- **Chapter 1:** the theoretical framework of the quantum mechanical electronic structure simulations is presented. After a brief introduction on the basic concepts of Density Functional Theory (DFT), the technical parameters of *ab-initio* calculations are discussed together with the methods to implemented the electronic properties of the materials and the energy barriers for simple chemical reaction in the system under investigation.

- **Chapter 2:** the theoretical framework of KMC method to study the dynamical evolution of a system is presented. After a brief introduction on the statistical concepts under the KMC method, specific issues (determining rates, time achievable by a simulation, and the corresponding lattice in which the physical system is mapped) have been addressed.

- **Chapter 3:** a comprehensive study of vacancy defects in epitaxial graphene on (111) Nickel substrate is reported. The atomic-scale structure and the electronic properties of empty and Ni-healed graphene vacancy defects were studied thoroughly in details. An excellent matching between simulated and observed STM images has allowed a full identification of such defects in real samples.

- **Chapter 4 and Appendix A:** the symmetry mismatch between graphene and Ni(100) substrate causes a variety of moiré superstructures. An original mathematical model has been proposed to solve the general problem of determining the common superlattice from two Bravais lattices: the model provides the moiré primitive vectors (Appendix A). Two representative structures have been considered for Gr/Ni(100) and used for DFT electronic structure calculations. The electronic properties were investigated combining Scanning Tunneling Microscopy (STM) and Scanning Tunneling Spectroscopy (STS) simulations, highlighting the peculiarities of the different moiré regions, allowing an unambiguous interpretation of experimental results.

- **Chapter 5 and Appendix B:** KMC and DFT simulations have been used to study the evolution of the stripe-moiré pattern observed by cooling down the sample. DFT showed that the segregation at the Gr/Ni(100) interface of residual carbon from Ni substrate induces detachments of otherwise chemisorbed graphene stripes. The KMC code (Appendix B), specifically implemented for this system, is based on DFT ground states energies and energy barriers of about fifty single and cooperative elementary processes.

- **Chapter 6:** the stability of (100) Nickel stepped surfaces has been investigated through the introduction of several quantities related to the formation surface energy. The interaction of graphene with polycrystalline Nickel has been studied through DFT simulations, using simple models combining together terraces and steps energies.

- **Conclusions and outlook:** the main results are summarized and the possible directions for future outlook pointed out.

I. Computational approach

1

Ab-initio approach

In this chapter the theory and computational methods behind the electronic calculations performed in this thesis work are presented. Density Functional Theory (DFT) is a ground-state theory in which the many-body Schroedinger equation is recast as a functional of the electronic density. DFT has proved to be highly successful in combining a feasible computational workload to a very good description of structural and electronic properties in a vast class of materials. For these reasons DFT has become a common tool in ab initio calculations aimed at describing and predicting properties of condensed matter and molecular systems. The chapter is organized in three parts: in the first part the basic concepts of the ab initio DFT, in particular the Kohn-Sham approach, is presented; in the second part, some data post processing for calculation of electronic properties (Density of States (DoS), Scanning Tunneling Microscopy (STM) and Scanning Tunneling Spectroscopy (STS)) is described; in the third part the calculation of energy barriers for simple reaction paths is presented.

1.1. Many-body Schröedinger equation and Born-Oppenheimer approximation

On a fundamental level, any physical system of interest in matter physics (molecules, clusters of atoms or molecules, solids, surfaces, etc.) can be considered as an ensemble of electrons and nuclei mutually interacting according to the laws of quantum mechanics. So, in principle, each property of these systems can be found resolving the many-body Schrödinger equation with no need of any empirical parameters (*ab-initio* calculation), apart from the mass and charge of electrons and nuclei.

For a generic physical system composed by N_I nuclei of charge $Z_I e$ and mass M_I and by *N* electrons of charge -*e* and mass *m* the Hamiltonian *H* of the total system is:

$$H = T_e(\{\mathbf{p}\}) + T_N(\{\mathbf{P}\}) + V_{ee}(\{\mathbf{r}\}) + V_{NN}(\{\mathbf{R}\}) + V_{eN}(\{\mathbf{r}\},\{\mathbf{R}\}) \tag{1.1}$$

where T_e and T_N are the kinetic energies of electrons and nuclei respectively, V_{ee} is the electron-electron interaction, V_{eN} the electron-nucleus interaction and V_{NN} the nucleus-nucleus interaction. With the notation $\{\mathbf{r}\}$ ($\{\mathbf{R}\}$) and $\{\mathbf{p}\}$ ($\{\mathbf{P}\}$) the coordinates and momenta of the electrons (nuclei) are indicated. Considering the electrostatic interaction and neglecting any relativistic term, we have:

$$T_e(\{\mathbf{p}\}) = \sum_{i=1}^{N} \frac{\mathbf{p}_i^2}{2m} \qquad T_N(\{\mathbf{P}\}) = \sum_{I=1}^{N_I} \frac{\mathbf{P}_I^2}{2M_I} \tag{1.2}$$

$$V_{ee}(\{\mathbf{r}\}) = \frac{1}{2}\sum_{i\neq j} \frac{e^2}{|\mathbf{r}_i - \mathbf{r}_j|} \qquad V_{NN}(\{\mathbf{R}\}) = \frac{1}{2}\sum_{I\neq J} \frac{Z_I Z_J e^2}{|\mathbf{R}_I - \mathbf{R}_J|} \tag{1.3}$$

$$V_{eN}(\{\mathbf{r}\},\{\mathbf{R}\}) = -\sum_{i}^{N}\sum_{I}^{N_I}\frac{Z_I e^2}{|\mathbf{r}_i - \mathbf{R}_I|} \tag{1.4}$$

Solving the Schrödinger equation ($H\Psi_{tot} = E_{tot}\Psi_{tot}$) for these many-body systems is not a simple problem and, in order to be able to solve the equation, some approximations are necessary.

First of all, because the motion of the nuclei is typically on a time scale much longer than the electronic scale, the nuclei and the electrons motions can be separated (Born-Oppenheimer approximation): in this way we can write an electronic Hamiltonian H_e that contains the electronic terms and depends on the nuclei positions only as a parameter.
The eigenvalue problem to be solved becomes now:

$$H_e\Psi(\{\mathbf{r}\};\{\mathbf{R}\}) = E(\{\mathbf{R}\})\Psi(\{\mathbf{r}\};\{\mathbf{R}\}), \tag{1.5}$$

with

$$H_e = T_e + V_{ee} + V_{eN} + V_{NN}, \tag{1.6}$$

The energy $E(\{\mathbf{R}\})$, that is a function of the $\{\mathbf{R}\}$ coordinates, is a *potential energy surface* and is responsible of the dynamics of the nuclei. Using the Hellmann-Feynman theorem [44], the force $\mathbf{F}_I$ acting on the nucleus *I* can be easily found from the relation:

$$\mathbf{F}_I \equiv -\frac{\partial E(\{\mathbf{R}\})}{\partial \mathbf{R}_I} = -\left\langle \Psi(\{\mathbf{r}\};\{\mathbf{R}\}) \middle| \frac{\partial H_e}{\partial \mathbf{R}_I} \middle| \Psi(\{\mathbf{r}\};\{\mathbf{R}\}) \right\rangle \tag{1.7}$$

1.2. Höhenberg-Kohn theorems

Solving Eq.1.5 for the electrons is still a formidable task and in the course of time different methods to find the solution have been proposed. The one that nowadays is the most used in ab initio electronic structure calculations is the Density Functional Theory (DFT) formulated by Hohenberg and Kohn in 1964 [45] which is a ground state theory for correlated many-body systems. DFT is based on two theorems, namely *Hohenberg-Kohn Theorems*, formulated and demonstrated in [45].

- **Theorem I**: For any system of interacting particles in an external potential V_{ext}, the potential V_{ext} is determined uniquely, apart from a constant, by the ground state density $n_0(\mathbf{r})$

$$\begin{tikzcd}
\mathbf{V}_{\mathrm{ext}} \arrow[d] & \mathbf{n_0}(\mathrm{r}) \arrow[l, "\text{H-K}"'] \\
\boldsymbol{\Psi}_{\mathrm{i}}(\{\mathrm{r}\}) \arrow[r] & \boldsymbol{\Psi}_{0}(\{\mathrm{r}\}) \arrow[u]
\end{tikzcd}$$

Figure 1.1: Schematic diagram of the first Hohenberg-Kohn (H-K) theorem. From the usual solution of the Schrödinger equation it is evident that the potential V_{ext} determines the ground state density $n_0(\mathbf{r})$: first determines all the eigenstates Ψ_i , hence also the ground state Ψ_0 , and eventually $n_0(\mathbf{r})$. The first Hohenberg-Kohn theorem says that is true also the vice versa: $n_0(\mathbf{r})$ determines V_{ext}

.

- **Theorem II**: For any external potential V_{ext}, it is possible to define the energy of the system as a functional of the density $n(\mathbf{r})$: $E = E[n]$. Moreover the ground state energy of the system is the minimum value of this functional and the density that minimizes the functional, keeping the number of electrons *N* constant, is the ground state density $n_0(\mathbf{r})$.

In this notation $V_{eN} = V_{ext} = \sum_i v_{ext}(\mathbf{r}_i)$ and then the *energy functional* $E[n]$ can be written as:

$$E[n] = F[n] + \int d\mathbf{r}\, v_{ext}(\mathbf{r}) n(\mathbf{r}) + E_{NN} \tag{1.8}$$

where

$$F[n] = T_e[n] + V_{ee}[n] \tag{1.9}$$

is independent from V_{ext} and common to every interacting electronic system.

Therefore, in principle, all ground state properties are completely determined from the minimization of the functional $E[n]$.

1.3. Kohn-Sham approach and Exchange-Correlation term

The main difficulty in applying the Hohenberg-Kohn theorems is that there are no prescriptions for the explicit determination of the universal functional $F[n]$ (Eq.1.9). This obstacle is overcome by the *Kohn-Sham approach*, that is the method actually used in the electronic structure calculations. The idea of Kohn and Sham [46] is to substitute the electronic interacting system with a more easily solvable auxiliary one, assuming that the ground state density of the original system is equal to that of some non-interacting system with an opportune fictitious potential. For this purpose let us rewrite the energy functional in Eq.1.8 in the following form:

$$E[n] = T_s[n] + \int d\mathbf{r}\, v_{ext}(\mathbf{r}) n(\mathbf{r}) + E_{Hartree}[n] + E_{NN} + E_{xc}[n], \tag{1.10}$$

where $T_s[n]$ is the kinetic energy functional of the auxiliary system and $E_{Hartree}[n]$ is the classical Coulomb interaction energy of the electron density $n(\mathbf{r})$ interacting with itself, which can be written as:

$$E_{Hartree}[n] = \frac{e^2}{2} \int d\mathbf{r}\, d\mathbf{r}' \, \frac{n(\mathbf{r}) n(\mathbf{r}')}{|\mathbf{r} - \mathbf{r}'|}. \tag{1.11}$$

All many-body effects of exchange and correlation are grouped into the exchange-correlation energy $E_{xc}[n]$ defined as:

$$E_{xc}[n] = T[n] - T_s[n] + V_{ee}[n] - E_{Hartree}[n]. \tag{1.12}$$

The electrons have also a spin, then the system has $N = N^{\uparrow} + N^{\downarrow}$ independent electrons and the ground state is obtained filling each of the N^{σ} orbitals $\Psi_i^{\sigma}(\mathbf{r})$ with the lowest eigenvalues of the auxiliary Hamiltonian (σ indicates the spin eigenvalue, $\sigma = \uparrow, \downarrow$).

The density $n(\mathbf{r})$ then is defined as:

$$n(\mathbf{r}) = \sum_{\sigma=\uparrow,\downarrow} n^{\sigma}(\mathbf{r}) = \sum_{\sigma=\uparrow,\downarrow} \sum_{i=1}^{N^{\sigma}} |\Psi_i^{\sigma}(\mathbf{r})|^2 \tag{1.13}$$

and

$$T_s[n] = \frac{1}{2} \sum_{\sigma=\uparrow,\downarrow} \sum_{i=1}^{N^{\sigma}} |\nabla \Psi_i^{\sigma}(\mathbf{r})|^2. \tag{1.14}$$

To obtain the Schrödinger-like equations determining the orbitals of the auxiliary system, we need to minimize the Eq.1.5 with respect to the density $n_\sigma(\mathbf{r})$. This leads to the *Kohn-Sham equations*:

$$H^\sigma_{KS}\Psi^\sigma_i(\mathbf{r}) = \varepsilon^\sigma_i\Psi^\sigma_i(\mathbf{r}), \tag{1.15}$$

where

$$H^\sigma_{KS} = -\frac{\hbar^2}{2m}\nabla^2 + v^\sigma_{eff}(\mathbf{r}) \tag{1.16}$$

and

$$v^\sigma_{eff}(\mathbf{r}) = v_{ext}(\mathbf{r}) + e^2\int d\mathbf{r}'\frac{n(\mathbf{r}')}{|\mathbf{r}-\mathbf{r}'|} + v^\sigma_{xc}(\mathbf{r}). \tag{1.17}$$

The last term $v_{xc}[n]$, that includes all the non classical electron interactions, is defined as:

$$v_{xc}[n] = \frac{\delta E_{xc}[n]}{\delta n^\sigma(\mathbf{r})}. \tag{1.18}$$

So the interacting many-body problem has been reduced to the computation of independent-particle equations (Eq.1.5), which must be solved self-consistently with the resulting density (Eq.1.13). It is important to note that, until this point, no approximations have been done. Hence, if the exact functional $E_{xc}[n]$ is known, the KS equations lead to the exact ground state density and energy (Eq.1.10) for the interacting system.

To implement DFT in a code and to solve the KS equations (Eq.1.15), some approximations and technicalities are needed. In the following, the most common technicalities adopted for the exchange-correlation term are explained.

The explicit form of exchange-correlation potential is not known and for this reason it is necessary to do a first approximation for an explicit form of $E_{xc}[n]$ term. However, because $E_{xc}[n]$ is defined explicitly separating the kinetic energy $T_s[n]$ and the long range Hartree term $E_{Hartree}[n]$, it is reasonable to assume that $E_{xc}[n]$ is a local functional of the density.

In the simplest approximation, called *Local Spin Density Approximation* (LSDA) [47], the exchange-correlation energy at each point in space is set to be equal to the exchange-correlation energy density of an homogeneous electron gas ε^{hom}_{xc} with that density:

$$E^{LSDA}_{xc}[n^\uparrow, n^\downarrow] = \int d\mathbf{r}\, n(\mathbf{r})\varepsilon^{hom}_{xc}(n^\uparrow(\mathbf{r}).n^\downarrow(\mathbf{r})). \tag{1.19}$$

The LSDA gives very accurate results, as expected, for systems with uniform or slowly varying densities and, surprisingly, gives also good results for systems with rapidly varying densities, such as surfaces. However, the LSDA typically underestimates interatomic distances and overestimates binding energies.

To overcome these difficulties another approach has been developed, called *Generalized Gradient Approximation* (GGA). In this approximation the exchange-correlation energy functional does not depend locally only on the density, as in the LSDA, but also on its gradient:

$$E^{GGA}_{xc}[n^\uparrow, n^\downarrow] = \int d\mathbf{r}\, n(\mathbf{r})\varepsilon^{hom}_{xc}(n(\mathbf{r}))F_{xc}(n^\uparrow, n^\downarrow, |\nabla n^\uparrow|, |\nabla n^\downarrow|), \tag{1.20}$$

where $\varepsilon^{hom}_{xc}(n(\mathbf{r}))$ is the exchange energy of a homogeneous unpolarised gas.

In most cases, although this is not a completely general rule, the GGA gives better results than LSDA. In this work the GGA with the parametrization of F_{xc} given by Perdew-Burke-Ernzerhof (PBE) [48] has been used.

The Self Consistent Field approach

To find the ground state of the system under investigation, the KS equations must be solved in a self-consistent way because the effective potential present in the KS equations is a functional of the density.

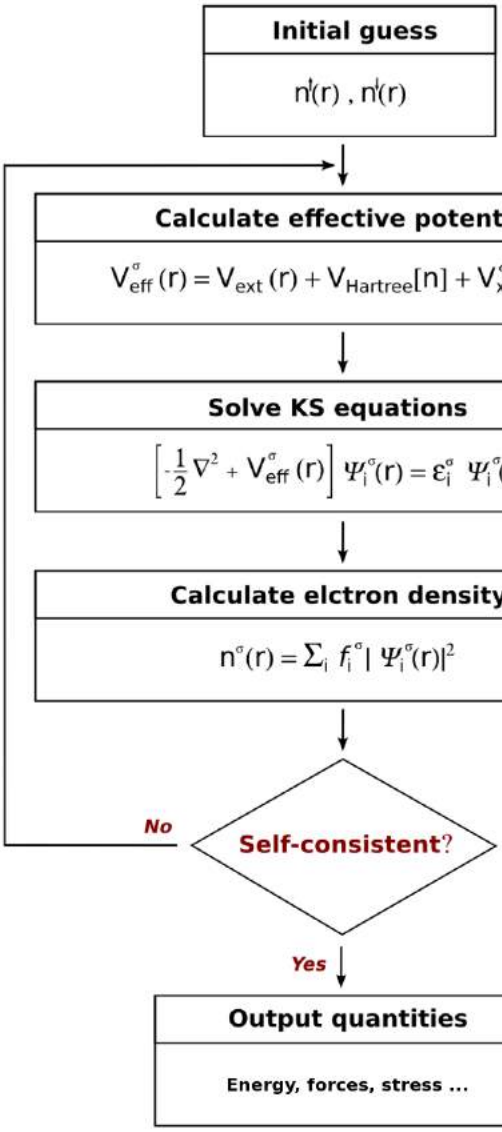

Figure 1.2: Schematic diagram of the self-consistent loop for the solution of the KS equations.

At the beginning an initial guess of the density must be made. By this, the effective potential entering in the KS equations is computed, the KS equations are solved and finally the density obtained by the KS orbitals is recalculated. At this point there are two possible situations: the input and output densities can differ by a quantity larger than the accuracy chosen for the computation; or the input and output densities are consistent (difference between the new density and the last is less than a threshold set at the beginning of calculation). If the first situation is true, the self-consistent loop must be restarted with a new initial guess of the density taken as an appropriate combination of input and output densities; while, if the second situation is satisfied, the KS are solved within the required threshold, the calculation ends and the output quantities are computed (total energy of the system, Hellman-Faynman forces, etc.) (Fig.1.2).

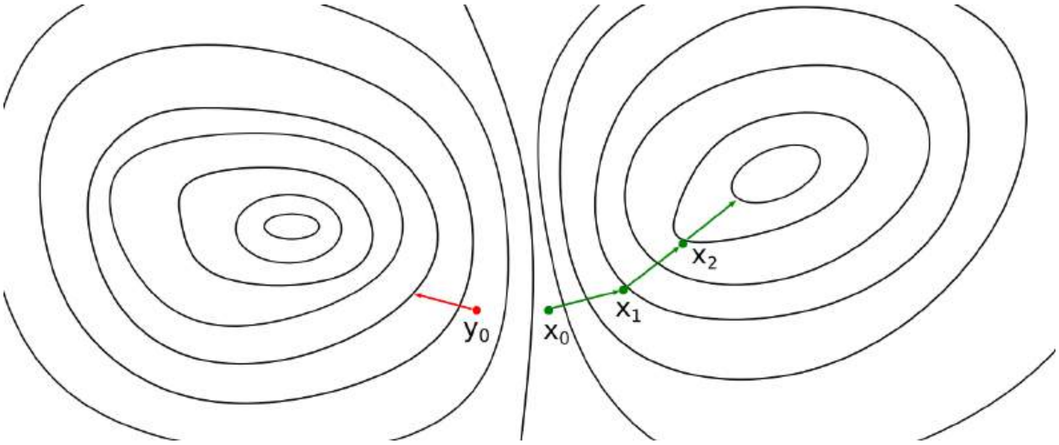

Figure 1.3: Generic potential surface energy with two local minima for a problem of $3N$ dimensional space. The final configuration of the system will depend on the chosen initial configuration (x_0 or y_0).

In the case of a relaxation calculation, i.e. an optimization of the atomic coordinates, this self-consistent cycle is repeated for the different configurations, updated using the forces computed at each cycle to minimize the total energy. At the beginning of each cycle the initial trial wave-function is obtained by the converged density of the previous cycle, in order to accelerate the convergence.

Finding the minimum energy configuration is not a trivial task, since it involves an optimization problem for the potential energy surface ($E(\{\mathbf{R}\})$ of Eq.1.7) to find the global minimum in a $3N$ dimensional space, where N is the number of atoms. Starting from an initial configuration x_0 (Fig.1.3), we use the Broyden-Fletcher-Goldfarb-Shanno (BFGS) quasi-Newton algorithm [49–52] to evaluate a sequence of configurations x_n that eventually will converge to the closest local minimum. The (n + 1)-th step in this iterative procedure is determined by looking at the gradient and the hessian of E; at the minimum, the gradient of the potential is zero, ending the relaxation process (actually for practical implementations, the ending condition is satisfied when the gradient reaches a given threshold). It is important to point out that this method, although quickly converging to a local minimum, does not guarantee that the ending configuration is the actual global minimum. This procedure is indeed dependent on the initial choice of x_0: by choosing a different starting configuration (e.g. y_0 in Fig.1.3), the ending point could be different and the energy of the two different minima should be compared. Therefore, one of the most important tasks before starting these kind of calculations, is to find a suitable guess for the initial configuration, either coming from experimental input or from symmetry considerations.

1.4. Technical details of ab-initio calculations

The scheme described in the previous section to solve the non-interacting KS system can be used to perform ab initio calculations. Quantum ESPRESSO (QE) [53] is the suite of codes that has been used in this thesis for the numerical solutions of these equations.

In this section the most important computational technicalities used to solve the KS equations are presented.

1.4.1. Plane wave basis set

Using a proper basis set, it is possible to reduce the eigenvalue problem of Eq.1.16 into a set of coupled algebraic equations.

QE uses Periodic Boundary Conditions (PBC) that are the natural boundary conditions for the description of extended periodic systems, such as crystals, and also for the implementation of plane wave (PW) as basis set. The periodicity is given by the dimensions of the simulation cell and, as a consequence, the Bloch theorem is valid also for non-periodic systems, such as surfaces, because this type of systems can be inserted in properly chosen supercells. In this way, it is possible to write the KS orbitals of Eq.1.15 in a general form:

$$\Psi^{\sigma}_{i,\mathbf{k}}(\mathbf{r}) = \sum_{\mathbf{G}} c^{\sigma}_{i,\mathbf{k}+\mathbf{G}} \Phi_{\mathbf{k}+\mathbf{G}} \tag{1.21}$$

where the $\Phi_{\mathbf{k}+\mathbf{G}}$ is also a PW set with the following form:

$$\Phi_{\mathbf{k}+\mathbf{G}} = \frac{1}{\sqrt{V}} e^{i(\mathbf{k}+\mathbf{G})\cdot\mathbf{r}} \tag{1.22}$$

In the equations above, *V* is the volume of the simulation cell, **k** is a Bloch vector in the first Brillouin Zone (BZ), **G** indicates a generic vector of the reciprocal lattice and *i* is now a band index.

From this point of view it is evident that PW is the simplest basis set for the expansion of the eigenstates of H^{σ}_{KS} and that allows to transform the KS equations in a matrix diagonalization problem given by:

$$\sum_{\mathbf{G}} \left(\left\langle \Phi_{\mathbf{k}+\mathbf{G}} | H^{\sigma}_{KS} | \Phi_{\mathbf{k}+\mathbf{G}'} \right) - \varepsilon^{\sigma}_{i,\mathbf{k}} \delta_{\mathbf{G},\mathbf{G}'} \right\rangle \Big) c^{\sigma}_{i,\mathbf{k}+\mathbf{G}'} = 0 \tag{1.23}$$

The number of PW in a real calculation cannot be infinite as in Eq.1.21 and is fixed by imposing a maximum value of **k** corresponding to a cutoff for the free electron kinetic energy by means of the parameter E_{cut}:

$$\frac{\hbar^2 |\mathbf{k} + \mathbf{G}|^2}{2m} < E_{cut}, \tag{1.24}$$

Since the PW is a complete basis set, the convergence of the results to the true values is controlled in a simple way by this parameter: the larger is E_{cut} , the better is the accuracy. Instead, with a basis set of localized functions the situation is much more complicated because the convergence depends on the particular choice of the basis functions.

A great advantage of the PW basis set, apart from being a complete set, is the possibility to exploit the Fast Fourier Transform (FFT) in calculating quantities, whereby it is useful to pass from real space to reciprocal space and vice versa. On the other hand, the periodic repetitions of the simulation cell to describe systems that are not naturally periodic can give rise to unwanted interactions of the system with its periodic images. These interactions can be minimized using large enough supercells, but at the expense of increasing the computational cost (with a PW basis set empty space is treated equally to the regions of interest).

1.4.2. Brillouin Zone Sampling

During the self-consistent process for the solution of the KS equations, several quantities, such as the electron density, have to be calculated by means of an integration over the BZ:

$$n(\mathbf{r}) = \frac{V}{2\pi^3} \sum_{\sigma} \sum_{i} \int_{BZ} d\mathbf{k}\, f^{\sigma}_{i,\mathbf{k}} \, |\Psi^{\sigma}_{i,\mathbf{k}}|^2, \tag{1.25}$$

where $f^{\sigma}_{i,\mathbf{k}}$ is the occupation number of the states $\Psi^{\sigma}_{i,\mathbf{k}}$ and *i* is the sum over the bands. The integration is carried out exploiting the special k-points method [54, 55] that allows to approximate the integral with a sum over few properly selected k-points.

In the calculations of this work the Monkhorst and Pack method is adopted [56], where the special k-points are chosen in a uniform grid and therefore the number of k-points can be easily scaled with the dimension of the simulation cell (the size of the BZ is inversely proportional to the size of the simulation cell). When the system examined is a metal, the conduction energy bands are partially filled and the integrand in Eq.1.25 is discontinuous at the Fermi surface in k-space. This delicate situation, requires a dense k-points sampling near the Fermi surface to get accurate results, and can be more efficiently handled approximating the discontinuous occupation numbers with smooth functions (in k-space $f^{\sigma}_{i,\mathbf{k}}$ is a step function with the discontinuity at the Fermi surface). The implementation of this method is due to Methfessel and Paxton [56] and is called *Methfessel-Paxton Smearing*.

1.4.3. Pseudopotentials

The main idea underneath the concept of Pseudopotentials (PP) is, once again, the replacement of a difficult problem with a simpler one. Because core states do not contribute in a significant manner to chemical bonding and to solid-state properties, it is reasonable to assume that these states are frozen near the atomic nuclei: this is namely the *frozen core approximation*. In this way the problem to be solved is now the one of a new system composed of only valence electrons that interact with ionic cores (nuclei + core-electrons) through some effective potential. The fundamental step in the PP theory consists in constructing these new pseudopotentials so as to reproduce in the more possible accurate way the behaviour of the valence electrons. In practice the pseudopotentials have to replace the divergent Coulomb potential near the ionic cores with a fictitious *softer* one. So the solutions of the new KS equations furnish valence wave-functions that are smoother than the true ones near the nuclei and without the core wriggles that would be caused by the condition of orthonormality with the core states.

This approach is useful because it reduces the number of PWs necessary to expand the valence states and so decreases considerably the computational cost of the calculation.

Moreover the development of modern Norm-Conserving pseudopotentials (NCPP) [57] has led to better results in electronic structure calculations due to the improved accuracy and transferability of the PP. In fact the NCPP are constructed taking all-electron calculations of the atom, i.e. KS calculations that include also the atomic core states, and are requested to fulfill certain conditions that allow to better reproduce some properties of the true potential. However it is observed that, for a number of atoms (e.g. oxygen, nitrogen and the first row transition metals), these NCPP are still *hard*, that is they need PWs with large wave vectors to be well described.

For this purpose Vanderbilt [58] developed a new type of PP, called Ultrasoft pseudopotentials (USPP), that are much softer in the core region than ordinary NCPP. The price to pay for this simplification is the appearance of an augmentation term in the expression of the electron density $n(\mathbf{r})$ (Eq.1.13) in the core region which, however, can be efficiently handled with a PW basis set [59]. Because the system under study in this thesis contains a nickel surface, that is a first row transition metal, the PP used in the simulations will be USP.

1.5. Calculating electronic properties

With QE it is possible to perform different tasks, such as computing the electronic structure, finding the relaxed ionic configuration, checking the existence of transition states and several others. Moreover several utilities for data post-processing are available, allowing e.g. to calculate the Density of States (DoS), Scanning Tunneling Microscopy (STM) images and quantities related to the Scanning Tunneling Spectroscopy (STS).

1.5.1. DoS

Apart from the calculation of energy-related quantities and structural properties, QE allows to perform some post processing to compute interesting quantities based either on the electronic density or Kohn-Sham orbitals.

The Density of States (DoS) for instance is an useful tool that provides a counting of the states at the energy E:

$$DoS(E) \propto \int_{BZ} d\mathbf{k}\, \delta(\varepsilon(\mathbf{k}) - E), \tag{1.26}$$

where $\varepsilon(\mathbf{k})$ is a generic eigenvalues of KS equations and is a function of $\mathbf{k}$. For simplicity, in Eq.1.26 the spin polarization is not explicitly indicated, but the extension to the case of magnetic systems is obvious.

To understand the character of the bonds between different atoms or the distribution of the electrons in the system, it is useful to introduce the *Projected Density of States* (PDoS) that gives information also in the real space:

$$PDoS(\alpha, E) \propto \int_{BZ} d\mathbf{k}\, |\left\langle \Phi_\alpha^{at} | \Psi_\mathbf{k} \right\rangle|^2\, \delta(\varepsilon(\mathbf{k}) - E), \tag{1.27}$$

where Φ_α^{at} is the atomic orbital with quantum numbers α centered on the atom of interest.

1.5.2. STM images

An important tool, useful for comparisons with experiments, is the possibility of simulating STM images. To compute that, a crucial quantity is the energy *Integrated Local Density of States* (ILDoS):

$$ILDoS(\mathbf{r}) = \int_{\varepsilon_F}^{\varepsilon_F + V_{bias}} dE\, LDoS(\mathbf{r}, E) \tag{1.28}$$

with

$$LDoS(\mathbf{r}, E) = \int_{BZ} d\mathbf{k}\, |\Psi_i(\mathbf{k})|^2\, \delta(\varepsilon(\mathbf{k}) - E), \tag{1.29}$$

where ε_F is the Fermi energy of the system and V_{bias} represents the electrostatic potential energy difference between the tip of the microscope and the sample.

In the Tersoff-Hamann approximation [60], where the tip is modeled as a spherical potential well in which only the s-wave solution is considered, it is possible to demonstrate that the tunneling current I between the tip and the sample is proportional to the ILDoS

$$I(\mathbf{r}) \approx ILDoS(\mathbf{r}). \tag{1.30}$$

There are two different types of STM images that can be realized: one is termed at constant-height and the other at constant-current. The constant-height mode is the easiest to simulate, since it simply requires to extract all the ILDoS values at a fixed height z in order to build the 2D constant-height STM image (Fig.1.4, left panel).

Instead, a constant-current STM map is simulated by chosing a certain value *I* for the current, defining in this way an ILDoS isosurface in the 3D space, and then search for each point of the *xy* plane of the cell the corresponding value of the height *z* that meets the chosen isosurface (Fig.1.4, right panel). This is formalized by a function $f(\mathbf{r}, E)$:

$$f(\mathbf{r},E)=\int_{\epsilon_F}^{\epsilon_F+V_{bias}} dE'\,LDoS(\mathbf{r},E')=C \tag{1.31}$$

where C is a constant value that depends on the chosen isosurface.

Since in general more than one z value can correspond to the same current I, as it happens for the cases where the isosurface presents curls, an isovalue-search algorithm starting from the vacuum region of the system and scanning has to be used. The isovalue-search goes through the discretized grid in real space "downward" toward the sample until crossing the isosurface once (Fig.1.4, right panel). In this thesis all the STM maps are simulated with the constant-current mode.

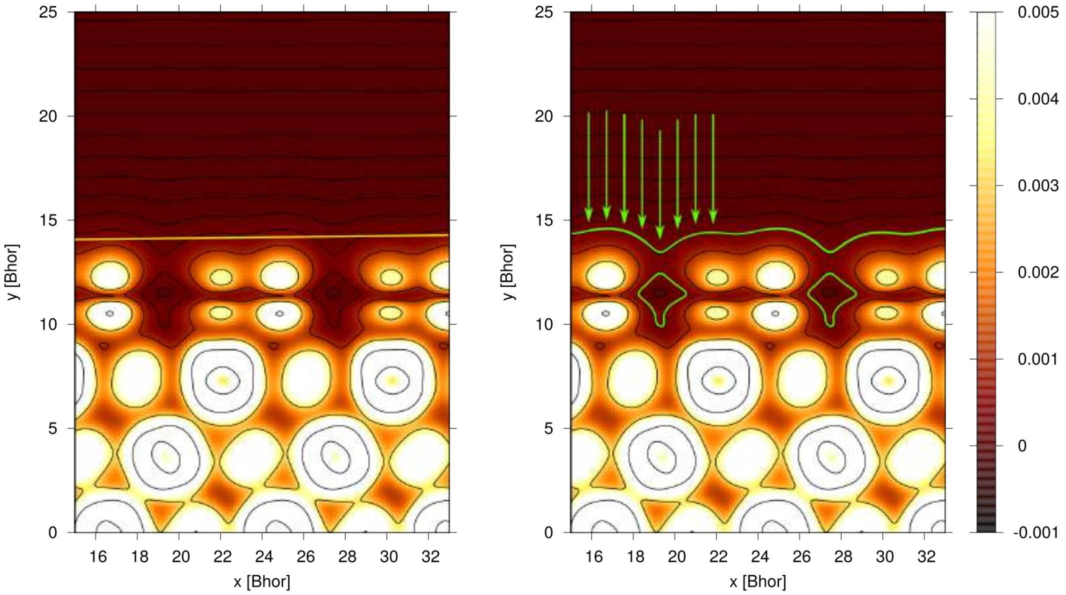

Figure 1.4: Explanation of the possible setup for simulating STM image. Both pictures show a 2D ILDoS plot for a system of graphene over Ni(111) (see chapter 3); the plane shown is orthogonal to the surface. In the left side, the constant height mode is sketched (yellow line), while in the right side, the constant current one is shown (green line), together with arrows indicating the operating mechanism of the isovalue-search algorithm.

Peculiar and tricky systems for the STM simulations are those which, due to the geometry construction of the cell, have surfaces not parallel to the axes of the cell, i.e., to the discretization grid. A clear example comes from the simulation of a stepped surface: in order to implement correctly the PBC and have a stepped surface, a "saw-tooth" atomic profile is necessary (see chapter 6, Fig.6.15). Consequently, the STM simulations will show a fictitious gradient originating from the tilted orientation due to the "saw-tooth" configuration and, moreover, all the repetitions of the cell will appear in the same level of the STM map, without reproducing the STM topography of a multi-level stepped surface (Fig.1.5, top panel). To overcome this problem, the STM maps are processed with the Gwyddion software [61] that allows to select a set of three points and force them to be in the same plane, tilting all the other points of the map with respect to this set of points (Fig.1.5, bottom panel): this solution overcomes both the problem of a fictitious color gradient inside a terrace and the one for the appearance of the adjacent cells.

1.5.3. STS

Scanning tunneling spectroscopy (STS) enables the local energy-resolved investigation of a sample's surface DOS by measuring the differential conductance (dI/dV), which is approximately proportional to the LDOS:

$$\frac{\mathrm{d}I(\mathbf{r},E)}{\mathrm{d}V} \propto LDoS(\mathbf{r},E). \tag{1.32}$$

As in the STM, it is possible to realize constant-height and constant-current STS maps. The constant-height mode requires to extract all the LDoS values at a fixed height *z* in order to build the 2D constant-height STS map.

As regards the constant-current mode, a constant-current STS map is built by all the LDoS values where the *z* components of **r** are those corresponding to a chosen current *I* isosurface. The isosurface is built as in the constant-current STM maps. Also in this case, the constant-current STS mode is formalized with a function $g((x,y),E)$:

$$g((x,y),E) = LDOS((x,y,[z:f(\mathbf{r},E)=C]),E) \tag{1.33}$$

where (x,y) are the x and y components of **r** and $f(\mathbf{r},E)$ is defined by Eq.1.31.

The algorithm to obtain constant current STS maps has been originally implemented during this thesis work.

1.6. Calculating energy barriers

The Nudged Elastic Band (NEB) [62] is a method for finding saddle points and minimum energy paths in the multidimensional energy surface, as a function of reaction coordinates, between known initial configuration reactants and final products.

A path connecting the initial and final states that typically has the greatest statistical weight is the Minimum Energy Path (MEP) (Fig.1.6). At any point along the path, the forces acting on the atoms are only pointing along the path. The energy is stationary for any perpendicular degree of freedom.

The maxima on the MEP are saddle points on the potential energy surface. The relative distance along the MEP is a natural choice for a reaction coordinate, and at the saddle point the direction of the reaction coordinate is given by the normal mode eigenvector corresponding to negative curvature. The MEP often has one or more minima in addition to the minima at the initial and final states. These correspond to stable intermediate configurations. The MEP will then have two or more maxima, each one corresponding to a saddle point: the overall rate is determined by the highest saddle point. It is, therefore, not sufficient to find a saddle point. It needs to have a good enough estimate of the shape of the MEP to be able to assign the highest saddle point in order to get an accurate estimate of the rate.

The NEB method works by optimizing a number of intermediate images along the reaction path. Each image finds the lowest possible energy while maintaining equal spacing to neighboring images. This constrained optimization is done by adding spring forces along the band between images and by projecting out the component of the force due to the potential perpendicular to the band. This force projection is referred to as "nudging." The spring forces then only control the spacing of the images along the band. When this projection scheme is not used, the spring forces tend to prevent the band from following a curved MEP, and the *true* force along the path causes the images to slide away from the high energy regions towards the minima, thereby reducing the density of images where they are most needed.

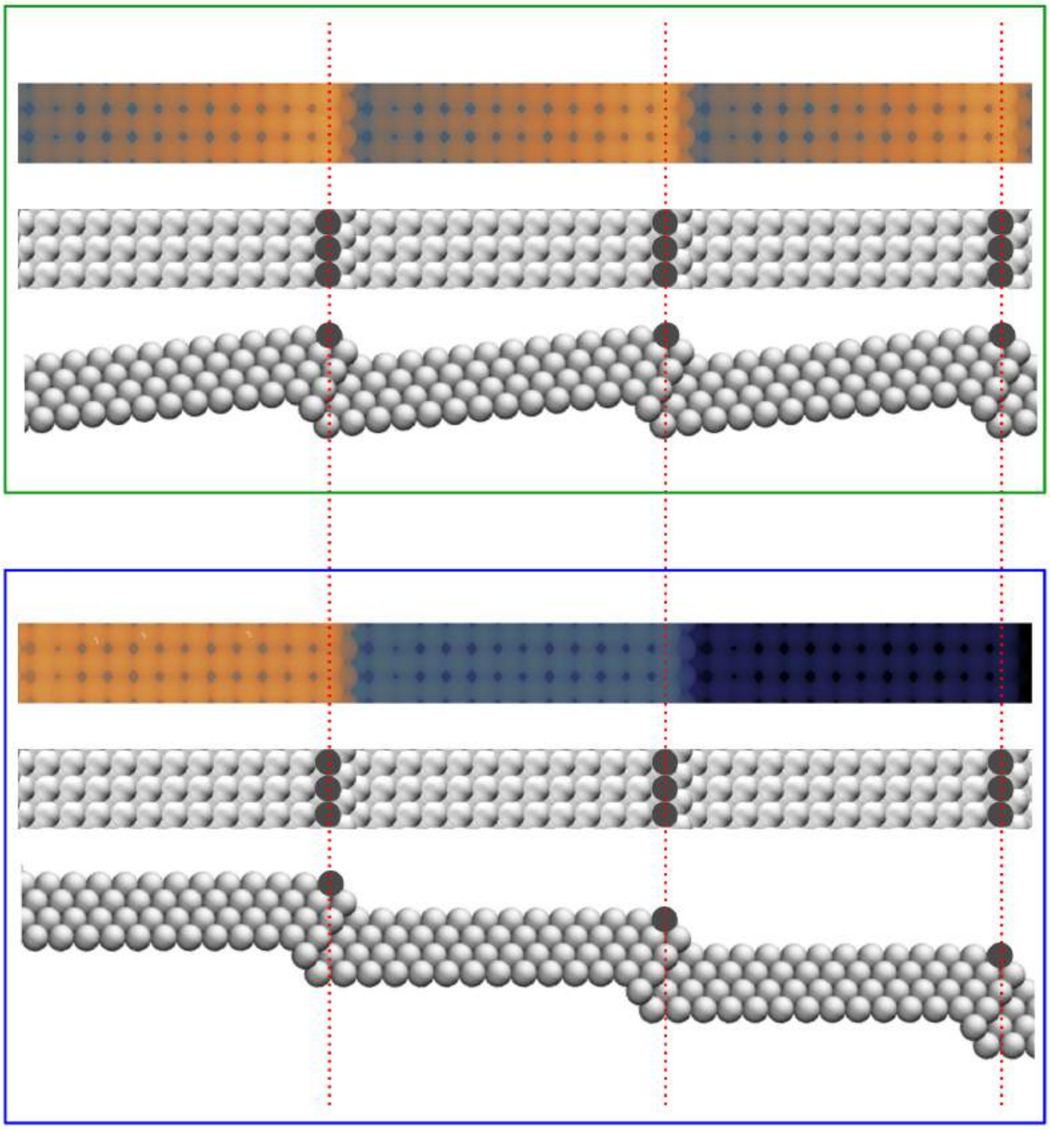

Figure 1.5: Example of constant current STM map straightened with respect to the surface of the simulation supercell. **Top panel:** STM simulation, top and side view of a three times repeated supercell of a Ni(100) stepped surface with a (111) bi-atomic step (see chapter 6). **Bottom panel:** STM simulation obtained tilting the STM map reported in the top panel, top and side view of the same supercell of the top panel with the side view tilted as a "real" stepped surface. The gray atoms are the nickels at the edge of the step.

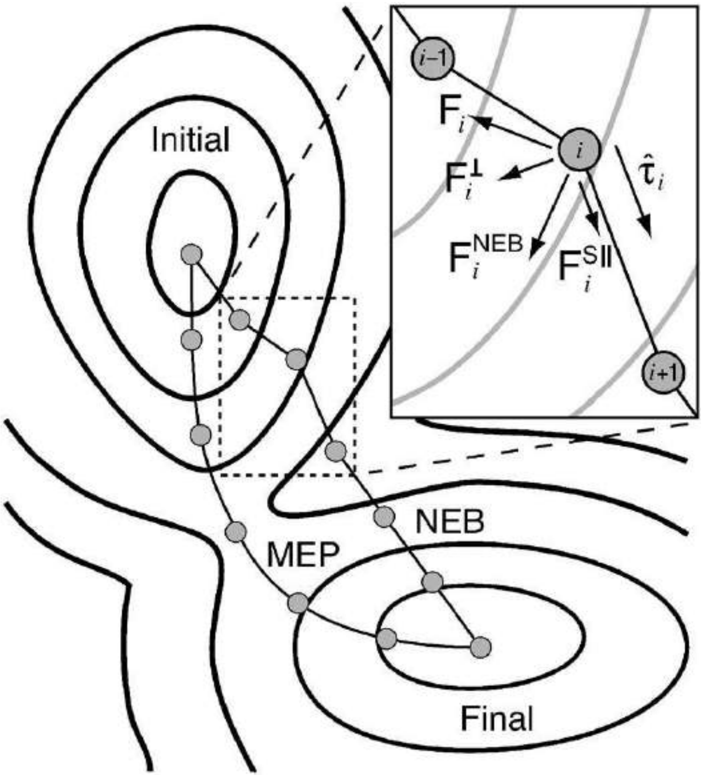

Figure 1.6: Schematic diagram of the a reactive path obtained by NEB calculation. Initial and final configurations are shown in a generic potential energy surface together with the first initial guessed path (NEB) that, as it shown by the box on right-bottom, due to the forces acting on the NEB images converges to the MEP path that is the one that minimize the forces on the images. Image taken from *University of Texas at Austin* web site (*http://theory.cm.utexas.edu/henkelman/research/saddle/*).

2

Kinetic Monte Carlo approach

In this chapter the theory and computational methods behind the dynamical simulations performed in this thesis work are presented. Monte Carlo refers to a broad class of algorithms that solve problems through the use of random numbers. This class of algorithms emerged as electronic computers came into use and the most famous of the Monte Carlo methods is the Metropolis algorithm [63]. Later, researchers began to develop a different kind of Monte Carlo algorithm for evolving systems dynamically from state to state called Kinetic Monte Carlo (KMC) [64]. In this chapter the fundamental concepts of the KMC theory are exposed. An appealing property of KMC is that it can, in principle, give the exact dynamical evolution of a system.

2.1. The time-scale problem

To simulate the dynamical evolution of systems of atoms, the main tool among the atomistic simulation methods is the Molecular Dynamics (MD), in which the classical equations of motion are propagated forward in time. This requires first choosing an interatomic potential for the atoms and a set of boundary conditions and, consequently, the behavior of the system emerges naturally, requiring no intuition or further external inputs. This is extremely appealing, and explains the popularity of the MD method. A serious limitation, however, is that accurate integration requires time steps short enough ($\sim 10^{-15}$ s) to resolve the atomic vibrations. Consequently, the total simulation time is typically limited to less than one microsecond, while important processes involved in the stability of the system, such as diffusion, often take place on much longer time scales. Kinetic Monte Carlo attempts to overcome this limitation by exploiting the fact that the long-time dynamics of this kind of systems typically consists of diffusive jumps from state to state. Rather than following the trajectory through every vibrational period, these state-to-state transitions are treated directly. The result is that KMC can reach vastly longer time scales, typically seconds and often well beyond.

In KMC the probability distribution function $p(t)$ for the time of first escape from the state in which the system is residing is

$$p(t) = k_{tot}\, e^{-k_{tot}t}, \tag{2.1}$$

and the average time for escape τ is just the first moment of the probability distribution

$$\tau = \int_0^\infty t\, p(t)\, dt = \frac{1}{k_{tot}}. \tag{2.2}$$

Because escape can occur along different pathways, we can make the same statement as above about each of these pathways. More precisely, we must consider all the possible escape pathways from one state to another, i.e., a pathway will be identified by a pair of indices, *i* and *j*, and characterized by a rate constant k_{ij}. The total escape rate must be the sum of these rates:

$$k_{tot} = \sum_j k_{ij}, \tag{2.3}$$

and, again, for each pathway there is an exponential first-escape time distribution

$$p_{ij}(t) = k_{ij}\, e^{-k_{ij}\, t}, \tag{2.4}$$

although only one event can be the first to happen. See [65, 66] for a more exhaustive discussion about the rate processes in the stochastic simulations.

Generating an exponentially distributed random number, i.e., a time t_{draw} drawn from the distribution Eq.2.1, is straightforward. After drawing a random number *r* on the interval (0,1), the t_{draw} is obtained reversing the definition of probability distribution (Eq.2.1):

$$t_{draw} = -\frac{1}{k}\, ln(r). \tag{2.5}$$

A time drawn in this way is an appropriate realization for the time of first escape for a first-order process with rate constant *k*. The same argument can be used to associate a time t_{ij} to each pathway with its own rate constant k_{ij}:

$$t_{ij} = -\frac{1}{k_{ij}}\, ln(r), \tag{2.6}$$

consequently, each KMC step of the simulation is associated to a different lapse of time and its value is computed by Eq.2.6. The total KMC simulation time will be the sum of the t_{ij} of each single step.

2.2. Determining the rates

Assuming as known all the possible pathways, the Transition State Theory (TST) [67] can be used to compute the rate constant for each pathway. Although TST is approximate, it is very good for solid-state diffusive events. The rate constant for escape from state *i* to state *j* is taken to be the equilibrium flux through a dividing surface separating the two states (Fig.2.1). One can imagine having a large number of two-state systems, each allowed to evolve long enough that many transitions between these states have occurred, so that they represent an equilibrium ensemble. Then, looking in detail at each trajectory in this ensemble, counting the number of forward crossings of the dividing surface per unit time, and dividing this by the number of trajectories, on average, that are in state *i* at any time, we obtain the TST rate constant k_{ij}^{TST}.

In canonical ensemble, k_{ij}^{TST} is proportional to the Boltzmann probability of being at the dividing surface relative to the probability of being anywhere in state *i*. The implicit assumption in TST is that successive crossings of the dividing surface are uncorrelated: each forward crossing of the dividing surface corresponds to a full reactive event that takes the system from state *i* to state *j*. However, there is the possibility that the trajectory may recross the dividing surface one or more times before either falling into state *j* or falling back into state *i*. If this happens, the TST rate constant overestimates the exact rate, because some reactive events use up more than a single outgoing crossing. Some dynamical corrections can be adopted in order to recover from these possible lacks [68–71].

In principle, classically exact rates can be computed for each pathway in the system. In practice, this is never done, in part because the TST approximation is fairly good for solid-state

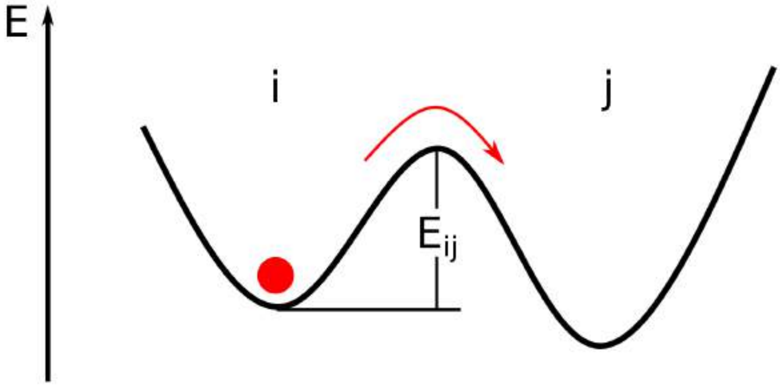

Figure 2.1: Schematic view of the transition state theory rate constant k_{ij} for a system for escape from state *i* to state *j*.

diffusive processes. In fact, most KMC studies are performed using a further approximation to TST, such as the *Harmonic approximation*. Harmonic TST (HTST) is very similar to the Vineyard theory [72, 73], and requires that the transition pathway is characterized by a saddle point on the potential energy surface. One assumes that the potential energy near the basin minimum is well described (out to displacements sampled thermally) with a second-order energy expansion, such as the vibrational modes, assuming the same also for the modes perpendicular to the reaction coordinate at the saddle point. The dividing surface is taken to be the saddle plane and for a system with *N* moving atoms the HTST rate constant k^{HTST} is:

$$k_j^{HTST} = \frac{\prod_i^{3N} \nu_i^{min}}{\prod_i^{3N-1} \nu_i^{sad}} e^{-\frac{E_{ij}}{k_B T}} \tag{2.7}$$

where E_{ij} is the energy barrier height at T=0 K (Fig.2.1) and k_B the Boltzmann constant. In the prefactor, the ν_i^{min} are the $3N$ normal mode frequencies at the minimum and ν_i^{sad} are the $3N-1$ nonimaginary normal mode frequencies at the saddle. The computation of k^{HTST} thus requires information only about the minimum and the saddle point for a given pathway. Further, since prefactors are often in the range of 10^{12} s^{-1} - 10^{13} s^{-1}, a common approximation is to choose a fixed value in this range to avoid the computational work of computing the normal modes for every saddle point.

2.3. Simulation time achievable with KMC

The total simulation time that can be achieved in a KMC simulation is strongly system dependent. Each KMC step advances the system by a time (on average) no greater than the inverse of the fastest rate for escape from the current state. This rate depends exponentially on the barrier height divided by the temperature (Eq.2.7), and the size of the lowest barrier can change, perhaps dramatically, as the system evolves. However nowadays computers can take roughly 10^{10} steps in a few CPU hours, according also on the type and size of the system. If we assume that for every state there is one fast escape pathway with a fixed lowest barrier E_{ij} and a prefactor of 10^{13}, then it is possible to achieve a simulation time of $10^{10}/(10^{13}\exp(-E_{ij}/k_BT))$. For E$_{ij}$ = 0.5 eV, this gives a total simulation time of 2.5×10^5 s at T=300K, 16 s at T=600K and 0.33 s at T=1000K. For a very low barrier, times are even

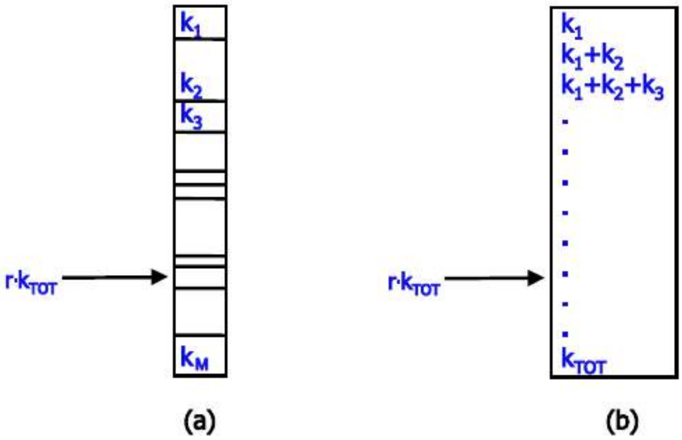

Figure 2.2: Schematic illustration of the procedure for picking the pathway to advance the system to the next state in the KMC algorithm. **(a)** Boxes placed end to end, each with a length proportional to the rate constant for its pathway. A random number $r \in [0.1]$, multiplied by k_{tot}, points to one box with the correct probability. **(b)** In a computer code, this is achieved by comparing rk_{tot} to elements in an array of partial sums. Figure taken from [71].

shorter but the temperature dependence is much weaker. These times are all significantly longer than one can achieve with direct MD simulations (typically between 1 ns and 1 μs).

2.4. The KMC procedure

Once the conceptual foundation of the KMC are established, it is straightforward to design a stochastic algorithm that will propagate the system from state to state correctly. It can be summarized as follows:

1. Set the time $t = 0$.
2. Choose an initial state *i*.
3. Form the list of all M_i possible transition rates k_{ij} in the system, from state *i* into a generic state *j*.
4. Calculate of the values $S_{i,n} = \sum_{j=1}^{n} k_{ij}$ where $k_{tot} = S_{i,M_i}$.
5. Get a uniform random number $r_1 \in [0, 1]$.
6. Find the state *ĩ* for which $S_{i,\tilde{\imath}-1} < r_1 k_{tot} < S_{i,\tilde{\imath}}$. The system will fall in state *ĩ*.
7. Get a uniform random number $r_2 \in [0, 1]$.
8. Update the time with $t = t + \Delta t$, with $\Delta t = -\frac{ln(r_2)}{k_{tot}}$.

Having the constant rates k_{ij}, the acceptance probability of falling in the *ĩ*-state is defined as:

$$\hat{k}_{i\tilde{\imath}} = S_{i,\tilde{\imath}} - S_{i,\tilde{\imath}-1} = \frac{k_{i\tilde{\imath}}}{k_{tot}}. \tag{2.8}$$

The k_{ij} has a non linear dependence on the temperature, and this dependence persists even when normalization is done in the $\hat{k}_{i\tilde{\imath}}$ definition (Eq.2.8). As one could expect, with temperature increasing the events become increasingly equiprobable (Fig.2.3). Thereby, at low temperature the evolution of the system is more driven by the height of the energy barriers. From a physics point of view, this corresponds to the fact that at low temperature the energy spectrum is less spread and, consequently, the evolution of a system under a certain potential can be predicted well. It can be also explained by the fact that a system resides more time in a minimum of the potential at low temperature then high temperature.

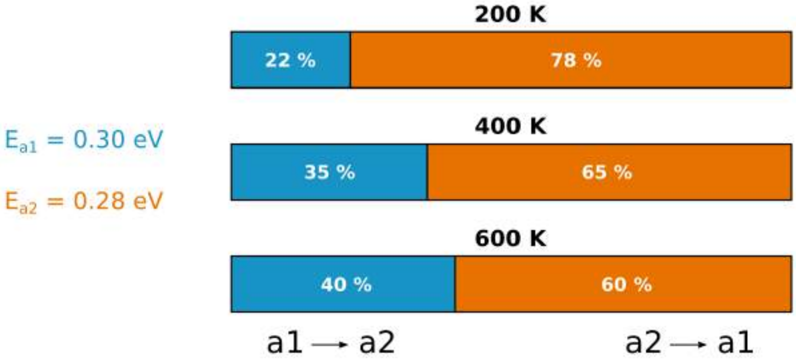

Figure 2.3: Transition probability of a system with two different states with different energy barriers and for three different temperatures. The energy barriers are reported in the left of the figure and the prefactor of Eq.2.7 is chosen equal to 10^{13}.

2.5. The lattice assumption and the rate catalog

In the KMC simulations, each atom in the system is mapped onto a unique point of a grid. A single step of the KMC may move one atom or many atoms, perhaps in a complicated way, but in the final state each atom will again map onto a unique grid point. Grid mapping also makes easy to exploit locality in determining rates. Once individuated the neighbor grid sites accessible by the considered site, the rate constant can be computed. The number of possible rates, ignoring the symmetry, is:

$$n_{rate} = (n_{type} + 1)^{n_{site}}, \tag{2.9}$$

where n_{site} is the number of sites explicitly accessible and n_{type} is the number of possible atom types that can be at each of those sites. Eq.2.9 came from the fact that each site, independently, might be the starting point for the atom diffusion, or have one atom of one of the n_{type} types.

The set of rates computed in this way comprises a rate catalog. By making the local environment larger, the rates will be more accurate, and in principle the environment can be as large as necessary to achieve the accuracy desired. In practice, the number of rates that will have to be computed grows by a power law in n_{site} and this requires to find a compromise with the accuracy that one wants to reach. For example, for vacancy moves in an fcc metal, including just nearest-neighbor sites of the jumping atom, $n_{site} = 12$ and $n_{type} = 1$, giving $2^{12} = 4096$ rates to be computed (many equivalent by symmetry). For a classical interatomic potential, this is feasible, using an automated procedure in which a Nudged Elastic Band (NEB) calculation [74] or some other saddle-finding algorithm is applied to each configuration. However, just increasing this to include next-nearest neighbors ($2^{18} = 2.6 \times 10^5$ rates, ignoring symmetry) or to consider a binary alloy ($3^{18} = 3.8 \times 10^8$ rates, ignoring symmetry) increases the computational work enormously.

Within the HTST, where the rate is specified by a barrier height and a prefactor (Eq.2.7), an easy simplification is to assume that the barrier height can be approximated by additive

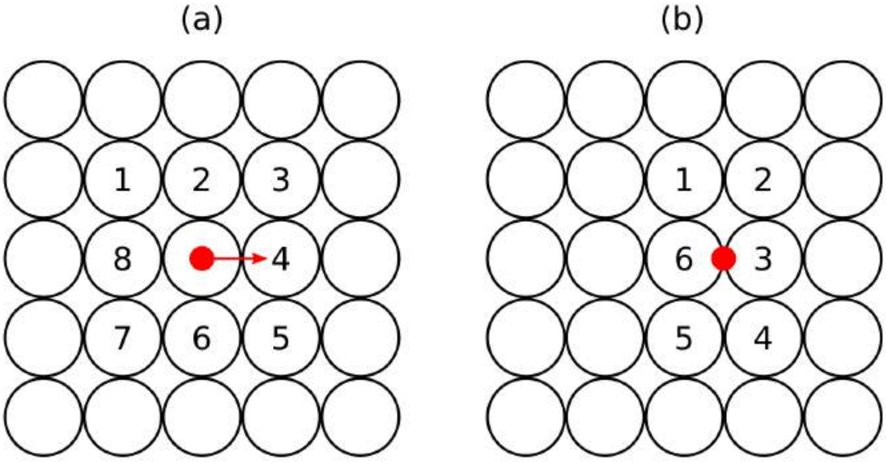

Figure 2.4: Schematic illustration of the rate catalog for the diffusion of an atom (red dot) over a surface. Sites are labeled by class for **(a)** the minimum and **(b)** the saddle point.

interactions. For example, beginning from the example shown in Fig.2.4 where an atom is diffusing over a surface, the neighboring atoms can be categorized as class *m1* (nearest neighbors to the diffusing atom when the system is at the minimum, sites 2, 4, 6 and 8), class *m2* (second nearest neighbors to the diffusing atom when the system is at the minimum, sites 1, 3, 5 and 7), class *s1* (first neighbors to the diffusing atom when the system is at the saddle point, sites 3, and 6), and class *s2* (second neighbors to the diffusing atom when the system is at the saddle point, sites 1, 2, 4 and 5) . The barrier energy is then approximated by

$$E_a = E_{sad} - E_{min} \tag{2.10}$$

where the energy of the minimum E_{min} and the energy of the saddle E_{sad} are given by

$$\begin{aligned} E_{min} &= E^0_{min} + n_{m1}E_{m1} + n_{m2}E_{m2} \\ E_{sad} &= E^0_{sad} + n_{s1}E_{s1} + n_{s2}E_{s2}. \end{aligned} \tag{2.11}$$

n_{m1} is the number of atoms in *m1* positions, and similarly for n_{m2}, n_{s1} and n_{s2}. In this way, the rate catalog is replaced by a small number of additive interaction energies that can be simply obtained by *ab-initio* quantum mechanics simulations. For the prefactor, $10^{12} - 10^{13}s^{-1}$ is a good estimate for many systems.

Finally, in any chemical system a fundamental statements must be done about the equilibrium behavior of the system that is useful for understanding the dynamical evolution when the system is out of equilibrium. Formally, exact equilibrium properties can be obtained by gathering statistics on a very large number of systems, whose time evolution has been performed for an extremely long time before the measurements are made. At equilibrium, the fractional population of state *i*, χ_i , is proportional to exp$(-G_i/k_BT)$, where G_i is the free energy of state *i*. For every pair of connected states *i* and *j*, the number of transitions per unit time (on average) from *i* to *j* must equal the number of transitions per unit time from *j* to *i*. Because the number of escapes per time from *i* to *j* is proportional to the population of state *i* times the rate constant for escape from *i* to *j*, the following relation must be satisfied:

$$\chi_i \, k_{ij} = \chi_j \, k_{ji} \tag{2.12}$$

and the system is said to "obey detailed balance". Because the equilibrium populations and the rate constants are constants for the system, this detailed balance equation, which must hold even when the system is not in equilibrium, places requirements on the rate constants.

If a rate catalog is constructed that violates detailed balance, then the dynamical evolution will not correspond to a physical system.

II. Graphene on polycrystalline nickel

3

Graphene on Ni(111): vacancy defects

This chapter addresses the problem of graphene vacancy defects present on epitaxial graphene growth over the (111) nickel surface. Starting from experimental STM images with unprecedented resolution, a wide analysis of the structural and electronic properties of empty and with nickel adatoms filled vacancy defects has been done. The atomic configuration of different defects was determined by a combination of high-resolution scanning tunneling microscopy (STM) and ab-initio density-functional theory (DFT) calculations. The stability and the bonding configuration of the observed Ni-doping defects are discussed in light of the calculated charge distribution. The results presented here have been submitted to *Nanoscale* [75].

3.1. State of the art and new experimental data

Future applications of graphene-based devices rely on the capability of tailoring its electronic and magnetic properties in a controllable way. For a similar aim, defect engineering is a widely exploited approach in the semiconductor industry, allowing control over the carrier type and density. Following this strategy, recent studies revealed the actual possibility to introduce doping defects in graphene to tune its properties [6–8]. For example, by adding proper gaseous precursor during the Chemical Vapor Deposition (CVD) process [9] or by means of low-energy ion implantation [10, 11], substitutional nitrogen atoms can be trapped inside carbon vacancies, strongly modifying the graphene electronic structure [9, 12]. New functionalities are predicted to arise when transition metal dopants (TM) are introduced. In particular, it is possible to induce a magnetic moment [13] and to add chemical activity [14, 15], enhancing the catalytic behavior of the layer with respect to small gaseous molecules of environmental importance [16]. Also from the theoretical side, an increasing number of researchers are concentrating their studies in such 2D-defected structures, following experimental progress. It is already known that an atomically thin layers of transition metal dichalcogenides (TMD) with vacancy defects doped by impurity atoms is a promising way for engineering the electronic structure of TMD [76], and there are even some theoretical studies on graphene doped vacancy defects over the (111) copper (Cu) surface, shedding light on how the substrate drastically changes the abundance and formation of these structures together with their diffusion energy barriers [17]. Nevertheless, concerning graphene on Ni(111), only small size empty defected structures (up to two carbon atoms missing) have been partially studied but without addressing their stability [18].

On the other side, despite these appealing potential properties, only few experimental realizations have been achieved so far [77, 78], and an approach to obtain metal-doped graphene

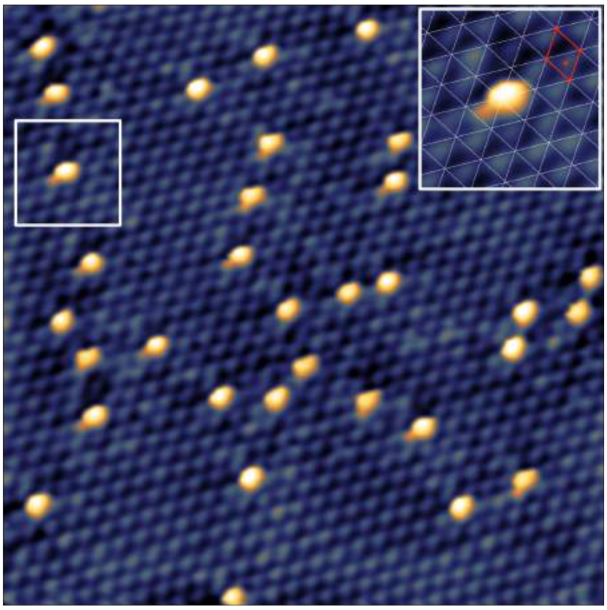

Figure 3.1: Defective epitaxial graphene on Ni(111). White square: a triple graphene vacancy defect is zoomed and the top(dark)- fcc(bright) graphene registry is highlighted by the white grid superimposed on the STM image; in red the primitive cell of graphene. [V=-50 mV, I=0.7 nA].

in a single growth step has not been reported yet. Our experimental colleagues have set an efficient method for growing epitaxial graphene on Ni(111) at 400°C and using ethylene as a carbon source [79]: Fig.3.1 shows a typical STM image of the system obtained with such method of growth. Under these conditions it is possible to obtain large graphene domains (up to few hundreds of nm wide) with a low concentration of domain boundaries [80]. However, at this low growth temperature, the layer is not perfect: a sizable number (about 1%) of point-like bright defects are created, as both isolated features and short chain structures. The concentration of these bright defects depends on the growth temperature, with larger defect densities obtained at lower temperatures. A closer inspection of Fig.3.1 allows us to distinguish different types of Ni-doping defects, characterized by different appearances. The STM images indicate a top-fcc registry of graphene with respect to the Ni(111) surface [80], which in turn allows the position and the orientation of different Ni doping configurations to be identified with respect to the graphene lattice, as shown for one of the observed defects in the inset of Fig.3.1, giving a clear hint for DFT simulations.
More recently, by combining direct STM imaging at the millisecond time scale with numerical simulations, individual Ni adatoms that catalyze the graphene growth on the Ni substrate by temporarily attaching at kink sites along the edges of growing graphene flakes were even clearly identified [81]. The Ni adatom promoting the edge growth can sometimes remain trapped at the edge of a growing flake, and is subsequently incorporated in the carbon network. This definitely proves that the observed point-like bright defects in the graphene layer are Ni doping centres.

3.2. Vacancy defects incorporating metal adatoms

On the basis of the experimental findings and using the density functional theory ab-initio approach, several different Ni doping configurations have been simulated, characterized by a variable number of missing carbon atoms (from 1 to 5) and containing 1 or 2 trapped Ni adatoms. The dangling bonds in the graphene network are passivated by the substrate and by the trapped Ni adatom(s), which leads in all cases to a localized bright feature in the simulated STM images. We classify the observed defects according to the number (n) and position (top or hollow-fcc, hereafter shortly indicated as fcc) on the Ni lattice of the carbon vacancies (V) and the number (m) of the Ni-doping atoms, mNi@nV. Thus, for example, 2Ni@4V(2top+2fcc) indicates a defect where 2 Ni-doping atoms are trapped in a cluster of 4 vacancies, where 2 top and 2 hollow-fcc carbon atoms are missing.

Fig.3.2 presents, for the main Ni doping configurations observed in our measurements, the stick and ball models of the optimized atomic configuration obtained by DFT (upper panel), along with the corresponding simulated (middle panel) and experimental (bottom panel) STM images. It has to be noted that the relative abundance of the different configurations depends on the growth conditions; as a rule of thumb, though, 1Ni@2V, 1Ni@3V(1top+2fcc) and, to a less extent, 1Ni@3V(2top+1fcc) typically dominate. The agreement between experimental and simulated images is remarkable in all cases. For the 1Ni@1V(1top) and 1Ni@2V(1top+1fcc), DFT calculations show that the dangling bonds (DBs) from the missing C atom(s) are all passivated by the trapped Ni adatom. For the 1Ni@2V(1top+1fcc) case, this implies that the shape of the Ni adatom appears asymmetric, with two protrusions towards the closest hollow-fcc C atoms at the defect edge. Due to the symmetry of this defect, three equivalent orientations, rotated by 120° are expected.

The Ni adatom lies in the graphene plane for all the observed defects, with the exception of 1Ni@1V(1top), where, due to steric effect, it is placed ~ 0.9 Å above the carbon layer. This result is slightly at variance with a previous report for epitaxial graphene on Cu(111), where the Cu adatom in comparable defects lies in between the surface and the graphene plane [77]. The different equilibrium configuration of the embedded adatoms can be rationalized in terms of the different structural matching of epitaxial graphene with Cu(111) vs. Ni(111) on one side, and of the different strength of the C-Cu vs. C-Ni interaction on the other. An asymmetry in the appearance of the defect characterizes also the three-C-atom vacancies. Here a single embedded Ni adatom cannot saturate all the DBs, yet there is not enough space for two Ni atoms. The remaining DBs are thus passivated by the substrate, which for 1Ni@3V(2top+1fcc) leads to a surface Ni atom partially lifted above the outermost metallic plane.

For all the defects described above, the formation energy has been calculated, starting from a perfect graphene layer. Following [77], we calculated the formation energy as:

$$E_{form} = E_{defGr/Ni} + nE_{C_{Gr}} - E_{Gr/Ni} - mE_{Ni_{bulk}} \tag{3.1}$$

where $E_{defGr/Ni}$ is the total energy of the defective system (Ni(111) substrate + defected graphene with trapped adatoms), $E_{Gr/Ni}$ is the total energy of the corresponding perfect system (pristine graphene on Ni(111) substrate, with the same dimensions of the defected one), $E_{C_{Gr}}$ is the total energy of the C atom in the free standing graphene, and $E_{Ni_{bulk}}$ is the total energy of a Ni atom in bulk. Using this definition, the defect formation energy is positive; the larger its value, the higher the cost to form the defect in the otherwise perfect system. Resulting energy values for the observed defects are reported below the stick-and-ball models in Fig.3.2 and summarized in the first line of Tab.3.1. The values are in line with those obtained by Wang et al. for comparable defects [77]. Most notably, all the calculated defect formation energies are very high, indicating that Ni-doping starting from a perfect graphene layer would be extremely difficult to obtain. Therefore, in order to produce a Ni-doped graphene layer, it is crucial to introduce the Ni-doping atoms directly during the graphene growth.

An alternative definition of the formation energy is possible, always starting from a perfect graphene layer but making reference to isolated C and Ni atoms rather than to the

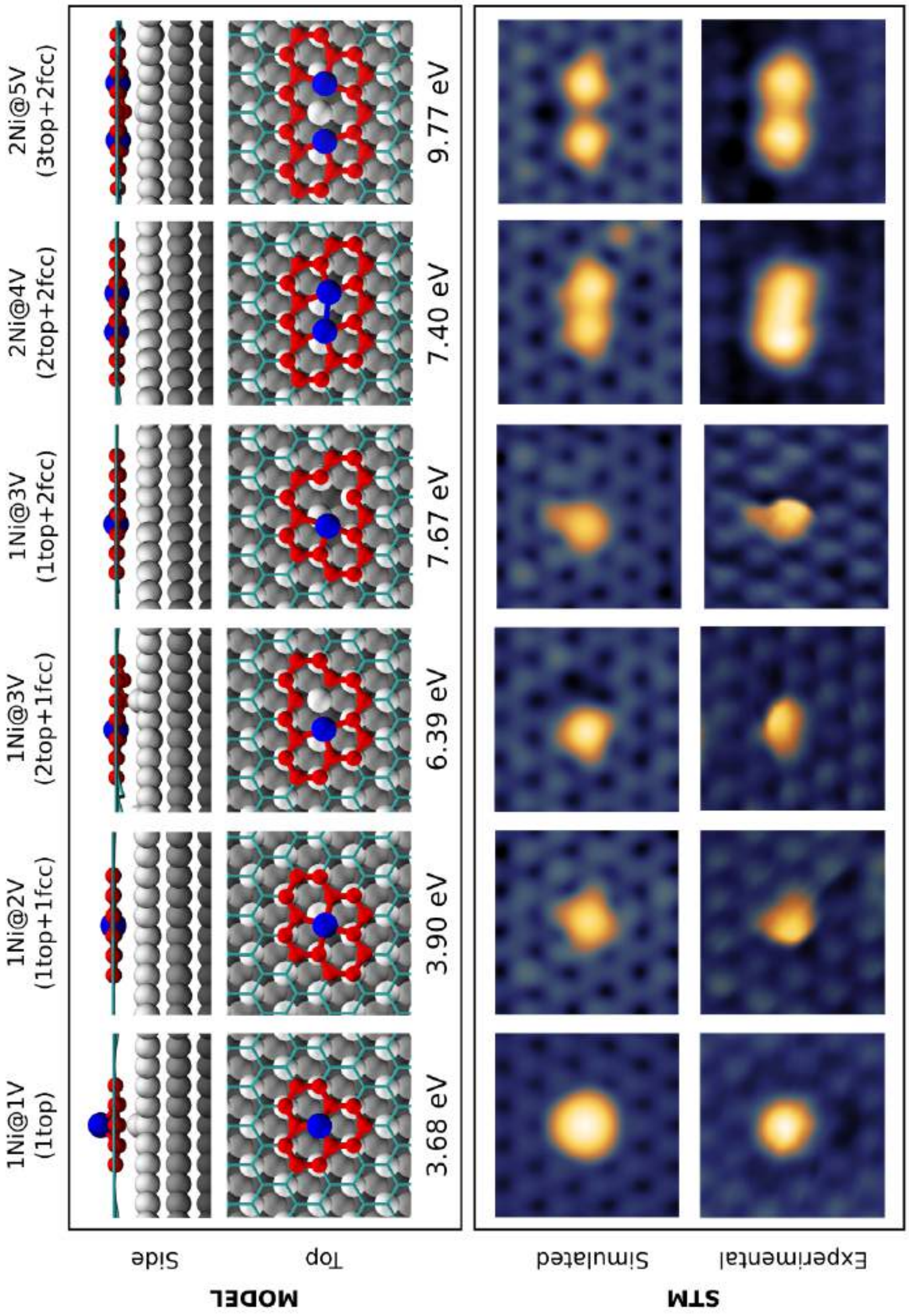

Figure 3.2: Some of the most commonly observed vacancy defects with 1 or 2 Ni adatoms trapped inside. **Top:** DFT optimized stick-and-ball models (side and top view) and calculated formation energies. Balls from light to dark grey: Ni atoms of the slab in the first, second, third layer with respect to the surface; blue balls: extra Ni adatoms; read balls: C atoms delimiting the vacancy defects. **Bottom:** simulated and experimental STM images. The different structures are classified according to the number (n) and the position of the missing carbons (V, vacancies) and the number of trapped Ni adatoms. **Computational parameters:** ILDOS iso-surface lying 2 Å above graphene and with ILDOS value of $5 \cdot 10^{-5}|e|/a_0^3$ for all the structures. **Scanning parameters:** 1V(1top) [V=-0.1V; I = 1 nA], 2V(1top+1fcc) [V=-0.1V; I = 1 nA], 3V(2top+1fcc) [V=-0.3V; I = 2 nA], TV(1top+2fcc) [V=-0.3V; I = 2 nA], 4V(2top+2fcc) [V=-0.3V; I = 1 nA] and 5V(3top+2fcc) [V=-0.3V; I = 1 nA]. [Images size: 1.2×1.2 nm^2]

E [eV]	1Ni@1V (1top)	1Ni@2V (1top+1fcc)	1Ni@3V (2top+1fcc)	1Ni@3V (1top+2fcc)	2Ni@4V (2top+2fcc)	2Ni@5V (3top+2fcc)
E_{form}	3.68	3.90	6.39	7.67	7.40	9.77
E'_{form}	4.07	3.22	4.64	5.92	5.19	6.31

Table 3.1: DFT calculated formation energy of vacancy defects in epitaxial graphene on Ni(111) with 1 or 2 Ni adatoms trapped inside. E_{form} and $E_{form'}$ are calculated with respect to the perfect system, with reference to the corresponding pristine graphene and Ni bulk configurations and with reference to isolated atoms, respectively, as specified in the text.

pristine graphene and Ni bulk structures, respectively, so that:

$$E'_{form} = E_{defGr/Ni} + nE_{C_{is}} - E_{Gr/Ni} - mE_{Ni_{is}} \tag{3.2}$$

where $E_{defGr/Ni}$ is again the total energy of the defective system (Ni(111) substrate + defected graphene with trapped adatoms), $E_{C_{is}}$ and $E_{Ni_{is}}$ are the total energies of the individual C and Ni atoms isolated in vacuum. It is clear that both E_{form} and E'_{form} are stoichiometrically correct, but E_{form} , which makes reference to the corresponding pristine configurations, provides a better connection with the thermodynamics of the real samples (Tab.3.1, second line). We want to stress out that considering the pristine configurations is equivalent consider the atomic reservoir of the pristine and bulk structures.

Although in theoretical calculations the dynamics of the adatom trapping process is not described, and we do not have access to realistic barrier formation, we can refer to the empty vacancies in order to estimate the stability of the trapped Ni adatom. Focusing on the defects including only one Ni adatom, which are the most common, we can subtract, from the total energy of the defective structure as a whole (vacancy with the adatom, $E_{defGr/Ni}$(1Ni@nV), the sum of the total energies of the empty vacancy passivated by the substrate $E_{defGr/Ni}$(nV) and of an isolated Ni atom ($E_{Ni_{is}}$). The energy difference is always negative, indicating a strong binding of the adatom to the vacancy. More specifically, we obtain -4.08 eV, -5.61 eV and -5.72 eV for 1Ni@1V(1top), 1Ni@2V(1top+1fcc), and 1Ni@3V(2top+1fcc), respectively. These values represent the energy gained by passivation of the DBs at the graphene vacancy by the trapped Ni adatom. They are comparable, in absolute value, with the cohesion energy of Ni bulk (4.87 eV/atom calculated in this work), and therefore stronger than the binding energy of a Ni adatom on the clean Ni(111) surface.

Electron density difference plots provide further indications of the binding of the adatom with the vacancy. The electron density difference is calculated by subtracting from the electron density distribution of the whole defective structure the one of the structure with the empty vacancy and the one of the trapped adatom, both kept in the frozen geometry that they have in the defective structure filled by Ni. The plots, reported in Fig.3.3, show that the most pronounced electron density rearrangement occurs between the trapped Ni atom and the borders of the graphene vacancy rather than with the substrate. Indeed, if we increase the isosurface value, the modified charge regions between the Ni adatom and the substrate vanish, while they are still present at the borders of the graphene vacancy. The electron density distribution thus indicates that the Ni adatom is more strongly bound to the graphene than to the substrate, suggesting the remarkable possibility of maintaining the Ni-doping even after decoupling the graphene layer from the Ni substrate, to transfer it elsewhere.

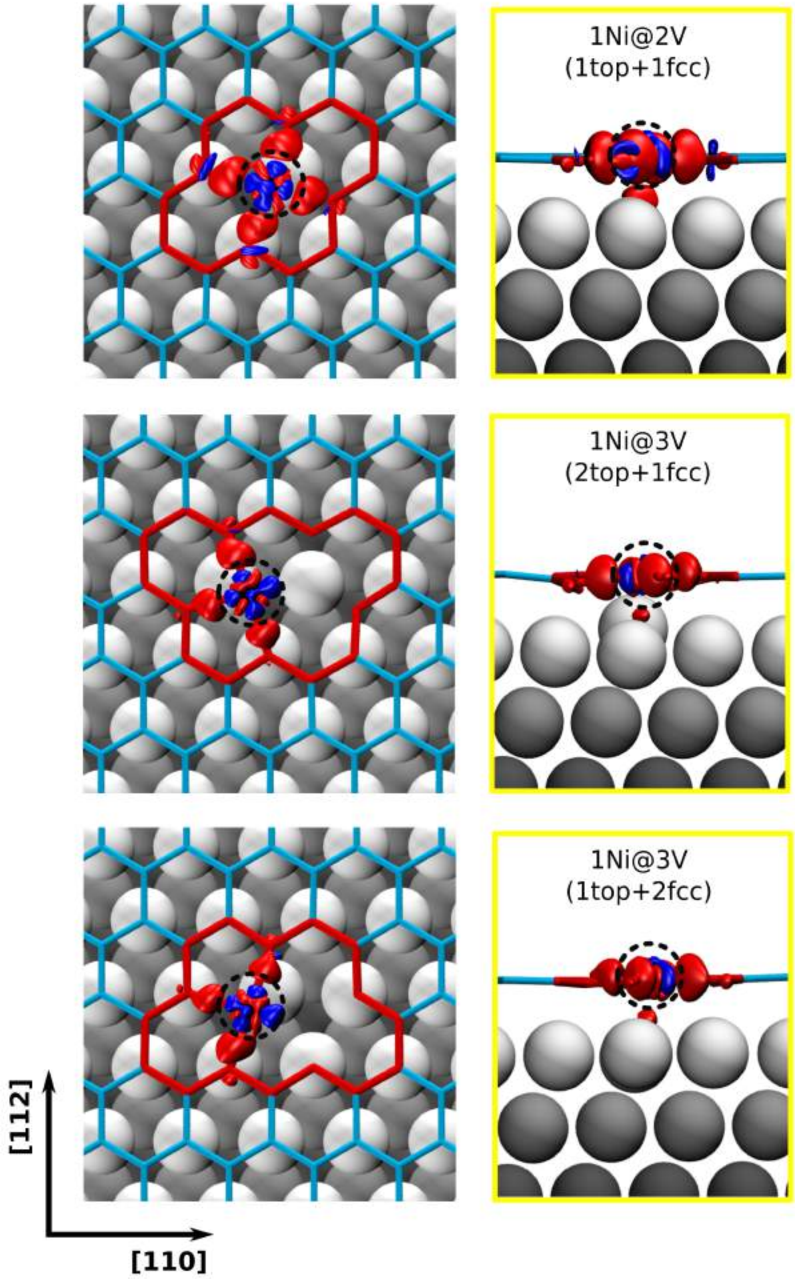

Figure 3.3: Electron density difference due to the filling of 2V(1top+1fcc), 3V(2top+1fcc) and 3V(1top+2fcc) in graphene with one Ni adatom, obtained by subtracting to the electron density distribution of the whole defective structure the one of the structure with the empty vacancy and the one of the trapped adatom, both kept in the frozen geometry that they have in the defective structure filled by Ni. Plots of the top views (left panels) and side views along the [110] direction (right panels) are shown for 1Ni@2V(1top+1fcc), 1Ni@3V(2top+1fcc) and 1Ni@3V(1top+2fcc) structures. Red/blue indicates abundance/depletion of electrons. The electron density difference isosurfaces are plotted at +/-0.007 $|e|/a_0^3$ for 1Ni@2V(1top+1fcc), and at at +/-0.01 $|e|/a_0^3$ 1Ni@3V(1top+2fcc) and 1Ni@3V(2top+1fcc).

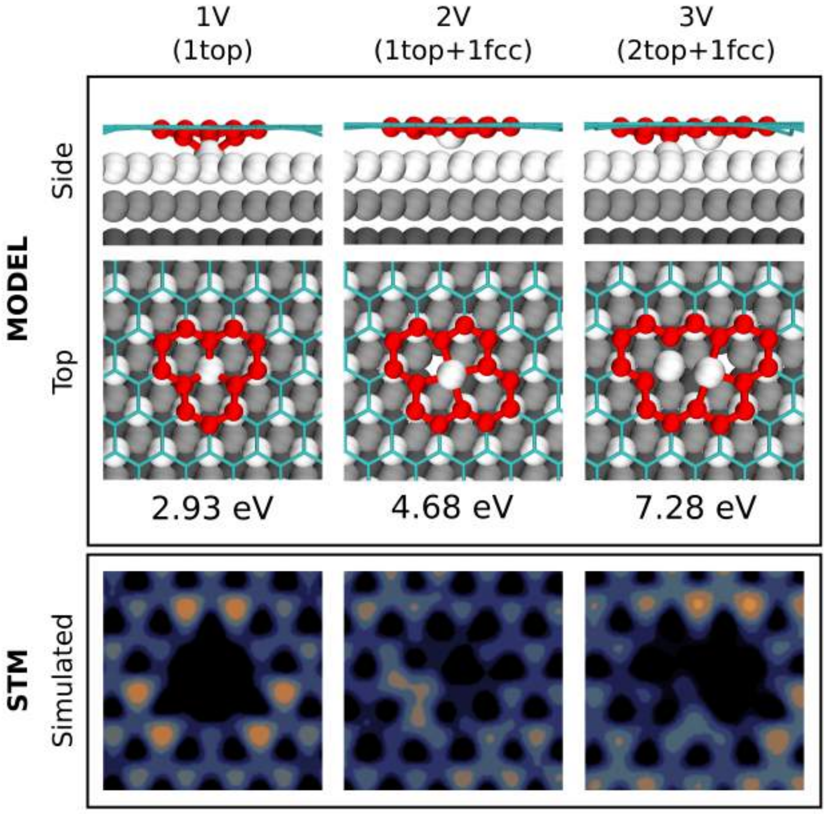

Figure 3.4: DFT calculated structures and properties of some small empty vacancy defects. **Top:** optimized stick-and-ball models (side and top view) and calculated binding energies of the defected graphene and the substrate with respect to the pristine graphene. **Bottom:** simulated STM images with contrast consistent with other figures. The different structures are classified according to the number (n) and the position of the missing carbons (V, vacancies). **Computational parameters:** ILDOS isosurface lying ~2 Å above graphene and with ILDOS value of $|e|/a_0^3$. See caption of Fig.3.2 for the color legend of the stick-and-ball models.

3.3. Empty vacancy defects

For completeness, also the structure and STM appearance of empty graphene vacancies were studied, although only rarely observed in our experiments. All the computational parameters, including the size of cell, are the same of Ni-doped vacancy defects for comparison. In particular, we investigated 1V(1 top), 2V(1top+1fcc), and 3V(2top+1fcc), corresponding to the three leftmost defects in Fig.3.2 without Ni adatoms, which are also, for 1V and 3V, the configurations with the lowest formation energy. In all cases, the surface Ni atoms below the vacancy are lifted towards the graphene plane (Fig.3.4). The structures of 1V and 2V are comparable to those reported in [18] and in [77] for the case of Gr/Cu(111). Remarkably, the lifted surface Ni atoms do not originate bright features in the simulated STM images, which rather show a dark appearance in the defect regions. This strongly supports the presence of Ni-doping adatoms in the bright defects experimentally observed and visible in Fig.3.2.

Empty vacancies can strongly anchor the graphene layer on the substrate [18] through the passivation of the dangling bonds (DBs) with the surface atoms, in analogy with the behavior of the edges of a graphene flake [40]. The stability of the defects, once formed, can be calculated as the binding energy E_b between the defected graphene sheet and the substrate. Following [18], E_b can be defined as:

$$E_b = E_{defGr/Ni} - E_{Gr_{relax}} - E_{Ni_{relax}} \tag{3.3}$$

E [eV]	1V (1top)	2V (1top+1fcc)	3V (2top+1fcc)
E_{form}	2.93	4.68	7.28
$E_{form'}$	9.71	18.24	27.61

Table 3.2: DFT calculated formation energy of empty vacancy defects in epitaxial graphene on Ni(111). E_{form} and $E_{form'}$ are calculated with respect to the perfect system, with reference to the corresponding pristine configurations and with reference to isolated atoms, respectively, as specified in the text.

where $E_{G_{relax}}$ and $E_{Ni_{relax}}$ are the total energies of the defected graphene sheet and the substrate, separately relaxed to reach their equilibrium configurations. The calculated binding energies of 1V(1top), 2V(1top+1fcc) and 3V(2top+1fcc) are -16.06 eV, -15.96 eV, and -17.63 eV respectively, referred to the simulation cell. For comparison with the results reported in [18] of -8.80 eV and -9.16 eV for 1V and 2V respectively, it is necessary to take into account the different cell size, corresponding to 72 C atoms in the pristine configuration in our case, and only to 24 atoms in [18]. Since our cell contains additional 48 C atoms, considering a binding energy per C atom to Ni(111) of -0.16 eV in case of pristine graphene [80], our results include an additional contribution of -7.68 eV to the binding energy, and therefore the values to be compared with [18] are -8.38 eV and -8.28 eV for 1V and 2V respectively. The residual difference could be ascribed mainly to the interaction between defects in the smaller cells and to different computational parameters.

Computational details

DFT calculations were performed through the Quantum ESPRESSO [53] code, using the plane-wave-basis set and employing the Generalized Gradient Approximation for the exchange-correlation functional in the Perdew-Burke-Ernzerhof parametrization (GGA-PBE) [48]. Spin-polarized calculations have been performed. In order to correctly describe the Gr/Ni(111) interaction [82–84], semiempirical corrections accounting for the van der Waals interactions were included with the DFT-D approach [85]. All the calculations were performed using a periodically repeated supercell containing in plane 6×6 graphene unit cells combined with a 3-layer Ni slab with (111) surface: the parallel slab repeated images were separated by 15 Å of vacuum. The supercell size eliminated interactions between the replicas of the defects. Concerning the Brillouin zone sampling, we adopted the Methfessel-Paxton smearing technique [86], the Monkhorst-Pack k-point mesh [56] with a 2×2×1 k-point grid centered on the Γ point for the self-consistent cycles. Convergence tests suggested to adopt a kinetic energy cutoff of 30 Ry for the plane waves basis set and an energy broadening of 0.01 Ry. The theoretical equilibrium lattice parameters of graphene and Ni(111) surface were found to be 2.46 Å and 2.49 Å respectively, in excellent agreement with the experimental values. STM simulations were done using the Tersoff-Hamann approach [60], according to which the tunneling current is proportional to the energy-Integrated Local Density of States (ILDOS). Constant-current and voltage values for the STM simulations have been chosen to match the experimental values. Stick-and-ball-model were rendered with the VMD software [87].

3.4. Summary

We have investigated the atomic-scale configuration of empty and Ni-healed graphene vacancy defects over Ni(111) using DFT calculations. Through the comparison between simulated and experimental STM images, we have identified the Ni-healed defected structures as the most preferred ones. The computed formation energy also supports this conclusion. We have also demonstrated through the analysis of the electron density distribution that the Ni adatom is always more strongly bound to the graphene layer than to the underlying substrate, thus suggesting the possibility to maintain the doping also after decoupling from the substrate.

4

Graphene on Ni(100): extended moiré structures

This chapter presents a study of the graphene moiré configurations over the (100) nickel surface. In the first part, the problem of the structural mismatch between graphene and Ni(100) is addressed, seeding a huge zoo of moiré configurations depending on the misorientation angle between the graphene and nickel lattices. Afterwards two different moiré patterns have been simulated, stripe and network moiré, highlighting their structural and electronic properties and comparing them with the experimental findings. Most of the results presented here have been published in *Carbon* [88].

4.1. State of the art and new experimental data

As it was already shown in the previous chapter, on Ni(111) but also on cobalt (Co) (0001) at specific growth conditions graphene can take the (1×1) registry with respect to the substrates, due to the very small lattice mismatch (2.46 Å for graphene vs. 2.49/2.50 Å for Ni(111)/Co(0001)), as well as to the relatively strong interfacial coupling (i.e. chemisorption) [40, 80, 89, 90]. For other strongly interacting systems, e.g. graphene on ruthenium (Ru) (0001), rhodium (111), rhenium (0001), etc., the large lattice mismatch cannot be accommodated by the elongation of the C-C bonds. As a consequence, moiré superstructures generally composed of a single rotational domain are found; the accumulated strain is released by a significant buckling of the graphene lattice, which leads to alternate strongly- and weakly-interacting regions across the moiré supercells [17, 24–28]. In contrast, the weak coupling between graphene and other transition metals (such as copper (Cu), iridium (Ir) and platinum) results in large interfacial spacing out of the range of chemisorption, smaller spatial corrugation of moirés with respect to strongly-coupled systems, and limited rotational alignment between graphene and the substrate [29–33]. From an electronic point of view, the band structures for chemisorbed graphene (such as that on Ni(111) or Ru(0001)) are fragmented or disrupted due to the hybridization of the graphene p state and the metal d orbital, while physisorbed graphene typically shows Dirac cones similar to its pristine form [91–93]. Therefore, the magnitude of energy gap opening, interface charge redistribution and π band shift from the Fermi level can all be used as fingerprints of the interaction intensity between overlayer and substrate.

The well-established knowledge on the interaction between graphene and three-fold single crystal surfaces, however, is inadequate to rationalize the behavior on realistic substrates used for graphene growth and applications, where polycrystalline transition metal substrates are typically utilized. This is because polycrystalline metals used for graphene growth are generally composed of grains exposing a variety of surface orientations, e.g. (111), (100), and (110) orientations in fcc transition metals [1, 42, 43]. It is therefore very important to understand the interaction between graphene and metal surface with an interfacial symmetry mismatch. As reported on Cu(100), Ir(100), Fe(110) and Ni(110), graphene moirés induced by the lattice mismatch with the substrate can present striped- or, sometimes, rhombic-network morphology, characterized by varying interaction strength with the substrate [34–38, 94]. However, the issue of symmetry-mismatched graphene-metal interfaces is still only partially explored and sometimes controversial [20, 38], therefore leaving plenty of room for further research.

New experimental measurements with unprecedented resolution have been done on graphene growth by CVD on a (100) nickel substrate by the group lead by C. Africh at IOM-CNR Laboratory of Basovizza. A variety of moiré superstructures have been observed by STM at the nanometer scale. Generally, graphene moiré originates from lattice mismatch and/or angular misorientation in two isosymmetric overlapping periodic lattices; herein the situation is further complicated by the symmetry mismatch (square vs hexagonal) of the two interface lattices. In Fig.4.1(a-c), from left to right, three STM images with increasing misorientation angle θ have been shown: the morphology of graphene moirés changes from parallel stripes to a rhombic network when increasing θ from 0° to 15°, similarly to graphene on Cu(100) [34]. The atomic structure of these moirés is revealed in the lower panel of Fig.4.1. Fig.4.1(d) shows a typical striped moiré pattern with θ=0°, where the Fourier transform (inset) confirms the alignment between moiré stripes and one graphene lattice vector. Fig.4.1(e and f) present zoom-ins on the squares in Fig.4.1(b). By increasing the misorientation angle, the rhombic network modulation in moiré patterns becomes more visible, as evident in Fig.4.1(e), where two graphene rotational domains with θ=9.5° (lower) and 12.5° (upper) coalesce seamlessly at the locally linear boundary (blue dashed line in Fig.4.1(b)).

4.1.1. The problem of structural mismatch

It is necessary to go deeper into the problem of misorientation angle between the graphene and Ni(100) lattices and rigorously define the angle θ just mentioned above. Graphene has a hexagonal lattice while Ni(100) a square lattice. Due to this different symmetries between overlayer and substrate, any rotation angle originates a moiré superstructure. The moiré superstructures transform from moiré stripe-like to rhombic modulations with the increase of angular misorientation [34]. Moreover, our DFT simulations demonstrate that the transformation of the moirés is accompanied by a variation of the transformation of moiré graphene adsorption behavior, from coexistence of alternating physi- and chemisorbed regions to exclusive chemisorption, indicating the potential to tailor the electronic or chemical properties of graphene at the nanometer scale.
The misorientation angle θ between graphene and Ni(100) is herein defined as the smallest angle by which graphene needs to rotate (clock- or anticlock-wise) in order to align one of its three zigzag directions with one of the two lattice vector directions of Ni(100) surface (Fig.4.2).

An interesting point that should be mentioned is that, through an analysis of more than 50 high-quality, atomic-resolved STM images on different domains (larger than $10 \times 10 nm^2$), it has been found that on both polycrystalline and single crystal samples the misorientation angle θ does not assume every possible value in the 0° and 15° range but only a set of discrete values. A thorough discussion of these results goes beyond the scope of this thesis, but we can say that the growth conditions appear to affect the relative weight of differently oriented domains: domains at 0° typically prevail, due to effects possibly related to growth dynamics [79], strain release in graphene [33] or lowering of system energy for particular registries [94]. To obtain further insight into the morphological and electronic structures at the graphene-metal interface, ab-initio DFT calculations were performed for moiré patterns with 0° (stripe

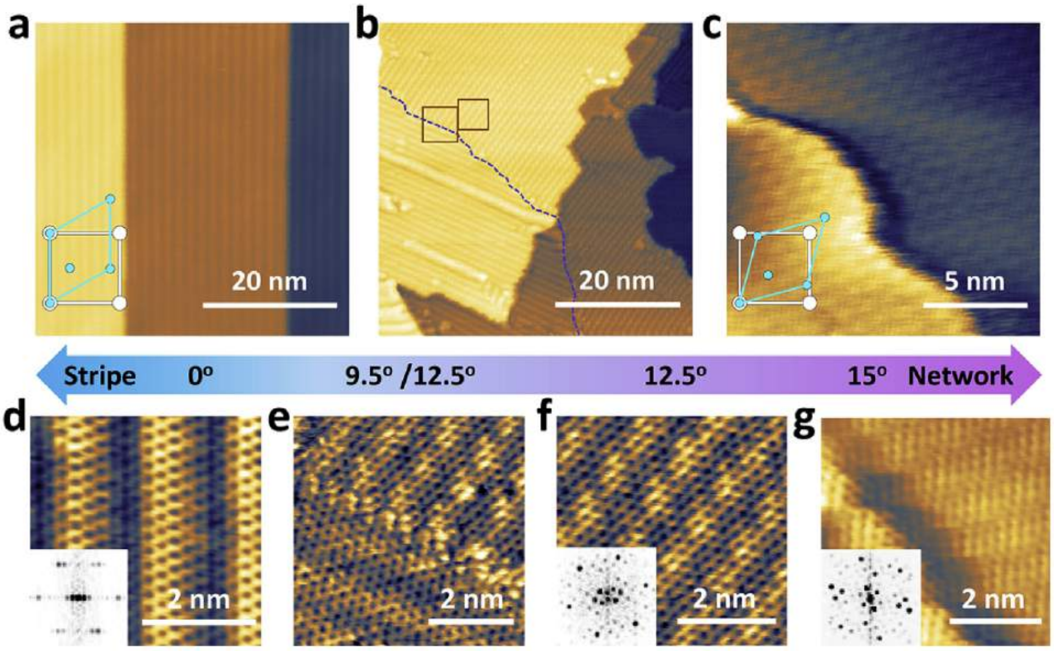

Figure 4.1: (a-c) STM topographic images of representative graphene moiré patterns exhibiting different periodicity and morphology (stripe and rhombic network). The graphene misorientation angles (θ) are: (a) ~0° [V_b=0.3 V, I_t=0.3 nA]; (b) left: 9.5° , right: 12.5° (separated by the domain boundary as a blue dashed line) [V_b=-0.3 V, I_t=0.3 nA]; (c) 15° [V_b=0.005 V, I_t=5 nA]. The double-headed arrow indicates the range of possible misorientation angles. Atomically resolved structures of the moirés shown in (a-c). (d) θ=0° [V_b=0.02 V, I_t=5 nA]. (e) Zoom-in at the left square in (b). θ=9.5°/12.5° in the lower/upper part [V_b=0.15 V, I_t=20 nA]. (f) Zoom-in at the right square in (b). θ=12.5° [V_b=0.15 V, I_t=20 nA]. (g) θ=15° [V_b=0.005 V, I_t=5 nA]. The insets of (d,f,g) are Fourier transforms of the corresponding graphene moirés [88].

moiré) and 11.3° (network moiré) and compared with the experimental findings.

4.2. Stripe moiré

For the stripe moiré (s-moiré), a first look at the experimental STM images (Fig.4.1.d) reveals the absence of modulation along the [011] direction, suggesting a perfect matching of the unit cell of Ni(100) and the graphene zigzag periodicity in that direction, despite the small mismatch ~1% between the lattice parameters a_{gr} and a_{Ni} of graphene and Ni(100). The periodicity in [01$\bar{1}$] crystallographic direction of Ni, is suggested by the observed modulation along that direction and by geometrical consideration. The latter indicates that, considering an ideal, unbuckled graphene layer, the matching condition along the [01$\bar{1}$] crystallographic direction of Ni is $n\sqrt{3}/2a_{gr} = ma_{Ni}$ (Fig.4.4). Approximate solutions can be found, neglecting the small mismatch between a_{gr} and a_{Ni} , the possible stretching of graphene in one direction and the buckling in the other. Once the periodicity of the supercell is chosen, the graphene is allowed to relax, and a certain buckling is actually found.

4.2.1. Structural model

A reasonable choice is a Ni(100) (12×1) rectangular supercell, with the long side oriented along the [01$\bar{1}$] crystallographic direction of Ni, containing 12 surface Ni atoms and 28

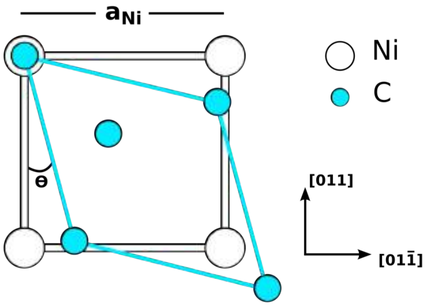

Figure 4.2: Schematic graph of the superposition of the Ni(100) square lattice and the graphene hexagonal lattice. The misiorentation angle θ between graphene and Ni(100) lattices is shown.

carbon atoms (Fig.4.5). This supercell corresponds to 7 periodic units of graphene along the armchair direction. A lattice parameter of 2.49 Å and 2.46 Å has been considered for Ni(100) and graphene respectively, as in the reality, along the [011] direction, while a common lattice parameter of 2.49 Å has been set along the [01$\bar{1}$] direction. In addition to the (12×1) model, a reduced model could be considered, described by a Ni(100) (7×1) rectangular supercell, with 7 surface Ni atoms and 16 carbon atoms, corresponding to 4 periodic units of graphene along the armchair direction. In this case each supercell contains only one beating. The agreement between the experimental and simulated STM is considerably worse than for the (12×1) supercell (Fig.4.6). Another possible choice is a (19×1) supercell, which contains 19 surface Ni atoms and 44 carbon atoms, corresponding to 11 periodic units of graphene along the armchair direction. Tests performed with such cell do not show significant improvements with respect to the less computationally expensive (12×1) supercell (Fig.4.6). Once the periodicity of the simulation cell has been chosen, the optimal relative registry between graphene and Ni(100) has to be identified. For this purpose, we first consider the configuration with a line of carbon atoms along the zigzag chain perfectly on top of Ni atoms, and then we continuously slide the graphene along its zigzag direction, i.e., the [011] direction of Ni. For each configuration we calculate the final equilibrium structure allowing atomic relaxation perpendicular to the surface. The results are shown in Fig.4.7, where the variation of the total energy is calculated with respect to the initial registry (blue curve). The variation is small, but well beyond the relative numerical accuracy of our calculations. The minimum energy configuration (configuration C in Fig.4.7) is the configuration that on average minimizes the C-Ni distances over the whole supercell, rather than the one with some C atoms perfectly on top of Ni (configurations A, E in Fig-4.7). The simulated STM image shows remarkable similarity to the experimental one (figures 3(b,c)), indicating that the model can be used to explore the characteristics of graphene on a reasonable ground. Finally, we found that the adsorption energy does not change shifting the graphene layer along its armchair direction, i.e., the [011] direction of Ni, thus indicating an anisotropic graphene sliding (Fig.4.7).

4.2.2. Electronic properties

Notably, the height of the lowest graphene regions (1.95 Å) in the s-moiré is comparable with that on Ni(111) and Ru(0001) [25, 80], indicative of strong interfacial coupling. On the other side, the higher adsorption height (2.95 Å, Fig.4.5) which is comparable with interlayer distance in graphite (3.34 Å) suggest physisorption. Periodically modulated physi- (ridge) and chemisorbed (valley) regions have also been reported for graphene on strongly interacting 3-fold metal surfaces, e.g. Ru(0001) [24]. The adsorption energy of graphene over Ni(100)

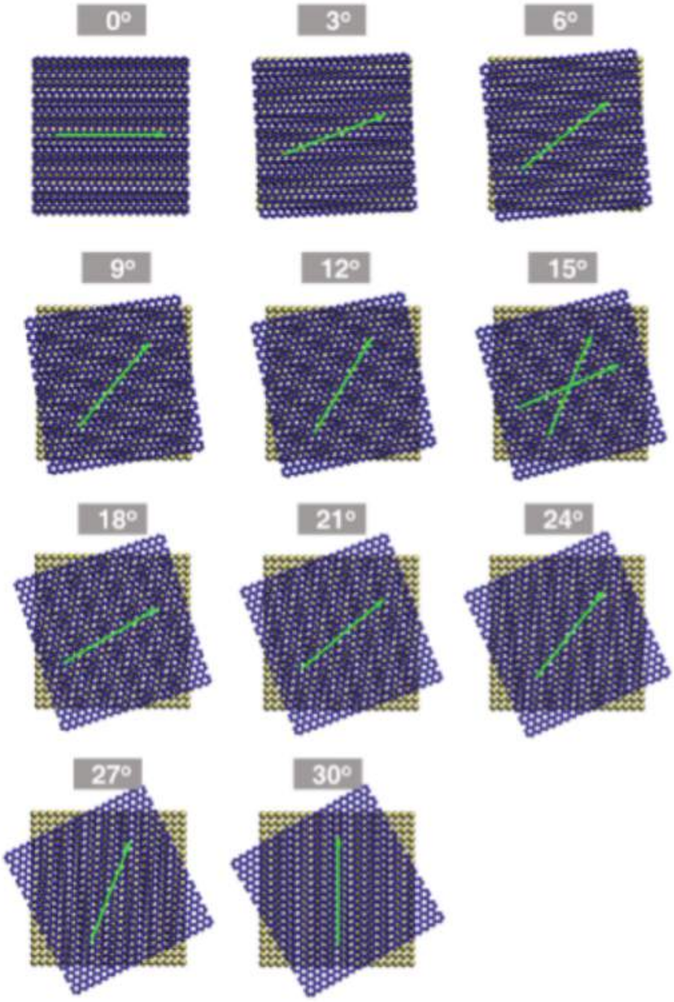

Figure 4.3: Schematic illustration of moiré structures with different rotation angles θ between the lattice vectors $a_{Ni(100)}$ of Ni(100) and the lattice vectors a_{gr} of graphene. The green and blue spheres represent nickel atoms on (100) surface and carbon atoms in graphene, respectively. With the increase of θ from 0° to 15°, the superstructure changes from a striped configuration to a rhombic network. The yellow arrow denotes the orientation of moiré pattern when the superstructure is striped or one side of the moiré supercell when the superstructure is a rhombic network. By gradually increasing the value of θ , the orientation marked by the yellow arrow changes in a continuous manner accordingly. When θ is 15°, the orientations marked by both the yellow arrows are equivalent. This means that at this angle the moiré super cell is an equilateral rhombus.

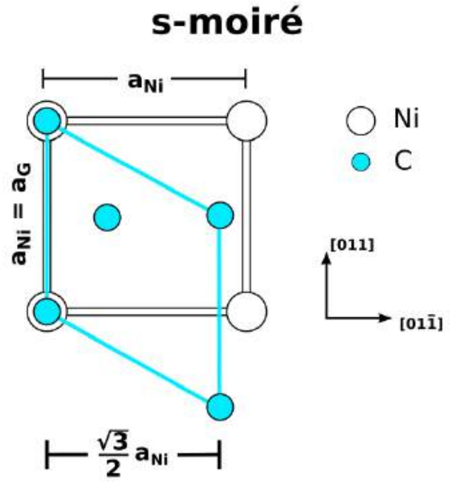

Figure 4.4: Schematic graph of the superposition of the Ni(100) square lattice and the graphene hexagonal lattice, when the zigzag chain of graphene is aligned with the crystallographic [011] direction of Ni [88].

was computed as:

$$E_{ads} = E_{Gr/Ni(100)} - E_{Gr} - E_{Ni(100)} \tag{4.1}$$

where $E_{Gr/Ni(100)}$ is the total energy of the system, while E_{Gr} and $E_{Ni(100)}$ are the energies of graphene and Ni(100) slab separately. In this calculation, the structure of graphene was considered frozen with the corrugation corresponding to the s-moiré configuration. The calculated average adsorption energy is -0.17 eV per carbon atom, similar to what reported for Ni(111) [80]. Although the contributions from the bright and dark regions cannot be separated, considering the highly anisotropic coupling intensity across the s-moiré domain, the adsorption energies of carbon atoms at the ridge/valley regions are expected to considerably deviate from the average value.

The different adsorption configurations for C atoms in s-moiré are corroborated by the electron density plot. Fig.4.8 shows the cross-section projection along the graphene armchair direction (red line in the upper panel). The interfacial electron distribution between graphene and the outermost nickel layer for the case of s-moiré is characterized by alternate regions of higher and lower electron density (Fig.4.8), indicating that chemisorption only exists when pattern gets closer to the Ni surface. These differences in the charge distribution of the C atoms (Fig.4.5) are likely to lead to different electronic structures and, possibly, chemical reactivity. In particular, the patterned electron density in-homogeneity for striped moirés could induce periodically modulated electrostatic field or almost one-dimensional regions of charge accumulation/depletion, which could be exploited for tuning the band structure of graphene, selective modification of its chemical activity, and patterned preparation of one-dimensional nanostructures.

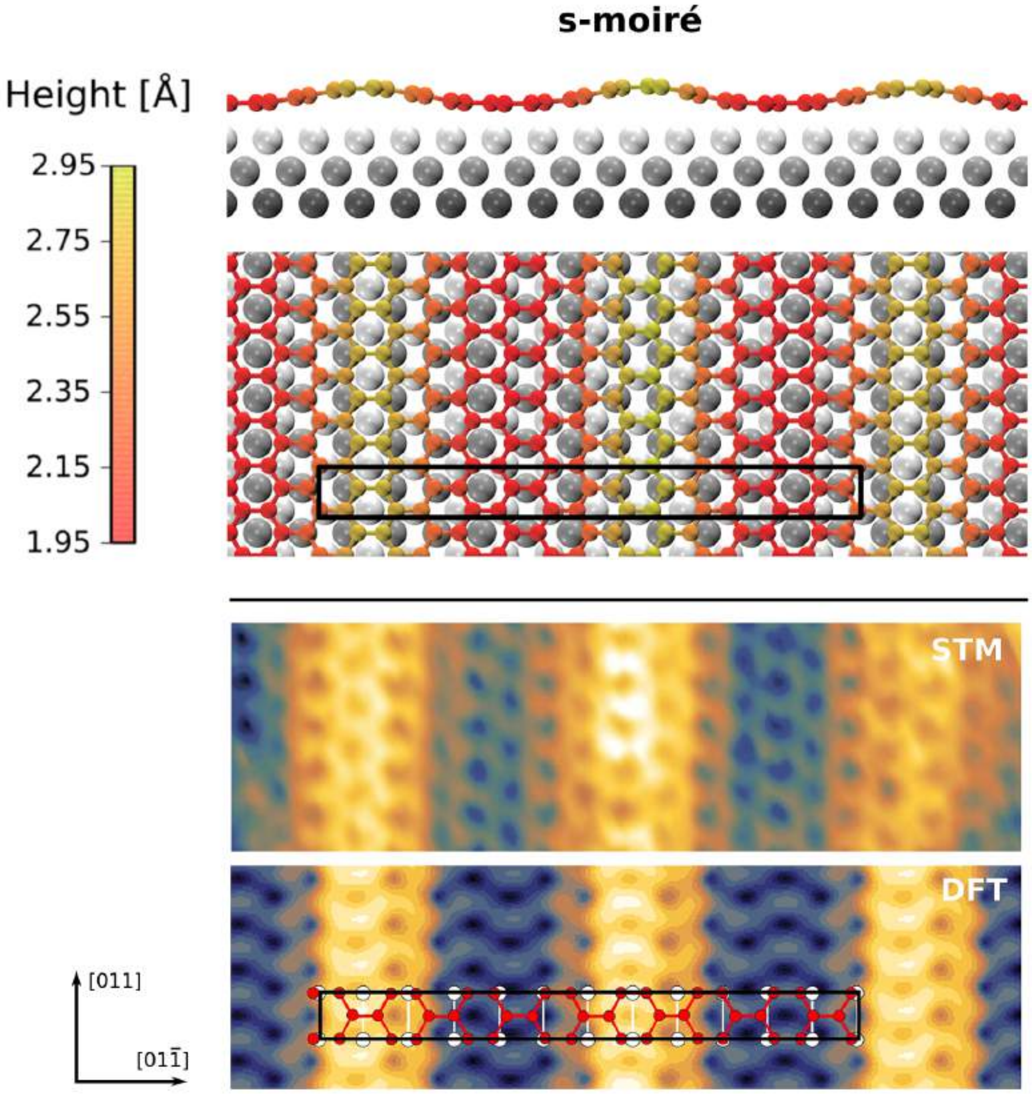

Figure 4.5: DFT simulations and experimental STM image of graphene moiré on Ni(100) with misorientation θ=0°. **Top panel:** side (upper) and top (lower) views of stick-and-ball models (graphene and Ni(100)). The supercells for DFT simulation are highlighted in the top view. The color bar denotes the height of carbon atoms relative to the outermost layer of nickel atoms. **Bottom panel:** experimental and simulated STM images of the moiré superstructure. **Scanning parameters:** $V_b = -0.01$ V, $I_t = 3$ nA. **Computational parameters:** Integrated Local Density of States (ILDOS) iso-surface lying $\sim 2\text{Å}$ above graphene with iso-values of $9 \times 10^{-6}|e|/a_0^3$ [88].

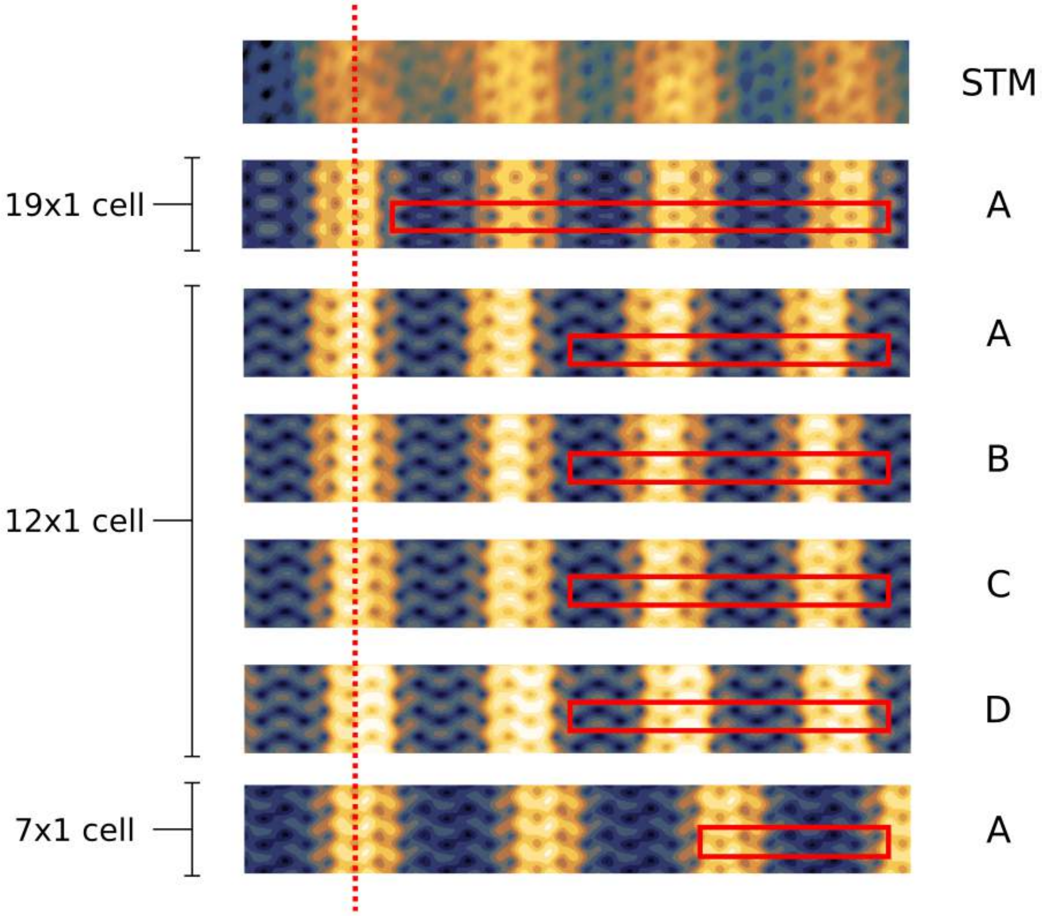

Figure 4.6: Comparison between experimental (STM) and simulated (19×1, 12×1, 7×1 cells) STM images of graphene on Ni(100) for the s-moiré configuration: the simulation cells are highlighted. The dashed line is a guide to the eye in correspondence of the alignment of one bright region. **19×1 and 7×1 cells:** only the STM simulation of the configuration that maximizes the number of carbon atoms that are perfectly on-top with respect to nickel surface is reported (configuration A). **12×1 cell:** the STM simulations of different configurations shifted along the [011] direction are reported (configurations A to D in Fig4.7) [88].

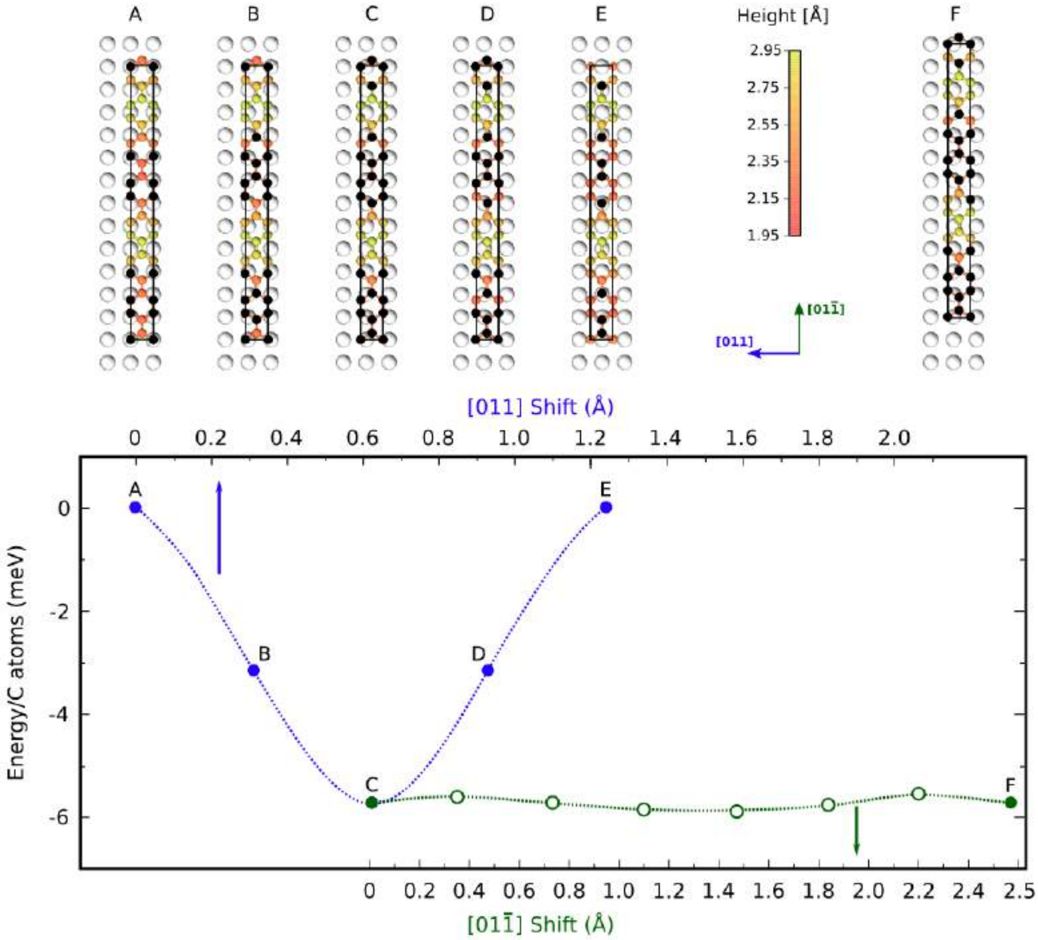

Figure 4.7: Top: Stick-and-ball models of the 12×1 cell for angle 0° moiré for different registry between Ni(100) and graphene. Top-left panels (A-E): graphene is shifted by displacements of 0.32Å along the [011] direction; configuration E is equivalent to A although here represented with a different simulation cell. Top-right panel: final configuration of graphene progressively shifted from (C) along the [011] direction; configuration F is equivalent to C. **Bottom:** corresponding energies. Blue: shift along the [011] direction. Green: shift along the [011] direction by displacements of 0.36Å [88].

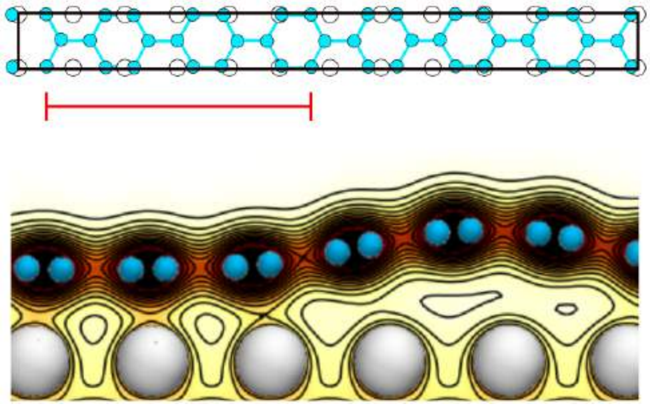

Figure 4.8: DFT-computed electron distribution at graphene-Ni(100) interface for s-moiré. Upper panels: moiré supercells for DFT simulation, with red lines indicating the orientation and the extension of the cross section for the projection of the electron distribution. The resulting plots are shown in the lower panels. Color scale from light yellow to dark brown indicate electron density going from minimum to maximum values [88].

Further evidences of morphological and electronic differences between bright and dark regions of the s-moiré can be obtained by analyzing the exponential decay of the STM tunneling current *I* upon increasing the tip-surface distance *s*. As well known, for small bias V the current goes as

$$I(V,\mathbf{r}) \propto e^{-2\,k(V)\,d} \int_{E_f-V}^{E_f} \rho(E,\mathbf{r})\,dE \tag{4.2}$$

where the decay constant *k(V)* is, to a first approximation, related to the local sample work function, while V is the applied bias and $\rho(E)$ the local electron density

$$\rho(E,\mathbf{r}) = \sum_{\alpha\,occ} \delta(E-E_\alpha)\,|\psi_\alpha(\mathbf{r})|^2 \tag{4.3}$$

The decay constants *k* can depend on the bias V. We can estimate *k* from our calculations, considering its relationship with $\rho(E,\mathbf{r})$. The case of V=+0.3 eV has been reported in Fig.4.9 and it has been found that the phys- region has highest *k* value (1.38 1/Å) then the chemisorbed region (1.28 1/Å). This finding goes again in the direction of the total charge plots and further underlines the difference in the electronic properties between the phys- and chemisorbed region of the s-moiré. The same analysis has been done for several different bias and always we obtained $k_{phys} > k_{chem}$ (Fig.4.10).

For some bias values (+0.3 eV, +0.9 eV and +2.0 eV) also the measured decay constants are available, thereby enabling to compare the theoretical *k* values with the experimental ones. A plot of k_{exp} vs k_{th} for both phys- and chemisorbed values has been done. From Fig.4.11, it can be observed a general linear trend that underlines an excellent agremeent between simulations and experimental measurements with an exception for the *k* value of the phys- region at V=+2.0 eV (violet triangle of Fig.4.11). The reason of that most probably lies in the approximation in the expression of $I(V,\mathbf{r})$: because of the high voltage (+2.0 eV), the STM tip affects the LDoS. Consequently, the tip contribution should be explicitly considered, and also its description.

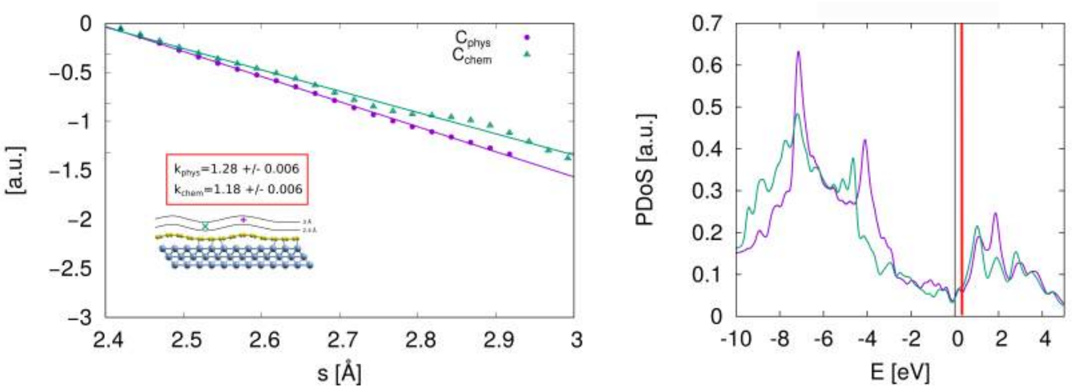

Figure 4.9: Left panel: decay of the tunneling current above chemisorption (green) and phys- (violet) regions of the s-moiré, displayed on a logarithmic scale. A higher decay constant on phys-region is evident. The *k* constants are related to a bias V=+0.3 eV and the fitting is done in the 2.4-3.0 Å range (the 0-height of the STM tip is set on the graphene layer, following its corrugation). All the values are normalized on the first *k* constant value of the plot (2.4 Å). **Right panel:** Local Density of State (LDOS) of a carbon of chemisorption (green) and another of phys- (violet) region of the s-moiré. The red line highlights the +0.3 eV bias.

4.3. Network moiré

The case of network moiré (n-moiré) is more complicated, due to the complete misalignment between the graphene and substrate lattice vectors. At variance with the elongated rectangular supercell for s-moiré (Fig.4.5), the supercell for any other angle is in general rhombic (Fig.4.3), in accordance with the tendency of moiré motif evolution for increasing θ (from stripes to rhombic networks).

4.3.1. Structural model

The choice of the simulation cell is even more arbitrary than for s-moiré, due to the absence of a clear common reference direction for the Ni(100) square lattice and for the graphene hexagonal lattice. We focus on a misorientation angle of 11.3°, where a convenient choice is a square cell, as indicated in Fig4.12. The particular case of n-moiré with θ=11.3° can be simulated by a relatively small square ($\sqrt{13} \times \sqrt{13}R33.7°$) supercell containing 16 surface Ni atoms and 30 carbon atoms (Fig.4.13, Fig.4.12). A small artificial, anisotropic strain was imposed to the graphene lattice to obtain a repeated registry between carbon and nickel atoms within a reasonable distance for DFT calculation, whereas the real moiré unit cell is probably much larger (Fig.4.12). Although a two-dimensional modulation is clearly visible in both experimental and simulated STM images (Fig.4.13), DFT predicts a very small corrugation (0.2 Å) and a distance from the substrate ranging from 1.95 Å to 2.15 Å (Fig.4.13).

4.3.2. Electronic properties

As opposed to the s-moiré, the n-moiré presents a very small corrugation (0.2 Å instead of 1 Å), indicating a stronger interfacial coupling in all the n-moiré regions (the lowest graphene regions lies a 1.95 Å form the nickel surface). This is also supported by the electron density plot. Fig.4.14 shows the cross-section projection along the graphene armchair direction (red line in the upper panel). The interfacial electron distribution between graphene and the outermost nickel layer for the case of n-moiré is characterized by a quite homogeneous electron

E [eV]	k_{phy} [1/Å]	k_{chem} [1/Å]	k_{phy}-k_{chem} [1/Å]
- 4.5	1.725	1.58	0.17
-0.3	1.20	1.06	0.14
- 0.2	1.25	1.08	0.17
- 0.1	1.27	1.14	0.13
E_f	1.225	1.19	0.035
+ 0.1	1.24	1.16	0.08
+ 0.2	1.29	1.16	0.13
+ 0.3	1.28	1.18	0.10
+ 0.9	1.20	1.12	0.18
+ 2.0	1.04	0.68	0.36

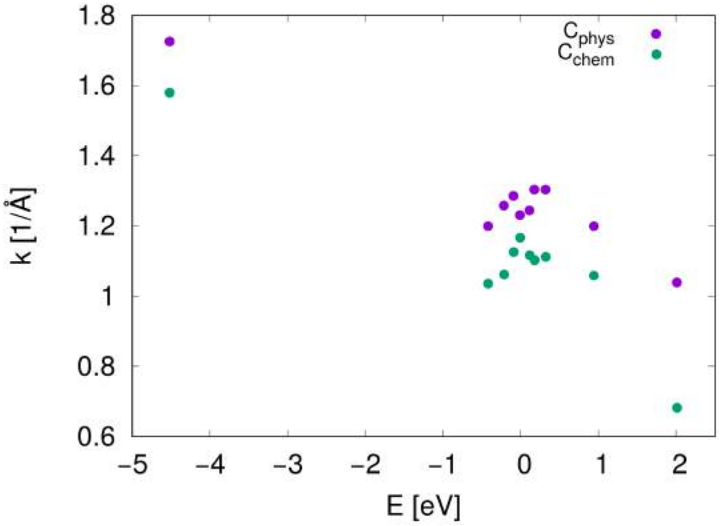

Figure 4.10: Upper panel: table of s-moiré decay constants of the tunneling current vs bias. The constants are computed for phys- (violet) and chemisorption (green) regions and also the differences between them are reported. **Bottom panel:** graphical representation of the decay constants.

density. Also in this case the adsorption energy of graphene over the Ni(100) was computed as Eq.4.1. The calculated average adsorption energy is -0.20 eV per carbon atom, slightly stronger than the s-moiré, in agreement with the strongest interaction with the surface due to the smaller distances of graphene from the substrate.

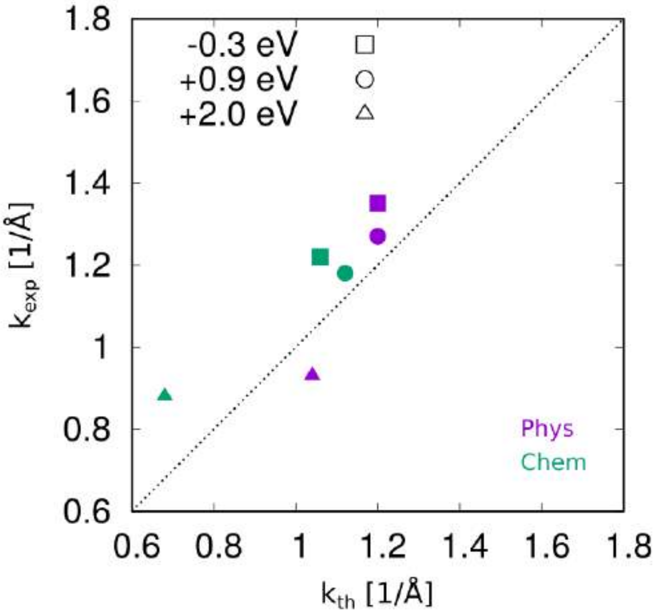

Figure 4.11: Comparison between experimental (k_{exp}) and theoretical (k_{th}) decay constants for the phys- (violet) and chemisorbed (green) regions of the s-moiré.

Computational details

DFT calculations were performed with Quantum ESPRESSO code [53], using plane-wave basis set and the Generalized Gradient Approximation for the exchange - correlation functional in the Perdew-Burke-Ernzerhof parametrization (GGA-PBE) [48]. In order to describe the graphene/Ni(100) interaction correctly, semi-empirical corrections accounting for the van der Waals interactions were included with the DFT-D approach [85]. Convergence tests suggested a kinetic energy cutoff of 30 Ry for the plane-wave basis set. The equilibrium lattice parameters characterizing the clean Ni(100) surface and the free-standing graphene are 2.49 Å and 2.46 Å respectively, equal to the experimental values. A periodically repeated slab geometry with 3 Ni layers and graphene adsorbed on one side was used, with a vacuum spacing of 13 Å between graphene and the parallel consecutive Ni(100) surface. With respect to the Ni(100) surface lattice, the simulation cell used throughout the work is a rectangular (12×1) supercell for s-moiré (Fig.4.5) while a square one ($\sqrt{13} \times \sqrt{13}R33.7°$) for the n-moiré (Fig.4.13). Regarding the s-moiré supercell, tests with different cell sizes have been performed (Fig.4.6). Concerning the Brillouin zone sampling, we adopted a Monkhorst-Pack k-point grid, $1 \times 12 \times 1$ (s-moiré) and $4 \times 4 \times 1$ (n-moiré), centered on the Γ [56] and the Methfessel-Paxton smearing technique with an energy broadening of 0.01 Ry [86]. The optimized atomic positions have been obtained minimizing the forces acting on each atom. Stick-and-ball models were rendered with the VMD software [87].

4.4. Summary

We have investigated the structure of graphene on the 4-fold Ni(100) substrate through a simple geometrical model due to the overlap and rotation of the two lattices. A variety of moiré patterns from quasi one-dimensional stripes to two-dimensional rhombic network has been found, depending on the angular interface misiorentation. We have studied in details by DFT two prototypical striped and network moiré, demonstrating the possibility of manipulating the electronic properties of graphene on the nanoscale through the rotational

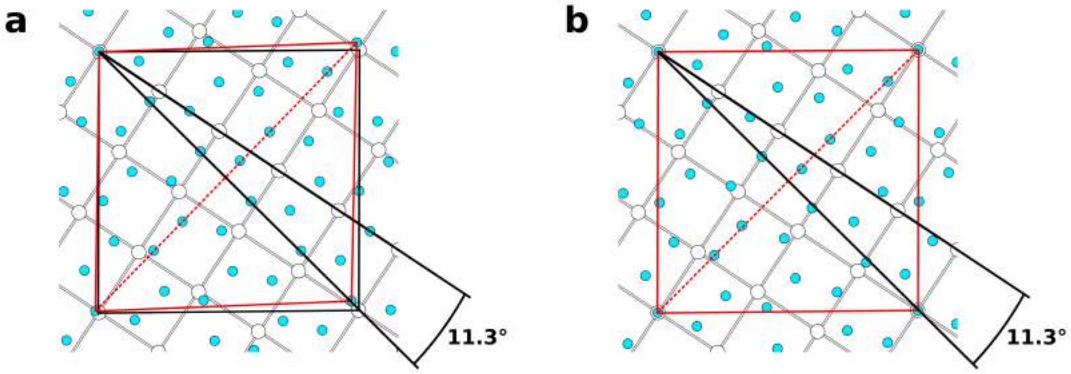

Figure 4.12: Sketch of the superposition of the ideal Ni(100) square lattice and the graphene hexagonal lattice with a misorientation angle of 11.3°, where one C atom of graphene is perfectly on-top of a surface Ni atom. **(a):** the graphene lattice is undistorted. The square drawn in black and the rhombus in red indicate possible choices of a repeated unit cell for Ni(100) lattice and graphene lattice, respectively, with very similar dimensions. We notice that the diagonals of the rhombohedral cell are very similar but not exactly equal: 9 a_{Gr} the dashed one, and $5\sqrt{3}a_{Gr}$ the other.**(b):** a small anisotropic distortion has been applied to the graphene lattice to transform the rhombohedral cell into the same square cell describing the Ni surface. The relative difference between the original lengths of the two diagonals of the rhombohedral graphene cell (about 4%) gives the order of magnitude of the strain applied to build the final model of the moiré cell. The coordinates of the C atoms internal to the cell have been properly rescaled by applying that strain, and a final optimization is obtained by DFT relaxation [88].

registry of graphene on the Ni(100) substrate.

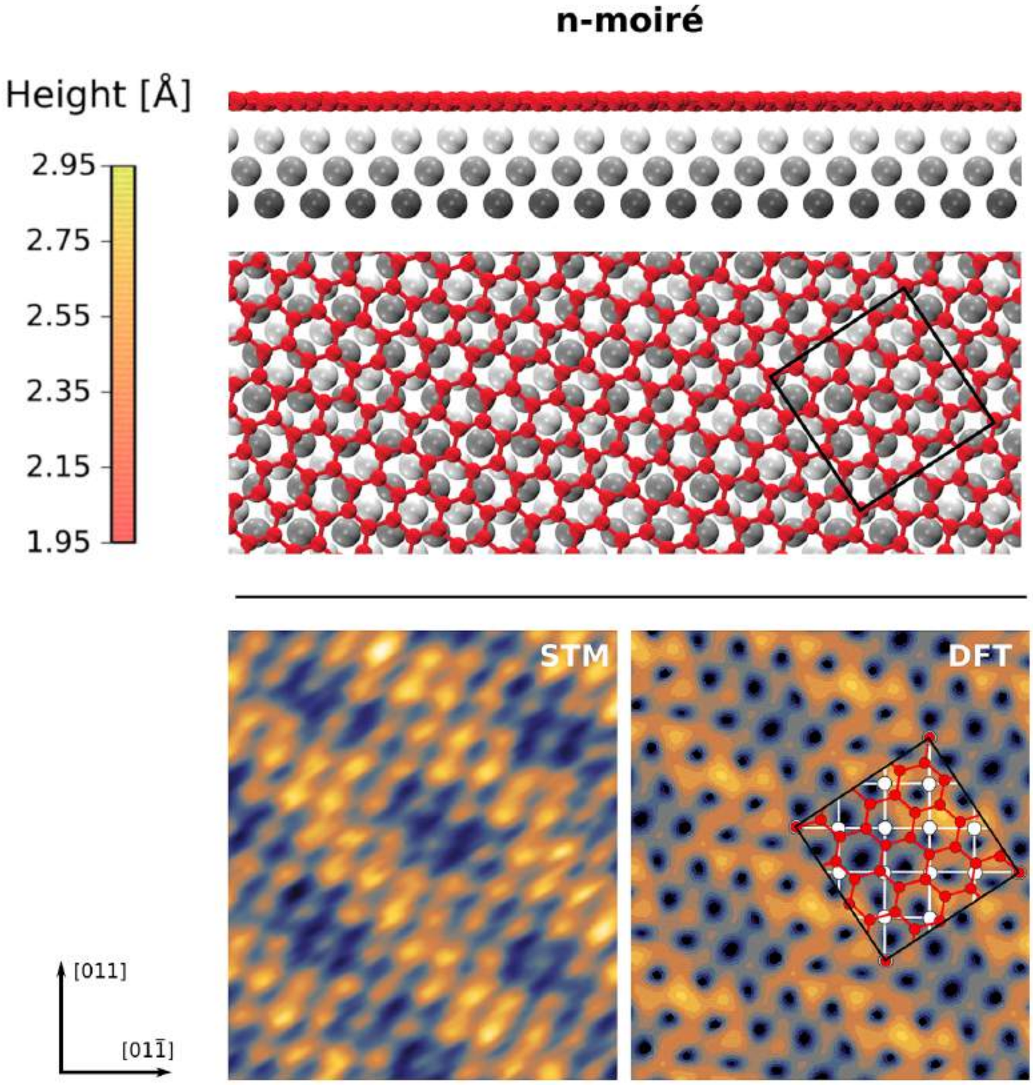

Figure 4.13: DFT simulations and experimental STM image of graphene moiré on Ni(100) with misorientation θ=11.3°. **Top panel:** side (upper) and top (lower) views of stick-and-ball models (graphene and Ni(100)). The supercells for DFT simulation are highlighted in the top view. The color bar denotes the height of carbon atoms relative to the outermost layer of nickel atoms. **Bottom panel:** experimental and simulated STM images of the moiré superstructure. **Scanning parameters:** $V_b = -0.2$V, $I_t = 1$ nA. **Computational parameters:** Integrated Local Density of States (ILDOS) iso-surface lying $\sim 2\text{Å}$ above graphene with iso-values of $1 \times 10^{-4}|e|/a_0^3$ [88].

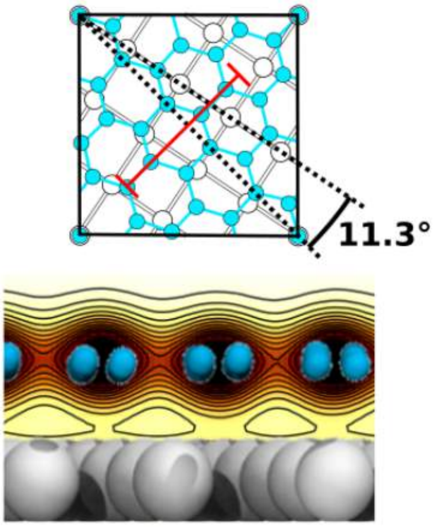

Figure 4.14: DFT-computed electron distribution at graphene-Ni(100) interface for n-moiré. Upper panels: moiré supercells for DFT simulation, with red lines indicating the orientation and the extension of the cross section for the projection of the electron distribution. The resulting plots are shown in the lower panels. Color scale from light yellow to dark brown indicate electron density going from minimum to maximum values [88].

5

Carbide segregation under graphene over Ni(100)

This chapter addresses the problem of the moiré superlattices stability. Due to the CVD mechanism of growing [95], some exceeding carbon atoms can get trapped at the nickel surface and diffuse across the outermost surface layers [Fig.5.1]. This mechanism has been studied as the cause of the stripe moiré irregularities due to a local detachment of parts of the chemisorbed regions shown by experimental STM images. The problem of the carbon diffusion has been addressed in three steps, combining DFT and KMC simulations to investigate the most stable carbon sites and the carbons diffusion between them. In the first part, through DFT, the stable adsorption sites for carbon atoms were identified considering only the bare (100) nickel surface, allowing to identify the preferential carbon diffusion pathways; in the second part, again through DFT, it has been investigated how the presence of graphene in a stripe moiré configuration influences the carbon diffusion at/across the surface; once the system has been characterized from a "static" point of view, KMC and DFT simulations have been used to study the evolution of the moiré patterns induced by carbide segregation at the Gr/Ni(100) interface observed by cooling down the sample.

5.1. State of the art and new experimental data

Chemical vapor deposition (CVD) is the most used method for large area graphene preparation involving metallic surfaces [39]. In general, a copper surface is considered as the best substrate, as exclusively graphene monolayers can be formed on it. On the other hand, nickel

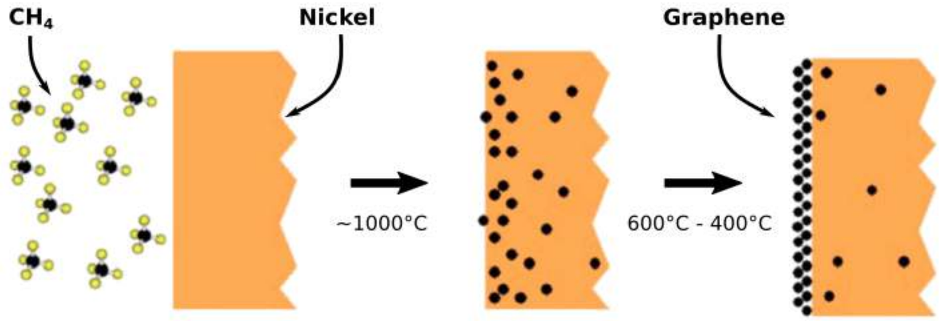

Figure 5.1: Schematic illustration of elementary steps involved in the CVD process. **Left panel:** methane is pumped in a chamber with a nickel substrate inside. **Middle panel:** the nickel substrate acts as a catalyst for the CH_4 dissociation: hydrogen evaporates as H_2 and carbon diffuses in the nickel bulk across the surface. **Right panel:** carbon atoms segregate and create graphene, while the exceeding carbons remain inside the substrate.

surfaces serve as a support for controlled few-layer graphene formation. Also, several other transition metals were investigated as possible substrates for the CVD process, for example ruthenium [96, 97], iridium [98, 99], palladium [100], platinum [101], rhodium [102], rhenium [103] or gold [104]. However none of these substrates seriously compete with copper, nickel or cobalt, either due to their cost, the quality and transferability of the produced graphene, or the possibility of an extension of the size of the grain graphene sheet.

CVD process can induce several different kind of defects in the graphene sheet. There have been only a few studies of the defects that may form during growth by CVD processes at metal surfaces [41]. It is likely that under various growth conditions defects may be kinetically trapped in the graphene sheet [88]. Another type of lattice symmetry breaking that forms in graphene grown by CVD on interacting metal surfaces (e.g. on Ni, Cu, Pt) is rotational domain boundaries [40].

New experimental measurements done by the group leaded by C. Africh at IOM-CNR Laboratory of Basovizza on s-moiré graphene growth by CVD on a (100) nickel substrate (see chapter 4) show some big bright regions in the graphene moiré due to the local detachment of the chemisorbed regions of the moiré (Fig.5.2). These defected regions of the s-moiré strongly depend on the CVD conditions (hydrocarbon flux, temperature etc.), they are stable in time and it seams that they are originated by exceeding carbon atoms originating from the CVD process and diffusing at/across the outermost surface layers. The exceeding carbon atoms are not enough to aggregate and produce other graphene sheets, tuning the graphene layer on the 3D graphite structure. Consequently, they are free to diffuse at the graphene-Ni(100) interface, inducing more or less extended irregularities in the s-moiré configuration.

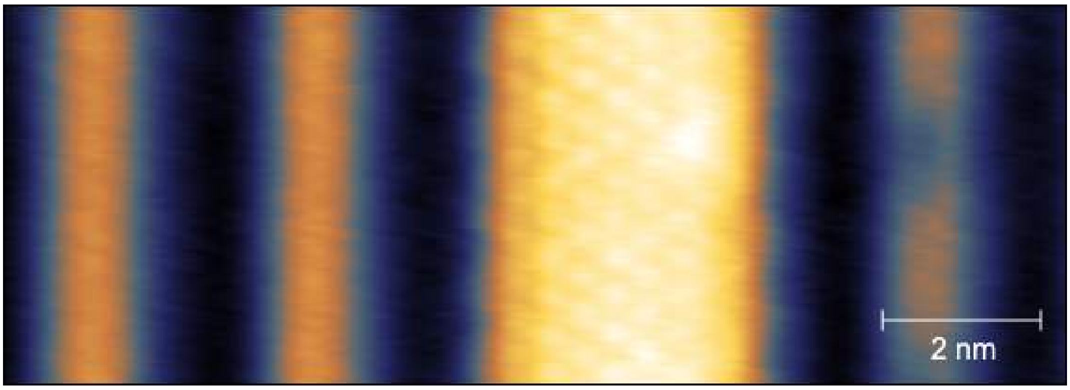

Figure 5.2: Experimental STM image of graphene on Ni(100) in s-moiré configuration. A consistent detachment is visible (larger bright stripe involving two "standard" bright stripes and the otherwise dark region in between). **Scanning parameters:** $V_b = -0.3$ V, $I_t = 4$ nA.

5.2. Modeling carbon segregation

As a first step towards carbon segregation modeling, the carbon diffusion at the bare (100) nickel surface was addressed.

5.2.1. Diffusion on bare Ni(100)

The carbon diffusion was investigated across the first three layers of the surface, finding relevant only those between the two outermost nickel layers (diffusion energy barriers between the 3rd and 2nd nickel layers are ~ 5 eV). *Hollow (h)* and *subtop (st)* were identified as stable adsorption sites for carbon atoms in the first two layers of the surface and, in particular, *h* was shown as the most stable one (~ 1 eV lower in energy with respect to *st*) (Fig.5.3). Three possible paths between two close *h* sites were identified, one through the second surface layer with the *st* site as transition state (TS) (Path I, Fig.5.3), two through the first surface layer with the *bridge* and the *top* as TS sites (Path II and Path III, Fig.5.3). *Ab-initio* Nudged Elastic Band (NEB) calculations allowed to compute the energy barriers between the initial and final site for each of the three paths: as it can be see from Fig.5.3, $h \rightarrow st \rightarrow h$ (Path I) is the most energetically favorable with an energy barrier of about 1.3 eV, and therefore the most probable.

5.2.2. Diffusion at the graphene-Ni(100) interface

Once designed the preferential diffusion path for the carbon atoms, a graphene layer with the stripe moiré configuration was added on top of the Ni(100) substrate with one or two carbon atoms in *h* or *st* sites. Five meaningful situations were simulated: two with one C in two different *h* sites, one with the C in the middle of the phys- region while the other with C close to the chemisorbed (Fig.5.4.b and Fig.5.4.d); two with two C in *h* sites under the phys- region but in the opposite side each other: both configurations have one C in the same position while the other one is closer to the chemisorbed region (Fig.5.4.a and Fig.5.4.e); one with one C in *st* close to the chemisorbed region (Fig.5.4.c). Except for the configurations *b* and *c*, the one with C in *st* and the other with C in *h* in the middle of the phys- region respectively, all the others with C atoms close to the chemisorbed region show a partial elevation of the moiré over the carbon site, reducing locally the widening of the chemisorbed region. These preliminary simulations were fundamental to clarify the origin of the stripe moiré irregularities, identifying in the presence of exceeding carbons at the graphene-nickel interface the origin of local detachments close to the chemisorbed regions of the s-moiré.

5.2.3. Selected paths from *ab-initio* studies

After having identified the origin of stripe moiré detachments, a set of specific ab-initio calculations were performed in order to be used as inputs for the KMC code. The essential part of a KMC code is the list of the velocities that is related to the energy barriers of the processes considered. The processes considered so far are related to diffusion between the most stable carbon adsorption sites: *hollow* and *subtop*. This implies four fundamental processes: $st \rightarrow h$, $h \rightarrow st$, $st \rightarrow st$, $h \rightarrow h$. The pathways are strongly dependent on the moiré region at which they take place. According to this, energy barriers for carbon diffusion under the phys- (yellow), intermediate (blue) and chemisorbed (black) regions and between them were computed and listed in Fig.5.5. Only Ni atoms of the first and second layers are schematically represented, with a color scale that indicates the height of the graphene layer (not shown). The energy values obtained are markedly different and the most favorable diffusion process (lowest energy barrier) is the one from a blue st to a yellow h site while the most inconvenient one is the diffusion inside the blue region. These preliminary results give a first hint of a preferential carbon diffusion towards the phys- region. The energy barriers value reported in Fig.5.5 are related to the diffusion of a single carbon atom at the surface, but the environment conditions in which these processes take place can affect considerably these energy values and, in particular, the presence of neighboring carbon atoms must be considered in order to model correctly the problem. All the pathways of Fig.5.5 were computed also in presence of one and two carbon neighbors. Two examples ($st \rightarrow h$, $h \rightarrow h$) of energy barriers

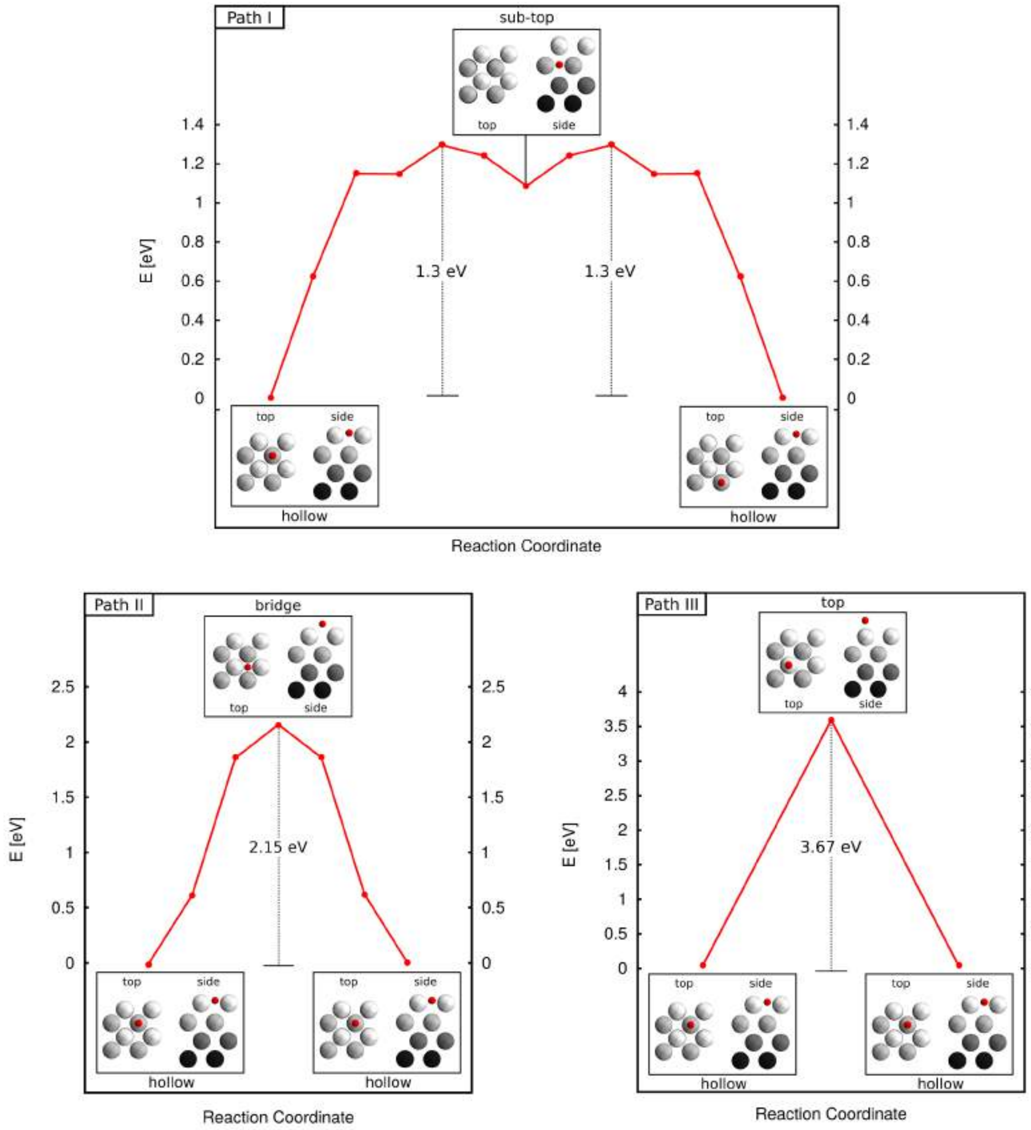

Figure 5.3: Reaction paths for a C atom to go from a *hollow* site to the next one hollow site in the first layer of the (100) nickel surface. The energy barriers are computed through NEB calculations. The 0-scale is set to the *hollow* site that is the most stable one: with this notation all the sites with a positive value of energy are less stable of *hollow*. **Path I:** $hollow \rightarrow hollow$ with $subtop$ as transition state. **Path II:** $hollow \rightarrow hollow$ with $bridge$ as transition state. **Path III:** $hollow \rightarrow hollow$ with top as transition state.

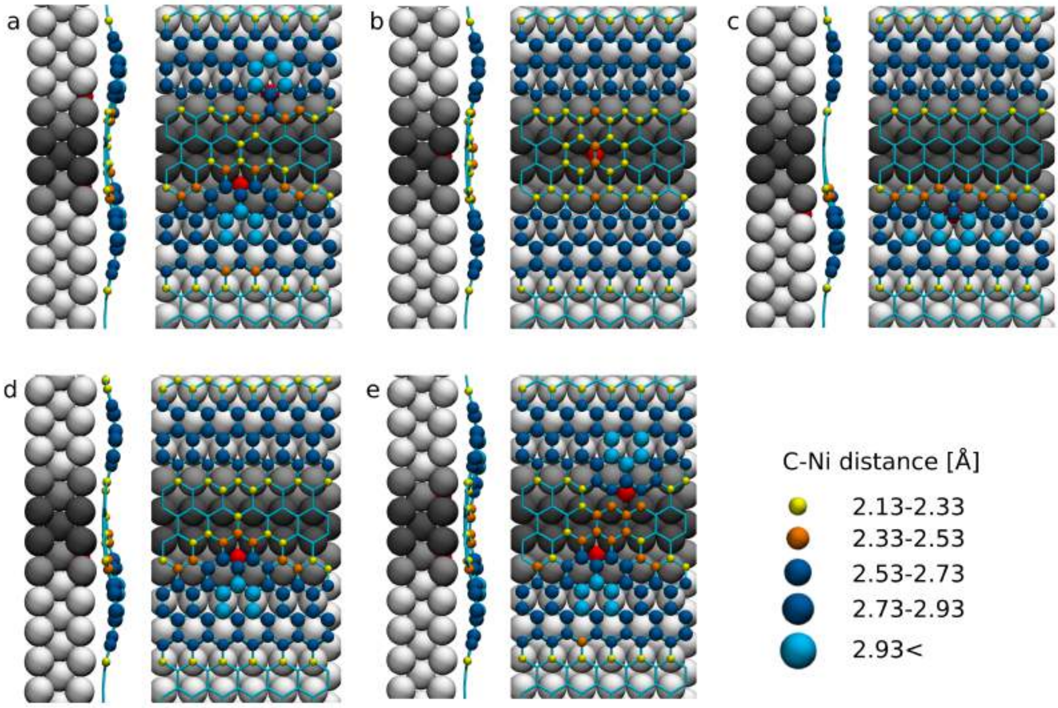

Figure 5.4: Summary of some Gr/Ni(100) configurations with extra carbon atoms (red atoms) final configurations simulated with DFT. The nickel substrate is colored with respect to the relative position of graphene: white under phys- graphene, black under chemisorbed graphene, gray in the intermediate region. The C atoms of the graphene are highlighted by different colors depending on their height with respect to the first layer of the surface (see the legend); side and top view of each configuration are reported.

in function of the number of the featured neighbors are reported in Fig.5.6. The upper panel of Fig.5.6 shows that the $st \to h$ diffusion is unaffected by the carbon neighbors, while for the inverse process each carbon neighbor contributes with 0.4 eV to lower the nominal activation energy obtained without neighbors (Fig.5.5). Instead, the $h \to h$ diffusion does not depend on the number of carbon neighbors (Fig.5.6, lower panel).

As shown in Fig.5.7 (top panel), one carbon atom in the blue region induces only a small local detachment of the chemisorbed region while one carbon atom in the black region does not induce any detachment. In order to have a complete detachment, a "cooperative" process involving two C atoms diffusing towards the some chemisorbed region from opposite sides is necessary. We mention a "cooperative" process because after a DFT relax calculation, the detachment induced by the carbon atoms is wider than the detachment that would be produced by the carbon atoms considered separately. A huge zoo of processes involving two or more carbon atoms can be taken into account and not all of them will be necessary cooperative. Anyway, a complete control on the diffusion pathways is necessary in order to have all the elementary bricks to built a correct KMC code for studying the dynamical evolution of the system as close as possible to the experimental conditions. About fifty elementary processes involving pairs of carbon atoms were studied and all those showing a C-C cooperative behavior were identified and implemented inside the code (see Appendix A). A significant sample of non-cooperative and cooperative processes has been reported in middle and bottom panels of Fig.5.7 respectively. From Fig.5.7 (middle and bottom panels) the conditions for a C-C cooperation comes out. First of all the carbon atoms must be always in *h* site and not separated by more than one nickel row along the stripe direction. Secondly,

from/to	bright	blue	dark
bright	0.46	0.50	1.20
blue	0.40	0.80	1.20
dark	0.45	0.50	1.80

(a) *subtop* → *hollow*

from/to	bright	blue	dark
bright	1.61	1.80	1.80
blue	-	-	-
dark	1.80	1.80	1.80

(b) *hollow* → *subtop*

from/to	bright	blue	dark
bright	0.66	0.80	0.80
blue	0.80	0.80	0.80
dark	0.80	0.80	0.80

(c) *subtop* → *subtop*

from/to	bright	blue	dark
bright	2.10	2.10	2.10
blue	1.60	1.80	2.10
dark	2.40	2.40	2.40

(d) *hollow* → *hollow*

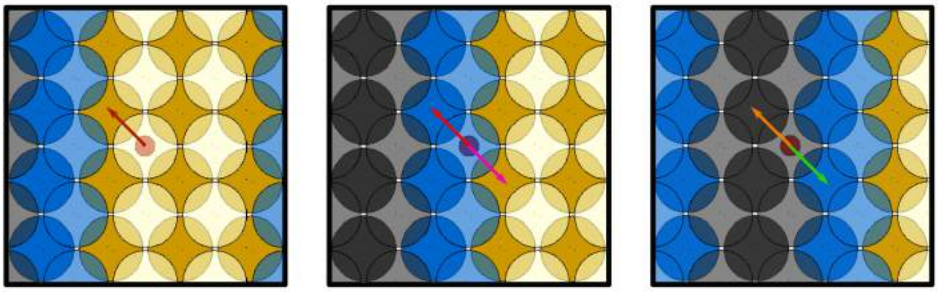

Figure 5.5: Top panel: diffusion energy barriers in eV of a C atom in the (100) nickel surface in presence of stripe moiré. The most important and frequent processes are highlighted with colors and schematized underneath with the same colors. The energy barriers were computed by NEB calculations. **Bottom panel:** schemes of the processes highlighted in the top panel. The nickel surface is colored with respect to the stripe moiré region of the covering graphene: yellow for the phys- region, blue for the intermediate region, black for the chemisorbed region. The free carbon atoms at the surface are visualized in red while graphene is not directly represented.

if the two carbon atoms are in two different moiré regions, they can not be separated by a distance corresponding to two nickel rows across the stripe direction.

Tests were performed also to identify the critical size of a detached graphene region that can spontaneously re-attach to nickel: a region equivalent to (3×5) primitive cells of Ni(100) is sufficient to have a stable detachment. Also this information has been implemented inside the KMC code.

The DFT simulations were performed with all the same structural and electronic parameters of the previous simulations.

5.2.4. Surface reconstruction

It is well-known that when carbon atoms adsorb on Ni(100) with coverage less than one third of a monolayer (ML), they occupy *h* sites and do not change the symmetry of the outermost metal layers. As the coverage exceeds 0.33 ML, the surface reconstructs with a “clock reconstruction” [21, 22]. Fig.5.8 illustrates schematically these two geometries, in which C atoms occupy the *h* sites. In the reconstructed structure, the top-most Ni atoms are displaced parallel to the surface by alternate clockwise and counterclockwise rotations around carbon atoms, forming a geometry of $(2 \times 2)p4g$ symmetry, while the second layer is mostly unperturbed with respect to the clean (100) nickel surface. The surface reconstruction is driven by a strong covalent bond between carbon and nickel atoms and is accompanied by the formation of the Ni_2C alloy [21].

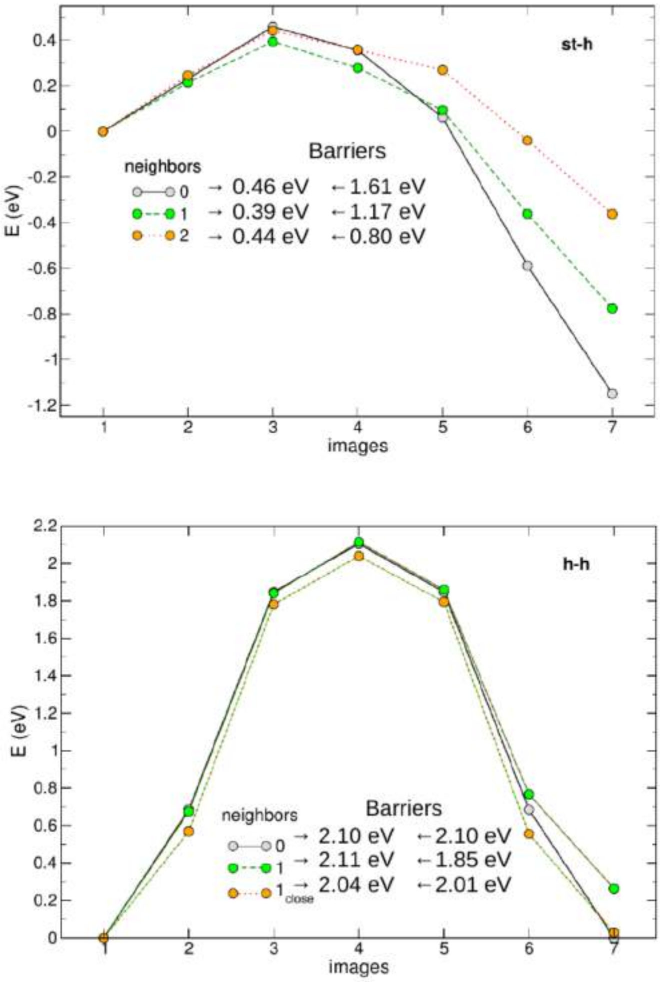

Figure 5.6: Diffusion energy barriers of a C atom in presence of carbon neighbors: no neighbors in white, one neighbor in green, two neighbor in yellow. Energy barriers computed by NEB calculations. The 0-scale is set to the *subtop* site in the first graph while to the *hollow* site in the second. **Top panel:** $subtop \rightarrow hollow$. **Bottom panel:** $hollow \rightarrow hollow$.

An open question is the possibility of having in the interface regions where the detachment is observed enough space and/or free C atoms (local carbon coverage of 0.50 ML) to induce a nickel surface reconstruction with the Ni_2C formation: a positive answer could explain the stability of the moiré detachments. We performed a systematic study, involving a local C concentration of 0.5 ML in a progressively extended region (we count the number of rows parallel to the stripe direction). We find a minimum threshold of 4 rows of 0.5 ML carbon coverage necessary to have surface reconstruction under a detached region. Reconstruction was not found under a simple phys- region (Fig.5.9).

5.2.5. KMC results for evaluation of moiré patterns

All the processes listed in the previous sections where implemented in a home-made KMC code with the goal of studying the dynamical evolution of the s-moiré pattern in presence of carbon segregation at the graphene-Ni(100) interface. The implementation of each individual kinetic process in the code and all the computational details are explained in Appendix B. Here the most significant results obtained with the KMC simulations are reported.

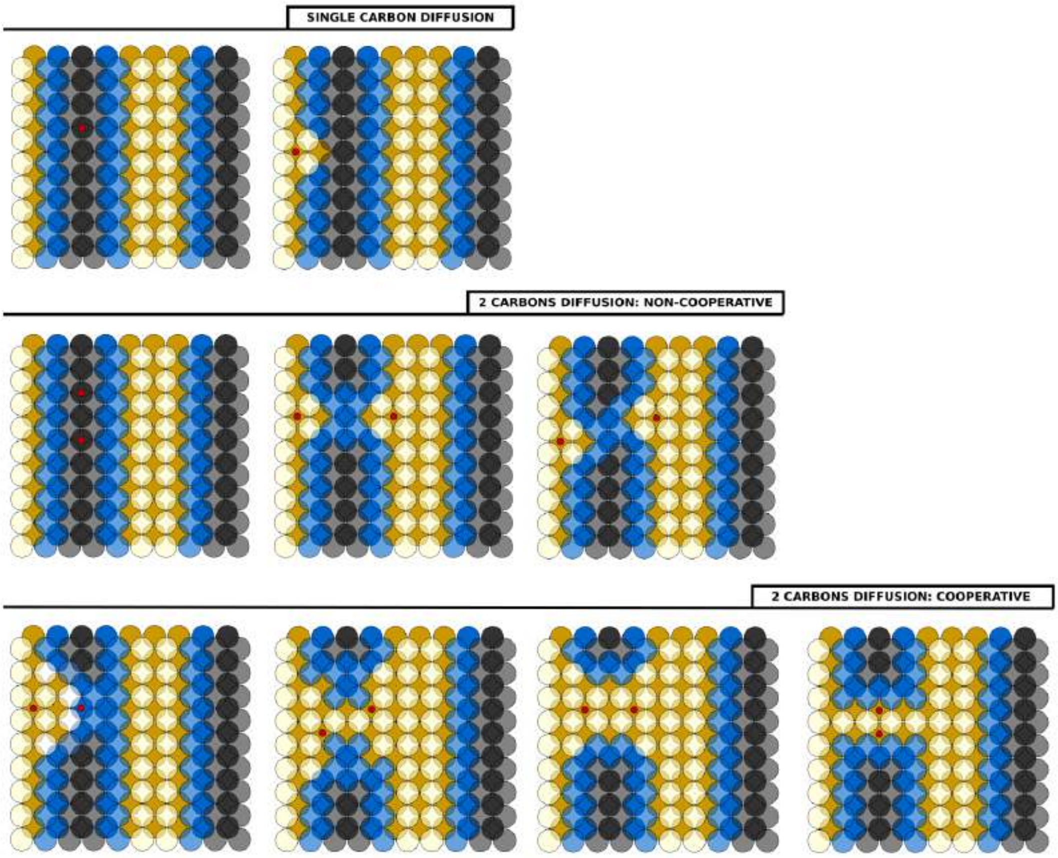

Figure 5.7: Summary of the most relevant configurations with one and two free carbon atoms at the nickel surface: the ground state structures obtained by DFT relax calculations are reported. The nickel surface is colored with respect to the stripe moiré region of the graphene over: yellow for the phys- region, blue for the intermediate region, black for the chemisorbed region. The free carbon atoms at the surface are visualized in red while graphene is not directly represented. **Top panel:** two configurations with a free single carbon atom. **Middle panel:** three examples of non-cooperative processes in presence of two neighbors carbon atoms. **Bottom panel:** four examples of cooperative processes in presence of two neighbors carbon atoms.

Fig.5.10 shows two frames of two simulations at different temperatures, 200 K (left panel) and 600 K (right panel), at the same "extra" carbon concentration of 16%. From a qualitative point of view we can immediately recognize surface regions with a local carbon coverage of 50% that indicate a spontaneous carbide formation [Fig.5.8]: this phenomenon happens at both temperatures, with a well ordered and more extended area at 200 K. It is important to highlight that the carbide formation process was not forced as an input of the KMC, but it occurs spontaneously during the simulation. We also noticed that the carbon atoms involved in the carbide formation maintain their positions longer than the other free carbons at the surface, giving rise to relatively stable structures. This consideration is strongly related to the detachment formations: as it can be seen from the 200 K frame, the carbide formation is more pronounced under the detached regions of the s-moiré, clearly connecting the carbide formation with the detachments stability. From a qualitative analysis of the simulations, we observe that the carbide formation is a synergic process that has as starting point in a cooperative carbons "attached" of a chemisorbed region of the s-moiré: if the number of carbons is enough to produce a local detachment and this persists in time sufficiently, other carbon atoms can "sneak" inside the detached region and further

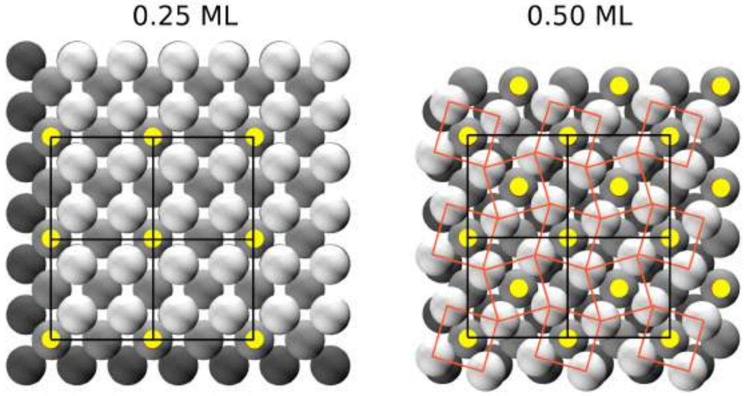

Figure 5.8: An illustration of the $p(2 \times 2)C_{0.25}/Ni(100)$ (left panel) and $p4gC_{0.5}/Ni(100)$ (right panel) geometric structures. The black lines show the in-plane size of the simulation cell while the orange grid shows Ni atom clockwise reconstruction caused by their rotation around the C atoms (yellow dots).

stabilize the detachment. Indeed, if the carbons form carbide, the detachment becomes stable and it can grow longitudinally by adding new carbon atoms at the carbide. If there is no carbide formation under the detachment, this will disappear before reaching a ~3 row Ni length. Fig.5.11 shows an example of detachment formation in presence of carbide. The steps necessary to stabilize a detachment are highlighted in the four frames of Fig.5.11, from the cooperative carbons "attach" up to the carbide formation under the detachment.

From a preliminary qualitative analysis it comes out that the presence and abundance of detachments are strictly related to three factors: the probability of the formation of the initial detachment, the probability to have carbide under the initial detachment, the carbide stability. All of these factors are related to the temperature, and the first two also depend on the free carbon concentration at the surface with the constrain that, after a certain concentration threshold, there will be carbide formation also under the phys- regions of the s-moiré.

It is possible to make even a quantitative analysis about the stability of the long detachments with respect to the small ones, as well about the dependence of the number of detachments on length, stability and temperature. To do that, the "lifetime" of the detachments with different lengths and at different temperatures has been measured from KMC simulations. Concerning the lengths of the detachments, a tolerance about 20% was applied: with this choice a detachment can oscillate in length for a quantity proportional to its length and be still counted as the same detachment.

Fig.5.10 allows to make a comparison between the type and the number of the detachments at 200 K (left panel) and 600 K (right panel). A high number of small detachments is present at 600 K while, at 200 K, there is a long detachment with a well ordered carbide structure underneath (right bottom part of the simulation cell). In the same position there is a similar detachment at 600 K, but smaller and with more disordered carbide structure where the carbon atoms are more jagged. The number of detachments with different length L (normalized on the number of KMC steps and on the number of phys- stripe of simulation cell) as a function of the temperature is reported in Fig.5.12 while Fig.5.13 represents the lifetime of detachments with different length L as a function of temperature. From Fig.5.12 it comes out that at increasing temperature corresponds an increasing number of small detachments (violet line) and a decreasing of longer detachments. A peak in the number of detachments is present at 325 K. Fig.5.13 shows an inversion on the lifetime of the detachments at different length with respect to the temperature: at low temperature, long detachments (up

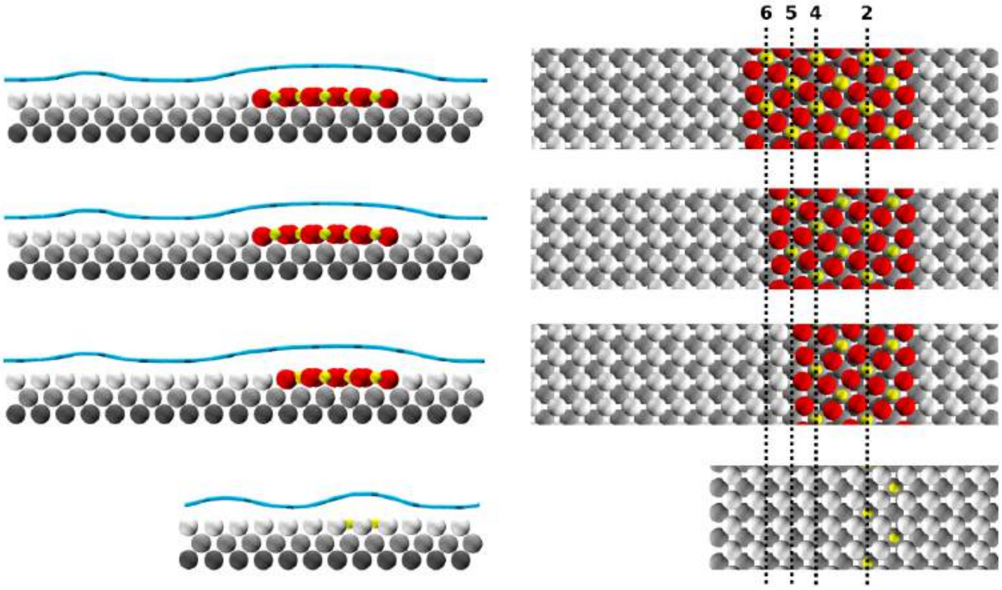

Figure 5.9: Side (left panel) and top (right panel) views of stripe moiré simulation supercells with a local carbide (yellow atoms) concentration of 0.50 ML under a pyhs- region (2 lines of C, fourth configuration) and under a completely detached region (4-5-6 lines of C, first three configurations) of the supercell. In all of the top views graphene is hidden in order to simplify the vision of the Ni(100)-C interaction. The configurations with 4,5,6 lines of C present the typical clockwise reconstruction (red Ni atoms) with the $p4gC_{0.5}/Ni(100)$ geometric structure. For the first three configurations a supercell 19×2 nickel atoms while for the fourths one a supercell of 12×2 nickels were used. Graphene (blue line) is reported only in the side views.

to ~50 Ni length) are more stable while, at high temperature, small detachments (<10 Ni length) become more stable. Summarizing all the informations of Fig.5.10-5.12-5.13 it can be concluded that at high temperature more detachments are present but shorter and less stable, while at low temperature less detachments are present but longer and more stable. This outcome is strongly related to the carbide formation and stability: at high temperatures carbide becomes unstable and has a higher probability to disgregate by thermal excitations.

5.2.6. STS

Beside the structural details, phys-, chemisorbed and detached regions of the s-moiré were investigated in terms of the exponential decay of the STM tunneling current increasing the tip-surface distances and in terms of constant height STS maps. Fig.5.14 shows the simulated and experimental *k* decay constant profile along a phys-, chemisorbed and detached consecutive graphene regions (Fig.5.14, bottom panel, A-B-C regions). The simulated *k* profiles are shown both raw and convoluted with a gaussian function in order to reduce the numerical noise. The highest *k* values are obtained over the detachment, totally in agreement with the experimental findings. These values are related to the quasi-pristine nature of the graphene in the detached regions due to the absence of interaction with the substrate, highlighting the different electronic properties with respect to the other regions of the moiré (*k* of the pristine graphene is ~1.7 Å^{-1})(Fig.5.15). From the experimental side a strong dependence of the *k* values on the tip-sample range of distances is found: as it is visible at -0.3 V bias (Fig.5.14, first set of panels), the theoretical *k* profile matches well with the green experimental *k* profile obtained farther (low current) from the graphene layer. In the comparison between experiments and simulations, we have to keep in mind that high current significally perturbs

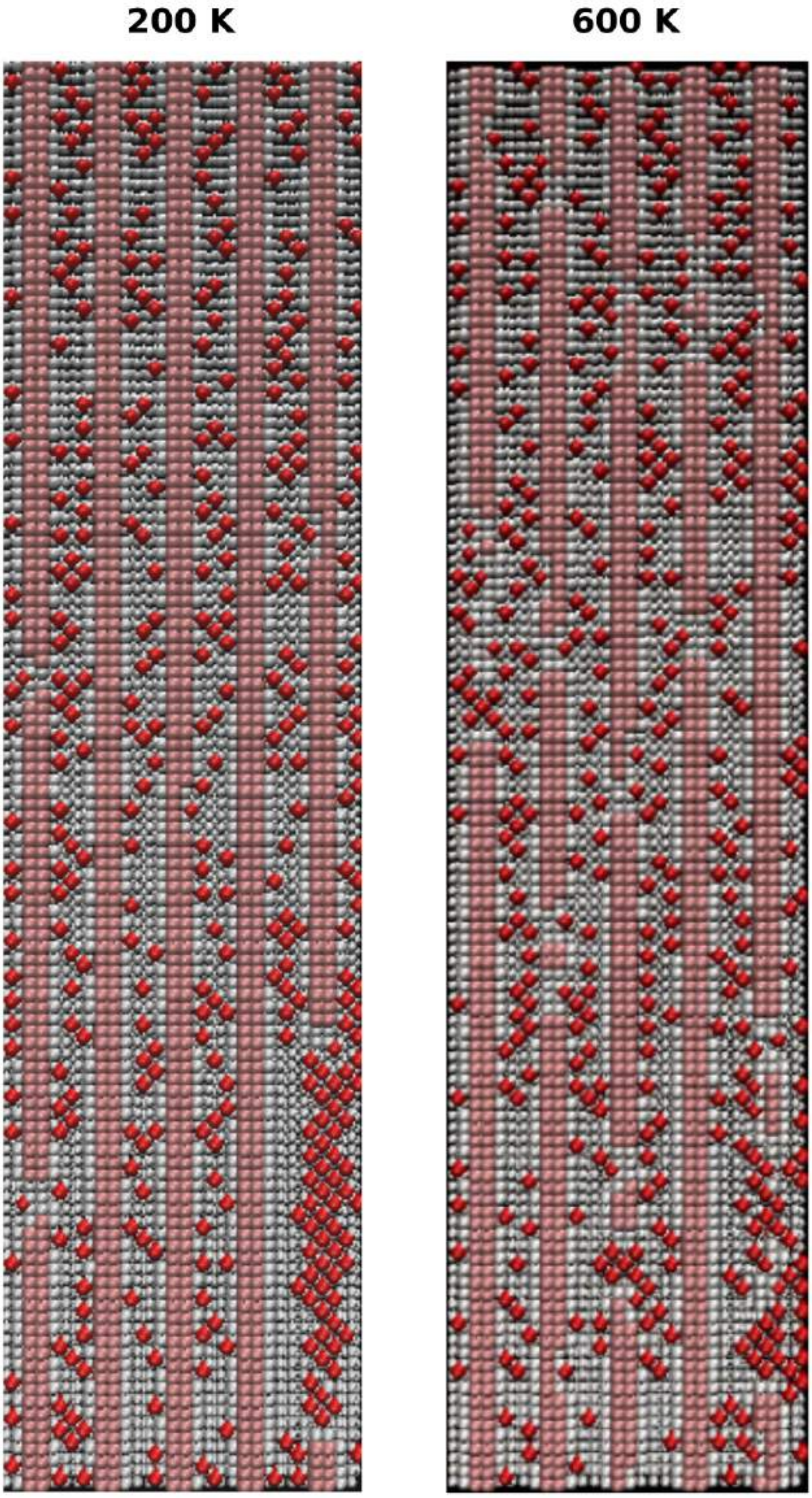

Figure 5.10: Frames of two different KMC simulations at 200 K (left panel) and 600 K (right panel). Pink and white stripes are nickel surface regions where graphene is phys- and chemisorbed respectively, while the red dots are the free carbons at the surface. Graphene is not shown. **Computational parameters:** free carbon density of 16%, size of the KMC simulation supercell 30×120 nickel atoms.

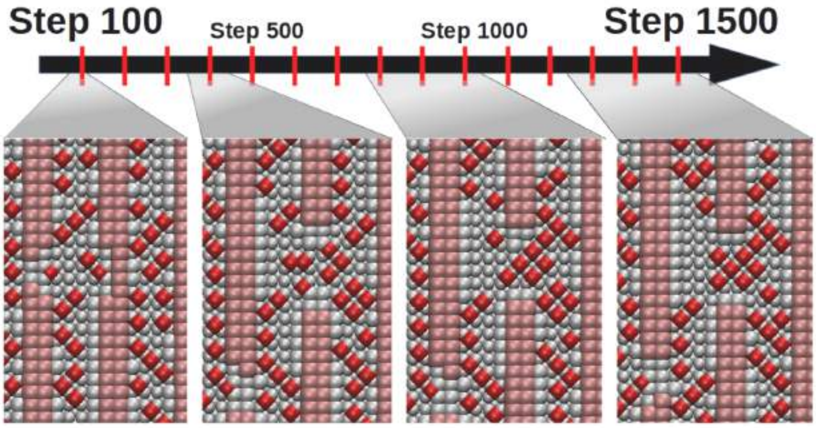

Figure 5.11: Four stages of a detachment arising with underlying carbide. The duration of each stage is indicated approximately along the time arrow on top of the figure. **Computational parameters:** T = 200 K, free carbon density of 16%, size of the KMC simulation supercell 30×120 nickel atoms.

the DOS of the sample but, due to the Thersoff-Hamman aproximation, this is not taken into account in our simulations. This is the origin of the scaling factor introduced in the last panel of Fig.5.14 (V=+2V) in order to have a good matching between the experimental and theoretical profiles. Anyway, the agreement between theory and experiment in the *k* profile description is good and goes in the direction of a clear distinction of the different regions of the moiré (phys-, chemisorbed, detached) also from an electronic point of view.

The STS maps are a very powerful tool for a detailed investigation of the electronic properties, resolved not only in space (like the STM maps) but also in energy. During the thesis work we have implemented an algorithm to extract them from the local density of states, as introduced in chapter 1. We performed a preliminary investigation of the detached regions using the calculated STS maps, and some images are reported in the last figures of this chapter (Fig.5.16-5.17-5.18). Several specific features are visible, very sensitive on the detailed configuration of the graphene moiré and of the underlying Ni surface, with different patterns of segregated carbons. The interpretation of the results and the comparison with the experiments, however, would require a careful analysis which has not yet been performed.

Computational details

The DFT simulations were performed with Quantum ESPRESSO code [53], using plane-wave basis set and Generalized Gradient Approximation for the exchange - correlation functional in the Perdew-Ernzerhof parametrization (GGA-PBE) [48]. The kinetic energy cutoff has been set at 30 Ry for the plane-wave basis set. The equilibrium lattice parameters of Ni(100) and graphene were fixed at 2.49 Å and 2.46 Å respectively. For studying the carbon preferential adsorption sites at the Ni(100) bare surface, a periodically repeated slab geometry with 4 Ni layers and one carbon atom in the considered site (h, st) was used, with a vacuum spacing of 15 Å between the outermost nickel layer of the surface and the consecutive Ni(100) surface replica. The in-plane shape of the simulation cell is a 2×2 Ni(100) primitive cell in order to avoid the C-C interaction. Once also the graphene over the Ni(100) was consider, to correctly simulate the stripe moiré periodicity, an in-plane supercell 12 nickel atoms long must be used (Fig.4.5) while, in order to avoid the interaction between adjacent images of extra carbon atoms of the graphene-Ni(100) interface, a width of 6 nickel atoms was considered (Fig.5.4). In this case, due to the computational effort caused by the huge number of atoms, a periodically repeated slab geometry with 3 Ni layers separated by 10 Å was adopted. Concerning the Brillouin zone sampling, we adpoted a Monkhorst-Pack k-point grids [56] of $3 \times 3 \times 1$ for the first cell and $2 \times 1 \times 1$ for the second one centered on Γ and the Methfessel-Paxton smearing technique with an energies broadening of 0.01 Ry [86]. The optimized atomic positions have been obtained minimizing the forces acting on each atom. Stick-and-ball models were rendered with the VMD software [87].

5.3. Summary

We have characterized the most stable carbon adsorption sites on the bare (100) nickel surface through DFT calculations. Combining DFT and KMC simulations, using also the results obtained from the study of the bare (100) nickel surface, we have investigated the s-moiré irregularities of graphene on Ni(100) due to the partial detachment of chemisorbed regions of the moiré. DFT allowed to understand the detailed atomic-scale structure, while KMC based on energy barriers computed by DFT, demonstrated a strong correlation between the stability of the detachments and the carbide (Ni_2C) formation, consistently with the experimental findings.

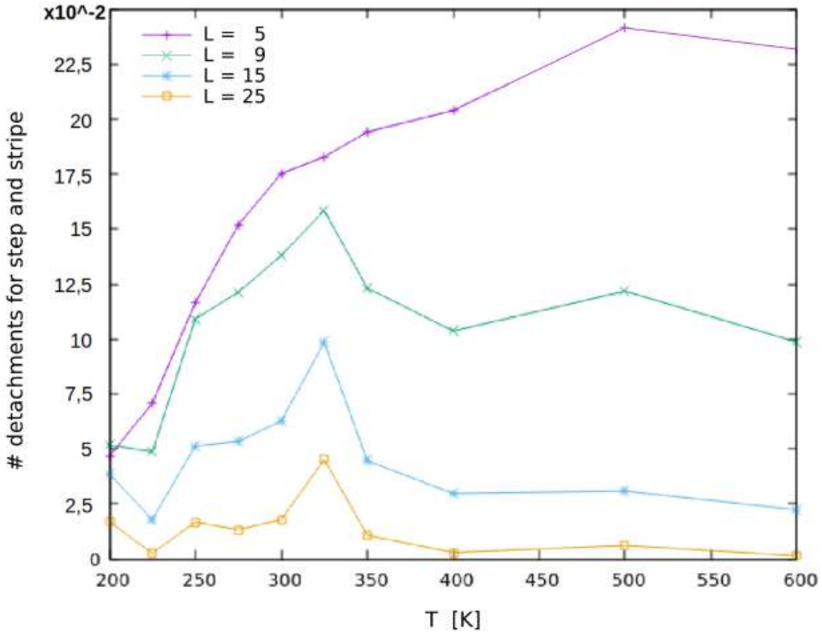

Figure 5.12: Density of detachments vs temperature. Different curves correspond to different length L of the detachments (5, 9, 15, 25 nickel atoms) with a tolerance threshold of 20%. **Computational parameters:** T = 200 K, free carbon density of 16%, size of the KMC simulation supercell 48×120 nickel atoms, 10^7 simulation steps.

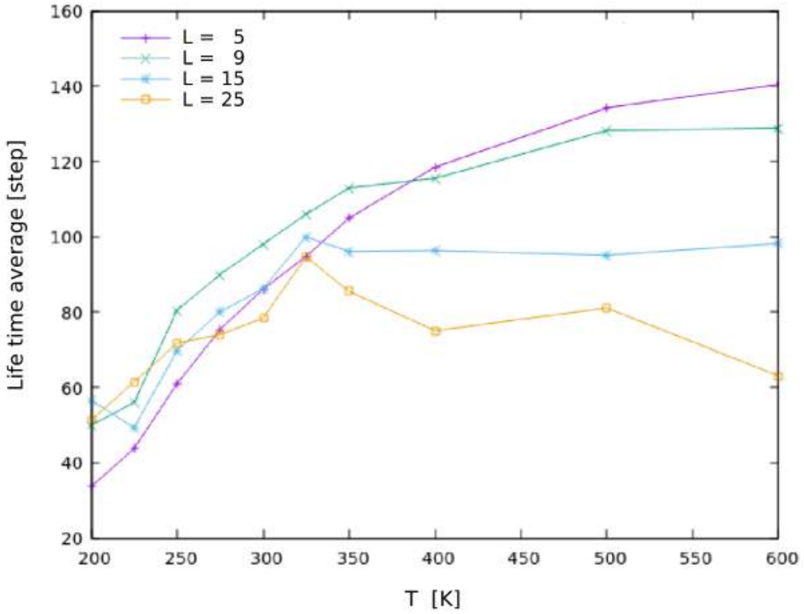

Figure 5.13: Life time average of detachments vs temperature. Different curves correspond to different length L of the detachments (5, 9, 15, 25 nickel atoms) with a tolerance threshold of 20%. **Computational parameters:** T = 200 K, free carbon density of 16%, size of the KMC simulation supercell 48×120 nickel atoms, 10^7 simulation steps.

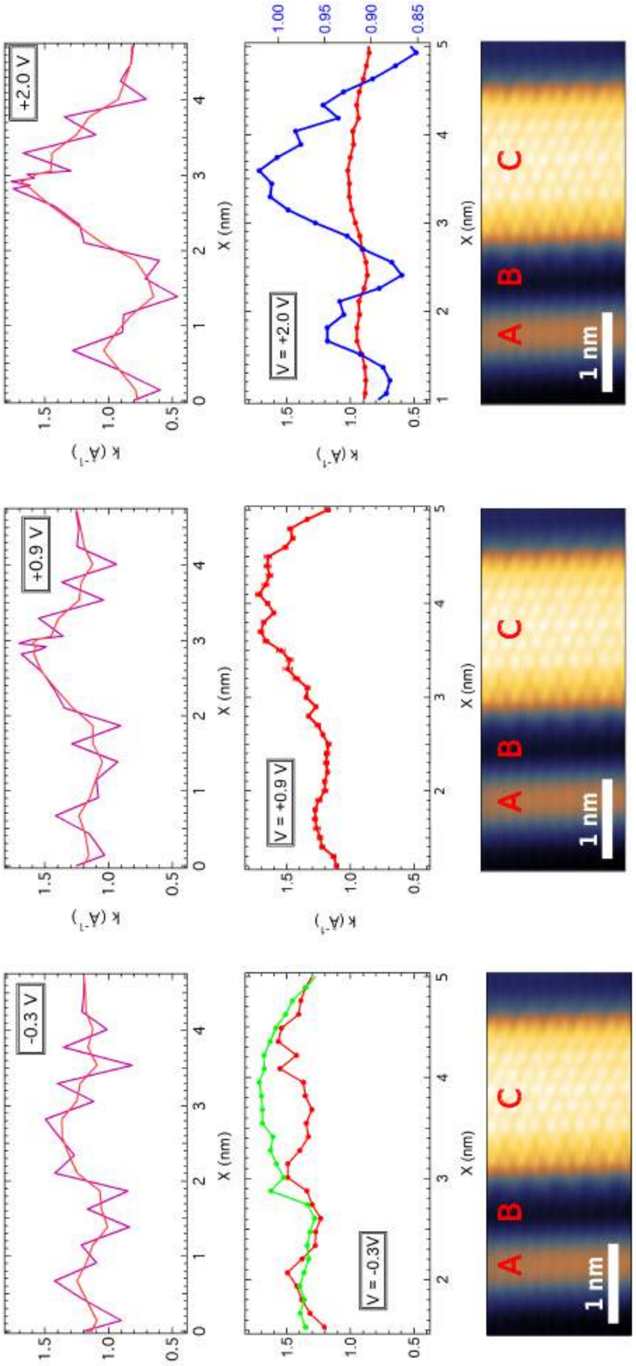

Figure 5.14: Comparison between simulated (top panel), experimental (middle panel) *k* tunneling current constants decay and the features of the experimental STM images (bottom panel). In the graphic at -0.3 V the red dots come out fitting close to the graphene layer (I=4.0 nA), while the green dots are fitting in a furthest range (I=8.0 nA). In the graphic at +2.0 V the blue dots are the same as the red ones but with a zoomed scale. **Experimental parameters:** I=4.0 nA (V=-0.3 V, green plot; V=+0.9 V; V= +2.0 V), I=8.0 nA (V=-0.3 V, red plot).

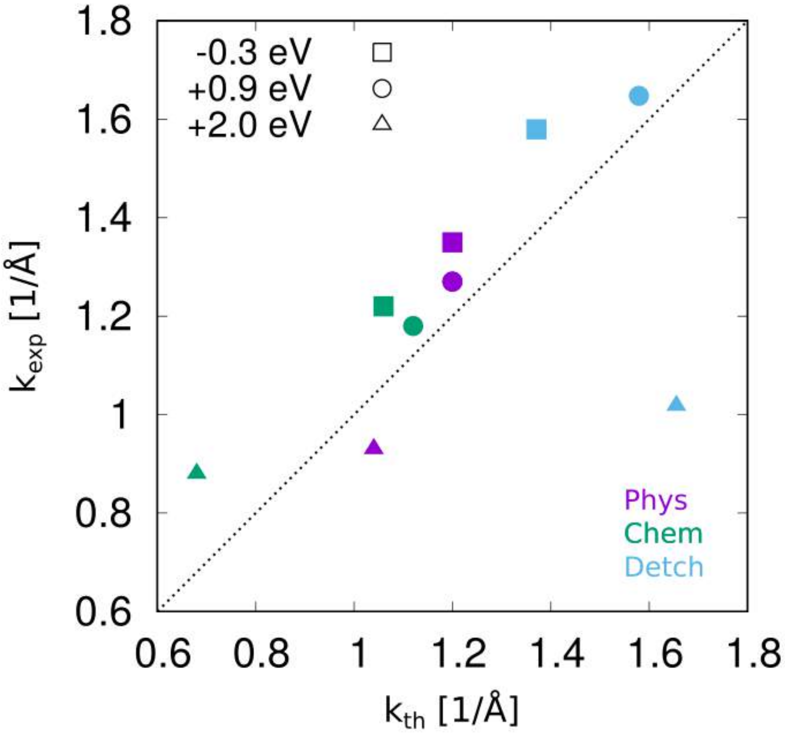

Figure 5.15: Comparison between experimental (k_{exp}) and theoretical (k_{th}) decay constants for the phys- (violet), chemisorbed (green) and detached (blue) regions of the s-moiré.

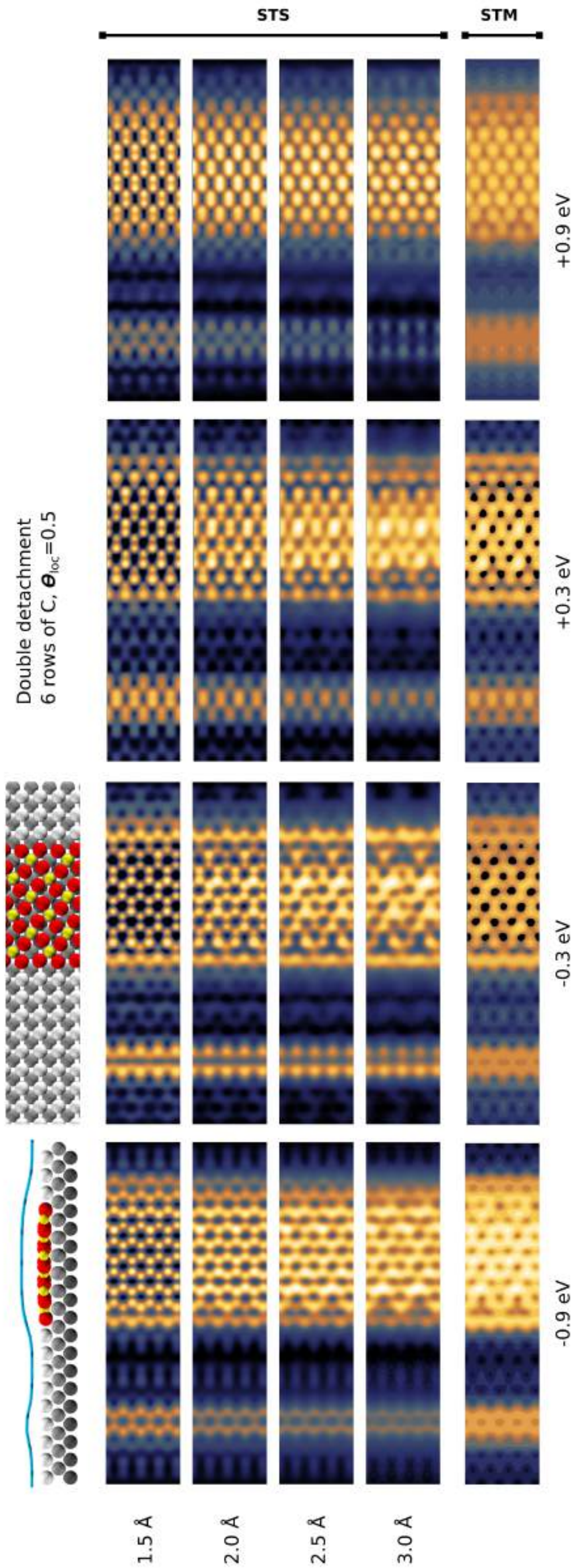

Figure 5.16: Constant height STS maps and constant current STM maps at different bias values of a simulation cell including phys-, chemisorbed and detached s-moiré regions. Simulation cell with six lines of carbons under the detached region with a local coverage of 0.5 ML. **Computational parameters:** for the STS maps the corresponding heights are shown at the left side; for the STM maps the ILDOS iso-surface lying 2.5 Å above graphene with ILDOS value of $8 \cdot 10^{-5}$ $|e|/a_0^2$.

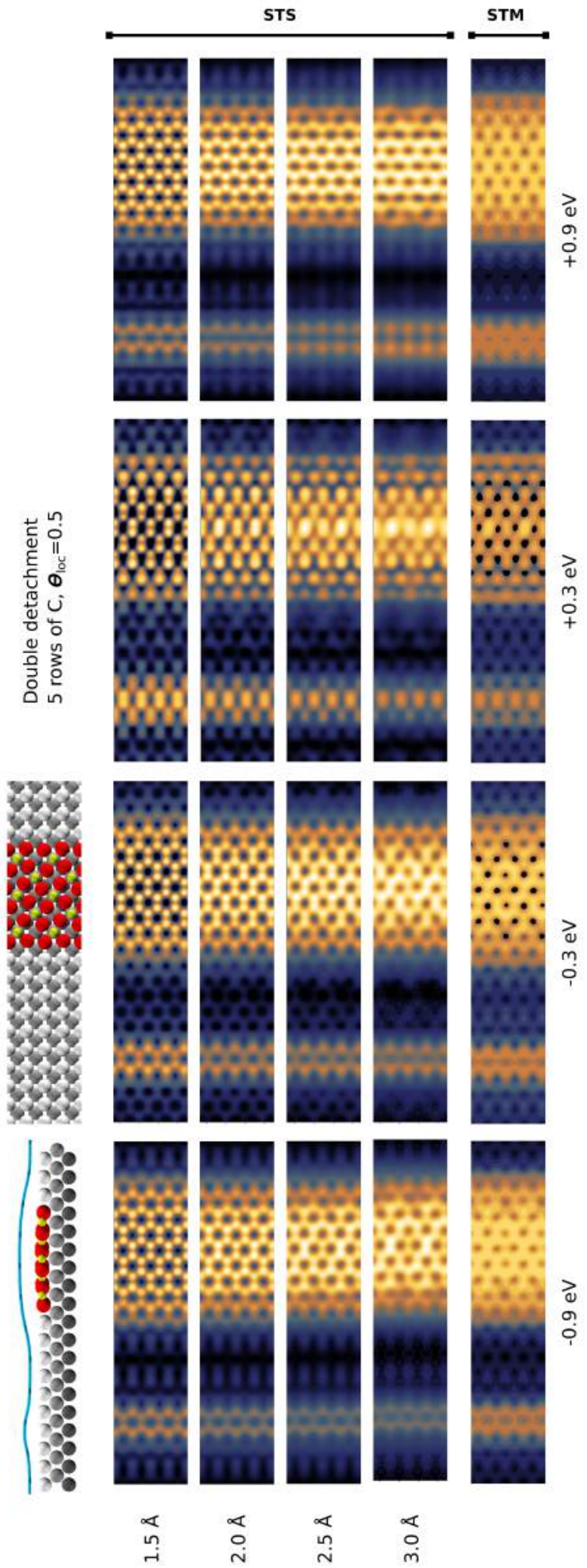

Figure 5.17: Constant height STS maps and constant current STM maps at different bias values of a simulation cell including phys-, chemisorbed and detached s-moiré regions.Simulation cell with five lines of carbons under the detached region with a local coverage of 0.5 ML. **Computational parameters:** for the STS maps the corresponding heights are shown at the left side; for the STM maps the ILDOS iso-surface lying 2.5 Å above graphene with ILDOS value of $8 \cdot 10^{-5}$ |e|/a$_0^2$.

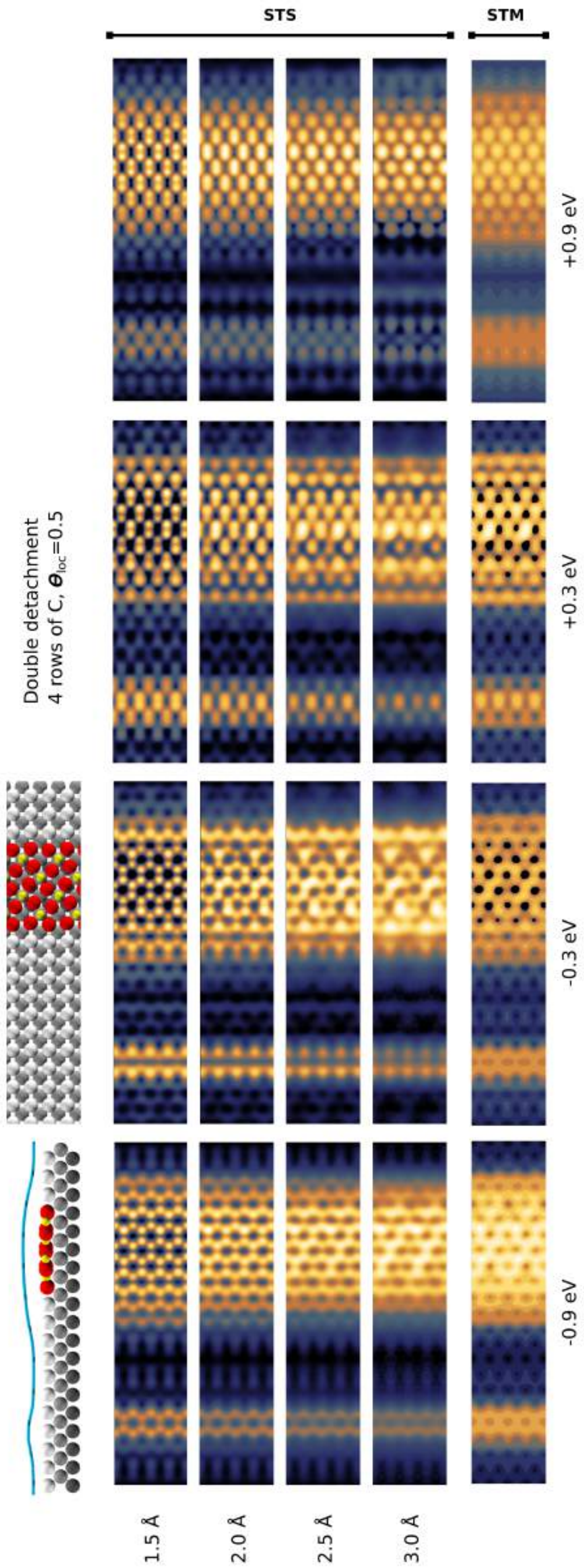

Figure 5.18: Constant height STS maps and constant current STM maps at different bias values of a simulation cell including phys-, chemisorbed and detached s-moiré regions. Simulation cell with four of carbons under the detached region with a local coverage of 0.5 ML. **Computational parameters:** for the STS maps the corresponding heights are shown at the left side; for the STM maps the ILDOS iso-surface lying 2.5 Å above graphene with ILDOS value of $8 \cdot 10^{-5}$ $|e|/a_0^2$.

6

Ni(100) stepped surfaces without/with graphene

In this chapter the problem of the stability of (100) nickel stepped surfaces is addressed without/with graphene overlayers. The first part of the chapter is devoted to the stepped surfaces modeling starting from a crystalline bulk: particular attention is given to the concept of vicinal surfaces. After that, some physical quantities related to the surface energy are introduced as indicators of the surface stability, taking into account also the presence of steps. Finally, also a graphene overlayer is considered on the stepped surfaces and some peculiar configurations are studied in order to explain some experimental evidences.

6.1. State of the art and new experimental data

At variance with graphene growth on single crystal transition metals, where the surface has atomic flat morphology and homogeneous crystallinity, polycrystalline metallic surfaces can contain highly stepped regions, step bunches, grain boundaries and even amorphous areas. This constitutes the "material gap" that affects not only the conventional surface science experiments typically performed using single-crystal samples, but also simulations, that become much more complicated when more realistic systems are considered. However, high quality graphene has been successfully grown also on polycrystalline surfaces, and the process has been monitored. With the aid of mesoscale in-situ monitoring techniques, such as low energy electron microscopy (LEEM) and scanning electron microscopy (SEM), the growth velocity of graphene on polycrystalline transition metals has been correlated with the relative overlayer-substrate orientation as well as the grain orientation [102]. Besides, the continuity of graphene can be uninfluenced by the grain boundaries at certain growth conditions. In post-growth atomic-scale images, graphene can still stay intact at highly corrugated regions, which indicates the strong carbon-carbon bonding [42]. However, it should be noted that investigation at the mesoscale may lack the atomic-level insight, while post-growth surface characterization at various length scales suffers the drawbacks of treating the surface dynamics at elevated temperature as a "black box" and oversimplifying the complexity of the interplay between graphene and the metallic substrates.

New in-operando STM experiments for graphene growth on polycrystalline nickel (Ni) substrates were carried out at TASC IOM-CNR with the aid of an add-on FAST module [81, 105]. Surface dynamics, normally inaccessible in conventional STM measurements due to the limited time resolution, has been recorded with atomic resolution and a frame rate up to 10 Hz on both flat terraces and step edges, clarifying the growth mechanisms. As shown in Fig.6.1, when graphene "meets" nickel steps during growth, the strong interface bonding will facilitate the simultaneous growth rather than the downhill "flow" of graphene over the edge. Interestingly, the consecutive narrow steps originated by the opening of step bunches often have a constant width, as can be seen in Fig.6.1. This raises naturally a question: can graphene grow downwards to a lower terrace at such growth conditions or it will always stay at the same height level?

In order to answer this question, DFT studies on the stability of Ni(100) stepped surfaces have been carried on in absence and presence of graphene with the aim of individuate the role of the graphene on a possible opening the regular nickel surface steps bunches.

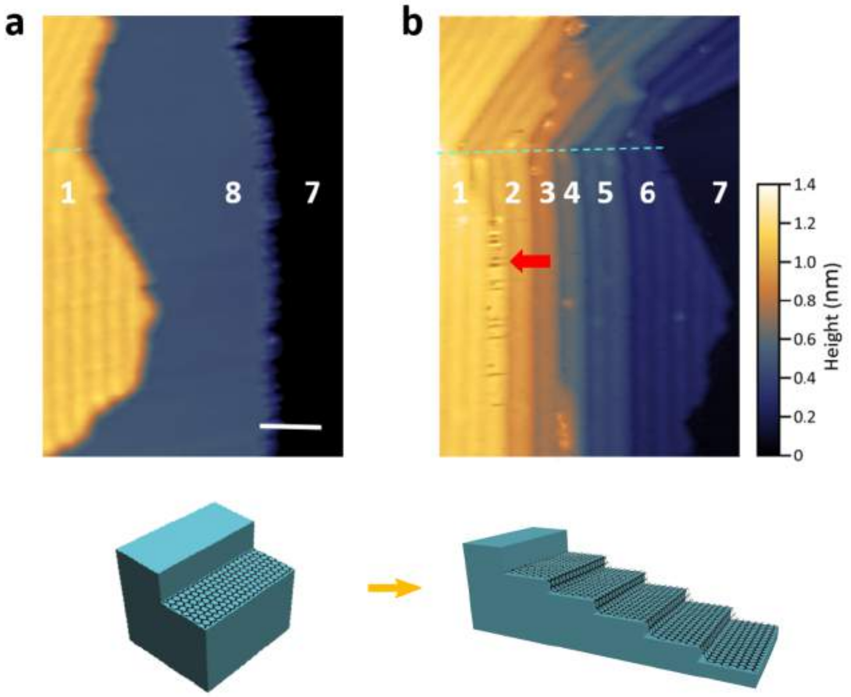

Figure 6.1: Experimental STM topography **(upper panel)** and corresponding schematic illustration **(lower panel)** of downhill carpeting of graphene at a step bunch. Frames were measured at: (a) 0 s, (b) 166 s. Relative heights in (b) are denoted by the color bar. Scale bar: 5 nm.

6.2. Clean vicinals and stepped surfaces

Surfaces can be imaged by splitting a bulk crystal in two or more parts. Atoms at the surface will have a lower coordination than in bulk. Due to the changed coordination, the surface geometry will relax or possibly even reconstruct, in order to let surface atoms find their new equilibrium positions. For ideal surfaces of cubic crystals, thus also for the fcc crystal, one normally distinguishes between, low Miller index (flat) surfaces, (100), (111) and (110) surfaces [Fig.6.2], and high Miller index (stepped) surfaces. Stepped surfaces can exhibit significantly different properties compared to flat surfaces due to the effect of the steps and possible defects (kinks, adatoms etc.).

Hereinafter, we focus on stepped surfaces with (100) terraces obtained by cutting the bulk with a small angle θ with respect to the (100) plane. Lets consider the $(11N)$ set of surfaces. $(11N) \rightarrow (001)$ for $N \rightarrow \infty$. These surfaces are called *vicinal surfaces* of the (100) surface and their steps are oriented along the $[1\bar{1}0]$ direction. Vicinal surfaces exhibit a regular array of steps with the peculiarity of having not enough space to add further atoms in between the terraces of the vicinal and the tangent plane to the edges of the terraces [Fig.6.3].

Fig.6.4 can help understanding how to represent a $(11N)$ vicinal surface in a fcc crystal. The cubic conventional cell (Fig.6.4.a) is repeated *N*-times in-plane and it is intersected with

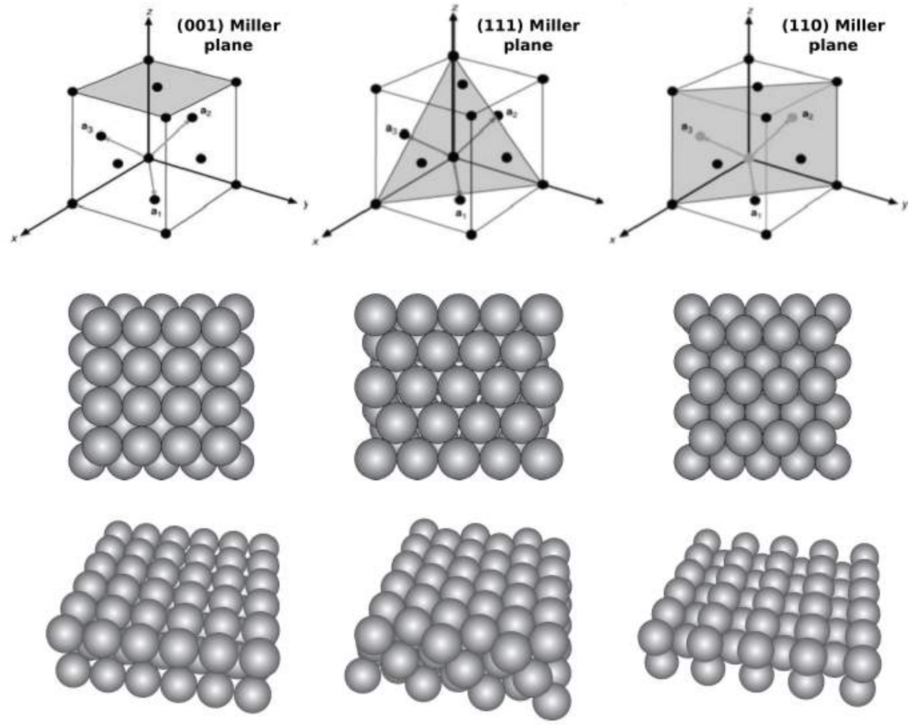

Figure 6.2: Low Miller index surfaces for a fcc crystal.

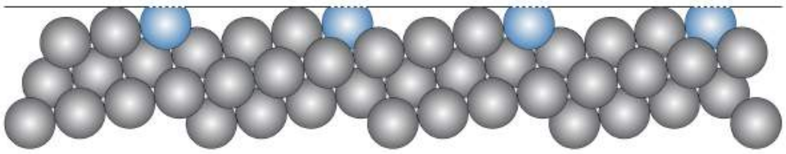

Figure 6.3: Example of a vicinal surface (here, (117)): the atoms of the vicinal are represented in gray while the line on top of the figure underlines that there is no space for further atoms (blue) under the tangent plane to the terraces edges.

the $(11N)$ plane as shown in Fig.6.4.b, where the atoms lying in the plane are highlighted in red. If all the atoms over the plane are disregarded, the atoms on the plane compose the upper edge of the step while the green row of atoms (Fig.6.4.c) is the lower edge of the step. The (100) plane is colored in yellow in Fig.6.4.c. The (111) plane (colored in blue) is the natural joining facet for two consecutive (100) terraces separated by a mono-atomic step.

All the other surfaces with steps are called with the generic name of *stepped surfaces*. Although in the reality these surfaces could have mainly steps and terraces with different lengths, only periodic stepped surfaces with steps and terraces of the same length have been considered here, being easier to simulate. Vicinal surfaces are a subset of this type of stepped surfaces. In the generic case, two contiguous (100) terraces are separated by a step composed by *h* atomic layers. Geometrically, joining consecutive terraces can be done by a (111) or (101) plane. In this work all the stepped surfaces models are built with (111) steps. This choice is justified by the highest stability of the (111) surface with respect to the (101) [Fig.6.6].

The link between vicinal surface indices $(11N)$ and the (100) and the (111) surfaces, terrace and step of the stepped surface respectively, is expressed by representative vectors of

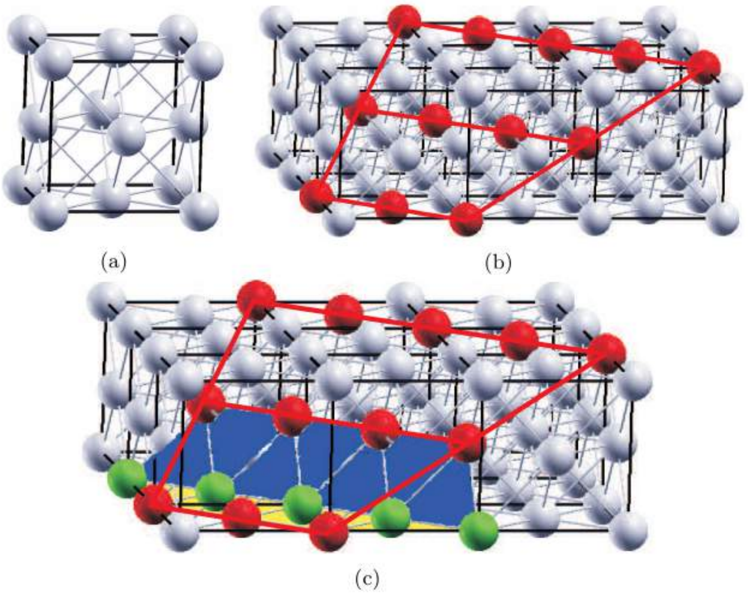

Figure 6.4: Building block for a (113) vicinal surface of a fcc crystal. Red dots: atoms of the vicinal surface; yellow plane: (100) crystal plane; blue plane: (111) crystal plane; green dots: edge atoms of the (111) step between two (100) crystal planes.

each surface:

$$[11N] = n[002] + [11\bar{1}], \tag{6.1}$$

where we can derive the relation between the index N and the number of rows n parallel to the lower edge of the step composing the (100) terrace:

$$N = 2n - 1 \qquad with \qquad n \in N, n \geq 1. \tag{6.2}$$

Since the (111) step has an angle $\alpha = 35.26°$ with respect to the *z*-axis (Fig.6.15), a geometrical factor *f* can be introduced. *f* represents the projection of the (111) external surface on the (100) surface and can be defined through Fig.6.5 as:

$$f = f(h) = \frac{l\cos(\theta) - b}{a_0} = \frac{l\cos(\theta) - (n-1)a_0}{a_0} = \frac{h}{2}. \tag{6.3}$$

As shown in Eq.6.3, *f* is a function of the number *h* of atomic layers of the step.

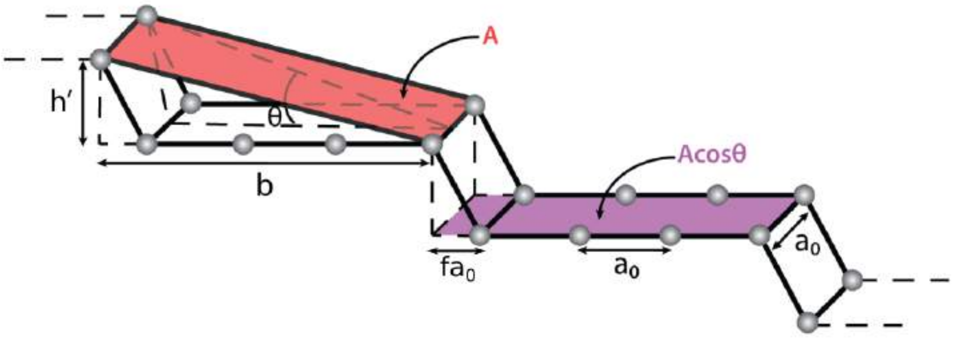

Figure 6.5: Geometrical model adopted to compute the formation energy of the stepped surfaces: all the parameters of the model are reported.

6.2.1. Stepped surfaces stability

To discuss the surface stability, it is necessary to define the surface energy per unit area, γ^{area}. This quantity is the additional energy of a system with a surface with respect to the bulk system and it represents the energy amount necessary to create a surface from a bulk crystal. Generally, the surface energy contribution is lower then the bulk energy contribution: this is consistent with the fact that surfaces are less stable with respect to the bulk. Otherwise, bulk would spontaneously crumble making surfaces. γ^{area} depends on the surface configuration and the more stable will be the surface, the lower will be its value.

Considering a slab configuration with two equivalent surfaces, γ^{area} is defined as:

(6.4)

where E_{slab} is the total energy of the slab, E_{bulk}^{atom} is the energy of an atom in the bulk, N_b is the number of the atoms of the slab, A is the surface area of the two surfaces of the slab. The factor $\frac{1}{2}$ is included because the slab configuration contains two equivalent surfaces.

The surface area of a stepped surface increases drastically increasing the terrace length and with the size of the step, while the number of atoms associated with primitive cell of a stepped surface is always one (Fig.6.15). For this reason, it is useful to define also the surface energy per atom γ^{atom} where, the surface energy, instead of normalizing w.r.t. the stepped surface area A, is normalized w.r.t. the number of atoms of the surface:

$$\gamma^{atom} = \frac{1}{2N_a}(E_{slab} - E_{bulk}^{atom}), \tag{6.5}$$

where N_a is the number of atoms of the surface (for stepped surfaces $N_a = 1$) while the other parameters are defined as in the Eq.6.4. In Fig.6.6 the γ^{atom} for the fcc low Miller index surfaces are reported in comparison with the values obtained by Vitos *et al.* [106]. The order is the same, although there is an important discrepancy between the two dataset, due to the computation methods: at variance with the present calculations based on DFT-GGA, Vitos *et al.* used the Linearized Muffin-Tin Orbital (LMTO) method, which is known to better match LDA results rather then GGA [107]. The (100) surface results to be the most stable while the (111) is found to be lower in energy with respect to the (101), justifying the choice of the step adopted is this work.

Through Fig.6.5, it is possible to derive geometrically the surface energy per atom associated to a stepped surface with a step of *h* atomic layers and a terrace made by *n* rows of atoms:

$$\gamma_{step}^{atom} = \gamma_{step}^{area}\, l a_0 = \gamma_{step}^{area}\, \sqrt{h'^2 + b^2}\, a_0 = \gamma_{step}^{area} \sqrt{\frac{h^2}{2} + (n - 1 + f)^2\, a_0^2}. \tag{6.6}$$

If $n = h = 1$, $f = \frac{1}{2}$, for the (111) surface the Eq.6.6 becomes:

$$\gamma_{111}^{atom} = \gamma_{111}^{area}\, \frac{\sqrt{3}}{2} a_0^2, \tag{6.7}$$

while for the (100) surface Eq.6.6 reads as:

$$\gamma_{100}^{atom} = \gamma_{100}^{area}\, a_0^2. \tag{6.8}$$

γ_{step}^{atom} has an extensive nature and this is clear considering the limits for $N \to \infty$ and $h \to \infty$:

$$\begin{aligned} \lim_{N\to\infty} \gamma_{step}^{atom} &= (n-1)\, \gamma_{100}^{atom}, \\ \lim_{h\to\infty} \gamma_{step}^{atom} &= h\, \gamma_{111}^{atom}. \end{aligned} \tag{6.9}$$

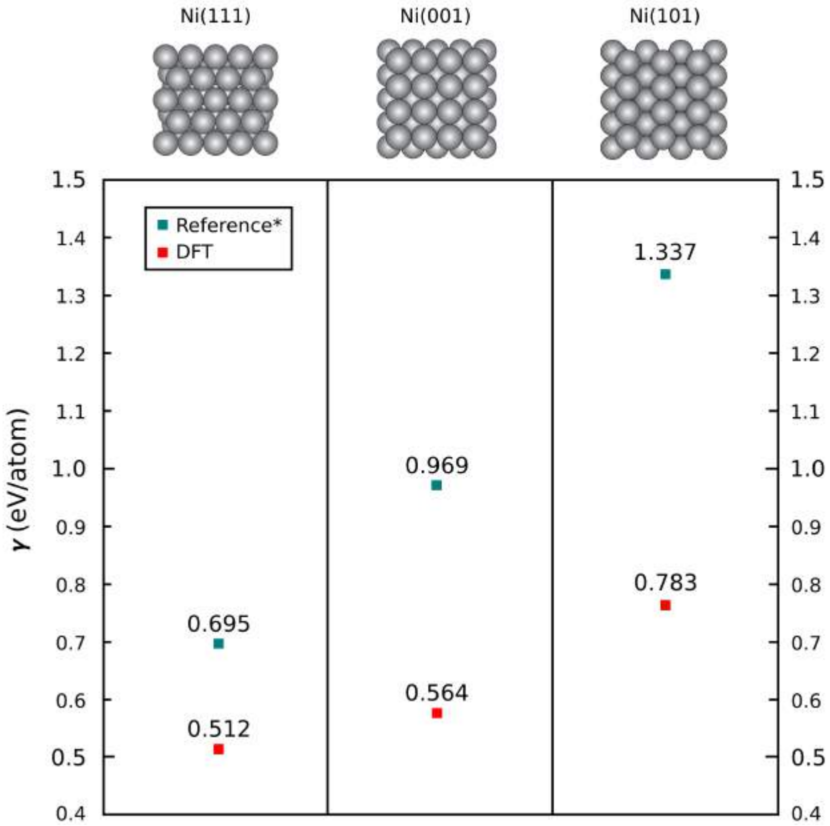

Figure 6.6: Formation energy for surface atom of low Miller index ideal surfaces of fcc crystal. Comparison with the values obtained by L. Vitos [106].

Indeed, if *h* is fixed, increasing *N*, $\theta \to 0°$ and the stepped surface goes to the (100) surface while the in-plane length of the supercell increases as $(n-1)\,A_0$; otherwise, if *N* is fixed and *h* increases, $\theta \to 54.74°$ (dihedral angle between (111) and (100) planes) and the stepped surface goes to the (111) surface with a surface area equal to *h* times the area of the primitive cell of the (111) surface, $\frac{\sqrt{3}}{2}a_0^2$. This two limits underline that γ_{step}^{atom} depends on the length of the terrace, and is an extensive quantity, even though is normalized on the atom numbers like the γ_{100}^{atom} and the γ_{111}^{atom} quantities that are clearly intensive quantities.

We introduce the surface energy per unit of projected area γ_p^{area}:

$$\gamma_p^{area} = \frac{\gamma_{step}^{atom}}{a_0\, l\, \cos(\theta)} = \frac{\gamma_{step}^{area}}{\cos(\theta)}. \tag{6.10}$$

Fig.6.7 shows the γ_p^{area} values as function of tan(θ). For $\theta \to 0°$ $(N \to \infty)$ the values have a linear trend with γ_{100}^{area} as limit value and $m = 0.0307$ as angular coefficient. This linear trend with small θ is not obvious and it is due to the decreasing of the interaction between contiguous steps caused by the increasing of distance among them $(N \to \infty)$.

After defining the surface energy, one can introduce the concept of step formation energy that will represent the supplementary energy necessary to create a single step on an infinite surface and will play a crucial role on the investigation of the steps stability. We start with a mono-atomic step that can be characterized by the step exceeding energy per unit length β. For $N \to \infty$, that means isolated mono-atomic steps, β can be thought as the surface energy difference between the vicinal and the (100) surfaces:

$$\beta = \gamma_{vic}^{area}\, l - \gamma_{100}^{area}\, b \tag{6.11}$$

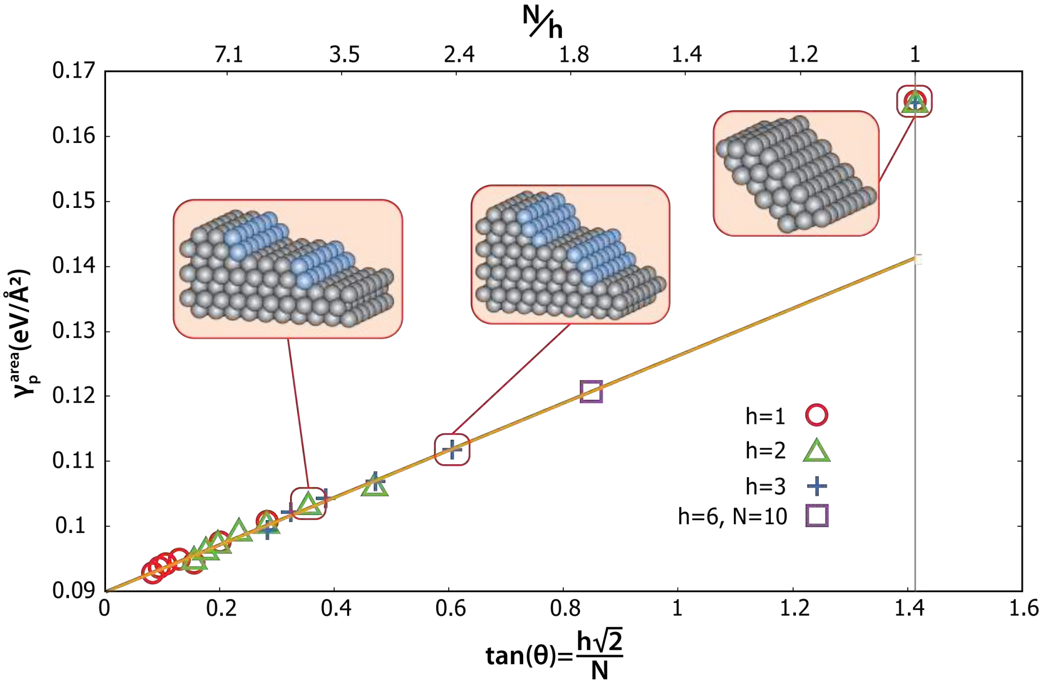

Figure 6.7: γ_p^{area} as function of tan(θ) for stepped nickel surfaces with different terrace lengths and step heights. The yellow line is the linear fit at small θ while the right limit is fixed equal to tan(θ) $= \sqrt{2}$ correspondent to $\theta = 54.74°$, dihedral angle between (100) and (111) planes and equivalent to a (100) stepped surface with an infinite (111) step. The pink boxes show some examples of studied stepped surfaces.

where *l* and *b* are defined as in Fig.6.5. Inverting Eq.6.11, we obtain:

$$\gamma_{vic}^{area}(\theta) = \gamma_{100}^{area}\cos(\theta) + \beta\,\frac{\sin(\theta)}{h'}, \tag{6.12}$$

that for the limit of isolated step ($\theta \to 0°$) becomes:

$$\gamma_{vic}^{area}(\theta) \approx \gamma_{100}^{area} + \beta\,\frac{\theta}{h'}. \tag{6.13}$$

Finally, the formation energy of a step per atom is defined:

$$E_{step} = a_0\,\beta = \gamma_{vic}^{atom} - (n - 1 + f)\,\gamma_{100}^{atom} \tag{6.14}$$

that, generalized for a generic stepped surface, reads as:

$$E_{step} = \gamma_{step}^{atom} - \left(n - 1 + \frac{h}{2}\right)\gamma_{100}^{atom} \tag{6.15}$$

where for a generic (111) step $f = \frac{h}{2}$. Eq.6.15 allows to compute E_{step} for stepped surface with finite terraces.

In Fig.6.8 the E_{step} values as a function of the height of the step and the length of the terrace have been reported. For $N \to 0$, it is found a decreasing trend going as $E_{step} = E_{step}^{\infty} + \alpha l^{-1.4}$ while, for $N \to \infty$, an asymptotic value proportional to the height of the step is reached. From Eq.6.15 an expression of γ_{step}^{area} as a function of E_{step} can be derived :

$$\gamma_{step}^{area} = \gamma_{100}^{area}\cos(\theta) + E_{step}\frac{\sin(\theta)}{h' a_0}. \tag{6.16}$$

If Eq.6.16 is considered together with Eq.6.10, for $N \to \infty$ we obtain:

$$E_{step}^{\infty} = 0.0307\,\frac{ha_0}{\sqrt{2}}, \tag{6.17}$$

where there is no dependence on the terrace length but only on the height of the step *h*, as it should be. Eq.6.17 gives the formation energy of an isolated mono-atomic step of $0.134\,eV/atom$, in agreement with the value of $0.115\,eV/atom$ reported in literature [106].

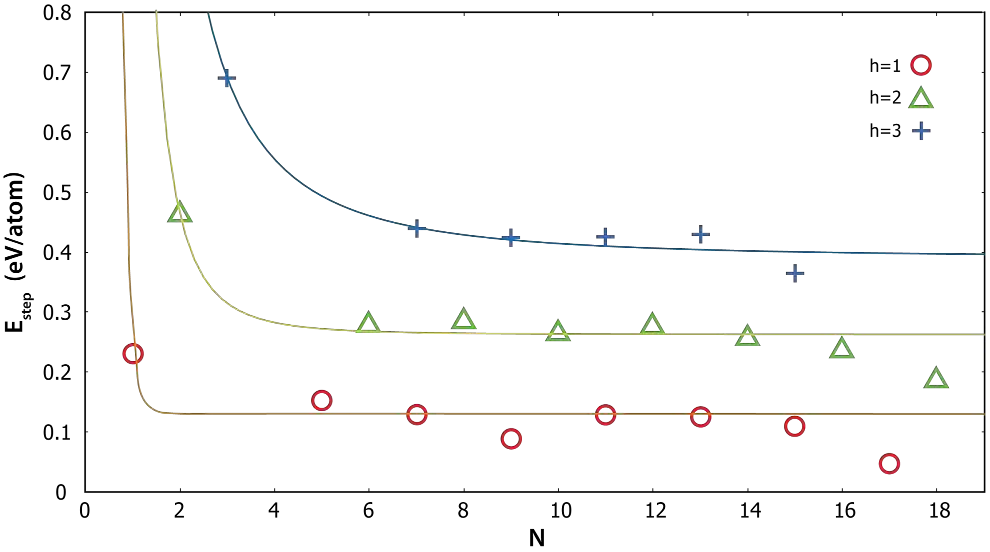

Figure 6.8: Formation energy for a (111) mono-, bi- and 3- atomic step in function of the (100) terrace length.

Finally, the step-step interaction as a function of the terrace length is computed trough the function $\chi(\theta)$ that represents the distances between the γ_p^{area} values and the linear fit for $\theta \to 0°$ in Fig.6.7

$$\chi(\theta) = \gamma_p^{area}(\theta) - \gamma_{100}^{area} - E_{step}^{\infty}\,\frac{\tan\theta}{h' a_0}. \tag{6.18}$$

Fig.6.9 shows $\chi(\theta) \simeq 0.10\tan(\theta)^3$ which has a monotonically increasing behavior with function of $\tan(\theta)$, underling an increase of the step-step interaction with the decrease the step-step distance.

This analysis was done for several stepped surface configurations, increasing the size of the terrace keeping fixed the height of the step and vice-versa, with the goal of investigating the stepped surface stability in relation to its intrinsic identified quantities and finding a relation between them. All the results are summarized in Tab.6.1. As can be seen, in the limit of isolated step $(n \geqslant 3)$, γ_p^{area} as a function of $\tan(\theta)$ has a linear trend for each of the considered heights of steps $(h = 1, 2, 3, 6)$. Moreover, with the increase of θ, the γ_p^{area} values deviate significantly from the linear trend, as shown by the $\chi(\theta)$ plot (Fig.6.9) (power dependence trend for larger $\tan(\theta)$ values). It can be concluded that there are no energy-stability reasons for surface steps bunch opening for the (100) bare nickel surface, driving the attention to a possible role of carbon-nickel interaction.

6.3. Stepped surfaces with graphene

Before considering graphene on stepped surfaces, graphene ribbons with different sizes over the (100) bare flat nickel surface have been studied with the aim of simulating the graphene

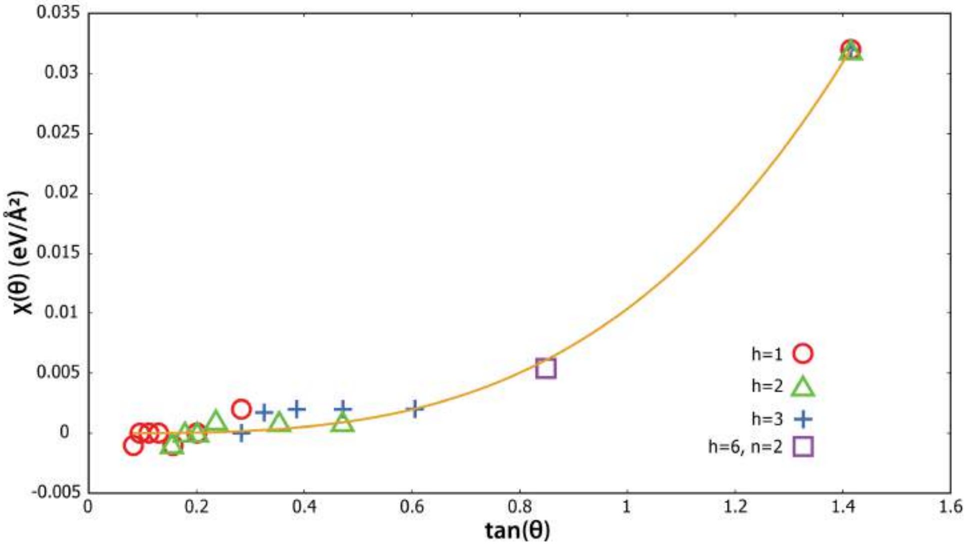

Figure 6.9: Step-step interaction $\chi(\theta)$ in function of tan(θ). Values for different step heights are reported.

growth, with particular attention at the graphene ribbon edge behavior. This preliminary study is designed to shed light on the growing mechanism of graphene over the Ni(100) flat surface in order to address better the same problem on stepped nickel surfaces. The ribbons are simulated in the s-moiré configuration (see section 4.2), with an infinite size along the moiré stripes and a finite size along the moiré periodicity. As shown in Fig.6.10, the left side of the ribbons is fixed to mimic the chemisorbed region of the s-moiré, while the rest of the ribbon is free to relax and find its preferential final structure. The idea of these models is simulating the growth of a semi-infinite graphene layer on the a Ni(100) surface where the increasing sizes of the ribbon somehow mimics the addition of new carbon atoms to the graphene layer: if the fixed portion of the graphene ribbon is always the same, this represents a rough, but efficient way to study the graphene growth by DFT simulations.

The ribbons have a zigzag left edge (chemisorbed region-like edge) and a Klein right edge (free edge): the Klein edge has been chosen for its better "anchoring" with the substrate with respect to the other possible graphene termination (zigzag and armchair). The DFT computational parameters are the same adopted for the s-moiré configuration (see section 4.2). Fig.6.10 shows the existence of a critical ribbon width of thirteen carbon atoms: after that, the ribbon accumulates too much stress to remain flat over the surface and, consequently, assumes a s-moiré-like configuration (the chemisorbed region followed by a phys- region). This is in perfect agreement with the experimental STM movies that show the graphene growth over both flat and Ni(100) stepped surface. STM movies show a sudden formation of a complete phys- region at the graphene layer face of raising instead of a gradual emergence, being in agreement with the drastic change of corrugation between the second and third configuration of Fig.6.10.

Also the graphene downhill landing and carpeting over the Ni(100) stepped surface, can been rationalized by DFT simulations. Fig.6.1 compares a step bunch before/after graphene coverage. To simplify the case, the step edge is along the crystallographic direction of Ni(100) (s-moiré configuration), and graphene has the zigzag edge aligned with this direction. For a step bunch composed of pure nickel, a relatively compact structure is favorable, i.e. at step edge a close-packed (111) surface is more stable than dispersed edges separated by Ni(100) narrow steps. This can be understood considering that the (111) face is energetically more stable for fcc metals than other less closed-packed faces (Fig.6.6). On the contrary, when it

h	n	$\tan(\theta)$	γ_{step}^{atom} [eV/atom]	γ_{step}^{area} [eV/Å^2]	γ_{p}^{area} [eV/Å^2]	E_{step} [eV/atom]
1	1	1.414	0.51	0.095	0.165	0.230
1	3	0.283	1.56	0.097	0.101	0.150
1	4	0.202	2.10	0.095	0.097	0.122
1	5	0.157	2.61	0.092	0.094	0.074
1	6	0.129	3.21	0.093	0.094	0.112
1	7	0.109	3.77	0.093	0.093	0.102
1	8	0.094	4.32	0.092	0.093	0.087
1	9	0.083	4.81	0.091	0.091	0.014
2	1	1.414	1.02	0.095	0.165	0.460
2	3	0.471	1.96	0.095	0.106	0.271
2	4	0.354	2.53	0.096	0.102	0.275
2	5	0.283	3.07	0.095	0.099	0.250
2	6	0.236	3.65	0.096	0.098	0.269
2	7	0.202	4.18	0.095	0.096	0.237
2	8	0.177	4.73	0.094	0.095	0.216
2	9	0.157	5.23	0.093	0.094	0.158
3	1	1.414	1.54	0.095	0.165	0.690
3	3	0.606	2.41	0.095	0.111	0.436
3	4	0.471	2.96	0.096	0.106	0.424
3	5	0.386	3.53	0.097	0.103	0.426
3	6	0.326	4.09	0.097	0.102	0.425
3	7	0.283	4.59	0.095	0.099	0.355
6	3	0.849	3.72	0.091	0.897	0.120

Table 6.1: Summary of all the γ_{step}^{atom} computed by DFT and their derived quantity in function of the height of the step h and the number of atom rows n of the terrace.

has been covered by graphene, the step bunch opens into consecutive (111) steps with an almost constant width of one atom (Fig.6.11).

If we define the graphene s-moiré periodicity λ as the distance between two consecutive phys- regions of the moiré (beatings), the "natural" λ of graphene grown on a Ni(100) flat surface is described in details in chapter 4 (Fig.4.6). The best matching between simulations and experiments is obtained with a simulation cell whose length corresponds to $19\,a_{Ni} = 47.31\,\text{Å} \Leftrightarrow 44$ carbons (11 graphene periods along the armchair direction), corresponding $1.74\,a_{Ni} \Leftrightarrow 4$ carbons where $a_{Ni} = 2.49\,\text{Å}$ is the lattice parameter of Ni(100) square lattice. In this moiré supercell 3 beatings (alternation of phys- and chemisorbed regions) are present and the corresponding moiré periodicity is $\lambda = 15.77\,\text{Å}$. The "tolerance" of the result can be estimated considering a smaller simulation cell giving an acceptable matching between simulations and experiments: $12\,a_{Ni} = 29.88\,\text{Å} \Leftrightarrow 28$ carbons (7 graphene periods along the armchair direction), i.e., that $1.71\,a_{Ni} \Leftrightarrow 4$ carbons. In this small moiré supercell 2 beatings are present and the corresponding moiré periodicity is $\lambda = 14.94\,\text{Å}$. If a Ni(100) stepped surfaces with (111) mono-atomic step is considered, similar ratio between the number of C atoms and Ni rows along the $[01\bar{1}]$ direction is expected and used to build the simulations supercell. Three configurations have been studied, where the supercells contain two terraces separated by a (111) mono-atomic step. This choice allows more freedom in the number of C atoms that must be considered (multiple of 4 on 2 terraces instead of one) without the problem of a possible shift of the graphene registry with respect to the surface terrace due to the mono-atomic step (Fig.6.15).

Configuration *a* (Fig.6.12.a) has two terrace 7 Ni long separated by a (111) mono-atomic step (in total 15 Ni) and 32 carbons: $13\,a_{Ni} = 32.37\,\text{Å} \Leftrightarrow 32$ carbons (i.e. $1.63\,a_{Ni} \Leftrightarrow 4$ carbons). This moiré supercell has 2 beatings and a $\lambda' = 16.19\,\text{Å}$, corresponding to $1.08\,\lambda$. Configuration *b* (Fig.6.12.b) has two terrace 8 Ni long separated by a (111) mono-atomic

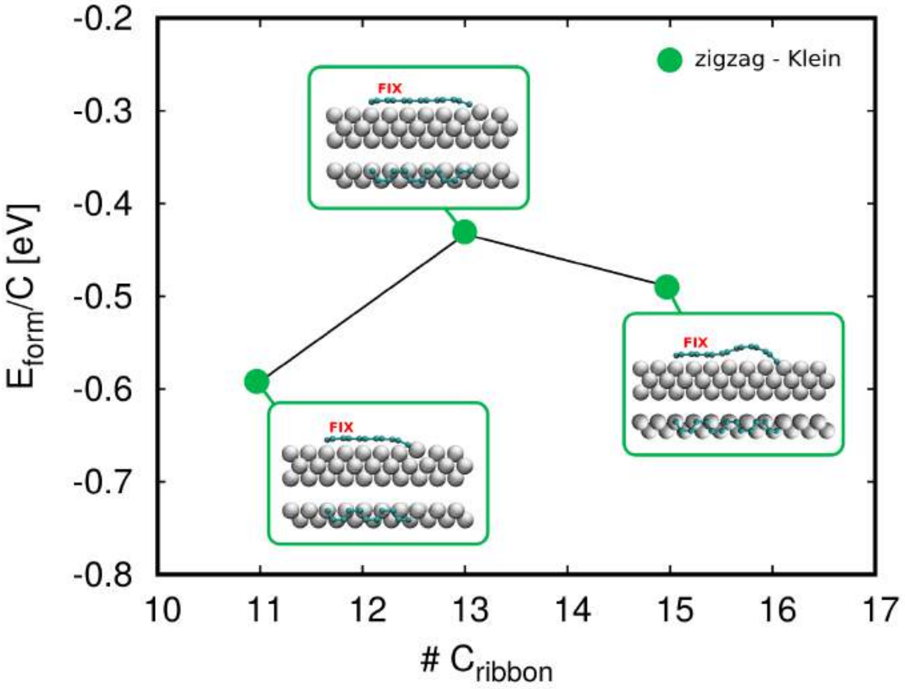

Figure 6.10: Formation energy of graphene ribbon on a Ni(100) surface as a function of the number of carbon atoms of the ribbon. The number of carbon atoms is taken having two different ribbon edges, zigzag and Klein respectively. The first four carbons of the ribbon are fixed< in *x* and *y*, while the rest of the ribbon is free to relax. [108]

step (in total 17 Ni) and 36 carbons: $15\,a_{Ni} = 37.35\,\text{Å} \Leftrightarrow 36$ carbons (i.e. $1.66\,a_{Ni} \Leftrightarrow 4$ carbons). This moiré supercell has 2 beatings and a $\lambda' = 18.68\,\text{Å}$, corresponding to $1.25\,\lambda$. Configuration *c* (Fig.6.12.c) has two terrace 9 Ni long separated by a (111) mono-atomic step (in total 19 Ni) and 40 carbons: $17\,a_{Ni} = 42.33\,\text{Å} \Leftrightarrow 44$ carbons (i.e. $1.72\,a_{Ni} \Leftrightarrow 4$ carbons). This moiré supercell has 2 beatings and a $\lambda' = 21.17\,\text{Å}$, corresponding to $1.34\,\lambda$. Configuration *d* (Fig.6.12.d) has two terrace 10 Ni long separated by a (111) mono-atomic step (in total 21 Ni) and 44 carbons: $19\,a_{Ni} = 47.31\,\text{Å} \Leftrightarrow 44$ carbons (i.e. $1.73\,a_{Ni} \Leftrightarrow 4$ carbons). This moiré supercell has 2 beatings and $\lambda' = 23.67\,\text{Å}$, corresponding to $1.58\,\lambda$.

We found that the configurations *b*, *c* and *d* are more stable, with a λ'/λ ratio closer to the experimentally estimated value of 1.4. The stability can be inferred from the compression/elongation on the carbon-carbon bonds with respect to the corresponding value of 1.42 Å of the free-standing graphene. The histogram of all the C-C bounds along the terraces and their average are reported in Fig.6.12 and in Fig.6.13 respectively. Fig.6.13 shows that configuration *c* is the less stretched (light blue dot), indicating it as the best candidate in explaining the experimental findings. Anyway, it should be noted that the moiré periodicity over the simulated stepped surface is 18.67 Å, 21.17 Å and 23.65 Å in the *b*, *c* and *d* configurations, respectively, which are larger than the one on the flat surface with the same graphene-substrate orientation. The ratio between the three periodicities, about 1.25, 1.34 and 1.58, is in all the cases comparable with the value measured by STM. We exclude configuration *a* where graphene is too stretched.

For configurations *b*, *c* and *d* constant current STM maps were simulated and repeated for four steps for an easier comparison with the experimental STM topography of a multilevel mono-atomic stepped surface. A representative region of the experimental STM map containing four steps is compared with the STM simulations in Fig.6.14: there is a good resemblance for the height profiles and the colors of the STM maps for all the three con-

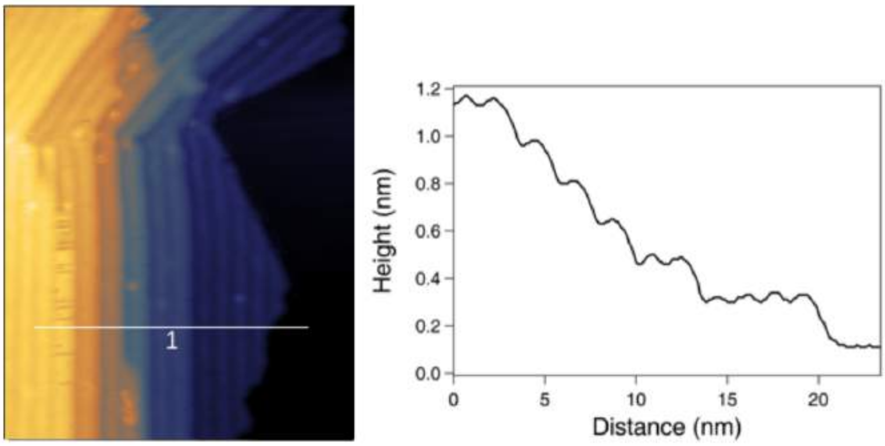

Figure 6.11: Experimental STM topography of downhill carpeting of graphene over a sequence of steps (**left panel**): the white line indicates the height profile path sketched in the graph (**right panel**). [108]

figurations. Concerning the increase of the s-moiré periodicity due to the presence of steps, configuration *c* matches really well the experimental periodicity with a correct STM map in-space color distribution. Regarding the other two configurations, the matching whit the experiment is not so good as in configuration *c*: configuration *b* underestimates while configuration *d* overestimates the ratio λ'/λ. For a even better matching it would be necessary to consider configurations that can accommodate more then two terraces in the same simulation supercell. We also notice that the number of C atoms in the simulation cell must be multiple of 4 (periodicity of graphene along the armchair direction), and the larger the cell, the weaker is the constraint. The choice of a reduced supercell was principally driven by the computational cost of the simulations, which increases also by the extremely elongated shape of the cell, where little local change in the charge density could induce strong instability of the system ("charge sloshing").

Computational details

DFT calculations were performed with Quantum ESPRESSO code [53], using plane-wave basis set and the Generalized Gradient Approximation for the exchange - correlation functional in the Perdew-Burke-Ernzerhof parametrization (GGA-PBE) [48]. Convergence tests suggested a kinetic energy cutoff of 30 Ry for the plane-wave basis set. The equilibrium lattice parameter a_0 characterizing the clean Ni(100) surface is 2.49 Å, equal to the experimental value. A periodically repeated slab geometry with different number of Ni layers was used, with a vacuum spacing of 15 Å between the slab repetitions. An orthorhombic supercell with an in-plane size of $l \times a_0$ was used, where *l* depends on the length of the terrace and on the height of the step through the following relation:

$$l = \cos(\theta) \cdot l_t + 0.816 \cdot l_s \tag{6.19}$$

where l_t is the length of the terrace, l_s is the length of the external surface of the step and 0.816 is the sin of the angle between [111] and [100] surfaces (Fig.6.15). A particular attention must be given to the number of atomic layers of the step: if the number of atomic layers is odd (for instance, a mono-atomic step), *l* has an angle $\delta = \arctan(a_0/2)$ with respect to the [110] direction, while, if the number of atomic layers is even (i.e. bi-atomic step), the in-plane supercell is rectangular (Fig.6.15, bottom panel). Concerning the Brillouin zone sampling, we adopted a Monkhorst-Pack $1 \times m \times 1$ k-point grid centered on Γ [56], where

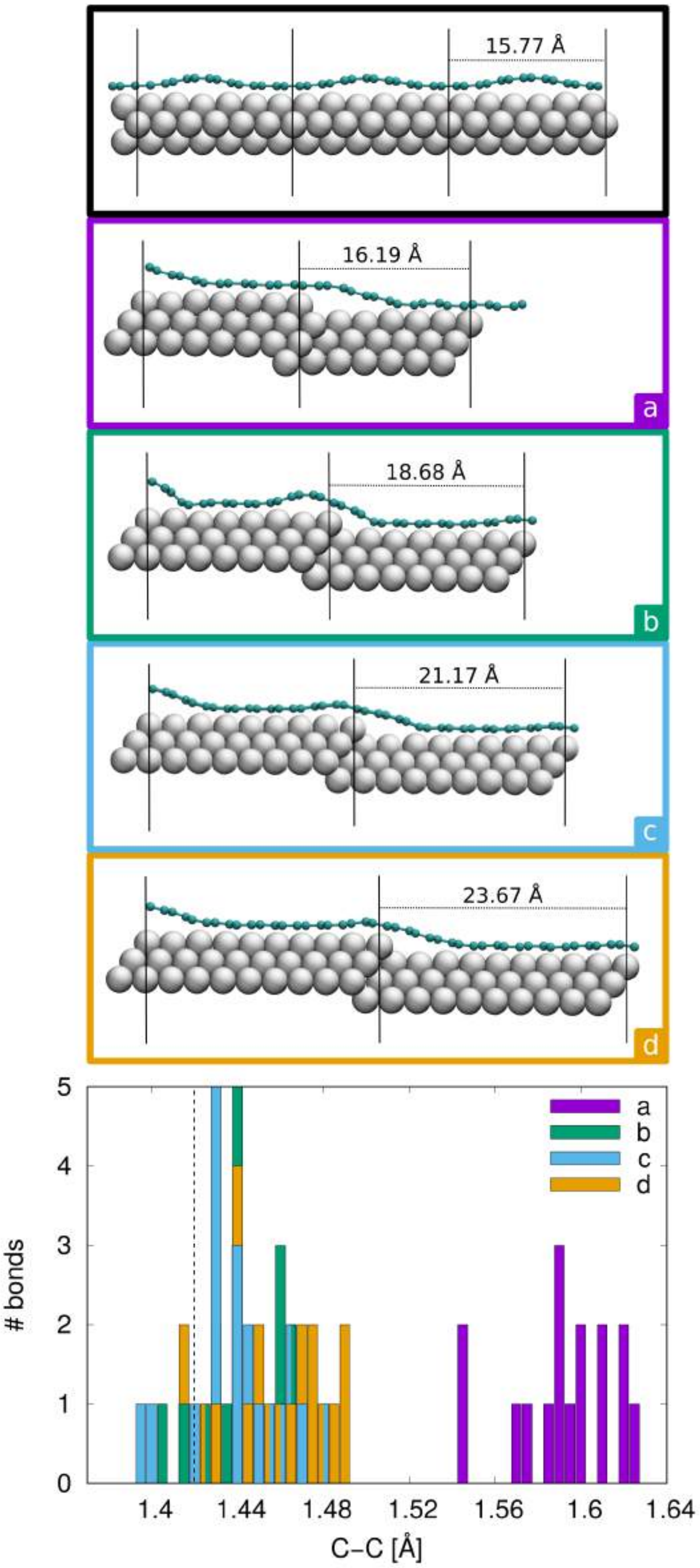

Figure 6.12: Stick-and-ball model and histogram of the C-C bond lengths of Ni(100) stepped surfaces with (111) mono-atomic step and a graphene layer settled on. Dotted line on the histogram indicates the pristine graphene C-C bond (1.42 Å). **(a)** Surface terraces 7 Ni long and graphene layer of 32 C. **(b)** Surface terraces 8 Ni long and graphene layer of 36 C. **(c)** Surface terraces 9 Ni long and graphene layer of 40 C. **(d)** Surface terraces 10 Ni long and graphene layer of 44 C. The black box on top of the figure contains the side view of the s-moiré surpercell 19 Ni long and having 44 C. [108]

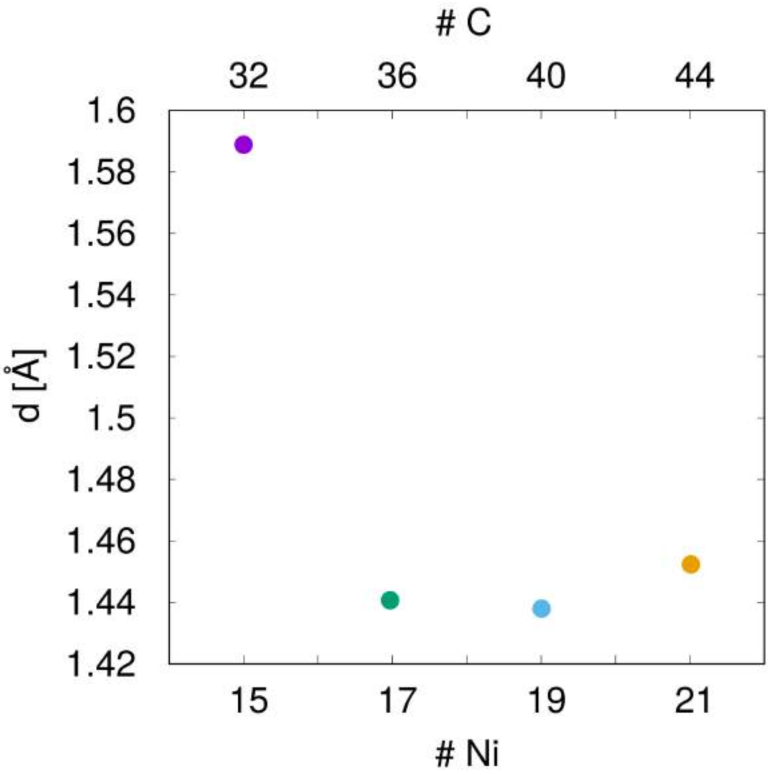

Figure 6.13: The average carbon-carbon bond lengths of graphene at the constant-width staircases with the corresponding configurations shown in Fig.6.12. The x-axis is labeled with the periodicity of the staircase length corresponding to the number of Ni atoms (lower x-axis) / C atoms (upper x-axis).

m scales with the in-plane size of the surpercell as the closest integer value of $3/(l\cos(\delta))$. The Methfessel-Paxton smearing technique with an energy broadening of 0.01 Ry [86] was adopted. The optimized atomic positions have been obtained minimizing the forces acting on each atom. Stick-and-ball models were rendered with the VMD software [87].

6.4. Summary

We have studied the the stability of the bare Ni(100) stepped surfaces with a geometrical model based on the surface energy and step formation energy. The ground state of the stepped surfaces has been computed by DFT simulations. The model have considered stepped surfaces structures with (111) steps up to a height of 6 atomic layers and with surface terraces length up to 9 nickel rows. We have found a decrease of step formation energy with the increase of the length of the terraces. We have also studied the ground state structure of graphene on Ni(100) stepped surfaces, finding that the optimization of interfaces bonding and graphene lattice stress release are the driving force of the wide narrow nickel staircase at constant width. The results were validated by the excellent agreement between the simulated and experimental STM images.

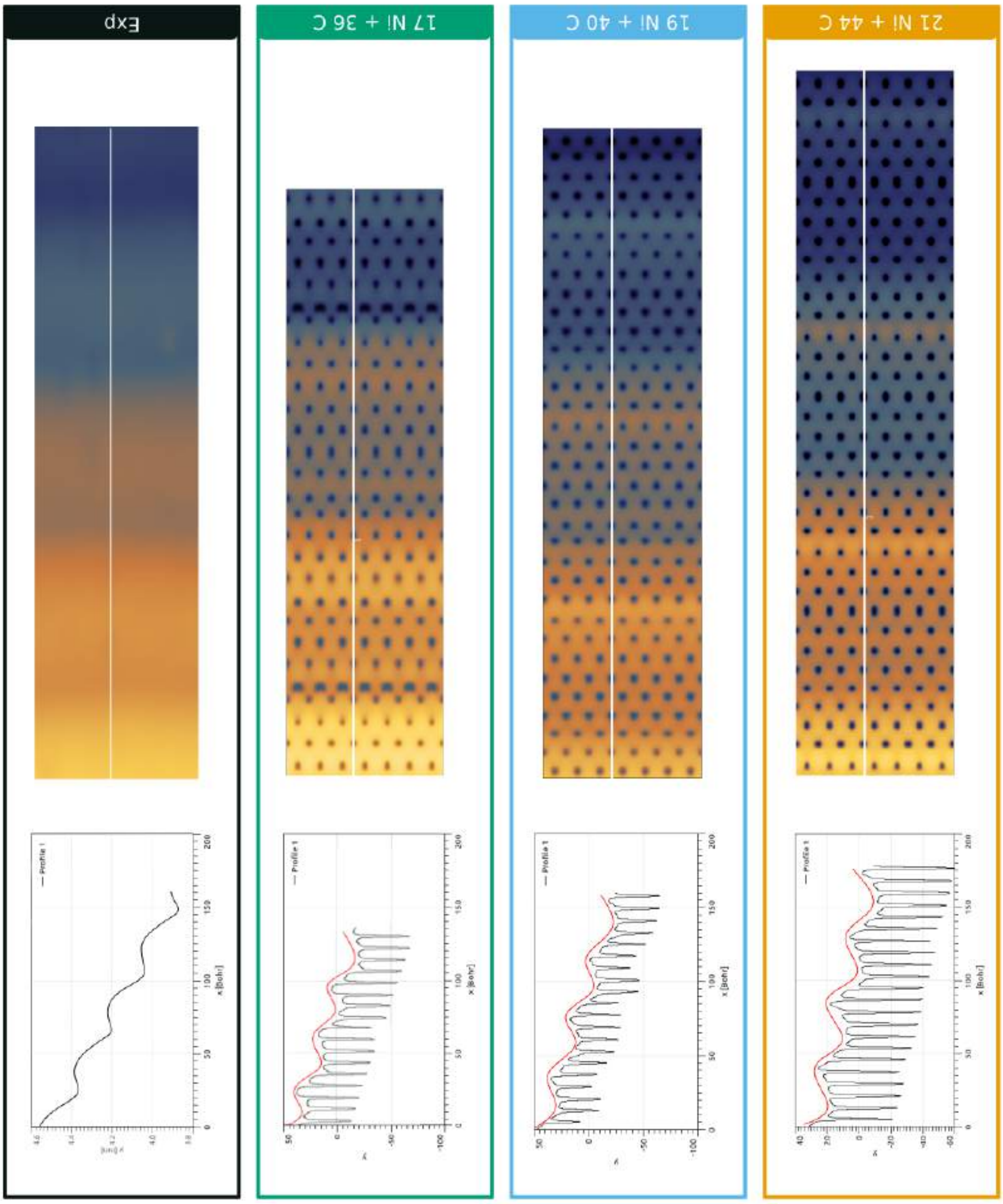

Figure 6.14: Black panel: height profile and STM topography of downhill carpeting of graphene at a step bunch of four (111) mono-atomic steps. **Green panel:** height profile and constat current STM simulation of stepped surface *b* repeated four times along the terrace direction (Fig.6.12). **Light blue panel:** height profile and constat current STM simulation of stepped surface *c* repeated four times along the terrace direction (Fig.6.12). **Orange panel:** height profile and constant current STM simulation of stepped surface *d* repeated four times along the terrace direction (Fig.6.12) of four (111) mono-atomic steps. In all the panels: the white line indicates the height profile path sketched in black in the graph, while the red line shows the surface corrugation without the atomic resolution. **Computational parameters:** ILDOS iso-surface lying 2 Å above graphene and with ILDOS value of $5 \cdot 10^{-5}|\mathrm{e}|/\mathrm{a}_0^3$ for both structures. [108]

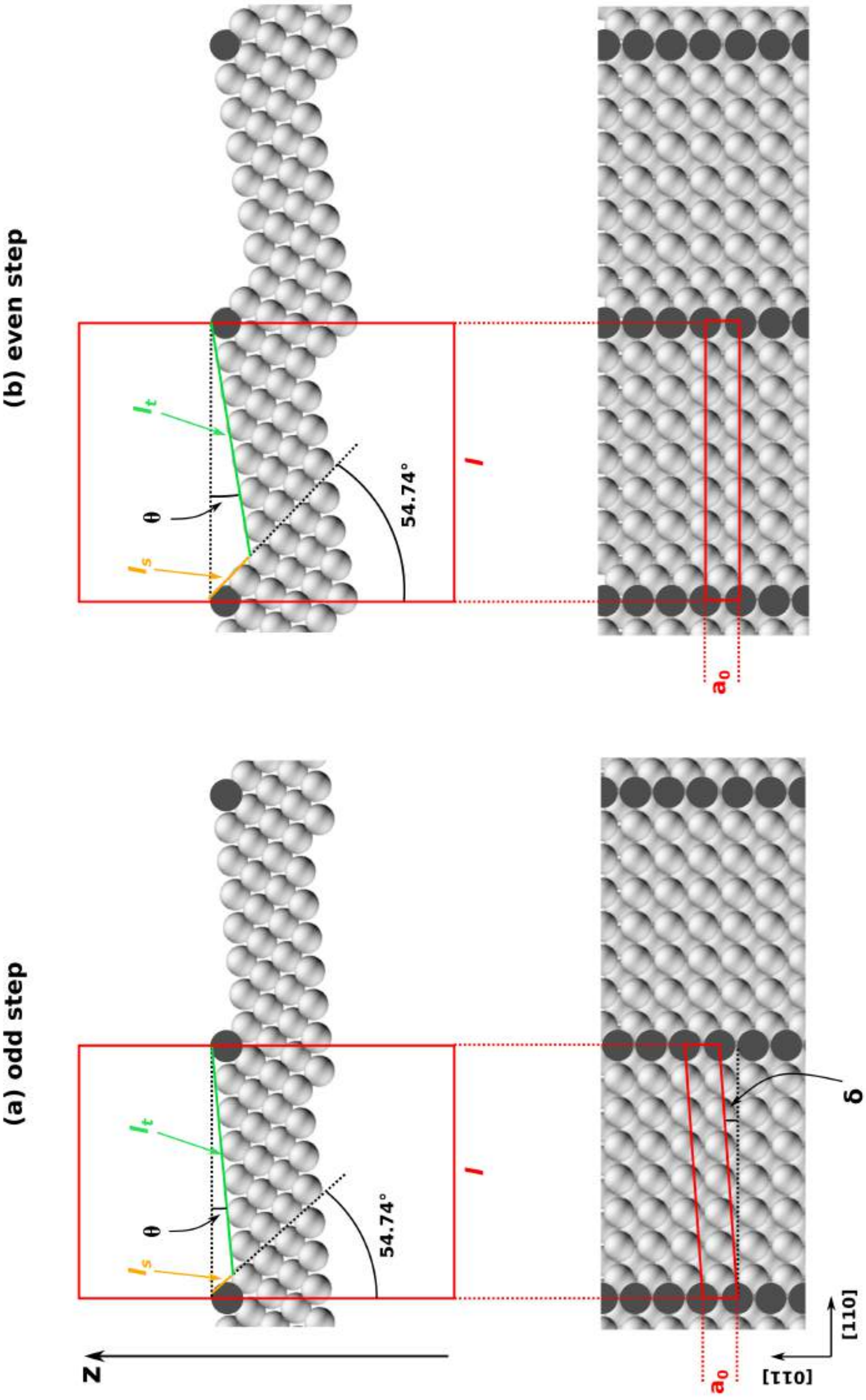

Figure 6.15: Side (top panel) and top view (bottom panel) of stepped surfaces with terraces of 8 Ni length separated by mono-atomic (left panel) and bi-atomic (right panel) steps. The crucial geometrical parameters for the construction of the supercell (red boxes) are highlighted to both possible situations, terraces separated by an odd step **(a)** and terraces separated by an even step **(b)**. l_s is the length of the external suface of the step, l_t is the length of the terrace, θ is the angle between the terrace and the tangent plane at edges of the steps,δ is the anglee between *l* and the [110] direction ($\neq 0$ only with an odd step).

Conclusions and outlook

In this thesis, extensive simulations of graphene grown on different Ni surfaces have been performed. In particular, vacancy defects in graphene over Ni(111), graphene over Ni(100) moiré superstructures and Ni(100) stepped surfaces have been studied, investigating morphology and electronic properties through *ab-initio* quantum mechanical simulations. The dynamical evolution of the stripe-moiré superstructure was investigated by a home made KMC code. All the results are compared with recent, in some case unpublished, experimental measurements.

Concerning vacancy defects in graphene over Ni(111), they were characterized in presence and absence of Ni adatom(s) trapped inside. STM simulations of graphene vacancy defects with Ni adatom(s) trapped inside perfectly match with the most abundant defected structures present in the experimental STM images, suggesting these are preferred defected structures with respect to empty vacancy defects. The computed formation energy also supports this conclusion. Remarkably, the Ni adatom is more strongly bound to the edge of the defect than to the substrate. This opens a promising way in production of transferable doped graphene.

Moiré superstructures originating from the structural and angular mismatch between hexagonal and square lattices of graphene and Ni(100) substrate were investigated in detail. By varying the misorientation angle in the range of 0°-15°, the graphene/Ni(100) system gradually slides from a stripe superstructure to a network superstructure (other angles give equivalent structures). Stripe-moiré (lattices mismatch angle of 0°) and network-moiré (lattices mismatch angle of 11.3°) were studied as representative examples, finding a coexistence of well-defined phys- and chemisorbed regions in the stripe-moiré and a more uniform chemisorption in the network-moiré. This result suggests that the stripe-moiré is a possible environment for selected catalysis due to the confined nano-environments at the graphene-nickel interface or above graphene. Relevant in variations the electronic properties of phys- and chemisorbed regions of the moiré have been found. Further studies in presence of small molecules of environmental importance, like H_2O, CO and CO_2, should be carried on, both over of the graphene layer and at the graphene-Ni(100) interface, in order to investigate promising potentials of this system related to reactivity. Some preliminary experimental STM movies have already shown peculiar reactivity of the stripe-moiré in presence of CO.

Part of the work on moiré superstructures has been devoted to develop a theoretical model to unambiguously identify the common supercells resulting from the overlap of two generic Bravais lattices. The model is purely geometric. A Python code was written for the specific case of hexagonal/square lattices (graphene/Ni(100)) and used to provide the supercells for the DFT simulations.

The stability and the dynamical evolution of the stripe-moiré due to the surface segregation and diffusion of exceeding carbon atoms from the CVD process was also studied. In particular, the detachment process of long portions of chemisorbed regions was addressed. KMC simulations combined with DFT simulations allow a detailed understanding of the atomic scale, showing that the number and types of detachments are strongly correlated to the carbon concentration considered. Moreover, KMC simulations already show a correlation between the stability of the detachments and the carbide (Ni_2C) formation, consistently with the experimental findings.

Appendix B is devoted to a detailed illustration of the KMC code written for this study.

Finally, the stability of bare Ni(100) stepped surfaces and the structural characterization of graphene on these surfaces were addressed. It was found that consecutive (100) terraces are preferentially joined by (111) facets and a linear relation between the step formation energy and the size of the steps is found. A decreasing of step formation energy was found increasing the length of the terraces, ascribing this to the lowering of the step-step interaction. Concerning the graphene growth on Ni(100) stepped surfaces, experimental STM movies show step bunch opening of the nickel surface, forming sequences of constant terraces with the same width during graphene growth in the stripe-moiré configuration. DFT simulations explain also this mechanism, which is accompanied by an increase of the characteristic length of the moiré periodicity. The matching between the experimental and the theoretical STM images further validate the model. Further work should be done in order to understand the origin of the steps bunch opening: dynamical simulations would be necessary to the purpose.

Some results have been already published or submitted: one on the graphene/Ni(100) moiré superstructures [88] and another on the graphene defected structures over Ni(111) [75]. Other papers concerning the surface step bunch opening due to the graphene growth [108], the structural model to identify the common primitive moiré supercell of two generic Bravais lattices [109] are almost ready for submission. Two papers about the detachment process of chemisorbed regions due to the CVD residual carbons diffusion at/across the surface (Chapter 5) and the KMC code developed to address this problem (Appendix B) are in preparation.

Acknowledgments go to:

- Italian Ministry of Foreign Affairs and International Cooperation, Directorate General for the Country Promotion through the Executive Program with Argentina for support in scientific visits in Córdoba.
- University of Trieste through the program Finanziamento di Ateneo per progetti di ricerca scientifica - FRA 2015 (P.I. M. Peressi) and FRA 2016 (P.I. E. Vesselli) mainly for support on participation to conferences and workshops.
- Computational resources have been obtained from CINECA through the ISCRA initiative and the agreement with the University of Trieste.

III. Appendix

Appendix A: KMC code

This appendix is devoted to go inside the technicalities of the KMC code developed from scratch to study the problem of carbon segregation at the Gr-Ni(100) interface already duly explained in chapter 5. The code has been written in collaboration with G. Soldano of the University of Córdoba (Argentina): the extension of the collaboration covered mainly all the three years of this PhD work, giving origin to different versions of the code. Here the final version of the code is presented with the aim of being reproducible by anyone. The code is written in Fortran 90 while some subroutines of post-processing, developed by C. Carnevale, are written in Python.

Configuration computed by DFT implemented on the KMC code

In writing of a KMC code is absolutely indispensable to have the complete control of the environment where the studied process is going to happen and how the dynamics will change it during the simulation. In the particular case of the phenomenon adressed in this work, the dynamical process is the carbon diffusion at the Gr-Ni(100) interface in the specific case of s-moiré (see chapter 5). The environment in which the carbon diffusion will take place is characterized by a regular alternation of chemisorbed (black) and phys- (yellow) graphene regions on the Ni(100), separated by intermediate regions (blue) (as it was already explain in chapter 5). Here, the effect of carbon diffusion on the s-moiré configuration due to the presence of free carbon atoms at the Gr-Ni(100) interface has been deeply investigated, both in the case of a single free carbon atom and two fairly close carbon atoms. The second case is important because of, in some peculiar situations, it is possible to have a carbon-carbon cooperative interaction that gives origin to a wider detached region with respect of the effect of two separated free carbons. All the configurations referred to below are computed by relax DFT calcultaions with the same computational parameters reported in section 5.2 and implemented as input of the KMC code.

As a first step, it has been considered the effect of one free carbon atom at the Gr-Ni(100) interface in the three different regions of the s-moiré: chemisorbed region, intermediate region and phys- region. For each region the *hollow (h)* and the *subtop (st)* have been considered as stable carbon atoms surface sites (*h* and *st* sites are defined as in section 5.2). The relaxed configurations are reported in Fig.6.16. Only a free carbon atom at *h* site in the intermediate region produces a local detachment of the graphene layer, involving the three closest nickel atoms that shift in the yellow region from the blue one. In all the other cases, no changes in the s-moiré configuration are highlighted.

Furthermore, two free carbon atoms are considered in the same simulation cell. In order to study a local detachment of a chemisorbed region, two scenari come out: two carbons at the same side of the chemisorbed region, or one carbon opposite to the other with respect to the chemisorbed region. If the two carbon atoms are far from eatch other, the associated

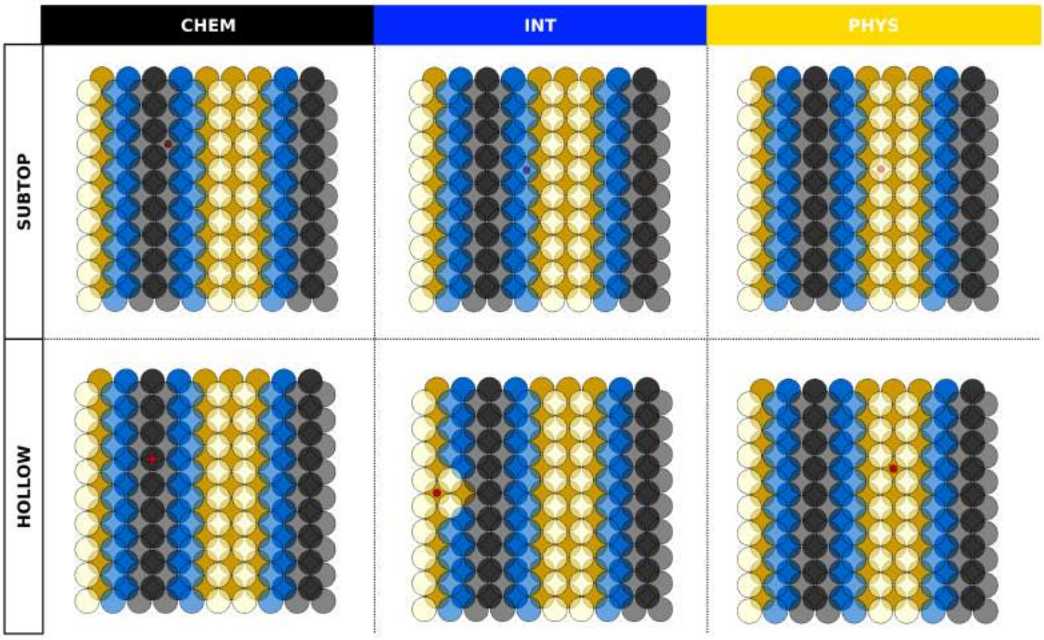

Figure 6.16: Effect of a free carbon atom at the Gr-Ni(100) interface. The carbon sites considered are the *hollow* and the *subtop*. All the configurations are obtained by relax DFT calcultaions. The nickel surface is colored with respect to the stripe moiré region of the graphene over: yellow for the phys- region, blue for the intermediate region, black for the chemisorbed region. The free carbon atom inside the surface is visualized in red while graphene is not directly represented.

graphene detachment is simply the sum of two non-coperative carbon atoms. However, if they are close enough, the detachmnet can be considerably larger. Our systematic study reveals 15 so-called cooperative detachments, in which a sort of synergy seems to take place producing a larger detachment than that causes by individual carbon atoms. All the final configurations obtained through relax DFT calcultaions are summarized in Fig.6.17. The configuration that maximize the total amount of detached region is the one with the carbons in the same row of the two opposite blue region of the black region while, if the two carbon are in the dark region but separated by one row of surface nickels, there is no detachment. Some tests with two carbon atoms further far one to each other then one column or on row of surface nickels have been done, but the results is equal to the case of two non-cooperative free carbons atoms.

KMC code implementation

Once all the most important configurations are individuated, the next step for the KMC implementation is to identify an easy and convenient way to map the s-moiré system on a periodic grid (see section 2.5). Each sites of the grid must be identified uniquely in order to have a complete control on the free carbon atoms diffusion during the simulations. Afterwards, internal mathematics rules for surface carbons diffusion will be implemented according to the periodic grid introduced before. Besides driving orderly the diffusion processes, these rules allow also to update the changes in the substrate regions according to the effects due to the carbon atoms moves.

Taking into account the symmetry of the substrate together with the periodicity of the s-moiré, a square grid has been chosen with a stripe periodicity of six squared. The dark region is the center of the each stripe and the cells of the stripe are numbered from 1 to 6. Rows are

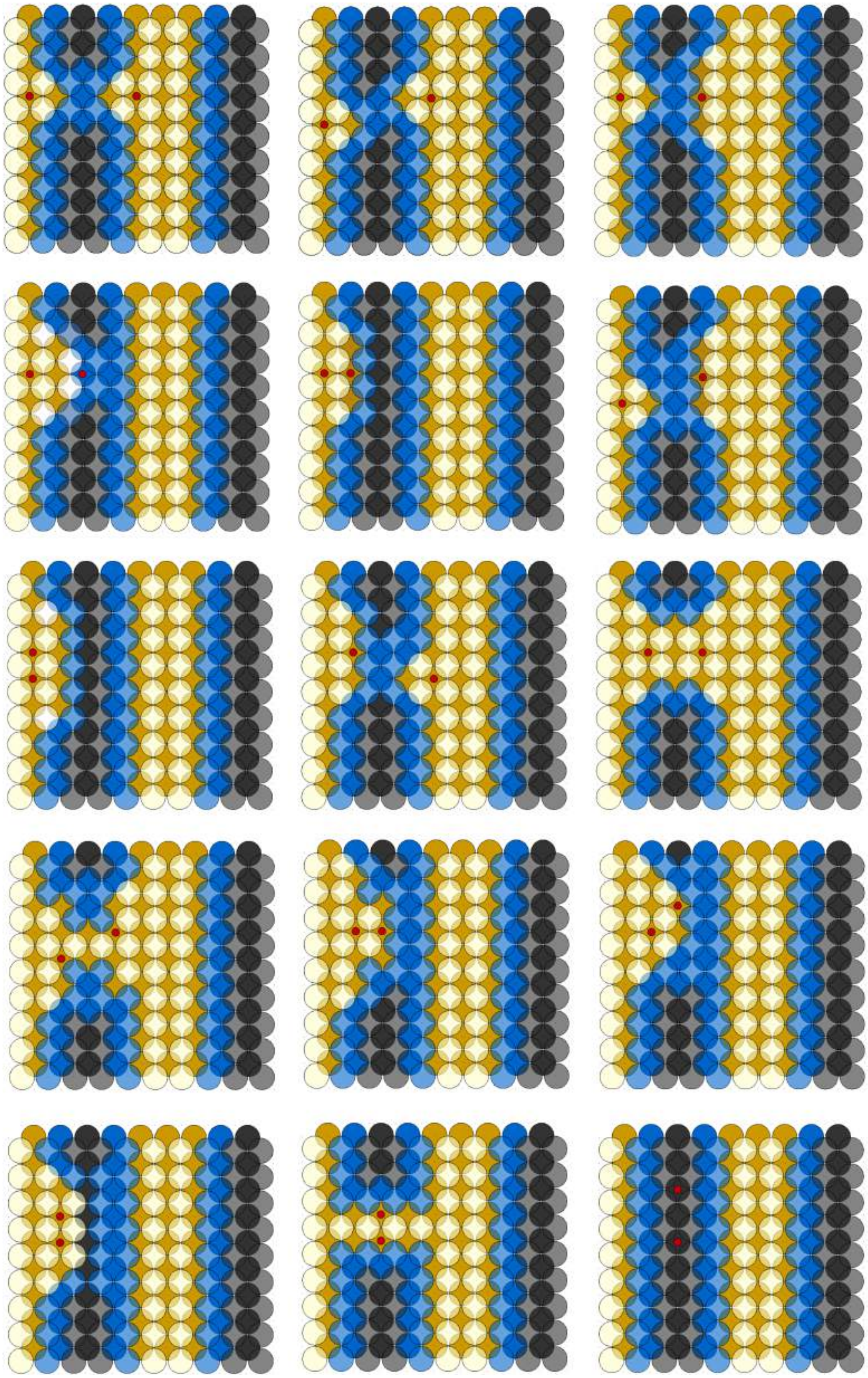

Figure 6.17: Effect of two free carbon atoms fairly close to each other at the Gr-Ni(100) interface. According to Fig.6.16 where only a carbon at the *hollow* site produces a local graphene detachment, only the *hollow* site for the the carbon atoms has been considered. All the configurations are obtained by relax DFT calcultaions. The color legend is the same of Fig.6.16.

numbered from bottom to top and the maximum number of rows will depend on the size of the substrate chosen for the simulation. Because of only the diffusion between the last two outermost layers of the surface has been considered, only two nickel layers are involved and they are numbered 1 and 2. Therefore, each site is labeled with the corresponding *(column, row, layer)* (Fig.6.18).

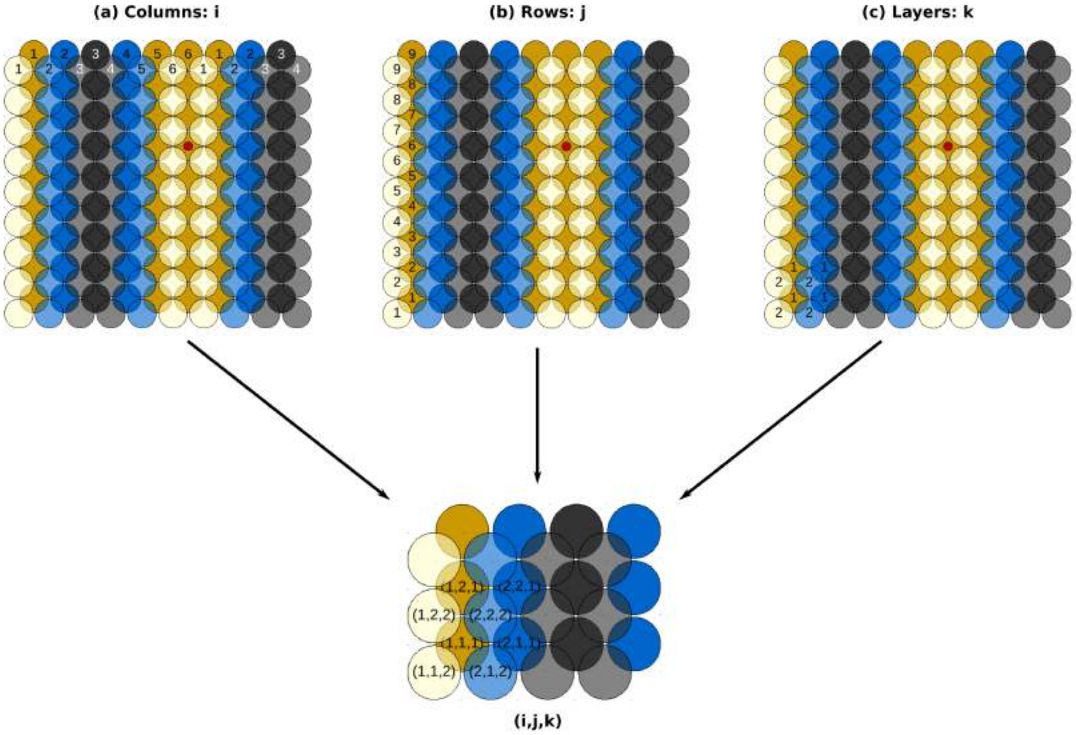

Figure 6.18: Building of the KMC periodic grid. **Top panel:** numbering of columns *i*, rows *j* and layers *k* of the substrate is shown. **Bottom panel:** each sites of the grid is uniquely identifidied by a set of indexes *(i,j,k)*. The color legend is the same of Fig.6.16.

A displacement, such as the one indicated by the white arrow in Fig.6.19, corresponds to a vector sum. To formalize this, the displacement vectors DV have been introduced so that all the carbon moves and many other code features are characterized by these. Each carbon can diffuse from its position to eight neighbor sites, four *h* and four *st*, and they are numbered from 1 to 8 (Fig.6.20). DV is a 8×3 matrix where each lines is associated to one of the available sites for the diffusion while the columns are the displacement vector components along $column\,(x)$, $row\,(y)$, $layer\,(z)$. The matrix incomes are -1,0,1, corresponding to subtract 1 to the index, unchanged the index, add 1 to the index of the row/column/layer (Fig.6.19). All the incomes of the DV matrix will be set to 0, except for the row of the site selected for the carbon move.

As it shown by Fig.6.16 and Fig.6.17, there are some cases where the carbon atoms diffusion change the local environment of the nickel substrate, inducing a local detachment of the graphene layer. Due to the stripe geometry of the system that induces a 1D-periodicity, the location of each neighbor and the total amount of the neighbors that change color depends only by the column at which the carbon atom is adsorbed. If mNBH(*i*) is the number of the neighbors that change the color associated to a carbon atom adsorbed in a generic site of a column *i*, it is introduced a $6 \times mNBH(i) \times 3$ matrix NBH that, for each of the six columns and for each of the neighbors that change the color (mNBH(*i*)), contains the xyz coordinates of the neighbor with respect to the site of the adsorbed carbon atoms (Fig.6.21

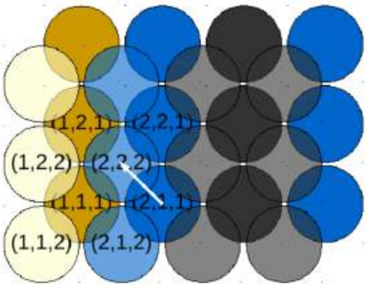

original site		displacement vector		final site
(2,1,1)	+	(0,1,1)	=	(2,2,2)

Figure 6.19: Example of implementation of one step of diffusion: in this particular case a free carbon atom is diffusing from a *st* to a *h* site. The color legend is the same of Fig.6.16.

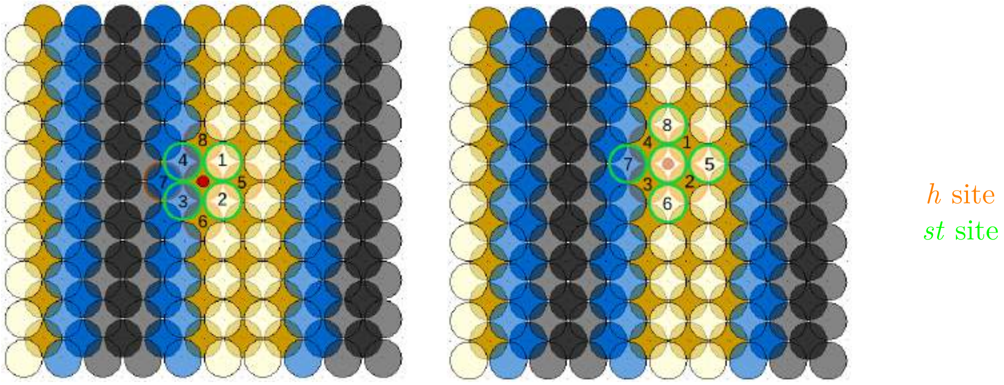

(a) carbon atom in *h* site

(b) carbon atom in *st* site

Figure 6.20: Identification of the eight sites (four *h* and four *st*) allow for the diffusion of one carbon atom originally in a *h* site (a) or in a *st* site (b). The color legend for the nickel substrate and the free carbons is the same of Fig.6.16.

and Fig.6.22). Again the incomes of the NBH matrix are -1,0,1 with the same meaning of the DV matrix. Finally, a $6 \times mNBH(i)$ matrix CNBH associates each neighbor that change the color with its new color. The incomes of the CNBH matrix are 1,2,3 that means yellow, blue, black region respectively (Fig.6.22).

If two carbon are close enough to make a cooperative detachment of the graphene layer, a matrix DTC is introduced to list the sites that are not directly affected in the detachment but that income in changes due to the effect of the carbon-carbon interaction. DCT assigns also to these sites their new colors. DTC is a $i_1 \times i_2 \times i_3 \times i_4 \times 3$ matrix where i_1 is the column index of the first carbon, i_2 is the column index of the second carbon, i_3 is the difference between the row indexes of the two carbons, i_4 is the site number and 3 are the site components along xyz referred to the first free carbon (Fig.6.23).

At each step of the KMC simulation, all the matrices are updated according to the carbon move.

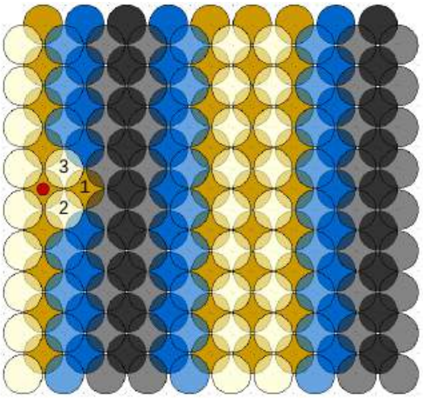

Site 1: (1,5,1) + (1,0,0) = (2,5,1)
Site 2: (1,5,1) + (1,0,1) = (2,5,2)
Site 3: (1,5,1) + (1,1,1) = (2,6,2)

DV(**1**,1) = 1   DV(**1**,2) = 0   DV(**1**,3) = 0
DV(**2**,1) = 1   DV(**2**,2) = 0   DV(**2**,3) = 1
DV(**3**,1) = 1   DV(**3**,2) = 1   DV(**3**,3) = 1

NBH(**1**,**1**,1) = 1   NBH(**1**,**1**,2) = 0   NBH(**1**,**1**,3) = 0
NBH(**1**,**2**,1) = 1   NBH(**1**,**2**,2) = 0   NBH(**1**,**2**,3) = 1
NBH(**1**,**3**,1) = 1   NBH(**1**,**3**,2) = 1   NBH(**1**,**3**,3) = 1

Figure 6.21: DV and NBH matrix associated to a carbon atom adsorbed on generic *h* site of the column 1. Red, green and blue indicate the vector displacement along *x*, *y*, *z* respectively. The color legend for the nickel substrate and the free carbons is the same of Fig.6.16.

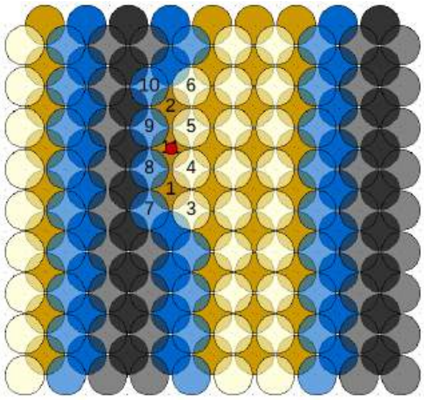

mNBH(**4**) = 11

CNBH(**4**,1:6) = 1 (yellow)
CNBH(**4**,7:11) = 2 (blue)
CNBH(**4**,11) = 1 (yellow)

NBH(**4**,**1**,1)=0   NBH(**4**,**1**,2)=-1   NBH(**4**,**1**,3)=0
NBH(**4**,**2**,1)=0   NBH(**4**,**2**,2)=1   NBH(**4**,**2**,3)=0
...   .
NBH(**4**,**10**,1)=0   NBH(**4**,**10**,2)=2   NBH(**4**,**10**,3)=1
NBH(**4**,**11**,1)=0   NBH(**4**,**11**,2)=0   NBH(**4**,**11**,3)=0

Figure 6.22: DV, NBH and CNBH matrix associated to a carbon atom adsorbed on generic *h* site of the column 4 that is highlighted in violet. The number of neighbors mNBH(4) that change the color is reported. Red, green and blue indicate the vector displacement along *x*, *y*, *z* respectively. The color legend for the nickel substrate and the free carbons is the same of Fig.6.16.

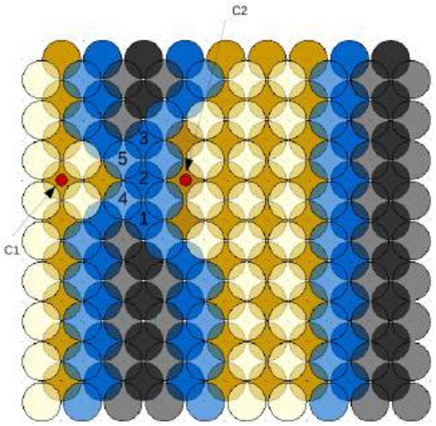

$\mathrm{mDTC}(1,4,0) = 5$

$\mathrm{cDTC}(1,4,0,1{:}5) = 2$ (blue)

$\mathrm{DTC}(1,4,0,\mathbf{1},1) = 2$ $\mathrm{DTC}(1,4,0,\mathbf{1},2) = -1$ $\mathrm{DTC}(1,4,0,\mathbf{1},3) = 0$
$\mathrm{DTC}(1,4,0,\mathbf{2},1) = 2$ $\mathrm{DTC}(1,4,0,\mathbf{2},2) = 0$ $\mathrm{DTC}(1,4,0,\mathbf{2},3) = 0$
... ...
$\mathrm{DTC}(1,4,0,\mathbf{5},1) = 2$ $\mathrm{DTC}(1,4,0,\mathbf{5},2) = 1$ $\mathrm{DTC}(1,4,0,\mathbf{5},3) = 1$

Figure 6.23: DTC matrix associated to a two carbon atoms C1 (column 1) and C2 (column 4) adsorbed at two *h* sites of the same row. The number of the sites not directly affected by the detachment, mDTC(1,4,0), and their new color, cDTC(1,4,0,1:5), are reported. The color legend for the nickel substrate and the free carbons is the same of Fig.6.16.

Code

```
Program GNi100
Implicit real(a-h,o-z)
integer step, hpic
integer NBH(5,11,3),mNBH(5),cNBH(5,11),CLG(99,3)
integer DTC(5,5,0:2,20,3),mDTC(5,5,0:2),cDTC(5,5,0:2,20)
integer P(2,8,3)
integer irn(6,2), rgn, dtch(5)
integer, allocatable, dimension(:,:) :: C
integer, allocatable, dimension(:,:,:) :: GRID,N1,N2
real, allocatable, dimension(:,:) :: VELO
real Ea(2,2,0:3,0:3), Erep(2,2), dEa(5,5,3)
common/nn/nx,ny,nc
common/Eact/P,Ea,Erep,dEa,Temp
common/kpix/ncpix
common/t/time
common/ColorNBH/NBH,mNBH,cNBH,DTC,mDTC,cDTC

open(1,file="Tar")
open(100,file="atoms.xyz")
open(101,file="C.xyz")
open(102,file="detachment.dat")
open(103,file="neighbors.dat")
open(105,file="regions.dat")

write(103,*)"#  time(s)     N_tot          N_h        N_st"
```

```
 write(105,*)"#  time(s)    Bright      Gray      Dark"

 read(1,*)nx, ny, nc, Conc
 read(1,*)nrun, hpic
 read(1,*)Temp, idum

 if(nc.eq.0)nc=nint(Conc*float(nx*4*ny))
 nstripes=nx
 nx=nx*6
 print*,"Simulation with",nc,"carbon atoms"
 allocate(C(nc,3))
 allocate(GRID(nx,ny,2))
 allocate(N1(nx,ny,2))
 allocate(N2(nx,ny,2))
 allocate(VELO(nc,8))
 GRID=0; C=0
 ncpix=nx*ny+nc
 nxg=nx/12*7; nctot=nc+nxg*4*ny; pi=acos(-1.)
 dtch=0

 irn(1  , 1)=1  ! Bright hlw
 irn(2  , 1)=2  ! Gray hlw
 irn(3  , 1)=3  ! Dark hlw
 irn(4  , 1)=2  ! Gray hlw
 irn(5:6, 1)=1  ! Bright hlw

 irn(1  , 2)=1  ! Bright subtop
 irn(2  , 2)=2  ! Gray subtop
 irn(3:4, 2)=3  ! Dark subtop
 irn(5  , 2)=2  ! Gray subtop
 irn(6  , 2)=1  ! Bright subtop

 call ColorMatrix

 call ProcessList


!______________Initial configuration
!   call picSurf(nx,ny,nc,irn)
!   stop

   print*,"Setting up the surface..."
  do i=1,nx
  do j=1,ny
  do k=1,2
        i6=mod(i,6)
        if(i6.eq.0)i6=6
        GRID(i,j,k)=-irn(i6,k)
  enddo
  enddo
```

```
  enddo

  do ic=1,nc
  100  i=int(ran2(idum)*float(nx))+1
       j=int(ran2(idum)*float(ny))+1
       if(GRID(i,j,2).gt.0)goto 100

         i6=mod(i,6)
         if(i6.eq.0)i6=6
                                 if(irn(i6,2).ne.1)goto 100
         GRID(i,j,2)=1
         C(ic,1)=i
         C(ic,2)=j
         C(ic,3)=2
  enddo

  print*,"Done. Now getting neighbors..."
  N1=0; N2=0
  do i=1,nx
  do j=1,ny
  do k=1,2
  if(GRID(i,j,k).gt.0)then
             do m=1,8
             ix=i+P(k,m,1)
             iy=j+P(k,m,2)
             call correctIJ(ix,iy)
             if(m.le.4)then
                  if(k.eq.1)N1(ix,iy,1)=N1(ix,iy,1)+1
                  if(k.eq.2)N2(ix,iy,1)=N2(ix,iy,1)+1
             else
                  if(k.eq.1)N1(ix,iy,2)=N1(ix,iy,2)+1
                  if(k.eq.2)N2(ix,iy,2)=N2(ix,iy,2)+1
             endif
             enddo
  endif
  enddo
  enddo
  enddo

!    call picCarbon(C)
!    call pixCar(GRID,C)
  call toVMD(GRID,C)


!______________KMC loop
 print*,"Done. Now running KMC..."
 time=0.
 DO step=1,nrun

  call getVel(step,i,j,GRID,C,  VELO)
```

```
   vt=sum(VELO)
   vr=ran2(idum)*vt
   vsum=0.
   do ic=1,nc
   do ip=1,8
   vsum=vsum+VELO(ic,ip)
   if(vsum.gt.vr)goto 110
   enddo
   enddo

   if(ic.gt.nc)ic=nc


!_______________________________ Get initial-final states
110 dt=-1./vt*log(ran2(idum))
     time=time+dt

     i=C(ic,1)
     j=C(ic,2)
     k=C(ic,3)

     in=i+P(k,ip,1)
     jn=j+P(k,ip,2)
     kn=k+P(k,ip,3)
     call correctIJ(in,jn)

     C(ic,1)=in
     C(ic,2)=jn
     C(ic,3)=kn
!_______________________________  Update Ngbs
               do m=1,8
               ix=i+P(k,m,1)
               iy=j+P(k,m,2)
               call correctIJ(ix,iy)
               if(m.le.4)then
                    if(k.eq.1)N1(ix,iy,1)=N1(ix,iy,1)-1
                    if(k.eq.2)N2(ix,iy,1)=N2(ix,iy,1)-1
               else
                    if(k.eq.1)N1(ix,iy,2)=N1(ix,iy,2)-1
                    if(k.eq.2)N2(ix,iy,2)=N2(ix,iy,2)-1
               endif
               enddo

               do m=1,8
               ix=in+P(kn,m,1)
               iy=jn+P(kn,m,2)
               call correctIJ(ix,iy)
               if(m.le.4)then
                    if(kn.eq.1)N1(ix,iy,1)=N1(ix,iy,1)+1
```

```
                  if(kn.eq.2)N2(ix,iy,1)=N2(ix,iy,1)+1
              else
                  if(kn.eq.1)N1(ix,iy,2)=N1(ix,iy,2)+1
                  if(kn.eq.2)N2(ix,iy,2)=N2(ix,iy,2)+1
              endif
              enddo


  i6=mod(i,6);  if(i6.eq.0)i6=6
  i6n=mod(in,6);  if(i6n.eq.0)i6n=6

!______________________________  Depletion of site

  GRID(i,j,k)=-GRID(i,j,k)

! ______________________________ Occupation of site
  GRID(in,jn,kn)=irn(i6n,kn) ! gets default color


! If C diffuses bellow the surface, no need to change colors
  kkn=k*kn
  if(kkn.eq.4)goto 555

! If C diffuses in the bright region, no need to change colors
  nn=k*10+i6
  mm=kn*10+i6n
  if(nn.eq.16.or.mm.eq.16)then
        if(ip.eq.2.or.ip.eq.4)goto 555
  endif

! The LG is build around (in,jn,kn) unless both "if" are satisfied
! in which case if build around (i,j,kn)
  ir=in; jr=jn; i6r=i6n
  if(i6n.eq.6.and.k.eq.1)then
  if(ip.eq.1.or.ip.eq.3)then
  ir=i; jr=j; i6r=i6
!   print*,"Horizontal move to region 6 in step",step
  endif
  endif


  call ResetColor(ir,jr,i6r,nx,ny,irn,GRID,  ncl,CLG)


!   Assign color for C local detachment within the LG
    do icg=1,ncl
    il=CLG(icg,1); jl=CLG(icg,2); kl=CLG(icg,3)
    if(kl.eq.1)then
        i6=mod(il,6) !; if(i6.eq.0)i6=6  i6 can't be 6 in LG
        do m=1,mNBH(i6)
```

```
          ix=il+NBH(i6,m,1)
          iy=jl+NBH(i6,m,2)
          iz=kl+NBH(i6,m,3)
          call correctIJ(ix,iy)
               ijk=GRID(ix,iy,iz); ijkABS=abs(ijk)
               icolor=cNBH(i6,m)
               if(icolor.lt.ijkABS)GRID(ix,iy,iz)=icolor*ijk/ijkABS
          enddo
     endif
     enddo


!    Assign color for C cooperative detachment within the LG-LG2
     do ii=1,ncl-1
     i1=CLG(ii,1); j1=CLG(ii,2); k1=CLG(ii,3)
     icol1=mod(i1,6)
          do jj=ii+1,ncl
          i2=CLG(jj,1); j2=CLG(jj,2); k2=CLG(jj,3)
          icol2=mod(i2,6)
          jh=j2-j1
          if(abs(jh).le.1.or.jh.eq.ny-1.or.jh.eq.-ny+1)then
               if(jh.eq.-1)then
               jh=2
               elseif(jh.eq.ny-1)then
               jh=2
               elseif(jh.eq.-ny+1)then
               jh=1
               endif
               do m=1,mDTC(icol1,icol2,jh)
               ix=i1+DTC(icol1,icol2,jh,m,1)
               iy=j1+DTC(icol1,icol2,jh,m,2)
               iz=k1+DTC(icol1,icol2,jh,m,3)
               call correctIJ(ix,iy)
               ijk=GRID(ix,iy,iz); ijkABS=abs(ijk)
               icolor=cDTC(icol1,icol2,jh,m)
               if(icolor.lt.ijkABS)GRID(ix,iy,iz)=icolor*ijk/ijkABS
               enddo

          endif
          enddo
     enddo


! ______________________________ Detach dark islands ( dj<=2 )
     if(i6n.ne.6)then
     i1=6*int(in/6)+3             ! center of the stripe
     else
     i1=6*int(i/6)+3
     endif
```

```
    do j1=1,ny-1
        j0=j1-1
        call correctJ(j0)
        j2=j1+1
        call correctJ(j2)
        j3=j1+2
        call correctJ(j3)
        idown=abs(GRID(i1,j0,1))
        icent=abs(GRID(i1,j1,1))
        iup01=abs(GRID(i1,j2,1))
        iup02=abs(GRID(i1,j3,1))
!              iup21=abs(GRID(i1-1,j2,2))
            iup22=abs(GRID(i1,j2,2))
!              iup23=abs(GRID(i1+1,j2,2))
        m1=2*idown*iup01-icent
        m2=2*idown*iup02-icent
        m3=2*icent*iup01-iup22
        if(m1.le.0.or.m2.le.0.or.m3.le.0)then
                do iii=1,5
                i2=i1-3+iii
                        do jjj=1,4
                        j5=j1-2+jjj
                        call correctJ(j5)
!                                         ______ Bright up the world
                            do kk=1,2
                            if(GRID(i2,j5,kk).gt.0)then
                            GRID(i2,j5,kk)=1
                            else
                            GRID(i2,j5,kk)=-1
                            endif
                            enddo
                        enddo
                enddo
        endif
    enddo



555 continue
    ii=mod(step,hpic)
    if(ii.eq.0) call toVMD(GRID,C)

    ii=mod(step,20)
    if(ii.eq.0) call GetDetachment(GRID,C,irn)

    if(ii.eq.0) call GetNeighbors(C,N1,N2)

! ! ______________________________________________________________
! ! _________________________ Check attachments & detachments
```

```
 ENDDO

 write(1,*)idum
 print*,"Time simulated", time, "s"
 End


! XXXXXXXXXXXXXXXXXXXXXXXXXXXXXXXXXXXXXXXXXXXXXXXXXXXXXXXXXXXXXX
 SUBROUTINE ColorMatrix
 Implicit real(a-h,o-z)
 integer NBH(5,11,3),mNBH(5),cNBH(5,11)
 integer DTC(5,5,0:2,20,3),mDTC(5,5,0:2),cDTC(5,5,0:2,20)
 common/ColorNBH/NBH,mNBH,cNBH,DTC,mDTC,cDTC

! ____________________________________________________________
! Matrix for local detachment

 NBH=0; mNBH=0; cNBH=1 ! bright

  NBH(1,1,1)= 1 ; NBH(1,1,2)= 0 ; NBH(1,1,3)= 0
  NBH(1,2,1)= 1 ; NBH(1,2,2)= 0 ; NBH(1,2,3)= 1
  NBH(1,3,1)= 1 ; NBH(1,3,2)= 1 ; NBH(1,3,3)= 1
 mNBH(1)=3


  NBH(5,1,1)=-1 ; NBH(5,1,2)= 0 ; NBH(5,1,3)= 0
  NBH(5,2,1)= 0 ; NBH(5,2,2)= 0 ; NBH(5,2,3)= 1
  NBH(5,3,1)= 0 ; NBH(5,3,2)= 1 ; NBH(5,3,3)= 1
 mNBH(5)=3


  NBH(2, 1,1)= 0 ; NBH(2, 1,2)=-1 ; NBH(2, 1,3)= 0
  NBH(2, 2,1)= 0 ; NBH(2, 2,2)= 1 ; NBH(2, 2,3)= 0
  NBH(2, 3,1)= 1 ; NBH(2, 3,2)=-1 ; NBH(2, 3,3)= 1
  NBH(2, 4,1)= 1 ; NBH(2, 4,2)= 0 ; NBH(2, 4,3)= 1
  NBH(2, 5,1)= 1 ; NBH(2, 5,2)= 1 ; NBH(2, 5,3)= 1
  NBH(2, 6,1)= 1 ; NBH(2, 6,2)= 2 ; NBH(2, 6,3)= 1
  NBH(2, 7,1)= 0 ; NBH(2, 7,2)=-1 ; NBH(2, 7,3)= 1
  NBH(2, 8,1)= 0 ; NBH(2, 8,2)= 0 ; NBH(2, 8,3)= 1
  NBH(2, 9,1)= 0 ; NBH(2, 9,2)= 1 ; NBH(2, 9,3)= 1
  NBH(2,10,1)= 0 ; NBH(2,10,2)= 2 ; NBH(2,10,3)= 1
  NBH(2,11,1)= 0 ; NBH(2,11,2)= 0 ; NBH(2,11,3)= 0
 mNBH(2)=11
 cNBH(2,3:6)=2


 NBH(4,:,:)=NBH(2,:,:)
 mNBH(4)=11
 cNBH(4,7:10)=2       ! gray
```

```
NBH(3,1,1)= 0 ; NBH(3,1,2)= 0 ; NBH(3,1,3)= 0
mNBH(3)=1
cNBH(3,1)=3

! ________________________________________________________________
! Matrix for cooperative detachment

DTC=0; mDTC=0; cDTC=1 ! bright

!_________________________________________________________ 1-4 & 4-1
DTC(1,4,0,1,1)= 2 ;     DTC(1,4,0,1,2)=-1 ;     DTC(1,4,0,1,3)= 0
DTC(1,4,0,2,1)= 2 ;     DTC(1,4,0,2,2)= 0 ;     DTC(1,4,0,2,3)= 0
DTC(1,4,0,3,1)= 2 ;     DTC(1,4,0,3,2)= 1 ;     DTC(1,4,0,3,3)= 0
DTC(1,4,0,4,1)= 2 ;     DTC(1,4,0,4,2)= 0 ;     DTC(1,4,0,4,3)= 1
DTC(1,4,0,5,1)= 2 ;     DTC(1,4,0,5,2)= 1 ;     DTC(1,4,0,5,3)= 1
mDTC(1,4,0)=5
cDTC(1,4,0,1:5)=2  ! gray

DTC(1,4,2,1,1)= 2 ;     DTC(1,4,2,1,2)=-2 ;     DTC(1,4,2,1,3)= 0
DTC(1,4,2,2,1)= 2 ;     DTC(1,4,2,2,2)=-1 ;     DTC(1,4,2,2,3)= 0
DTC(1,4,2,3,1)= 2 ;     DTC(1,4,2,3,2)= 0 ;     DTC(1,4,2,3,3)= 0
DTC(1,4,2,4,1)= 2 ;     DTC(1,4,2,4,2)= 1 ;     DTC(1,4,2,4,3)= 0
DTC(1,4,2,5,1)= 2 ;     DTC(1,4,2,5,2)=-1 ;     DTC(1,4,2,5,3)= 1
DTC(1,4,2,6,1)= 2 ;     DTC(1,4,2,6,2)= 0 ;     DTC(1,4,2,6,3)= 1
DTC(1,4,2,7,1)= 2 ;     DTC(1,4,2,7,2)= 1 ;     DTC(1,4,2,7,3)= 1
mDTC(1,4,2)=7
cDTC(1,4,2,1:7)=2  ! gray

DTC(1,4,1,1,1)= 2 ;     DTC(1,4,1,1,2)=-1 ;     DTC(1,4,1,1,3)= 0
DTC(1,4,1,2,1)= 2 ;     DTC(1,4,1,2,2)= 0 ;     DTC(1,4,1,2,3)= 0
DTC(1,4,1,3,1)= 2 ;     DTC(1,4,1,3,2)= 1 ;     DTC(1,4,1,3,3)= 0
DTC(1,4,1,4,1)= 2 ;     DTC(1,4,1,4,2)= 2 ;     DTC(1,4,1,4,3)= 0
DTC(1,4,1,5,1)= 2 ;     DTC(1,4,1,5,2)= 0 ;     DTC(1,4,1,5,3)= 1
DTC(1,4,1,6,1)= 2 ;     DTC(1,4,1,6,2)= 1 ;     DTC(1,4,1,6,3)= 1
DTC(1,4,1,7,1)= 2 ;     DTC(1,4,1,7,2)= 2 ;     DTC(1,4,1,7,3)= 1
mDTC(1,4,1)=7
cDTC(1,4,1,1:7)=2  ! gray

!____________________________________________________________-2-5 & 5-2
 DTC(2,5,0,1,1)= 1 ;     DTC(2,5,0,1,2)=-1 ;     DTC(2,5,0,1,3)= 0
 DTC(2,5,0,2,1)= 1 ;     DTC(2,5,0,2,2)= 0 ;     DTC(2,5,0,2,3)= 0
 DTC(2,5,0,3,1)= 1 ;     DTC(2,5,0,3,2)= 1 ;     DTC(2,5,0,3,3)= 0
 DTC(2,5,0,4,1)= 2 ;     DTC(2,5,0,4,2)= 0 ;     DTC(2,5,0,4,3)= 1
 DTC(2,5,0,5,1)= 2 ;     DTC(2,5,0,5,2)= 1 ;     DTC(2,5,0,5,3)= 1
mDTC(2,5,0)=5
cDTC(2,5,0,1:5)=2  ! gray

DTC(2,5,2,1,1)= 1 ;    DTC(2,5,2,1,2)=-2 ;    DTC(2,5,2,1,3)= 0
DTC(2,5,2,2,1)= 1 ;    DTC(2,5,2,2,2)=-1 ;    DTC(2,5,2,2,3)= 0
```

```
DTC(2,5,2,3,1)= 1 ;   DTC(2,5,2,3,2)= 0 ;   DTC(2,5,2,3,3)= 0
DTC(2,5,2,4,1)= 1 ;   DTC(2,5,2,4,2)= 1 ;   DTC(2,5,2,4,3)= 0
DTC(2,5,2,5,1)= 2 ;   DTC(2,5,2,5,2)=-1 ;   DTC(2,5,2,5,3)= 1
DTC(2,5,2,6,1)= 2 ;   DTC(2,5,2,6,2)= 0 ;   DTC(2,5,2,6,3)= 1
DTC(2,5,2,7,1)= 2 ;   DTC(2,5,2,7,2)= 1 ;   DTC(2,5,2,7,3)= 1
mDTC(2,5,2)=7
cDTC(2,5,2,1:7)=2  ! gray

DTC(2,5,1,1,1)= 1 ;   DTC(2,5,1,1,2)=-1 ;   DTC(2,5,1,1,3)= 0
DTC(2,5,1,2,1)= 1 ;   DTC(2,5,1,2,2)= 0 ;   DTC(2,5,1,2,3)= 0
DTC(2,5,1,3,1)= 1 ;   DTC(2,5,1,3,2)= 1 ;   DTC(2,5,1,3,3)= 0
DTC(2,5,1,4,1)= 1 ;   DTC(2,5,1,4,2)= 2 ;   DTC(2,5,1,4,3)= 0
DTC(2,5,1,5,1)= 2 ;   DTC(2,5,1,5,2)= 0 ;   DTC(2,5,1,5,3)= 1
DTC(2,5,1,6,1)= 2 ;   DTC(2,5,1,6,2)= 1 ;   DTC(2,5,1,6,3)= 1
DTC(2,5,1,7,1)= 2 ;   DTC(2,5,1,7,2)= 2 ;   DTC(2,5,1,7,3)= 1
mDTC(2,5,1)=7
cDTC(2,5,1,1:7)=2  ! gray

DTC(2,4,0,1,1)= 1 ;   DTC(2,4,0,1,2)=-2 ;   DTC(2,4,0,1,3)= 0
DTC(2,4,0,2,1)= 1 ;   DTC(2,4,0,2,2)=-1 ;   DTC(2,4,0,2,3)= 0
DTC(2,4,0,3,1)= 1 ;   DTC(2,4,0,3,2)= 0 ;   DTC(2,4,0,3,3)= 0
DTC(2,4,0,4,1)= 1 ;   DTC(2,4,0,4,2)= 1 ;   DTC(2,4,0,4,3)= 0
DTC(2,4,0,5,1)= 1 ;   DTC(2,4,0,5,2)= 2 ;   DTC(2,4,0,5,3)= 0
DTC(2,4,0,6,1)= 2 ;   DTC(2,4,0,6,2)= 0 ;   DTC(2,4,0,6,3)= 1
DTC(2,4,0,7,1)= 2 ;   DTC(2,4,0,7,2)= 1 ;   DTC(2,4,0,7,3)= 1
DTC(2,4,0,8,1)= 1 ;   DTC(2,4,0,8,2)= 0 ;   DTC(2,4,0,8,3)= 1
DTC(2,4,0,9,1)= 1 ;   DTC(2,4,0,9,2)= 1 ;   DTC(2,4,0,9,3)= 1
mDTC(2,4,0)=9
cDTC(2,4,0,1)=2  ! gray
cDTC(2,4,0,5)=2  ! gray

 DTC(2,4,2, 1,1)= 1 ;   DTC(2,4,2, 1,2)=-3 ;   DTC(2,4,2, 1,3)= 0
 DTC(2,4,2, 2,1)= 1 ;   DTC(2,4,2, 2,2)=-2 ;   DTC(2,4,2, 2,3)= 0
 DTC(2,4,2, 3,1)= 1 ;   DTC(2,4,2, 3,2)=-1 ;   DTC(2,4,2, 3,3)= 0
 DTC(2,4,2, 4,1)= 1 ;   DTC(2,4,2, 4,2)= 0 ;   DTC(2,4,2, 4,3)= 0
 DTC(2,4,2, 5,1)= 1 ;   DTC(2,4,2, 5,2)= 1 ;   DTC(2,4,2, 5,3)= 0
 DTC(2,4,2, 6,1)= 1 ;   DTC(2,4,2, 6,2)= 2 ;   DTC(2,4,2, 6,3)= 0
 DTC(2,4,2, 7,1)= 2 ;   DTC(2,4,2, 7,2)= 1 ;   DTC(2,4,2, 7,3)= 0
 DTC(2,4,2, 8,1)= 0 ;   DTC(2,4,2, 8,2)=-2 ;   DTC(2,4,2, 8,3)= 0
 DTC(2,4,2, 9,1)= 2 ;   DTC(2,4,2, 9,2)= 0 ;   DTC(2,4,2, 9,3)= 1
 DTC(2,4,2,10,1)= 2 ;   DTC(2,4,2,10,2)= 2 ;   DTC(2,4,2,10,3)= 1
 DTC(2,4,2,11,1)= 1 ;   DTC(2,4,2,11,2)=-2 ;   DTC(2,4,2,11,3)= 1
 DTC(2,4,2,12,1)= 1 ;   DTC(2,4,2,12,2)= 0 ;   DTC(2,4,2,12,3)= 1
mDTC(2,4,2)=12
cDTC(2,4,2,1:2)=2 ! gray
cDTC(2,4,2,5:6)=2  ! gray
cDTC(2,4,2,10:11)=2  ! gray

 DTC(2,4,1, 1,1)= 1 ;   DTC(2,4,1, 1,2)=-2 ;   DTC(2,4,1, 1,3)= 0
 DTC(2,4,1, 2,1)= 1 ;   DTC(2,4,1, 2,2)=-1 ;   DTC(2,4,1, 2,3)= 0
```

```
  DTC(2,4,1, 3,1)= 1 ;   DTC(2,4,1, 3,2)= 0 ;   DTC(2,4,1, 3,3)= 0
  DTC(2,4,1, 4,1)= 1 ;   DTC(2,4,1, 4,2)= 1 ;   DTC(2,4,1, 4,3)= 0
  DTC(2,4,1, 5,1)= 1 ;   DTC(2,4,1, 5,2)= 2 ;   DTC(2,4,1, 5,3)= 0
  DTC(2,4,1, 6,1)= 1 ;   DTC(2,4,1, 6,2)= 3 ;   DTC(2,4,1, 6,3)= 0
  DTC(2,4,1, 7,1)= 2 ;   DTC(2,4,1, 7,2)=-1 ;   DTC(2,4,1, 7,3)= 0
  DTC(2,4,1, 8,1)= 0 ;   DTC(2,4,1, 8,2)= 2 ;   DTC(2,4,1, 8,3)= 0
  DTC(2,4,1, 9,1)= 2 ;   DTC(2,4,1, 9,2)=-1 ;   DTC(2,4,1, 9,3)= 1
  DTC(2,4,1,10,1)= 2 ;   DTC(2,4,1,10,2)= 1 ;   DTC(2,4,1,10,3)= 1
  DTC(2,4,1,11,1)= 1 ;   DTC(2,4,1,11,2)= 1 ;   DTC(2,4,1,11,3)= 1
  DTC(2,4,1,12,1)= 1 ;   DTC(2,4,1,12,2)= 3 ;   DTC(2,4,1,12,3)= 1
mDTC(2,4,1)=12
cDTC(2,4,1,1:2)=2  ! gray
cDTC(2,4,1,5:6)=2  ! gray
cDTC(2,4,1,9)=2    ! gray
cDTC(2,4,1,12)=2   ! gray

  DTC(3,3,1, 1,1)= 0 ;   DTC(3,3,1, 1,2)=-1 ;   DTC(3,3,1, 1,3)= 0
  DTC(3,3,1, 2,1)=-1 ;   DTC(3,3,1, 2,2)= 0 ;   DTC(3,3,1, 2,3)= 0
  DTC(3,3,1, 3,1)= 0 ;   DTC(3,3,1, 3,2)= 0 ;   DTC(3,3,1, 3,3)= 0
  DTC(3,3,1, 4,1)= 1 ;   DTC(3,3,1, 4,2)= 0 ;   DTC(3,3,1, 4,3)= 0
  DTC(3,3,1, 5,1)=-1 ;   DTC(3,3,1, 5,2)= 1 ;   DTC(3,3,1, 5,3)= 0
  DTC(3,3,1, 6,1)= 0 ;   DTC(3,3,1, 6,2)= 1 ;   DTC(3,3,1, 6,3)= 0
  DTC(3,3,1, 7,1)= 1 ;   DTC(3,3,1, 7,2)= 1 ;   DTC(3,3,1, 7,3)= 0
  DTC(3,3,1, 8,1)= 0 ;   DTC(3,3,1, 8,2)= 2 ;   DTC(3,3,1, 8,3)= 0
  DTC(3,3,1, 9,1)= 0 ;   DTC(3,3,1, 9,2)= 0 ;   DTC(3,3,1, 9,3)= 1
  DTC(3,3,1,10,1)= 1 ;   DTC(3,3,1,10,2)= 0 ;   DTC(3,3,1,10,3)= 1
  DTC(3,3,1,11,1)=-1 ;   DTC(3,3,1,11,2)= 1 ;   DTC(3,3,1,11,3)= 1
  DTC(3,3,1,12,1)= 0 ;   DTC(3,3,1,12,2)= 1 ;   DTC(3,3,1,12,3)= 1
  DTC(3,3,1,13,1)= 1 ;   DTC(3,3,1,13,2)= 1 ;   DTC(3,3,1,13,3)= 1
  DTC(3,3,1,14,1)= 2 ;   DTC(3,3,1,14,2)= 1 ;   DTC(3,3,1,14,3)= 1
  DTC(3,3,1,15,1)= 0 ;   DTC(3,3,1,15,2)= 2 ;   DTC(3,3,1,15,3)= 1
  DTC(3,3,1,16,1)= 1 ;   DTC(3,3,1,16,2)= 2 ;   DTC(3,3,1,16,3)= 1
mDTC(3,3,1)=16
cDTC(3,3,1,1)=2 ! gray
cDTC(3,3,1,8:10)=2  ! gray
cDTC(3,3,1,15:16)=2  ! gray


  DTC(3,3,2, 1,1)= 0 ;   DTC(3,3,2, 1,2)=-2 ;   DTC(3,3,2, 1,3)= 0
  DTC(3,3,2, 2,1)=-1 ;   DTC(3,3,2, 2,2)=-1 ;   DTC(3,3,2, 2,3)= 0
  DTC(3,3,2, 3,1)= 0 ;   DTC(3,3,2, 3,2)=-1 ;   DTC(3,3,2, 3,3)= 0
  DTC(3,3,2, 4,1)= 1 ;   DTC(3,3,2, 4,2)=-1 ;   DTC(3,3,2, 4,3)= 0
  DTC(3,3,2, 5,1)=-1 ;   DTC(3,3,2, 5,2)= 0 ;   DTC(3,3,2, 5,3)= 0
  DTC(3,3,2, 6,1)= 0 ;   DTC(3,3,2, 6,2)= 0 ;   DTC(3,3,2, 6,3)= 0
  DTC(3,3,2, 7,1)= 1 ;   DTC(3,3,2, 7,2)= 0 ;   DTC(3,3,2, 7,3)= 0
  DTC(3,3,2, 8,1)= 0 ;   DTC(3,3,2, 8,2)= 1 ;   DTC(3,3,2, 8,3)= 0
  DTC(3,3,2, 9,1)= 0 ;   DTC(3,3,2, 9,2)=-1 ;   DTC(3,3,2, 9,3)= 1
  DTC(3,3,2,10,1)= 1 ;   DTC(3,3,2,10,2)=-1 ;   DTC(3,3,2,10,3)= 1
  DTC(3,3,2,11,1)=-1 ;   DTC(3,3,2,11,2)= 0 ;   DTC(3,3,2,11,3)= 1
  DTC(3,3,2,12,1)= 0 ;   DTC(3,3,2,12,2)= 0 ;   DTC(3,3,2,12,3)= 1
```

```
  DTC(3,3,2,13,1)= 1 ;    DTC(3,3,2,13,2)= 0 ;    DTC(3,3,2,13,3)= 1
  DTC(3,3,2,14,1)= 2 ;    DTC(3,3,2,14,2)= 0 ;    DTC(3,3,2,14,3)= 1
  DTC(3,3,2,15,1)= 0 ;    DTC(3,3,2,15,2)= 1 ;    DTC(3,3,2,15,3)= 1
  DTC(3,3,2,16,1)= 1 ;    DTC(3,3,2,16,2)= 1 ;    DTC(3,3,2,16,3)= 1
 mDTC(3,3,2)=16
 cDTC(3,3,2,1)=2 ! gray
 cDTC(3,3,2,8:10)=2  ! gray
 cDTC(3,3,2,15:16)=2  ! gray

!________________________________________________________-3-5 & 5-3
  DTC(3,4,0, 1,1)= 0 ;    DTC(3,4,0, 1,2)=-2 ;    DTC(3,4,0, 1,3)= 0
  DTC(3,4,0, 2,1)= 0 ;    DTC(3,4,0, 2,2)=-1 ;    DTC(3,4,0, 2,3)= 0
  DTC(3,4,0, 3,1)= 0 ;    DTC(3,4,0, 3,2)= 0 ;    DTC(3,4,0, 3,3)= 0
  DTC(3,4,0, 4,1)= 0 ;    DTC(3,4,0, 4,2)= 1 ;    DTC(3,4,0, 4,3)= 0
  DTC(3,4,0, 5,1)= 0 ;    DTC(3,4,0, 5,2)= 2 ;    DTC(3,4,0, 5,3)= 0
  DTC(3,4,0, 6,1)=-1 ;    DTC(3,4,0, 6,2)=-1 ;    DTC(3,4,0, 6,3)= 0
  DTC(3,4,0, 7,1)=-1 ;    DTC(3,4,0, 7,2)= 0 ;    DTC(3,4,0, 7,3)= 0
  DTC(3,4,0, 8,1)=-1 ;    DTC(3,4,0, 8,2)= 1 ;    DTC(3,4,0, 8,3)= 0
  DTC(3,4,0, 9,1)= 1 ;    DTC(3,4,0, 9,2)= 0 ;    DTC(3,4,0, 9,3)= 1
  DTC(3,4,0,10,1)= 1 ;    DTC(3,4,0,10,2)= 1 ;    DTC(3,4,0,10,3)= 1
  DTC(3,4,0,11,1)= 0 ;    DTC(3,4,0,11,2)=-1 ;    DTC(3,4,0,11,3)= 1
  DTC(3,4,0,12,1)= 0 ;    DTC(3,4,0,12,2)= 0 ;    DTC(3,4,0,12,3)= 1
  DTC(3,4,0,13,1)= 0 ;    DTC(3,4,0,13,2)= 1 ;    DTC(3,4,0,13,3)= 1
  DTC(3,4,0,14,1)= 0 ;    DTC(3,4,0,14,2)= 2 ;    DTC(3,4,0,14,3)= 1
  DTC(3,4,0,15,1)=-1 ;    DTC(3,4,0,15,2)= 0 ;    DTC(3,4,0,15,3)= 1
  DTC(3,4,0,16,1)=-1 ;    DTC(3,4,0,16,2)= 1 ;    DTC(3,4,0,16,3)= 1
 mDTC(3,4,0)=16
 cDTC(3,4,0,1)=2 ! gray
 cDTC(3,4,0,5)=2
 cDTC(3,4,0,11)=2
 cDTC(3,4,0,14)=2

  DTC(3,4,2, 1,1)= 0 ;    DTC(3,4,2, 1,2)=-3 ;    DTC(3,4,2, 1,3)= 0
  DTC(3,4,2, 2,1)= 0 ;    DTC(3,4,2, 2,2)=-2 ;    DTC(3,4,2, 2,3)= 0
  DTC(3,4,2, 3,1)= 0 ;    DTC(3,4,2, 3,2)=-1 ;    DTC(3,4,2, 3,3)= 0
  DTC(3,4,2, 4,1)= 0 ;    DTC(3,4,2, 4,2)= 0 ;    DTC(3,4,2, 4,3)= 0
  DTC(3,4,2, 5,1)= 0 ;    DTC(3,4,2, 5,2)= 1 ;    DTC(3,4,2, 5,3)= 0
  DTC(3,4,2, 6,1)=-1 ;    DTC(3,4,2, 6,2)=-2 ;    DTC(3,4,2, 6,3)= 0
  DTC(3,4,2, 7,1)=-1 ;    DTC(3,4,2, 7,2)=-1 ;    DTC(3,4,2, 7,3)= 0
  DTC(3,4,2, 8,1)=-1 ;    DTC(3,4,2, 8,2)= 0 ;    DTC(3,4,2, 8,3)= 0
  DTC(3,4,2, 9,1)= 1 ;    DTC(3,4,2, 9,2)=-1 ;    DTC(3,4,2, 9,3)= 1
  DTC(3,4,2,10,1)= 1 ;    DTC(3,4,2,10,2)= 0 ;    DTC(3,4,2,10,3)= 1
  DTC(3,4,2,11,1)= 1 ;    DTC(3,4,2,11,2)= 1 ;    DTC(3,4,2,11,3)= 1
  DTC(3,4,2,12,1)= 1 ;    DTC(3,4,2,12,2)= 2 ;    DTC(3,4,2,12,3)= 1
  DTC(3,4,2,13,1)= 0 ;    DTC(3,4,2,13,2)=-2 ;    DTC(3,4,2,13,3)= 1
  DTC(3,4,2,14,1)= 0 ;    DTC(3,4,2,14,2)=-1 ;    DTC(3,4,2,14,3)= 1
  DTC(3,4,2,15,1)= 0 ;    DTC(3,4,2,15,2)= 0 ;    DTC(3,4,2,15,3)= 1
  DTC(3,4,2,16,1)= 0 ;    DTC(3,4,2,16,2)= 1 ;    DTC(3,4,2,16,3)= 1
  DTC(3,4,2,17,1)= 0 ;    DTC(3,4,2,17,2)= 2 ;    DTC(3,4,2,17,3)= 1
  DTC(3,4,2,18,1)=-1 ;    DTC(3,4,2,18,2)=-1 ;    DTC(3,4,2,18,3)= 1
```

```
  DTC(3,4,2,19,1)=-1 ;   DTC(3,4,2,19,2)= 0 ;   DTC(3,4,2,19,3)= 1
  DTC(3,4,2,20,1)=-1 ;   DTC(3,4,2,20,2)= 1 ;   DTC(3,4,2,20,3)= 1
 mDTC(3,4,2)=20
 cDTC(3,4,2,1)=2 ! gray
 cDTC(3,4,2,5)=2
 cDTC(3,4,2,12:13)=2
 cDTC(3,4,2,17)=2

  DTC(3,4,1, 1,1)= 0 ;   DTC(3,4,1, 1,2)=-1 ;   DTC(3,4,1, 1,3)= 0
  DTC(3,4,1, 2,1)= 0 ;   DTC(3,4,1, 2,2)= 0 ;   DTC(3,4,1, 2,3)= 0
  DTC(3,4,1, 3,1)= 0 ;   DTC(3,4,1, 3,2)= 1 ;   DTC(3,4,1, 3,3)= 0
  DTC(3,4,1, 4,1)= 0 ;   DTC(3,4,1, 4,2)= 2 ;   DTC(3,4,1, 4,3)= 0
  DTC(3,4,1, 5,1)= 0 ;   DTC(3,4,1, 5,2)= 3 ;   DTC(3,4,1, 5,3)= 0
  DTC(3,4,1, 6,1)=-1 ;   DTC(3,4,1, 6,2)= 0 ;   DTC(3,4,1, 6,3)= 0
  DTC(3,4,1, 7,1)=-1 ;   DTC(3,4,1, 7,2)= 1 ;   DTC(3,4,1, 7,3)= 0
  DTC(3,4,1, 8,1)=-1 ;   DTC(3,4,1, 8,2)= 2 ;   DTC(3,4,1, 8,3)= 0
  DTC(3,4,1, 9,1)= 1 ;   DTC(3,4,1, 9,2)=-1 ;   DTC(3,4,1, 9,3)= 1
  DTC(3,4,1,10,1)= 1 ;   DTC(3,4,1,10,2)= 0 ;   DTC(3,4,1,10,3)= 1
  DTC(3,4,1,11,1)= 1 ;   DTC(3,4,1,11,2)= 1 ;   DTC(3,4,1,11,3)= 1
  DTC(3,4,1,12,1)= 1 ;   DTC(3,4,1,12,2)= 2 ;   DTC(3,4,1,12,3)= 1
  DTC(3,4,1,13,1)= 0 ;   DTC(3,4,1,13,2)=-1 ;   DTC(3,4,1,13,3)= 1
  DTC(3,4,1,14,1)= 0 ;   DTC(3,4,1,14,2)= 0 ;   DTC(3,4,1,14,3)= 1
  DTC(3,4,1,15,1)= 0 ;   DTC(3,4,1,15,2)= 1 ;   DTC(3,4,1,15,3)= 1
  DTC(3,4,1,16,1)= 0 ;   DTC(3,4,1,16,2)= 2 ;   DTC(3,4,1,16,3)= 1
  DTC(3,4,1,17,1)= 0 ;   DTC(3,4,1,17,2)= 3 ;   DTC(3,4,1,17,3)= 1
  DTC(3,4,1,18,1)=-1 ;   DTC(3,4,1,18,2)= 0 ;   DTC(3,4,1,18,3)= 1
  DTC(3,4,1,19,1)=-1 ;   DTC(3,4,1,19,2)= 1 ;   DTC(3,4,1,19,3)= 1
  DTC(3,4,1,20,1)=-1 ;   DTC(3,4,1,20,2)= 2 ;   DTC(3,4,1,20,3)= 1
 mDTC(3,4,1)=20
 cDTC(3,4,1,1)=2 ! gray
 cDTC(3,4,1,5)=2
 cDTC(3,4,1,9)=2
 cDTC(3,4,1,13)=2
 cDTC(3,4,1,17)=2

!___________________________________________________________ 2-3 & 3-2
  DTC(2,3,0, 1,1)= 1 ;   DTC(2,3,0, 1,2)=-2 ;   DTC(2,3,0, 1,3)= 0
  DTC(2,3,0, 2,1)= 1 ;   DTC(2,3,0, 2,2)=-1 ;   DTC(2,3,0, 2,3)= 0
  DTC(2,3,0, 3,1)= 1 ;   DTC(2,3,0, 3,2)= 0 ;   DTC(2,3,0, 3,3)= 0
  DTC(2,3,0, 4,1)= 1 ;   DTC(2,3,0, 4,2)= 1 ;   DTC(2,3,0, 4,3)= 0
  DTC(2,3,0, 5,1)= 1 ;   DTC(2,3,0, 5,2)= 2 ;   DTC(2,3,0, 5,3)= 0
  DTC(2,3,0, 6,1)= 2 ;   DTC(2,3,0, 6,2)=-1 ;   DTC(2,3,0, 6,3)= 0
  DTC(2,3,0, 7,1)= 2 ;   DTC(2,3,0, 7,2)= 0 ;   DTC(2,3,0, 7,3)= 0
  DTC(2,3,0, 8,1)= 2 ;   DTC(2,3,0, 8,2)= 1 ;   DTC(2,3,0, 8,3)= 0
  DTC(2,3,0, 9,1)= 1 ;   DTC(2,3,0, 9,2)= 0 ;   DTC(2,3,0, 9,3)= 1
  DTC(2,3,0,10,1)= 1 ;   DTC(2,3,0,10,2)= 1 ;   DTC(2,3,0,10,3)= 1
  DTC(2,3,0,11,1)= 2 ;   DTC(2,3,0,11,2)=-1 ;   DTC(2,3,0,11,3)= 1
  DTC(2,3,0,12,1)= 2 ;   DTC(2,3,0,12,2)= 0 ;   DTC(2,3,0,12,3)= 1
  DTC(2,3,0,13,1)= 2 ;   DTC(2,3,0,13,2)= 1 ;   DTC(2,3,0,13,3)= 1
  DTC(2,3,0,14,1)= 2 ;   DTC(2,3,0,14,2)= 2 ;   DTC(2,3,0,14,3)= 1
```

```
  DTC(2,3,0,15,1)= 3 ;   DTC(2,3,0,15,2)= 0 ;   DTC(2,3,0,15,3)= 1
  DTC(2,3,0,16,1)= 3 ;   DTC(2,3,0,16,2)= 1 ;   DTC(2,3,0,16,3)= 1
 mDTC(2,3,0)=16
 cDTC(2,3,0,1)=2 ! gray
 cDTC(2,3,0,5)=2
 cDTC(2,3,0,11)=2
 cDTC(2,3,0,14)=2

  DTC(2,3,1, 1,1)= 1 ;   DTC(2,3,1, 1,2)=-2 ;   DTC(2,3,1, 1,3)= 0
  DTC(2,3,1, 2,1)= 1 ;   DTC(2,3,1, 2,2)=-1 ;   DTC(2,3,1, 2,3)= 0
  DTC(2,3,1, 3,1)= 1 ;   DTC(2,3,1, 3,2)= 0 ;   DTC(2,3,1, 3,3)= 0
  DTC(2,3,1, 4,1)= 1 ;   DTC(2,3,1, 4,2)= 1 ;   DTC(2,3,1, 4,3)= 0
  DTC(2,3,1, 5,1)= 1 ;   DTC(2,3,1, 5,2)= 2 ;   DTC(2,3,1, 5,3)= 0
  DTC(2,3,1, 6,1)= 2 ;   DTC(2,3,1, 6,2)=-1 ;   DTC(2,3,1, 6,3)= 0
  DTC(2,3,1, 7,1)= 2 ;   DTC(2,3,1, 7,2)= 0 ;   DTC(2,3,1, 7,3)= 0
  DTC(2,3,1, 8,1)= 2 ;   DTC(2,3,1, 8,2)= 1 ;   DTC(2,3,1, 8,3)= 0
  DTC(2,3,1, 9,1)= 1 ;   DTC(2,3,1, 9,2)= 0 ;   DTC(2,3,1, 9,3)= 1
  DTC(2,3,1,10,1)= 1 ;   DTC(2,3,1,10,2)= 1 ;   DTC(2,3,1,10,3)= 1
  DTC(2,3,1,11,1)= 1 ;   DTC(2,3,1,11,2)= 2 ;   DTC(2,3,1,11,3)= 1
  DTC(2,3,1,12,1)= 1 ;   DTC(2,3,1,12,2)= 3 ;   DTC(2,3,1,12,3)= 1
  DTC(2,3,1,13,1)= 2 ;   DTC(2,3,1,13,2)=-1 ;   DTC(2,3,1,13,3)= 1
  DTC(2,3,1,14,1)= 2 ;   DTC(2,3,1,14,2)= 0 ;   DTC(2,3,1,14,3)= 1
  DTC(2,3,1,15,1)= 2 ;   DTC(2,3,1,15,2)= 1 ;   DTC(2,3,1,15,3)= 1
  DTC(2,3,1,16,1)= 2 ;   DTC(2,3,1,16,2)= 2 ;   DTC(2,3,1,16,3)= 1
  DTC(2,3,1,17,1)= 2 ;   DTC(2,3,1,17,2)= 3 ;   DTC(2,3,1,17,3)= 1
  DTC(2,3,1,18,1)= 3 ;   DTC(2,3,1,18,2)= 0 ;   DTC(2,3,1,18,3)= 1
  DTC(2,3,1,19,1)= 3 ;   DTC(2,3,1,19,2)= 1 ;   DTC(2,3,1,19,3)= 1
  DTC(2,3,1,20,1)= 3 ;   DTC(2,3,1,20,2)= 2 ;   DTC(2,3,1,20,3)= 1
 mDTC(2,3,1)=20
 cDTC(2,3,1,1)=2 ! gray
 cDTC(2,3,1,5)=2
 cDTC(2,3,1,12:13)=2
 cDTC(2,3,1,17)=2

  DTC(2,3,2, 1,1)= 1 ;   DTC(2,3,2, 1,2)=-2 ;   DTC(2,3,2, 1,3)= 0
  DTC(2,3,2, 2,1)= 1 ;   DTC(2,3,2, 2,2)=-1 ;   DTC(2,3,2, 2,3)= 0
  DTC(2,3,2, 3,1)= 1 ;   DTC(2,3,2, 3,2)= 0 ;   DTC(2,3,2, 3,3)= 0
  DTC(2,3,2, 4,1)= 1 ;   DTC(2,3,2, 4,2)= 1 ;   DTC(2,3,2, 4,3)= 0
  DTC(2,3,2, 5,1)= 1 ;   DTC(2,3,2, 5,2)= 2 ;   DTC(2,3,2, 5,3)= 0
  DTC(2,3,2, 6,1)= 2 ;   DTC(2,3,2, 6,2)=-1 ;   DTC(2,3,2, 6,3)= 0
  DTC(2,3,2, 7,1)= 2 ;   DTC(2,3,2, 7,2)= 0 ;   DTC(2,3,2, 7,3)= 0
  DTC(2,3,2, 8,1)= 2 ;   DTC(2,3,2, 8,2)= 1 ;   DTC(2,3,2, 8,3)= 0
  DTC(2,3,2, 9,1)= 1 ;   DTC(2,3,2, 9,2)=-2 ;   DTC(2,3,2, 9,3)= 1
  DTC(2,3,2,10,1)= 1 ;   DTC(2,3,2,10,2)=-1 ;   DTC(2,3,2,10,3)= 1
  DTC(2,3,2,11,1)= 1 ;   DTC(2,3,2,11,2)= 0 ;   DTC(2,3,2,11,3)= 1
  DTC(2,3,2,12,1)= 1 ;   DTC(2,3,2,12,2)= 1 ;   DTC(2,3,2,12,3)= 1
  DTC(2,3,2,13,1)= 2 ;   DTC(2,3,2,13,2)=-2 ;   DTC(2,3,2,13,3)= 1
  DTC(2,3,2,14,1)= 2 ;   DTC(2,3,2,14,2)=-1 ;   DTC(2,3,2,14,3)= 1
  DTC(2,3,2,15,1)= 2 ;   DTC(2,3,2,15,2)= 0 ;   DTC(2,3,2,15,3)= 1
  DTC(2,3,2,16,1)= 2 ;   DTC(2,3,2,16,2)= 1 ;   DTC(2,3,2,16,3)= 1
```

```
  DTC(2,3,2,17,1)= 2 ;   DTC(2,3,2,17,2)= 2 ;   DTC(2,3,2,17,3)= 1
  DTC(2,3,2,18,1)= 3 ;   DTC(2,3,2,18,2)=-1 ;   DTC(2,3,2,18,3)= 1
  DTC(2,3,2,19,1)= 3 ;   DTC(2,3,2,19,2)= 0 ;   DTC(2,3,2,19,3)= 1
  DTC(2,3,2,20,1)= 3 ;   DTC(2,3,2,20,2)= 1 ;   DTC(2,3,2,20,3)= 1
 mDTC(2,3,2)=20
 cDTC(2,3,2,1)=2 ! gray
 cDTC(2,3,2,5)=2
 cDTC(2,3,2,9)=2
 cDTC(2,3,2,13)=2
 cDTC(2,3,2,17)=2

 END




! XXXXXXXXXXXXXXXXXXXXXXXXXXXXXXXXXXXXXXXXXXXXXXXXXXXXXXXXXXXXXX
 SUBROUTINE ProcessList
  Implicit real(a-h,o-z)
  integer P(2,8,3)
  real Ea(2,2,0:3,0:3), Erep(2,2), dEa(5,5,3)
 common/Eact/P,Ea,Erep,dEa,Temp

!_______Surface Diffusion
 P(1,1,1)= 1 ; P(1,1,2)= 0 ; P(1,1,3)= 0 !right
 P(1,2,1)= 0 ; P(1,2,2)=-1 ; P(1,2,3)= 0 !down
 P(1,3,1)=-1 ; P(1,3,2)= 0 ; P(1,3,3)= 0 !left
 P(1,4,1)= 0 ; P(1,4,2)= 1 ; P(1,4,3)= 0 !up

!_______Immersion
 P(1,5,1)= 1 ; P(1,5,2)= 0 ; P(1,5,3)= 1
 P(1,6,1)= 0 ; P(1,6,2)= 0 ; P(1,6,3)= 1
 P(1,7,1)= 0 ; P(1,7,2)= 1 ; P(1,7,3)= 1
 P(1,8,1)= 1 ; P(1,8,2)= 1 ; P(1,8,3)= 1

!_______Emergence & Sub-surface Diffusion
 P(2,1,1)= 0 ; P(2,1,2)=-1 ; P(2,1,3)=-1
 P(2,2,1)=-1 ; P(2,2,2)=-1 ; P(2,2,3)=-1
 P(2,3,1)=-1 ; P(2,3,2)= 0 ; P(2,3,3)=-1
 P(2,4,1)= 0 ; P(2,4,2)= 0 ; P(2,4,3)=-1
 P(2,5:8,:)=P(1,1:4,:)


!_______Erep
  Erep(1,1)=0.400
  Erep(1,2)=0.000
  Erep(2,1)=0.000
  Erep(2,2)=0.160

  !_______Ea
```

```
    Ea=0.

!!  st  —-> h
    Ea(2,1,1,1)=0.46
    Ea(2,1,1,2)=0.5
    Ea(2,1,1,3)=1.2
    Ea(2,1,2,1)=0.4
    Ea(2,1,2,2)=0.8
    Ea(2,1,2,3)=1.2
    Ea(2,1,3,1)=0.45
    Ea(2,1,3,2)=0.5
    Ea(2,1,3,3)=1.8

!!  h  —-> st
    Ea(1,2,1,1)=1.61
    Ea(1,2,1,2)=1.8
    Ea(1,2,1,3)=1.8
    Ea(1,2,3,1)=1.8
    Ea(1,2,3,2)=1.8
    Ea(1,2,3,3)=1.8

!!  st  —-> st
    Ea(2,2,1,1)=0.66
    Ea(2,2,1,2)=0.8
    Ea(2,2,1,3)=0.8
    Ea(2,2,2,1)=0.8
    Ea(2,2,2,2)=0.8
    Ea(2,2,2,3)=0.8
    Ea(2,2,3,1)=0.8
    Ea(2,2,3,2)=0.8
    Ea(2,2,3,3)=0.8

!!  h  —-> h
    Ea(1,1,1,1)=2.10
    Ea(1,1,1,2)=2.10
    Ea(1,1,1,3)=2.10
    Ea(1,1,2,1)=1.60
    Ea(1,1,2,2)=1.80
    Ea(1,1,2,3)=2.10
    Ea(1,1,3,1)=2.40
    Ea(1,1,3,2)=2.40
    Ea(1,1,3,3)=2.40


!dEa  —-> Diffusion  bright  region
    dEa=0.
    f1=0.95
    f2=1.05
    dEa(1,2,1)=f1   ;    dEa(2,1,1)=f2
    dEa(2,3,1)=f1   ;    dEa(3,2,1)=f2
```

```
   dEa(5,4,1)=f1   ;    dEa(4,5,1)=f2
   dEa(4,3,1)=f1   ;    dEa(3,4,1)=f2

   Ea=0.2
 End


 SUBROUTINE ResetColor(ir,jr,i6r,nx,ny,irn,GRID,  ncl,CLG)
 implicit real(a-h,o-z)
 integer irn(6,2),GRID(nx,ny,2),CLG(99,3)

  ncl=0 ! sum of C within the LG
  CLG=0 ! i,j,k values for C within the LG

! The LG width correspond to 1 bump
  do ii=1,5
  iLG=ir-i6r+ii
  call correctI(iLG)
        do jj=1,9
        jLG=jr-5+jj
        call correctJ(jLG)

        !   ______________________________ Reset colors
            kk=1
            ig=mod(iLG,6);  if(ig.eq.0)ig=6
            if(GRID(iLG,jLG,kk).gt.0)then
                    ncl=ncl+1
                    CLG(ncl,1)=iLG; CLG(ncl,2)=jLG; CLG(ncl,3)=kk
                    GRID(iLG,jLG,kk)=irn(ig,kk) ! gets default color
            else
                    GRID(iLG,jLG,kk)=-irn(ig,kk) ! gets default color
            endif

            kk=2
            ig=mod(iLG,6);  if(ig.eq.0)ig=6
            if(GRID(iLG,jLG,kk).gt.0)then
                GRID(iLG,jLG,kk)=irn(ig,kk)     ! gets default color
            else
                GRID(iLG,jLG,kk)=-irn(ig,kk)
            endif
        enddo

!   ______________________________ Include C atoms OUTSIDE LG
        kk=1
        do jj=5,7
        jLG=jr+jj                 !C atoms ABOVE to the LG
            call correctJ(jLG)
            if(GRID(iLG,jLG,kk).gt.0)then
                    ncl=ncl+1
                    CLG(ncl,1)=iLG; CLG(ncl,2)=jLG; CLG(ncl,3)=kk
```

```
          endif
      jLG=jr-jj             !C atoms BELOW to the LG
          call correctJ(jLG)
          if(GRID(iLG,jLG,kk).gt.0)then
                 ncl=ncl+1
                 CLG(ncl,1)=iLG; CLG(ncl,2)=jLG; CLG(ncl,3)=kk
          endif
      enddo
 enddo
 END


SUBROUTINE getVel(step,i,j,GRID,C,  VELO)
implicit real(a-h,o-z)
integer P(2,8,3)
integer GRID(nx,ny,2), C(nc,3), step
real VELO(nc,8)
real Ea(2,2,0:3,0:3), Erep(2,2), dEa(5,5,3)
common/nn/nx,ny,nc
common/Eact/P,Ea,Erep,dEa,Temp

A0=1.E13
BkT=8.617332478E-5*Temp
alpha=0.1

VELO=0.
do ic=1,nc
   i=C(ic,1) ; j=C(ic,2) ; k=C(ic,3)
   iR0=GRID(i,j,k)  ! 1 2 3 (occ. regions)


   ! get repulsion from initial site
   Rep0=0.
   do n=1,8
   in=i+P(k,n,1)
   jn=j+P(k,n,2)
   kn=k+P(k,n,3)
   call correctIJ(in,jn)
   iR=-GRID(in,jn,kn)
       if(iR.lt.0)Rep0=Rep0+Erep(k,kn) ! if neighbor is occupied
   enddo

   i6=mod(i,6)
   do n=1,8
   in=i+P(k,n,1)
   jn=j+P(k,n,2)
   kn=k+P(k,n,3)
   call correctIJ(in,jn)
   iR=-GRID(in,jn,kn)
       if(iR.gt.0)then ! if neighbor is empty
```

```
                   ! get repulsion from final site
               Rep=-Erep(k,kn)
               do m=1,8
               inn=in+P(kn,m,1)
               jnn=jn+P(kn,m,2)
               knn=kn+P(kn,m,3)
               call correctIJ(inn,jnn)
               if(GRID(inn,jnn,knn).gt.0)Rep=Rep+Erep(kn,knn)
               enddo

    Ea1=Ea(k,kn, iR0,iR)

!______ if it goes towards/away the detached zone,
!______ Ea decrease/increase
        i6n=mod(in,6)
        ii=i6+i6n
        if(ii.ne.0)then
        i1=6*int(in/6)+3
        icol=abs(GRID(i1,j,1))

        fact=dEa(i6,i6n,icol)
        endif


        VELO(ic,n)=A0*exp(-Ea1/BkT)
        endif
    enddo
 enddo
 END



!____________________________________________________________
!------------------------------------------------------------------
 SUBROUTINE correctIJ(i,j)
 implicit real(a-h,o-z)
 common/nn/nx,ny,nc

 if(i.gt.nx)i=i-nx
 if(i.lt.1) i=nx+i
 if(j.gt.ny)j=j-ny
 if(j.lt.1) j=ny+j
 End

 SUBROUTINE correctI(i)
 implicit real(a-h,o-z)
 common/nn/nx,ny,nc
 if(i.gt.nx)i=i-nx
 if(i.lt.1) i=nx+i
 End
```

```
SUBROUTINE correctJ(j)
implicit real(a-h,o-z)
common/nn/nx,ny,nc
if(j.gt.ny)j=j-ny
if(j.lt.1)j=ny+j
End



SUBROUTINE GetDetachment(GRID,C,irn)
implicit real(a-h,o-z)
common/nn/nx,ny,nc
common/t/time
integer GRID(nx,ny,2), C(nc,3), irn(6,2), rg(4,2)
real reg(4,2)

!________________________________________ Detachment
i=3
ndet0=0

do while(i.le.nx)
   do j=1,ny
   m=abs(GRID(i,j,1))
        if(m.eq.1)ndet0=ndet0+1
   enddo
i=i+6
enddo
write(102,*)time,ndet0

!________________________________________ Regions
rg=0
do ic=1,nc
i=C(ic,1); j=C(ic,2); k=C(ic,3)
i6=mod(i,6); if(i6.eq.0)i6=6; ir=irn(i6,k)
        rg(ir,k)=rg(ir,k)+1
enddo
reg=float(rg)/float(nc)
s1=sum(reg(1,:)); s2=sum(reg(2,:)); s3=sum(reg(3,:))
write(105,*)time, s1, s2, s3
End



SUBROUTINE GetNeighbors(C,N1,N2)
implicit real(a-h,o-z)
common/nn/nx,ny,nc
common/t/time
integer C(nc,3), nh(2), nst(2), N1(nx,ny,2), N2(nx,ny,2)
```

```
nh=0; nst=0
do ic=1,nc
i=C(ic,1); j=C(ic,2); k=C(ic,3)
   if(k.eq.1)then
   nh(1)=nh(1)+N2(i,j,1)
   nh(2)=nh(2)+N1(i,j,1)
   else
   nst(1)=nst(1)+N1(i,j,2)
   nst(2)=nst(2)+N2(i,j,2)
   endif
enddo
nht=nh(1)+nh(2)
nstt=nst(1)+nst(2)
nt=nht+nstt
write(103,*)time, nt, nht, nstt
End




SUBROUTINE picSurf(nx,ny,nc,irn)
implicit real(a-h,o-z)
integer irn(6,2)

Nat=nx*ny*2
write(100,*)Nat
write(100,*)
dz=1.6
z1=10.
z2=z1-dz

do i=1,nx
                    ii=mod(i,6)
                    if(ii.eq.0)ii=6
      do j=1,ny
      x=float(2*i)-1
      y=float(2*j)-1
      write(100,*)irn(ii,2), x,y,z1
      x=x+1; y=y+1
      write(100,*)irn(ii,1), x,y,z2
      enddo
enddo
End




SUBROUTINE toVMD(GRID,C)
implicit real(a-h,o-z)
integer GRID(nx,ny,2), C(nc,3)
```

```
 common/nn/nx,ny,nc
 common/kpix/ncpix

 NR1=nx*ny*2
 NR2=nx/6*7*ny
 NR3=nx/6*4*ny
 Nat=NR1 +NR2 +NR3
 write(100,*)Nat
 write(100,*)

!_______________Metal Surface
 dz=1.6
 z1=10.
 z2=z1-dz
 i2=0
 i3=0

  do i=1,nx
  x1=float(2*i)-1
  x2=x1+1
        do j=1,ny
        y1=float(2*j)-1
        y2=y1+1
        mg=abs(GRID(i,j,1));
        if(mg.gt.99)mg=mg/100;
        if(mg.gt.9)mg=mg/10
            if(mg.eq.1)then
            write(100,*)"H  ", x2,y2,z2
            else
            write(100,*)"H   2 2 -2"
            endif

        mg=abs(GRID(i,j,2));
        if(mg.gt.99)mg=mg/100;
        if(mg.gt.9)mg=mg/10
            if(mg.eq.1)then
            write(100,*)"H  ", x1,y1,z1
            else
            write(100,*)"H   2 2 -2"
            endif
        enddo
  enddo

  do i=1,nx
  x1=float(2*i)-1
  x2=x1+1
        do j=1,ny
        y1=float(2*j)-1
        y2=y1+1
        mg=abs(GRID(i,j,1));
```

```
         if(mg.gt.99)mg=mg/100;
         if(mg.gt.9)mg=mg/10
              if(mg.eq.2)then
              write(100,*)"He",  x2,y2,z2
              i2=i2+1
              endif

        mg=abs(GRID(i,j,2));
         if(mg.gt.99)mg=mg/100;
         if(mg.gt.9)mg=mg/10
              if(mg.eq.2)then
              write(100,*)"He",  x1,y1,z1
              i2=i2+1
              endif
        enddo
enddo
              NN2=NR2-i2
              do  i=1,NN2
              write(100,*)"He   2  2  -2"
              enddo


do  i=1,nx
x1=float(2*i)-1
x2=x1+1
        do  j=1,ny
        y1=float(2*j)-1
        y2=y1+1
              if(abs(GRID(i,j,1)).eq.3)then
              write(100,*)"Li",  x2,y2,z2
              i3=i3+1
              endif

              if(abs(GRID(i,j,2)).eq.3)then
              write(100,*)"Li",  x1,y1,z1
              i3=i3+1
              endif
        enddo
enddo
              N3=NR3-i3
              do  i=1,N3
              write(100,*)"Li   2  2  -2"
              enddo


!___________________Carbide
 write(101,*)nc
 write(101,*)
 do  i=1,nc
```

```
 k=C(i,3)
 z=10.-float(k-1)*dz
 ix=2*C(i,1)-(k-1)
 iy=2*C(i,2)-(k-1)
 write(101,*)"C ", ix,iy,z, "0"
 enddo

 End




!____________________________________________________________________
!--------------------------------------------------------------------------
 SUBROUTINE CheckMe(step,nx,ny,N1,GRID)
 implicit real(a-h,o-z)
 integer step
 integer P(2,8,3)
 integer N1(nx,ny,2),GRID(nx,ny,2)

 i=1
 do while(i.le.nx)
    do j=1,ny
         mg0=GRID(i,j,1)
         iy=j-1; call correctIJ(i,iy); mg1=GRID(i,iy,1)
         iy=j+1; call correctIJ(i,iy); mg2=GRID(i,iy,1)
         mgt=mg1+mg2


! _____________________________ Bright Dark
         if(mg0.eq.-3)then
              if(mg1.eq.-10.or.mg2.eq.-10)then
              nBDB=nBDB+1
              write(*,'(a4,x,i7,2x,a14,x,i2,x,i2)')"step",step,"B-D
i,j:",i,j
              stop
              endif
         endif


! _____________________________ NotBright Bright Bright NotBright
         if(mg0.eq.-1.or.mg0.eq.-10)then
         if(mg2.eq.-1.or.mg2.eq.-10)then
         if(mg1.eq.-20.or.mg1.eq.-3)then
         iy=j+2; call correctIJ(i,iy); mg3=GRID(i,iy,1)
         if(mg3.eq.-20.or.mg3.eq.-3)then
              print*,"step", step, "NB-B-B-NB"
              write(*,'(i2,x,i2)')i,j
              stop
         endif
```

```
          endif
          endif
          endif

! ________________________________ Dark Green Dark
          if(mg0.eq.-20.and.mgt.eq.-6)then
               print*,"step", step, "D-G-D"
               write(*,'(i2,x,i2)')i,j
               stop
          endif

! ________________________________ Dark Bright Green
!            if(mg0.eq.-1.or.mg0.eq.-10)then
          if(mg0.eq.-10)then
          if(mgt.eq.-23)then
               print*,"step", step, "D-B-G","mg0",mg0
               write(*,'(i2,x,i2)')i,j
               stop
          endif
          endif

! ________________________________ Bright Dark Bright
          if(mg0.eq.-3)then
               if(mgt.eq.-20)then
               nBDB=nBDB+1
               write(*,'(a4,x,i7,2x,a14,x,i2,x,i2)')"step",step,"B-D-B
i,j:",i,j
               stop
               endif
          endif

! ________________________________ Bright Green Bright
          if(mg0.eq.-20)then
               if(mgt.eq.-20)then
               nBGB=nBGB+1
               write(*,'(a4,x,i7,2x,a14,x,i2,x,i2)')"step",step,"B-G-B
i,j:",i,j
               stop
               endif
          endif
! ________________________________ Incomplete Detach
          if(GRID(i,j,1).eq.10)then
               mgt2=abs(mg1)+abs(mg2)
               if(mgt2.ne.20)then
               print*,"step", step, "Incomplete Detach"
               write(*,'(i2,x,i2)')i,j
               stop
               endif
          endif
```

```
! ________________________________ Dark with bright at left & right
          if(mg0.eq.-3)then
          ix=i-1; call correctIJ(ix,j); mgx1=GRID(ix,j,1)
          ix=i+1; call correctIJ(ix,j); mgx2=GRID(ix,j,1)
          mgxt=mgx1+mgx2
               if(mgxt.eq.-20)then
               print*,"step", step, "B<-D->B"
               write(*,'(i2,x,i2)')i,j
               stop
               endif
          endif


! ________________________________ Dark edge without nbs
          if(mg0.eq.-10)then
          if(mg1.eq.-3.or.mg2.eq.-3)then
                    il=i-1; call correctIJ(il,j); mgl=GRID(il,j,1)
                    ir=i+1; call correctIJ(ir,j); mgr=GRID(ir,j,1)
                    if(mgl.ne.1)then
                    if(mgr.ne.1)then
                    print*,"Dark edge without nbs",step,i,j
                    print*,mgl, mgr
                    stop
                    endif
                    endif
          endif
          endif


     enddo
 i=i+6
 enddo
 End





  FUNCTION ran2(idum)
  INTEGER idum,IM1,IM2,IMM1,IA1,IA2,IQ1,IQ2,IR1,IR2,NTAB,NDIV
  REAL ran2,AM,EPS,RNMX
!    DOUBLE PRECISION ran2,AM,EPS,RNMX
  PARAMETER (IM1=2147483563,IM2=2147483399,AM=1.d0/IM1,IMM1=IM1-1)
  PARAMETER (IA1=40014,IA2=40692,IQ1=53668,IQ2=52774,IR1=12211,IR2=3791)
  PARAMETER (NTAB=32,NDIV=1+IMM1/NTAB,EPS=1.2d-16,RNMX=1.d0-EPS)
  INTEGER idum2,j,k,iv(NTAB),iy
  SAVE iv,iy,idum2
  DATA idum2/123456789/, iv/NTAB*0/, iy/0/
   if (idum.le.0) then
     idum=max(-idum,1)
```

```
      idum2=idum
      do 11 j=NTAB+8,1,-1
         k=idum/IQ1
         idum=IA1*(idum-k*IQ1)-k*IR1
         if (idum.lt.0) idum=idum+IM1
         if (j.le.NTAB) iv(j)=idum
11       continue
      iy=iv(1)
   endif
   k=idum/IQ1
   idum=IA1*(idum-k*IQ1)-k*IR1
   if (idum.lt.0) idum=idum+IM1
   k=idum2/IQ2
   idum2=IA2*(idum2-k*IQ2)-k*IR2
   if (idum2.lt.0) idum2=idum2+IM2
   j=1+iy/NDIV
   iy=iv(j)-idum2
   iv(j)=idum
   if(iy.lt.1)iy=iy+IMM1
   ran2=min(AM*iy,RNMX)
   return
   END
```

Appendix B: Moiré relations for two generic 2D Bravais lattices

In this appendix it will be derive a set of equations in the real space that allows to construct the primitive cells of the moiré superstructure generated by two generic 2D Bravais lattices. This set of equations in real space describes the commensurability conditions of the structures involved, and the common cell is determined within a finite commensurability threshold. From a physical point of view, this threshold corresponds to a residual strain in one or both constituting 2D Bravais lattices. This is strongly related to the elasticity of the material under consideration so that, in principle, different thresholds can be justified on physical grounds for different materials with the same lattice structure. Given a certain threshold, there is an infinite number of solutions for the moiré supercell, and the most interesting is the one giving a minimum size supercell with the smallest residual strain. In particular, we have developed and implemented an algorithm for the specific case of graphene grown on Ni(100) substrate, obtaining an excellent agreement with the experimental data [88].

State of the art

The discovery of graphene paved the way for a new and completely unexplored field in condensed matter physics concerning the creation of novel materials through layer-by-layer combinations of 2D systems [110, 111]. The resulting 3D structures, possibly involving different types of substrate [112], are usually called van der Waals heterostructures because they are held together in the bulk only by weak van der Waals forces. As a consequence, they can be easily manipulated at the level of each single layer [113].

A deep knowledge and characterization of these structures is increasingly necessary both from an experimental and theoretical point of view. Among the theoretical approaches, the first principle atomistic Density Functional Theory (DFT) is the most accurate one, but it strongly relies on the possibility to model the primitive cell of such systems, that is not always a trivial task. Indeed, typically, the Bravais lattices of the 2D materials stacked in the heterostructures have a mismatch condition and in most cases they are not commensurate. On the other hand, using periodic boundary conditions to simulate extended systems, it is necessary to identify a primitive cell as close as possible to the real system structure. Using an appropriate primitive cell for DFT simulations is really important: small variations in the cell structure and size can seriously affect the calculated equilibrium configuration and properties of the system under investigation[88]. In the recent literature, the problem has been afforded for some specific cases such as hexagonal/hexagonal coincidence lattices [114] and hexagonal/generic (metals) lattices [115]. A general solution for two generic non-coincidence 2D Bravais lattices has been found in the reciprocal space [116], or in the real space but has to be driven by experimental suggestions [117]. Some open-source codes [118, 119] are able to build a primitive cell of a moiré superstructure taking into account the reciprocal strain configuration of one lattice with respect to the other.

Mathematical derivation of the moiré relations

We consider two generic 2D Bravais lattices generated by the vectors ($\mathbf{a_{gr_1}}$,$\mathbf{a_{gr_2}}$) and ($\mathbf{a_{s_1}}$,$\mathbf{a_{s_2}}$) respectively. The superimposition together with a possible misorientation of one lattice with respect to the other can originate a 2D moiré superstructure. We identify the basis of the superlattice with a couple of vectors ($\mathbf{a_{m_1}}$,$\mathbf{a_{m_2}}$). The lattice-lattice relation can be expressed by the known commensurate relation defining the moiré superlattice [117]. In order to describe the structural 2D complexity, a set of eight integers (i, j, k, l, m, n, q, r) is needed, (i, j, k, l) for the first Bravais lattice and (m, n, q, r) for the second one:

$$\begin{gathered}\begin{pmatrix}\mathbf{a_{m_1}}\\ \mathbf{a_{m_2}}\end{pmatrix} = \mathsf{M}_{gr}\begin{pmatrix}\mathbf{a_{gr_1}}\\ \mathbf{a_{gr_2}}\end{pmatrix} = \mathsf{M}_{s}\begin{pmatrix}\mathbf{a_{s_1}}\\ \mathbf{a_{s_2}}\end{pmatrix}\\ \text{with}\\ \mathsf{M}_{gr} = \begin{pmatrix} i & j\\ k & l\end{pmatrix} \quad \text{and} \quad \mathsf{M}_{s} = \begin{pmatrix} m & n\\ q & r\end{pmatrix}\end{gathered} \tag{6.20}$$

As it appears from the definition, the (i, j, k, l, m, n, q, r) integers correspond to the decomposition of the superstructure lattice vectors ($\mathbf{a_{m_1}}$,$\mathbf{a_{m_2}}$) into the basis of the first ($\mathbf{a_{gr_1}}$,$\mathbf{a_{gr_2}}$) and the second ($\mathbf{a_{s_1}}$,$\mathbf{a_{s_2}}$) lattice. A direct relation between the two Bravais lattices is deduced from the Eq.6.20:

$$\begin{aligned}\begin{pmatrix}\mathbf{a_{gr_1}}\\ \mathbf{a_{gr_2}}\end{pmatrix} &= \mathsf{M}_{gr}^{-1}\mathsf{M}_{s}\begin{pmatrix}\mathbf{a_{s_1}}\\ \mathbf{a_{s_2}}\end{pmatrix}\\ &= \frac{1}{il-jk}\begin{pmatrix} lm-jq & ln-jr\\ -km+iq & -kn+ir\end{pmatrix}\begin{pmatrix}\mathbf{a_{s_1}}\\ \mathbf{a_{s_2}}\end{pmatrix}\\ &= \begin{pmatrix} a & b\\ c & d\end{pmatrix}\begin{pmatrix}\mathbf{a_{s_1}}\\ \mathbf{a_{s_2}}\end{pmatrix}\end{aligned} \tag{6.21a}$$

with

$$\begin{aligned} a &= \frac{lm-jq}{il-jk}, \quad b = \frac{ln-jr}{il-jk},\\ c &= \frac{-km+iq}{il-jk}, \quad d = \frac{-kn+ir}{il-jk}\end{aligned} \tag{6.21b}$$

Once we have obtained the geometrical link between the two lattices, we are going to exploit the connection with the physics of the system. The main formula appearing in our work is the one relating a, b, c, d and the physical parameters $p_1, p_2, \phi_1, \phi_2, \theta$. ϕ_1, ϕ_2, θ are connected to the misorientation condition while p_1, p_2 are the scaling factors of the lattices [Fig.6.24]. In order to find this relation we have to study the transformation associating the two vectors $\mathbf{a_{gr_1}}$ and $\mathbf{a_{gr_2}}$ with the vectors $\mathbf{a_{s_1}}$ and $\mathbf{a_{s_2}}$. By looking at Fig.6.24 together with the Eq.6.21a, this can be easily achieved taking the scalar products $\mathbf{a_{s_1}} \cdot \mathbf{a_{gr_1}}$, $\mathbf{a_{s_2}} \cdot \mathbf{a_{gr_1}}$, $\mathbf{a_{s_1}} \cdot \mathbf{a_{gr_2}}$ and $\mathbf{a_{s_2}} \cdot \mathbf{a_{gr_2}}$. Explicitly, we find:

$$\begin{aligned}\mathbf{a_{s_1}} \cdot \mathbf{a_{gr_1}} &= a|\mathbf{a_{s_1}}|^2 + b|\mathbf{a_{s_1}}||\mathbf{a_{s_2}}|\cos(\phi_1+\theta)\\ &= |\mathbf{a_{s_1}}||\mathbf{a_{gr_1}}|\cos(\phi_1)\end{aligned} \tag{6.22a}$$

$$\begin{aligned}\mathbf{a_{s_2}} \cdot \mathbf{a_{gr_1}} &= b|\mathbf{a_{s_2}}|^2 + a|\mathbf{a_{s_1}}||\mathbf{a_{s_2}}|\cos(\phi_1+\theta) \\ &= |\mathbf{a_{s_2}}||\mathbf{a_{gr_1}}|\cos(\theta)\end{aligned} \tag{6.22b}$$

$$\begin{aligned}\mathbf{a_{s_1}} \cdot \mathbf{a_{gr_2}} &= c|\mathbf{a_{s_1}}|^2 + d|\mathbf{a_{s_1}}||\mathbf{a_{s_2}}|\cos(\phi_1+\theta) \\ &= |\mathbf{a_{s_1}}||\mathbf{a_{gr_2}}|\cos(\phi_1+\phi_2+\theta)\end{aligned} \tag{6.22c}$$

$$\begin{aligned}\mathbf{a_{s_2}} \cdot \mathbf{a_{gr_2}} &= d|\mathbf{a_{s_2}}|^2 + c|\mathbf{a_{s_1}}||\mathbf{a_{s_2}}|\cos(\phi_1+\theta) \\ &= |\mathbf{a_{s_2}}||\mathbf{a_{gr_2}}|\cos(\phi_2)\end{aligned} \tag{6.22d}$$

where a, b, c, d are defined by Eq.6.21b, $\phi_1 = \angle(\mathbf{a_{gr_1}}, \mathbf{a_{s_1}})$, $\phi_2 = \angle(\mathbf{a_{gr_2}}, \mathbf{a_{s_2}})$, $\theta = \angle(\mathbf{a_{gr_1}}, \mathbf{a_{s_2}})$. It is important to stress that given a pair of 2D Bravais lattices and a certain misorientation condition between the two, the parameters $p_1, p_2, \phi_1, \phi_2, \theta$ are fixed.

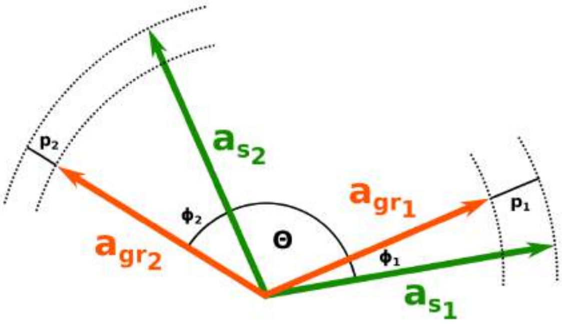

Figure 6.24: Structural interpretation of moiré superlattice. In orange and green the basis vectors of the two 2D Bravais lattices. p_1 and p_2 are the scaling factors while ϕ_1, ϕ_2, θ are related to the misorientation condition between the lattices [109].

For a certain pair of Bravais lattices with a fixed misorientation angle, the system Eq.6.22 has consistent solutions only if the two Bravais lattices are commensurate. In other words, we can always find real values for the parameters a, b, c, d that solve Eq.6.22 but these numbers are often irrational, thus not compatible with the commensurability condition Eq.6.21b. In order to avoid this problem, we decided to consider a threshold on the commensurability condition which results in a threshold on the parameters a, b, c, d. Given two 2D Bravais lattices, from the system Eq.6.22 one can compute the theoretical values of a, b, c, d at a certain misorientation angle. All the sets of parameters a, b, c, d that will deviate from the theoretical values no more than the fixed threshold will be accepted as solutions of Eq.6.22. From a physical point of view, the threshold assumed on the commensurability can be interpreted as a strain on the basis vectors of one of the two lattices. This possibility is strongly related to the elasticity of the material under consideration so that, in principle, different thresholds can be justified on physical grounds for different materials with the same lattice structure. Given a certain threshold, there is an infinite number of solutions for the moiré supercell. Indeed, as can be easily seen from the definitions [Eq.6.21b], an infinite number of combinations of the eight integers (i, j, k, l, m, n, q, r) give the same values for the parameters a, b, c, d. This in turn corresponds to the fact that a moiré superlattice is a Bravais lattice itself and, consequently, can be described by an infinite set of cells.

As mentioned at the beginning, we are interested to find the primitive cells of the moiré superlattice, namely the (infinite) subset of cells with the minimum cell volume. Being in 2D, the cell volume of the moiré superlattice is defined as $\mathrm{V}_{cell} = |\mathbf{a_{m_1}} \times \mathbf{a_{m_2}}|$, where $\times$ denotes the cross product, and it can be expressed in terms of the basis of the two 2D Bravais lattices using Eq.6.20:

$$\begin{aligned}|\mathbf{a_{m_1}} \times \mathbf{a_{m_2}}| &= |i\mathbf{a_{gr_1}} \times l\mathbf{a_{gr_2}} + j\mathbf{a_{gr_2}} \times k\mathbf{a_{gr_1}}| \\ &= |m\mathbf{a_{s_1}} \times r\mathbf{a_{s_2}} + q\mathbf{a_{s_2}} \times n\mathbf{a_{s_1}}|\end{aligned} \tag{6.23}$$

The minimization of the volume must be done over the set of integer numbers (i, j, k, l, m, n, q, r) providing a certain value of a, b, c, d, according to definition [Eq.6.21b], that correspond (within the threshold) to the values fixed by the geometry of the problem through Eq.6.22. Explicitly, we are looking for the quantity V_{min}:

$$\begin{aligned} V_{min} = & \min_{\substack{i,j,k,l \\ \phi_1,\phi_2,\theta fixed}} |i\mathbf{a_{gr_1}} \times l\mathbf{a_{gr_2}} + j\mathbf{a_{gr_2}} \times k\mathbf{a_{gr_1}}| \\ = & \min_{\substack{m,n,q,r \\ \phi_1,\phi_2,\theta fixed}} |m\mathbf{a_{s_1}} \times r\mathbf{a_{s_2}} + q\mathbf{a_{s_2}} \times n\mathbf{a_{s_1}}| \end{aligned} \tag{6.24}$$

The system of equations Eq.6.22, that we have dubbed "moiré superlattice relations", relating the superlattice parameters with the geometry of the system, together with the condition on the volume Eq.6.24 constitute the core of our systematic procedure to obtain the moiré primitive cell.

A further comment is in order at this point. Since we are considering a threshold on the commensurability of the lattices, we will find as primitive cell of the moiré superstructure different hypotheses of cells with different volume, but all of them will satisfy the commensurability threshold and minimization conditions. Moreover, different (i, j, k, l, m, q, r, s) solutions of the system of equations will identify different shape/orientation of the same cell. A comparison with experiments will indicate which cell will be “the best primitive cell" of the moiré superstructure. However, we want to stress that our method allows to identify a subset of possible primitive cells of the moiré superstructure, drastically decreasing their number and the effort to identify them.

Algorithm details

We have written a Python code in order to implement the logical steps previously mentioned. These can be summarized in four main points, as reported in a schematic flowchart Fig.6.25. We are going to supply precise details for each step below.

1. *Implementation of the moiré superstructure.*
   First of all the algorithm fixes the symmetry of the two 2D Bravais lattices, the module of the basis vectors and their misorientation angle. The lattices are considered simply superimposed, without interaction. Through the Eq.6.22 the code computes the theoretical a, b, c, d parameters of the moiré superstructure.

2. *Generation of the cells.*
   The algorithm requires to fix a range of values for each integer (i, j, k, l, m, q, r, s) and computes all the possible combinations (i, j, k, l, m, q, r, s), together with the corresponding parameters a, b, c, d according to [Eq.6.21b]. In principle the range should be $(-\infty, +\infty)$ but, due to the limited calculation capacity of the computer and the computational effort, it must be taken as finite. A wider range of values should correspond to a higher probability to catch the best set (i, j, k, l, m, q, r, s) for the primitive cell of the moiré superstructure. This issue has been tackled developing a parallel version of the code that allows to increase the range and be more accurate in the identification of the primitive cell of the system.

3. *Moiré relations resolution.*
   The algorithm requires to fix the commensurability threshold on the parameters a, b, c, d.

Subsequently, the code compares the values of a, b, c, d computed for each combination of the eight integers (i, j, k, l, m, q, r, s) listed before with the theoretical values obtained through [Eq.6.22]. If the difference between the two values lies within the threshold, the combination (i, j, k, l, m, q, r, s) will be classified as a possible moiré supercell, otherwise it will be discarded. In order to find the best threshold value for the system under consideration, one can start with a reasonable initial value that takes into account the nature of the 2D Bravais lattices and decrease it until one has no longer solutions. We will consider the last threshold value that gives solutions as the most accurate.

4. *Identification of the primitive cells subset.*
   The algorithm identifies the primitive cells of the moiré superstructure as a subset of all the (i, j, k, l, m, q, r, s) solutions associated to the most accurate threshold value. The ensemble of the solutions will be composed by some of the possible primitive cells together with some of their related conventional cells: the primitive cell and its corresponding conventional cells will have (exactly) the same computed parameters (a, b, c, d). We want to stress again that the number of solutions is limited because of the finite range considered in the second step. For each different set of parameters (a, b, c, d), all of them compatible within the chosen threshold, the algorithm will find the combination of integers (i, j, k, l, m, q, r, s) with the minimum in-plane volume [Eq.6.24], including them in the subset of the primitive cells of the moiré superstructure.

Application to Graphene/Ni(100)

The nickel (100) surface has a square lattice while graphene is characterized by a hexagonal lattice: hereinafter we will identify the lattice basis vectors of Ni(100) and graphene with ($\mathbf{a_{s_1}}$,$\mathbf{a_{s_2}}$) and ($\mathbf{a_{gr_1}}$,$\mathbf{a_{gr_2}}$) respectively. The system will show different kinds of moiré superstructures tuned by the graphene and Ni(100) lattices misorientation. We are going to explicitly write the moiré relations for this system, exploiting the primitive cell of the moiré structure for the $\phi_1 = 48^\circ$ configuration. Finally, our results will be compared with the experimental measurements.

Results

In order to write explicitly the moiré relations, we exploit the structural properties and the symmetry of the system. The basis vectors of the graphene lattice have the same modulus and the same applies to the Ni(100) lattice. Considering $|\mathbf{a_{s_1}}| = |\mathbf{a_{s_2}}| = A$ and $|\mathbf{a_{gr_1}}| = |\mathbf{a_{gr_2}}| = pA$, Eq.6.22 and Eq.6.24 turns out as:

$$a = p\frac{\cos(\phi_1) - \cos(\theta)\cos(\phi_1 + \theta)}{\sin^2(\phi_1 + \theta)} \tag{6.25a}$$

$$b = p\frac{\cos(\theta) - \cos(\phi_1)\cos(\phi_1 + \theta)}{\sin^2(\phi_1 + \theta)} \tag{6.25b}$$

$$c = p\frac{\cos(\phi_1 + \phi_2 + \theta) - \cos(\phi_2)\cos(\phi_1 + \theta)}{\sin^2(\phi_1 + \theta)} \tag{6.25c}$$

$$d = p\frac{\cos(\phi_2) - \cos(\phi_1 + \phi_2 + \theta)\cos(\phi_1 + \theta)}{\sin^2(\phi_1 + \theta)} \tag{6.25d}$$

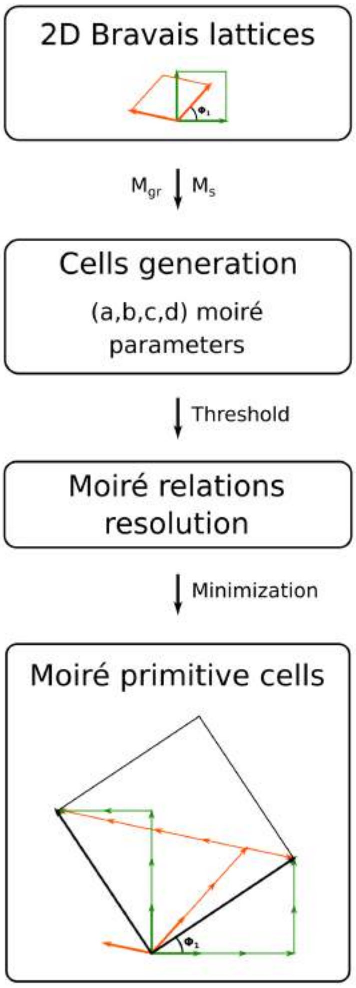

Figure 6.25: Flowchart diagram of the algorithm for finding the primitive cell of a moiré superstructure. **First step:** the two 2D Bravais lattices together with their misorientation condition are defined. **Second step:** through the matrix $\mathbf{M}_{gr}$ and $\mathbf{M}_s$, all the possible cells of the moiré superstructure are generated. **Third step:** considering a commensurability threshold, a subset of possible primitive cells is identified. **Fourth step:** the minimization on the cell volume gives the primitive cells of the moiré superstructure [109].

$$\begin{aligned} V_{min} &= \min_{\substack{i,j,k,l \\ \phi_1,\phi_2,\theta fixed}} p^2|(il-jk)\sin(\theta+\phi_2)| \\ &= \min_{\substack{m,n,q,r \\ \phi_1,\phi_2,\theta fixed}} |(mr-qn)\sin(\theta+\phi_1)| \end{aligned} \tag{6.25e}$$

In the case of graphene on a square substrate one has $\phi_1+\theta=\pi/2$ and $\phi_2=\phi_1+\pi/6$. As a result, the Eq.6.25 read as follows:

$$a = p\cos(\phi_1) \tag{6.26a}$$

$$b = p\sin(\phi_1) \tag{6.26b}$$

$$c = -p\left(\frac{\sqrt{3}}{2}\sin(\phi_1)+\frac{1}{2}\cos(\phi_1)\right) \tag{6.26c}$$

$$d = p\left(\frac{\sqrt{3}}{2}\cos(\phi_1)-\frac{1}{2}\sin(\phi_1)\right) \tag{6.26d}$$

$$\min_{\substack{i,j,k,l\\ \phi_1,\phi_2,\theta fixed}} p^2\frac{\sqrt{3}}{2}|il-jk| = \min_{\substack{m,n,q,r\\ \phi_1,\phi_2,\theta fixed}} |mr-qn| \qquad (6.26e)$$

Considering as lattice parameters of graphene and Ni(100) 2.46 Å and 2.49 Å respectively, the scaling factor of the system is $p = 0.988$. Evaluating the Eq.6.26a-6.26b-6.26c-6.26d in $\phi_1 = 48°$, the parameters a, b, c, d of the system are:

$$(a, b, c, d) = (0.661068, 0.734191, -0.966363, 0.205406). \qquad (6.27)$$

The primitive cells found with our method are reported in Fig.6.27. The tolerability threshold on the a, b, c, d parameters is 4%, corresponding to a maximum strain of the graphene layer equal to 5.7% and in total agreement with the already known elasticity properties of graphene [120]. If we decrees more the threshold value we no longer have solutions for the primitive cells of the system. Because of the smaller in-plane volume, we decide to implement the first primitive cell [Fig.6.27a] as a simulation cell. As shown in one of our works published in *Carbon* [88], the chosen primitive cell is also stable after a DFT relax calculation. The final configuration of the primitive cell has a corrugation of the graphene layer of 0.2 Å that gives origin to a network moiré superstructure, in agreement with the experimental evidences. A clear proof of the quality of our result is the comparison between the experimental and simulated Scanning Tunneling Microscopy constant current maps: the agreement is almost perfect [Fig.6.26].

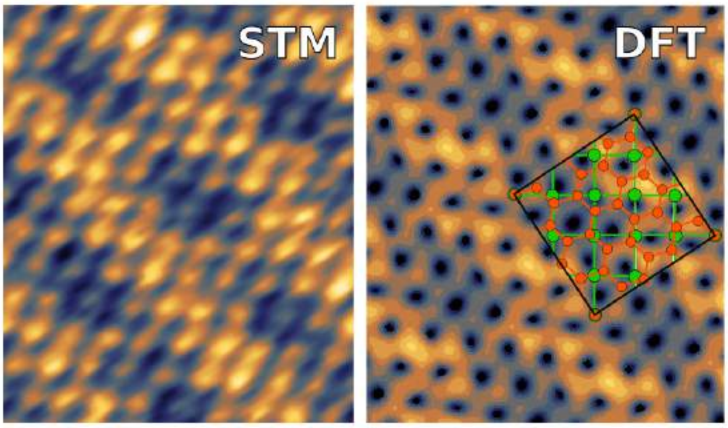

Figure 6.26: Comparison between experimental (STM) and simulated (DFT) Scanning Tunneling Microscopy constant current maps of graphene/Ni(100) with a graphene lattice (orange) misorientation angle $\phi_1 = 48°$ w.r.t. the Ni(100) lattice (green). **Scanning parameters:** $V_b = -0.2$ V, $I_t = 1$ nA. DFT parameters: Inegrated Local Density of States (ILDOS) iso-surface lying ~ 2 Å above graphene with iso-values of $9 \cdot 10^{-6}\,|e|/a_0^3$ [109].

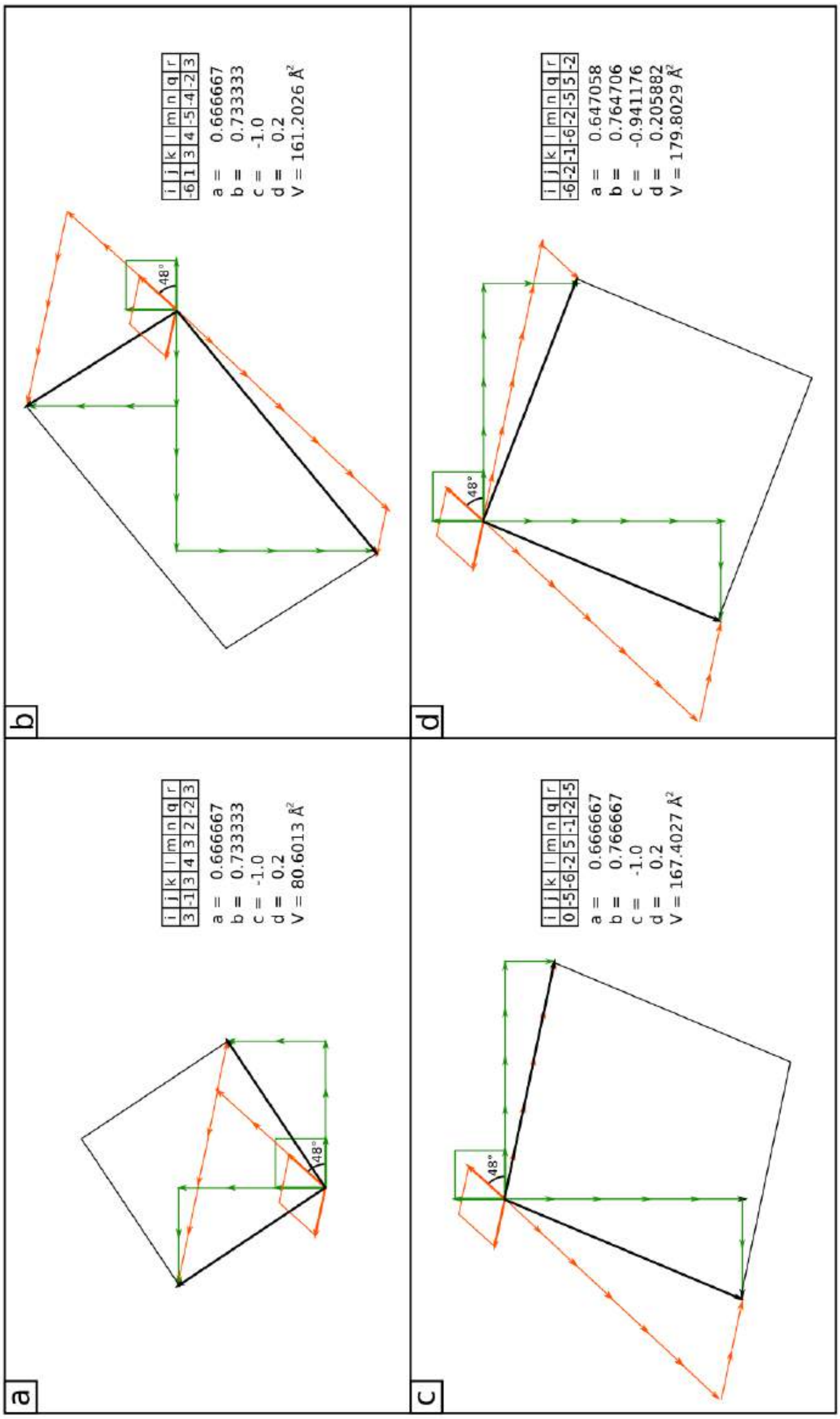

Figure 6.27: Primitive cells of the graphene/Ni(100) moiré superlattice (black) with a graphene lattice (orange) misorientation angle $\phi_1 = 48°$ w.r.t. the Ni(100) lattice (green). For each cell are reported the (i, j, k, l, m, q, r, s) indexes, the a, b, c, d parameters and the in-plane volume. The primitive cells are obtained implementing our method on a homemade Phython code where the (i, j, k, l, m, q, r, s) range is $(-7, 7)$ for each index and the tolerability threshold of the a, b, c, d parameters is set at 4%. [109]

Bibliography

[1] R. S. Weatherup, B. C. Bayer, R. Blume, C. Ducati, C. Baehtz, R. Schlögl, and S. Hofmann. In situ characterization of alloy catalysts for low-temperature graphene growth. *Nano Lett.*, 11:4154, 2011.

[2] Q. Fu and X. Bao. Surface chemistry and catalysis confined under two-dimensional materials. *Chem. Soc. Rev.*, 46:1842, 2017.

[3] R. Rameshan, V. Vonk, D. Franz, J. Drnec, S. Penner, A. Garhofer, F. Mittendorfer, A. Stierle, and B. Klötzer. Role of precursor carbides for graphene growth on Ni(111). *Sci. Rep.*, 8:2662, 2018.

[4] M. Weser, Y. Rehder, K. Horn, M. Sicot, M. Fonin, A. B. Preobrajenski, E. N. Voloshina, E. Goering, and Y. S. Dedkov. Induced magnetism of carbon atoms at the graphene/Ni(111) interface. *App. Phys. Lett.*, 96:012504, 2010.

[5] H. Tetlow, J. Posthuma de Boer, I. J. Ford, D. D. Vedensky, J. Coraux, and L. Kantorovich. Growth of epitaxial graphene: Theory and experiment. *Phys. Rep.*, 542:195, 2014.

[6] S. Bae, H. Kim, Y. Lee, X. Xu, J. S. Park, Y. Zheng, J. Balakrishnan, T. Lei, H. R. Kim, Y. I. Song, Y. J. Kim, K. S. Kim, B. Özyilmaz, J. H. Ahn, B. H. Hong, and S. Iijima. Roll-to-roll production of 30-inch graphene films for transparent electrodes. *Nature Nanotechnology*, 5:574, 2010.

[7] D. Wei, Y. Liu, Y. Wang, H. Zhang, L. Huang, and G. Yu. Synthesis of N-doped graphene by chemical vapor deposition and its electrical properties. *Nano Lett.*, 9:1752, 2009.

[8] D. Deng, X. Chen, L. Yu, X. Wu, Q. Liu, Y. Liu, H. Yang, H. Tian, Y. Hu, P. Du, R. Si, J. Wang, X. Cui, H. Li, J. Xiao, T. Xu, J. Deng, F. Yang, P. N. Duchesne, P. Zhang, J. Zhou, L. Sun, J. Li, X. Pan, and X. Bao. A single iron site confined in a graphene matrix for the catalytic oxidation of benzene at room temperature. *Sci. Adv.*, 1:e150046, 2015.

[9] L. Zhao, R. He, K. T. Rim, T. Schiros, K. Soo Kim, H. Zhou, C. Gutiérrez, S. P. Chockalingam, C. J. Arguello, L. Pálová, D. Nordlund, M. S. Hybertsen, D. R. Reichman, T. F. Heinz, P. Kim, A. Pinczuk, G. W. Flynn, and A. N. Pasupathy. Visualizing individual nitrogen dopants in monolayer graphene. *Nano Lett.*, 13:4659, 2013.

[10] M. Telychko, P. Mutombo, M. Ondráček, P. Hapala, F. C. Bocquet, J. Kolorenč, M. Vondráček, P. Jelínek, and M. Švec. Achieving high-quality single-atom nitrogen doping of graphene/SiC(0001) by ion implantation and subsequent thermal stabilization. *ACS Nano*, 8:7318, 2014.

[11] A. Sala, G. Zamborlini, T. O. Menteș, and A. Locatelli. Fabrication of a 2D heterojunction in graphene via low energy N_2^+ irradiation. *Small*, 11:5927.

[12] H. Terrones, R. Lv, M. Terrones, and M. S. Dresselhaus. The role of defects and doping in 2D graphene sheets and 1D nanoribbons. *Rep. Prog. Phys.*, 75:062501, 2012.

[13] A. V. Krasheninnikov, P. O. Lehtinen, A. S. Foster, P. Pyykkö, and R. M. Nieminen. Embedding transition-metal atoms in graphene: Structure, bonding, and magnetism. *Phys. Rev. Lett.*, 102:126807, 2009.

[14] M. Kaukonen, A. V. Krasheninnikov, E. Kauppinen, and R. M. Nieminen. Doped graphene as a material for oxygen reduction reaction in hydrogen fuel cells: A computational study. *ACS Cat.*, 3:159, 2012.

[15] S. Wannakao, T. Nongnual, P. Khongpracha, T. Maihom, and J. Limtrakul. Reaction mechanisms for CO catalytic oxidation by N_2O on Fe-embedded graphene. *J. Phys. Chem. C*, 116:16992, 2012.

[16] N. Guo, S. Liu, and C. Zhang. Greatly enhancing catalytic activity of graphene by doping the underlying metal substrate. *Sci. Rep.*, 5:12058, 2015.

[17] B. Wang, M. Caffio, C. Bromley, H. Früchtl, and R. Schaub. Coupling epitaxy, chemical bonding, and work function at the local scale in transition metal-supported graphene. *ACS Nano*, 4:5773, 2010.

[18] A. Ambrosetti and P. L. Silvestrelli. The chemical role of Ni(111) and Cu(111) substrates. *J. Phys. Chem. C*, 121:19828, 2017.

[19] C. F. McConville, D. P. Woodruff, and S. D. Kevan. The electronic structure of graphitic overlayers on Ni(100). *Surf. Sci. Lett.*, 171:L447, 1986.

[20] D. A. Pudikov. Electronic structure of graphene on Ni surfaces with different orientation. *Mater. Chem. Phys.*, 179:189, 2016.

[21] S. Stolbov, S. Hong, A. Kara, and T. S. Rahman. Origin of the C-induced $p4g$ reconstruction of Ni(001). *Phys. Rev. B*, 72:155423, 2005.

[22] G. Hörmandinger, J. B. Pendry, F. M. Leibsle, P. W. Murray, R. W. Joyner, and G. Thornton. Scanning-tunneling-microscopy investigation of the Ni(100)-p(2×2)C surface. *Phys. Rev. B*, 48:8356, 1993.

[23] R. Martinez-Gordillo, C. Varvenne, H. Amara, and C. Bichara. $\mathrm{Ni_2C}$ surface carbide to catalyze low-temperature graphene growth. *Phys. Rev. B*, 97:205431, 2018.

[24] S. Marchini, S. Günther, and J. Wintterlin. Scanning tunneling microscopy of graphene on Ru(0001). *Phys. Rev. B*, 76:075429, 2007.

[25] W. Moritz, B Wang, M.L. Bocquet, T. Brugger, T. Greber, J. Wintterlin, and S. Günther. Structure determination of the coincidence phase of graphene on Ru(0001). *Phys. Rev. Lett.*, 104:136102, 2010.

[26] E. N. Voloshina, Y. S. Dedkov, S. Torbrügge, A. Thissen, and M. Fonin. Graphene on Rh(111): scanning tunneling and atomic force microscopies studies. *Appl. Phys. Lett.*, 100:241606, 2012.

[27] E. Miniussi, M. Pozzo, A. Baraldi, E. Vesselli, R. R. Zhan, G. Comelli, M. A. Mentes, T.O. ans Niño, A. Locatelli, S. Lizzit, and Alfé D. Thermal stability of corrugated epitaxial graphene grown on Re(0001). *Phys. Rev. Lett.*, 106:216101, 2011.

[28] C. Tonnoir, A. Kimouche, J. Coraux, L. Magaud, B. Delsol, B. Gilles, and C. Chapelier. Induced superconductivity in graphene grown on rhenium. *Phys. Rev. Lett.*, 111:246805, 2013.

[29] Z. Sun, S. K. Hämäläinen, J. Sainio, J. Lahtinen, D. Vanmaekelbergh, and P. Liljeroth. Topographic and electronic contrast of the graphene moiré on Ir(111) probed by scanning tunneling microscopy and noncontact atomic force microscopy. *Phys. Rev. B*, 83:081415, 2011.

[30] A. B. Preobrajenski, M. Ling Ng, A. S. Vinogradov, and N. Martensson. Controlling graphene corrugation on lattice-mismatched substrates. *Phys. Rev. B*, 78:073401, 2008.

[31] L. Gao, J. R. Guest, and N. P. Guisinger. Epitaxial graphene on Cu(111). *Nano Lett.*, 10:3512, 2010.

[32] L. Meng, R. Wu, L. Zhang, L. Li, S. Du, Y. Wang, and H. J. Gao. Multi-oriented moiré superstructures of graphene on Ir(111): experimental observations and theoretical models. *J. Phys. Condens. Matter*, 24:314214, 2012.

[33] P. Merino, M. Svec, A. L. Pinardi, G. Otero, and J. A. Martín-Gago. Strain-driven moir é superstructures of epitaxial graphene on transition metal surfaces. *ACS Nano*, 5:5627, 2011.

[34] J. W. Cho, L. Gao, J. Tian, H. Cao, W. Wu, Q. Yu, E. N. Yitamben, B. Fisher, J. R. Guest, Y. P. Chen, and N. P. Guisinger. Atomic-scale investigation of graphene grown on Cu foil and the effects of thermal annealing. *ACS Nano*, 5:3607, 2011.

[35] A. Locatelli, C. Wang, C. Africh, N. Stojić, T. O. Mentes, G. Comelli, and N. Binggeli. Temperature-driven reversible rippling and bonding of a graphene superlattice. *ACS Nano*, 7:6955, 2013.

[36] D. Usachov, A. Dobrotvorskii, A. Varykhalov, O. Rader, W. Gudat, A. Shikin, and V. Adamchuk. Experimental and theoretical study of the morphology of commensurate and incommensurate graphene layers on Ni single-crystal surfaces. *Phys. Rev. B*, 78:085403, 2008.

[37] Y. Murata, V. Petrova, B. B. Kappes, A. Ebnonnasir, I. Petrov, Y. H. Xie, C. V. Ciobanu, and S. Kodambaka. Moiré uperstructures of graphene on faceted nickel islands. *ACS Nano*, 4:6509, 2010.

[38] A. Politano. Quasi-freestanding graphene on Ni(110): a graphene/metal contact with suppressed interface states. *Nano Res.*, 9:1795, 2016.

[39] J. Plutnar, M. Pumera, and Z. Sofer. The chemistry of CVD graphene. *J. Mater. Chem. C*, 6:6082, 2018.

[40] L. L. Patera, F. Bianchini, G. Troiano, C. Dri, C. Cepek, M. Peressi, C. Africh, and G. Comelli. Temperature-driven changes of the graphene edge structure on Ni(111): substrate vs hydrogen passivation. *Nano Lett.*, 15:56, 2015.

[41] M. Batzill. The surface science of graphene: Metal interfaces, CVD synthesis, nanoribbons, chemical modifications, and defects. *Surf. Sci. Rep.*, 67:83, 2012.

[42] H. I. Rasool, E. B. Song, M. J. Allen, J. K. Wassei, R. B. Kaner, K. L. Wang, B. H. Weiller, and J. K. Gimzewski. Continuity of graphene on polycrystalline copper. *Nano Lett.*, 11:251, 2011.

[43] Y. Zhang, L. Gomez, F. N. Ishikawa, A. Madaria, K. Ryu, C. Wang, A. Badmaev, and C. Zhou. Comparison of graphene growth on single-crystalline and polycrystalline Ni by chemical vapor deposition. *J. Phys. Chem. Lett.*, 1:3101, 2010.

[44] R. P. Feynman. Forces in molecules. *Phys. Rev.*, 56:340, 1939.

[45] P. Hohenberg and W. Kohn. Inhomogeneous electron gas. *Phys. Rev.*, 136:B864, 1964.

[46] W. Kohn and L. J. Sham. Self-consistent equations including exchange and correlation effects. *Phys. Rev.*, 140:A1133, 1965.

[47] P. Haas, F. Tran, and P. Blaha. Calculation of the lattice constant of solids with semilocal functionals. *Phys. Rev. B*, 79:085104, 2009.

[48] J. P. Perdew, K. Burke, and M. Ernzerhof. Generalized gradient approximation made simple. *Phys. Rev, Lett.*, 77:3865, 1996.

[49] C. G. Broyden. The convergence of a class of double-rank minimization algorithms 1. general considerations. *IMA Journal of Applied Mathematics*, 6:76, 1970.

[50] R. Fletcher. A new approach to variable metric algorithms. *The Computer Journal*, 13:317, 1970.

[51] D. Goldfarb. A family of variable-metric methods derived by variational means. *Math. Comp.*, 24:23, 1970.

[52] D. F. Shanno. Conditioning of quasi-newton methods for function minimization. *Math. Comp.*, 24(111):647, 1970.

[53] P. Giannozzi, S. Baroni, N. Bonini, M. Calandra, R. Car, C. Cavazzoni, D. Ceresoli, G. L. Chiarotti, M. Cococcioni, I. Dabo, A. Dal Corso, S. De Gironcoli, S. Fabris, G. Fratesi, R. Gebauer, U. Gerstmann, C. Gougoussis, A. Kokalj, M. Lazzeri, L. Martin-Samos, N. Marzari, F. Mauri, R. Mazzarello, S. Paolini, A. Pasquarello, L. Paulatto, C. Sbraccia, S. Scandolo, G. Sclauzero, A. P. Seitsonen, A. Smogunov, P. Umari, and R. M. Wentzcovitch. QUANTUM ESPRESSO: a modular and open-source software project for quantum simulations of materials. *J. Phys. Condens. Matter*, 21:395502, 2009.

[54] A. Baldereschi. Mean-value point in the Brillouin Zone. *Phys. Rev. B*, 7:5212, 1973.

[55] D. J. Chadi and Marvin L. Cohen. Special points in the Brillouin Zone. *Phys. Rev. B*, 8:5747, 1973.

[56] H. J. Monkhorst and J. D. Pack. Special points for Brilloiun-Zone integrations. *Phys. Rev. B*, 13:5188, 1976.

[57] D. R. Hamann, M. Schlüter, and C. Chiang. Norm-Conserving pseudopotentials. *Phys. Rev. Lett.*, 43:1494, 1979.

[58] D. Vanderbilt. Soft self-consistent pseudopotentials in a generalized eigenvalue formalism. *Phys. Rev. B*, 41:7892, 1990.

[59] K. Laasonen, A. Pasquarello, R. Car, C. Lee, and D. Vanderbilt. Car-Parrinello molecular dynamics with vanderbilt ultrasoft pseudopotentials. *Phys. Rev. B*, 47:10142, 1993.

[60] J. Tersoff and D. R. Hamann. Theory of the scanning tunneling microscope. *Phys. Rev. B*, 31:805, 1985.

[61] D. Necas and P. Klapetek. Gwyddion: an open-source software for SPM data analysis. *Cent. Eur. J. Phys.*, 10:181, 2012.

[62] G. Henkelman, B. P. Uberuaga, and H. Jónsson. A climbing image nudged elastic band method for finding saddle points and minimum energy paths. *J. Chem. Phys.*, 113(22):9901, 2000.

[63] N. Metropolis, A. W. Rosenbluth, M. N. Rosenbluth, A. H. Teller, and E. Teller. Equation of state calculations by fast computing machines. *J. Chem. Phys.*, 21:1087, 1953.

[64] J. R. Beeler. Displacement spikes in cubic metals. i. α-iron, copper, and tungsten. *Phys. Rev.*, 150:470, 1966.

[65] D. T. Gillespie. A general method for numerically simulating the stochastic time evolution of coupled chemical reactions. *J. Comp. Phys.*, 22:403, 1976.

[66] K. A. Fichthorn and W. H. Weinberg. Theoretical foundations of dynamical Monte Carlo simulations. *J. Chem. Phys.*, 95:1090, 1991.

[67] H. Eyring. The activated complex in chemical reactions. *J. Chem. Phys.*, 3:107, 1935.

[68] D. R. Bates. Collisions processes not involving chemical reactions. Resonance effects in atom-atom collisions. *Discuss. Faraday Soc.*, 33:7, 1962.

[69] R. E. Christoffersen. *Algorithms for Chemical Computations, Copyright, ACS Symposium Series, FOREWORD*, pages i–iv.

[70] D. Chandler. Statistical mechanics of isomerization dynamics in liquids and the transition state approximation. *J. Chem. Phys.*, 68:2959, 1978.

[71] A. F. Voter. A Monte Carlo method for determining free-energy differences and transition state theory rate constants. *J. Chem. Phys.*, 82:1890, 1985.

[72] G. H. Vineyard. Frequency factors and isotope effects in solid state rate processes. *J. Phys. Chem. Solids*, 3:121, 1957.

[73] P. Hänggi, P. Talkner, and M. Borkovec. Reaction-rate theory: fifty years after Kramers. *Rev. Mod. Phys.*, 62:251, 1990.

[74] G. Henkelman, B. P. Uberuaga, and H. Jónsson. A climbing image nudged elastic band method for finding saddle points and minimum energy paths. *J. Chem. Phys.*, 113:9901, 2000.

[75] V. Carnevali, L. L. Patera, G. Prandini, M. Jugovac, G. Comelli, M. Peressi, and C. Africh. Transition metal doping of epitaxial graphene by direct incorporation of nickel adatoms. *Submitted.*

[76] H. P. Komsa, J. Kotakoski, S. Kurasch, O. Lehtinen, U. Kaiser, and A. V. Krasheninnikov. Two-dimensional transition metal dichalcogenides under electron irradiation: Defect production and doping. *PRL*, 109:035503, 2012.

[77] H. Wang, Q. Wang, Y. Cheng, K. Li, Y. Yao, Q. Zhang, C. Dong, P. Wang, U. Schwingenschlögl, W. Yang, and X. X. Zhang. Doping monolayer graphene with single atom substitutions. *Nano Lett.*, 12:141, 2012.

[78] O. Cretu, A. V. Krasheninnikov, J. A. Rodríguez-Manzo, L. Sun, R. M. Nieminen, and F. Banhart. Migration and localization of metal atoms on strained graphene. *PRL*, 105:196102, 2010.

[79] L. L. Patera, C. Africh, R. S. Weatherup, R. Blume, S. Bhardwaj, C. Castellarin-Cudia, A. Knop-Gericke, R. Schloegl, G. Comelli, S. Hofmann, and C. Cepek. In situ observations of the atomistic mechanisms of Ni catalyzed low temperature graphene growth. *ACS Nano*, 7:7901, 2013.

[80] F. Bianchini, L. L. Patera, M. Peressi, C. Africh, and G. Comelli. Atomic scale identification of coexisting graphene structures on Ni(111). *J. Phys. Chem. Lett.*, 5:467, 2014.

[81] L. L. Patera, F. Bianchini, C. Africh, C. Dri, G. Soldano, M. M. Mariscal, M. Peressi, and G. Comelli. Real-time imaging of adatom-promoted graphene growth on nickel. *Science*, 359:1243, 2018.

[82] W. Zhao, S. M. Kozlov, O. Höfert, K. Gotterbarm, M. P. A. Lorenz, F. Viñes, C. Papp, A. Görling, and H. P. Steinrück. Graphene on Ni(111): Coexistence of different surface structures. *J. Phys. Chem. Lett.*, 2:759, 2011.

[83] S. M. Kozlov, F. Viñes, and A. Görling. Bonding mechanisms of graphene on metal surfaces. *J. Phys. Chem. Lett.*, 116:7360, 2012.

[84] D. Cheng, G. Barcaro, J. C. Charlier, M. Hou, and A. Fortunelli. Homogeneous nucleation of graphitic nanostructures from carbon chains on Ni(111). *J. Phys. Chem. Lett.*, 115:10537, 2011.

[85] S. Grimme. Density functional theory with london dispersion corrections. *WIREs Comput. Mol. Sci.*, 1:211, 2011.

[86] M. Methfessel and A. T. Paxton. High-precision sampling for Brillouin-Zone integration in metals. *Phys. Rev. B*, 40:3616, 1989.

[87] W. Humphrey, A. Dalke, and K. Schulten. VMD: visual molecular dynamics. *J. Mol. Graph.*, 14:33, 1996.

[88] Z. Zou, V. Carnevali, M. Jugovac, L. L. Patera, A. Sala, M. Panighel, C. Cepek, G. Soldano, M. M. Mariscal, M. Peressi, G. Comelli, and C. Africh. Graphene on nickel (100) micrograins: Modulating the interface interaction by extended moiré superstructures. *Carbon*, 130:441, 2018.

[89] Y. F. Zhang, T. Gao, S. Xie, B. Dai, L. Fu, Y. Gao, Y. Chen, M. Liu, and Z. Liu. Different growth behaviors of ambient pressure chemical vapor deposition graphene on Ni(111) and Ni films: a scanning tunneling microscopy study. *Nano Res*, 5:402, 2012.

[90] D. Eom, D. Prezzi, K. T. Rim, H. Zhou, M. Lefenfeld, S. Xiao, C. Nuckolls, M. S. Hybertsen, T. F. Heinz, and G. W. Flynn. Structure and electronic properties of graphene nanoislands on Co(0001). *Nano Lett.*, 9:2844, 2009.

[91] A. Dahal and M. Batzill. Graphene-nickel interfaces: a review. *Nanoscale*, 6:2548, 2014.

[92] C. Enderlein, Y. S. Kim, A. Bostwick, E. Rotenberg, and K. Horn. The formation of an energy gap in graphene on ruthenium by controlling the interface. *N. J. Phys.*, 12:033014, 2010.

[93] I. Pletikosi, M. Kralj, P. Pervan, R. Brako, J. Coraux, A. T. N'Diaye, C. Busse, and T. Michely. Dirac cones and minigaps for graphene on Ir(111). *Phys. Rev. Lett.*, 102:056808, 2009.

[94] N. A. Vinogradov, A. A. Zakharov, V. Kocevski, J. Rusz, K. A. Simonov, O. Eriksson, A. Mikkelsen, E. Lundgren, A. S. Vinogradov, N. Martensson, and A. B. Preobrajenski. Formation and structure of graphene waves on Fe(110). *Phys. Rev. Lett.*, 109:026101, 2012.

[95] X. Li, W. Cai, J. An, S. Kim, J. Nah, D. Yang, R. Piner, A. Velamakanni, I. Jung, E. Tutuc, S. K. Banerjee, L. Colombo, and R. S. Ruoff. Large-area synthesis of high-quality and uniform graphene films on copper foils. *Science*, 324:1312, 2009.

[96] P. W. Sutter, J. I. Flege, and E. A. Sutter. Epitaxial graphene on ruthenium. *Nature Mat.*, 7:406, 2008.

[97] J. Gao and F. Ding. The study on the medium-sized carbon islands on Ru(0001) surface. *J. Cluster Sci.*, 26:347, 2015.

[98] S. Nie, A. L. Walter, N. C. Bartelt, E. Starodub, A. Bostwick, E. Rotenberg, and K. F. McCarty. Growth from below: Graphene bilayers on Ir(111). *ACS Nano*, 5:2298, 2011.

[99] A. Dangwal Pandey, K. Krausert, D. Franz, E. Grånäs, R. Shayduk, P. Müller, T. F. Keller, H. Noei, V. Vonk, and A. Stierle. Single orientation graphene synthesized on iridium thin films grown by molecular beam epitaxy. *J. Appl. Phys.*, 120:075304, 2016.

[100] X. An, F. Liu, Y. J. Jung, and S. Kar. Large-area synthesis of graphene on palladium and their Raman spectroscopy. *J. Phys. Chem. C*, 116:16412, 2012.

[101] N. Aslam, V. Longo, C. Rodenbücher, F. Roozeboom, W. M. M. Kessels, K. Szot, R. Waser, and S. Hoffmann-Eifert. Impact of composition and crystallization behavior of atomic layer deposited strontium titanate films on the resistive switching of Pt/STO/TiN devices. *J. Appl. Phys.*, 116:064503, 2014.

[102] R. S. Weatherup, A. J. Shahani, Z. J. Wang, K. Mingard, A. J. Pollard, M. G. Willinger, R. Schloegl, P. W. Voorhees, and S. Hofmann. In situ graphene growth dynamics on polycrystalline catalyst foils. *Nano Letters*, 16:6196, 2016.

[103] E. Miniussi, M. Pozzo, A. Baraldi, E. Vesselli, R. R. Zhan, G. Comelli, T. O. Menteș, M. A. Niño, A. Locatelli, S. Lizzit, and D. Alfè. Thermal stability of corrugated epitaxial graphene grown on Re(0001). *Phys. Rev. Lett.*, 106:216101, 2011.

[104] T. Oznuluer, E. Pince, E. O. Polat, O. Balci, O.and Salihoglu, and C. Kocabas. Synthesis of graphene on gold. *Appl. Phys. Lett.*, 98:183101, 2011.

[105] F. Esch, C. Dri, A. Spessot, C. Africh, G. Cautero, D. Giuressi, R. Sergo, R. Tommasini, and G. Comelli. The FAST module: An add-on unit for driving commercial scanning probe microscopes at video rate and beyond. *Review of Scientific Instruments*, 82:053702, 2011.

[106] L. Vitos, H.L. Skriver, and J. Kollár. The formation energy for steps and kinks on cubic transition metal surfaces. *Surf. Sci.*, 425:212, 1999.

[107] L. Vitos, A. V. Ruban, H. L. Skriver, and J. Kollár. The surface energy of metals. *Surf. Sci.*, 411:186, 1998.

[108] Z. Zou, V. Carnevali, M. Peressi, G. Comelli, and C. Africh. Operando atomic-scale study of graphene cvd growth on polycrystalline nickel. *In preparation*.

[109] V. Carnevali, S. Marcantoni, and M. Peressi. Moirè relations for a superlattice generated by two generic bravais lattices. *In preparation*.

[110] A. K. Geim and I. V. Grigorieva. Van der Waals heterostructures. *Nature*, 499:419, 2013.

[111] K. S. Novoselov, A. Mishchenko, A. Carvalho, and A. H. Castro Neto. 2D materials and van der Waals heterostructures. *Science*, 353:6298, 2016.

[112] H. Kroemer. Nobel Lecture: Quasielectric fields and band offsets: teaching electrons new tricks. *Rev. Mod. Phys.*, 2001.

[113] V. Nicolosi, M. Chhowalla, M. G. Kanatzidis, M. S. Strano, and J. N. Coleman. Liquid exfoliation of layered materials. *Science*, 340:1420, 2013.

[114] P. Zeller and S. Günther. What are the possible moiré patterns of graphene on hexagonally packed surfaces? Universal solution for hexagonal coincidence lattices, derived by a geometric construction. *New J. Phys.*, 16:083028, 2014.

[115] P. Zeller, X. Ma, and S. Günther. Indexing moiré patterns of metal-supported graphene and related system: strategies and pitfalls. *New J. Phys.*, 17:013015, 2017.

[116] K. Hermann. Periodic overlayers and moiré patterns: theoretical studies of geometric properties. *J. Phys.: Condens. Matter*, 24:314210, 2012.

[117] A. Artaud, L. Magaud, T. Le Quang, V. Guisset, P. David, C. Chapelier, and J. Coraux. Universal classification of twisted, strained and sheared graphene moiré superlattices. *Sci. Rep.*, 6:25670, 2016.

[118] D. Stradi, L. Jelver, S. Smidstrup, and K. Stokbro. Method for determining optimal supercell representation of interfaces. *J. Phys.: Condens. Matter*, 6:185901, 2017.

[119] P. Lazic. *CellMatch*: Combining two unit cells into a common supercell with minimal strain. *Comp. Phys. Comm.*, 197:324, 2015.

[120] D. Akinwande, C. J. Brennan, J. Scott Bunch, P. Egberts, J. R. Felts, H. Gao, R. Huang, J. S. Kim, Y. Li, T.and Li, K. M. Liechti, N. Lu, H. S. Park, E. J. Reed, P. Wang, B. I. Yakobson, T. Zhang, Y. W. Zhang, Y. Zhou, and Y. Zhuo. A review on mechanics and mechanical properties of 2D materials-graphene and beyond. *EML*, 13:42, 2017.